

Electronic Thesis and Dissertation Repository

---

4-17-2015 12:00 AM

## Design Wind Loads for Solar Modules Mounted Parallel to the Roof of a Low-rise Building

Sarah Elizabeth Stenabaugh, *The University of Western Ontario*

Supervisor: Dr. G.A. Kopp, *The University of Western Ontario*

A thesis submitted in partial fulfillment of the requirements for the Doctor of Philosophy degree in Civil and Environmental Engineering

© Sarah Elizabeth Stenabaugh 2015

Follow this and additional works at: <https://ir.lib.uwo.ca/etd>



Part of the [Civil Engineering Commons](#)

---

### Recommended Citation

Stenabaugh, Sarah Elizabeth, "Design Wind Loads for Solar Modules Mounted Parallel to the Roof of a Low-rise Building" (2015). *Electronic Thesis and Dissertation Repository*. 2817.  
<https://ir.lib.uwo.ca/etd/2817>

This Dissertation/Thesis is brought to you for free and open access by Scholarship@Western. It has been accepted for inclusion in Electronic Thesis and Dissertation Repository by an authorized administrator of Scholarship@Western. For more information, please contact [wlsadmin@uwo.ca](mailto:wlsadmin@uwo.ca).

DESIGN WIND LOADS FOR SOLAR MODULES MOUNTED PARALLEL TO  
THE ROOF OF A LOW-RISE BUILDING

(Thesis format: Monograph)

by

«Sarah Elizabeth Stenabaugh»

Graduate Program in Civil and Environmental Engineering

A thesis submitted in partial fulfillment  
of the requirements for the degree of  
Doctor of Philosophy

The School of Graduate and Postdoctoral Studies  
The University of Western Ontario  
London, Ontario, Canada

© Sarah Elizabeth Stenabaugh 2015

## Abstract

The focus of this study was to assess the wind induced pressures on an array of solar modules mounted parallel to the roof surface of a low-rise building. Wind tunnel studies were conducted on an array on a 1/20 scale building model with either a flat roof or a 30° roof slope. Specific attention was made to determine the effect of the spacing between individual modules,  $G$ , and the mounting height above the roof surface,  $H$ , resulting in a dataset of 80 configurations. Large  $G$  yielded improved wind resistance by lowering the external peak suctions and peak net suctions. Large  $H$  beyond a small cavity depth was determined to be detrimental for wind resistance as the peak external suctions were higher in magnitude and the cavity pressures more uniform (resulting in larger magnitude net suctions). Pressure equalization between the external and cavity pressures resulted in the net pressures being typically lower than the external pressures. The pressure equalization coefficient,  $C_{eq}$  is utilized to quantify the change in the peak net wind pressure from the peak external pressure and is noted to be a robust parameter as values can be approximated as a single curve when plotted against  $G/H$  for a given tributary area. The magnitude of the curve is not largely affected by roof slope. Roof edge effects and array edge effects caused by flow separation off the roof and array were noted to increase the magnitude of the suctions on modules around the perimeter of the roof surface and array respectively. Applicable roof and array zone dimensions were defined by examining point pressures and area-averaged pressures. The bare roof interior and edge zones for low-rise buildings were noted to be appropriate to capture the effects of building-induced flow separation. The array edge zone was approximated based on  $H$  and the module thickness,  $t$ , such that the array edge zone was  $\approx 1(H + t)$  to  $2(H + t)$  around the perimeter of the array. A design factor,  $\gamma$ , was developed by enveloping  $C_{eq}$  values and is intended to be applied to codified components and cladding external pressure coefficients. It is a function of the roof zone (roof zone factor,  $\gamma_R$ ), the array zone (array edge factor,  $\gamma_E$ ),  $A$  and  $G/H$ . The design recommendations could serve to fill a current void in existing design standards with respect to loads for air-permeable, double-layer, roof systems such as solar arrays mounted parallel to roof surfaces.

## Keywords

wind loading; wind-induced pressures; air-permeable, double-layer, roof system; pressure equalization; photovoltaic (PV) arrays; low-rise buildings; codification

## Co-Authorship Statement

Dr. Gregory Kopp has been a very supportive and involved supervisor. He encouraged me through the process of defining the research problem and seeing through my plan. Under his guidance I designed and instrumented the wind tunnel model, supervised the tests and analyzed the data including the writing of all MATLAB code. The preparation of figures and text was done by me, aided by questions and input from Dr. Kopp. I received valuable design input from the University Machine Shop Services, who fabricated the model, and assistance from fellow students with testing the numerous configurations.

Selected elements from the work presented herein have been published in the Journal of Wind Engineering and Industrial Aerodynamics. The article, “Wind loads on photovoltaic arrays mounted parallel to sloped roofs on low-rise buildings”, was published online on the 30<sup>th</sup> of January, 2015. It presents a validation of the sloped roof model, pressure coefficients, and pressure equalization coefficients (elements of chapters 3 & 5). This article was coauthored by Yumi Iida, Dr. Gregory Kopp and Dr. Panagiota Karava. Yumi Iida was an exchange student at the Boundary Layer Wind Tunnel Laboratory in 2007 and 2008. She assisted with conducting the wind tunnel studies and was instrumental in making the sheer number of configurations manageable. Dr. Kopp as my supervisor aided with the overall direction, theme and message of the paper through many discussions. Dr. Karava was my undergraduate thesis supervisor and started me on this subject. Her guidance in the initial stages is very much appreciated.

Jeong Hee Oh was kind enough to provide me with some data from his doctoral experiments for discussions related to cavity pressure distributions. All of his data has been cited and his generosity is appreciated. It should be noted that while some data from this set of experiments, and those of Jeong Hee, have already been published, none of the figures, tables or text from this thesis have been presented in the exact same manner to respect copyright of all authors involved. I have generated new figures in each instance and have changed the text while preserving, and enhancing the message as understanding advanced.

## Acknowledgments

My experience at the Boundary Layer Wind Tunnel Laboratory at the University of Western Ontario has been a positive one, largely due to the assistance and encouragement I received from a number of individuals associated with the lab and facilities.

Thank you to my supervisor, Dr. Greg Kopp, for providing me with opportunities to gain knowledge and experience. Thank you to the wind tunnel technicians, Mr. Gerry Dafoe and Mr. Anthony Burggraaf, for their assistance and patience. The staff at University Machine Shop Services fabricated my experimental model and their attention to detail and design capabilities were instrumental to my research. Mrs. Karen Norman is nothing short of amazing and has been a continuous source of support and guidance. Thank you to my fellow students, most notably Dr. Adam Kirchhefer and Dr. Maryam Refan, for their advice and perspective, for lending a helping hand and for their friendship. I look forward to maintaining these connections throughout our careers, wherever they take us.

I will never be able to thank my family enough, for their never-failing support and for encouraging me to pursue my dreams. Thank you for helping to make this thesis a reality.

# Table of Contents

Abstract.....	ii
Co-Authorship Statement.....	iv
Acknowledgments.....	v
Table of Contents.....	vi
List of Tables.....	ix
List of Figures.....	x
List of Appendices.....	xxii
List of Nomenclature.....	xxiii
1 Introduction.....	1
1.1 Background and Motivation.....	1
1.2 Previous testing of tilted solar arrays mounted on flat roofs.....	2
1.3 Previous testing of solar modules mounted parallel to roofs.....	4
1.4 Loose-laid paving systems.....	5
1.5 Pressure equalization.....	9
1.6 Design Standards.....	13
1.7 Objectives.....	21
2 Experimental set-up and analysis procedure.....	23
2.1 Choice of model scale.....	23
2.2 Terrain simulation.....	26
2.3 Building model and instrumentation.....	29
2.4 Area-averages.....	35
2.5 Pressure equalization coefficient.....	37
3 Overview of measured pressure coefficients.....	39

3.1	Comparison with previous studies .....	40
3.2	External (upper surface) pressure distributions on the sloped roof model .....	43
3.3	Cavity (lower surface) pressures on the sloped roof model.....	47
3.4	Net pressure distributions on the sloped roof model .....	51
3.5	Area-averaged pressure coefficients .....	59
3.6	Pressure coefficients on the flat roof model .....	62
3.7	Summary .....	68
4	Pressure Equalization.....	70
4.1	Instantaneous Pressure Equalization.....	70
4.2	Parameter describing cavity pressure distributions for a single module.....	73
4.3	Parameter describing cavity pressure distributions for multiple modules .....	77
4.4	Effective cavity length .....	84
5	Pressure equalization coefficient.....	86
5.1	Effects of $G$ and $H$ on $C_{eq}$ .....	86
5.2	Effects of area-averaging .....	88
5.3	Effects of roof slope.....	90
5.4	Effect of simulated larger modules.....	91
5.5	Effect of module aspect ratio .....	96
5.6	Summary .....	98
6	Array and roof zones.....	100
6.1	Definition of the “array edge effect distance” or zone .....	101
6.2	Quantification of the array edge zone using the flat roof model .....	105
6.3	Validation of the array edge zone using the sloped roof model .....	114
6.4	Wind loading on the interior array zone .....	116
6.5	Determination of applicable roof zones.....	121

6.6 Effects of the shroud .....	124
6.7 Summary .....	130
7 Development of design guidelines .....	131
8 Conclusions .....	144
References .....	149
Appendix A: Wind tunnel testing details .....	156
Appendix B: Different contouring approaches for peak pressure coefficient distributions .....	164
Curriculum Vitae .....	173

## List of Tables

Table 1: Gap, height and array dimensions .....	31
Table 2: $G/H$ and Phi values calculated using the equation and definition for the single cavity for multiple $H$ data adapted from Oh and Kopp 2015 .....	76
Table 3: Phi values a small cavity depth from Oh and Kopp 2015 $G = 1$ mm; $H = 1.2$ mm and the current study $G = 12$ cm; $H = 2$ cm on the flat roof.....	81
Table 4: Phi values for a large cavity system from Oh and Kopp 2015 $G = 1$ mm; $H = 15$ mm and the current study $G = 12$ cm; $H = 20$ cm on the flat roof.....	83
Table 5: Roof edge zone widths from design standards and literature for flat roof model .....	123
Table 6: Analysis cases representing combinations of array and roof zones considered for the development of the roof zone factor, $\gamma_R$ , and the array zone factor, $\gamma_E$ .....	132
Table A1: Sloped-roof configurations (base configurations, original 42).....	158
Table A2 : Flat-roof configurations .....	159
Table A3 : Shroud sloped-roof configurations .....	159
Table A4: Shroud flat-roof configurations .....	160
Table A5 : Tributary area combinations .....	163

# List of Figures

Figure 1-1: Sketch of the conical vortices from a cornering wind direction with secondary separation and reattachment lines (adapted from Holmes, 2007 and Bienkiewicz and Sun, 1992) .....	7
Figure 1-2: Roof zones and external pressure coefficients for 27 – 45° gable roof slopes adapted from ASCE 7-10 (2010) .....	15
Figure 1-3: Roof zones and nominal net pressure coefficients adapted from SEAOC PV2-2012 (2012).....	19
Figure 1-4: Sketch of edge and sheltered modules with array edge factors adapted from SEAOC PV2-2012 (2012) .....	20
Figure 2-1: Photo of sloped roof model.....	27
Figure 2-2: Mean wind speed and streamwise turbulence intensity profiles.....	28
Figure 2-3: Longitudinal spectrum measurements from the wind tunnel for $z_0 = 0.01$ m	29
Figure 2-4: Drawings of the array denoting the gap, G, and height, H, variables .....	31
Figure 2-5 Scale model of a) the flat-roof model and b) the sloped model with the shroud surrounding the array .....	32
Figure 2-6 Photos of the array taped in the 2x2 set-up (left) and 4x4/3x4 (right).....	33
Figure 2-7: Simulated larger module dimensions.....	34
Figure 3-1: Mean point pressure coefficients from the sloped roof model - comparison with previous studies.....	41
Figure 3-2: Mean point pressure coefficients from the flat roof model - comparison with previous studies.....	42

Figure 3-3: Contour map of instantaneous external point pressures resulting in peak external suction $G \approx 0$ ; $H \approx 0$ (left) and mean external point pressures for the peak wind direction of $112.5^\circ$ (right) .....	44
Figure 3-4: Contour map of instantaneous external point pressures resulting in peak external suction $G \approx 0$ ; $H = 20$ cm (left) and mean external point pressures for the peak wind direction of $292.5^\circ$ (right) .....	45
Figure 3-5: Contour map of instantaneous external point pressures resulting in peak external suction $G = 12$ cm; $H \approx 0$ (left) and mean external point pressures for the peak wind direction of $315^\circ$ (right) .....	46
Figure 3-6: Contour map of instantaneous cavity point pressures at the instant of peak external suction for the $G = 12$ cm; $H \approx 0$ configuration (left) and mean cavity point pressures for the peak (external) wind direction of $315^\circ$ (right) .....	46
Figure 3-7: Contour map of instantaneous cavity point pressures resulting in peak cavity suction $G \approx 0$ ; $H \approx 0$ (left) and mean cavity point pressures for the peak wind direction of $67.5^\circ$ (right) .....	48
Figure 3-8: Contour map of instantaneous cavity point pressures resulting in peak cavity suction $G \approx 0$ ; $H = 20$ cm (left) and mean cavity point pressures for the peak wind direction of $90^\circ$ (right) .....	49
Figure 3-9: Contour map of instantaneous cavity point pressures resulting in peak cavity suction $G = 12$ cm; $H = 20$ cm (left) and mean cavity point pressures for the peak wind direction of $90^\circ$ (right) .....	50
Figure 3-10: Contour map of instantaneous cavity point pressures at the occurrence of the peak external suction $G = 12$ cm; $H = 20$ cm (left) and mean cavity point pressures for the peak external wind direction of $67.5^\circ$ (right) .....	51

Figure 3-11: Contour map of a) instantaneous net point pressures resulting in peak net suction  $G \approx 0$ ;  $H \approx 0$ , b) mean net point pressures for the peak wind direction of  $112.5^\circ$ , c) instantaneous external and d) cavity point pressures that resulted in peak net suction 53

Figure 3-12: Contour map of a) instantaneous net point pressures resulting in peak net suction  $G \approx 0$ ;  $H = 20$  cm, b) mean net point pressures for the peak wind direction of  $292.5^\circ$ , c) instantaneous external and d) cavity point pressures that resulted in peak net suction..... 54

Figure 3-13: Contour map of a) instantaneous net point pressures resulting in peak net suction  $G = 12$  cm;  $H \approx 0$ , b) mean net point pressures for the peak wind direction of  $315^\circ$ , c) instantaneous external and d) cavity point pressures that resulted in peak net suction..... 55

Figure 3-14: Distribution of the external-cavity point pressure correlation coefficients for the peak wind direction of  $112.5^\circ$  ( $G \approx 0$ ;  $H \approx 0$ )..... 56

Figure 3-15: Distribution of the external-cavity point pressure correlation coefficients for the peak wind direction of  $292.5^\circ$  ( $G \approx 0$ ;  $H = 20$  cm)..... 57

Figure 3-16: Distribution of the external-cavity point pressure correlation coefficients for the peak wind direction of  $315^\circ$  ( $G = 12$  cm;  $H \approx 0$ )..... 58

Figure 3-17: The worst case values of the peak (suction) external area-averaged over a single module on (a) the external, upper, surface, (b) in the cavity, and (c) net with respect to  $H$ ..... 60

Figure 3-18: The worst case values of the peak (suction) external area-averaged over a single module on (a) the external, upper, surface, (b) in the cavity, with respect to  $G$  .... 60

Figure 3-19: Contour map of instantaneous external point pressure coefficients resulting in peak external uplift  $G = 12$  cm;  $H \approx 0$  (left) and mean external point pressure coefficients for the peak wind direction of  $45^\circ$  on the flat roof (right)..... 63

Figure 3-20: Contour map of instantaneous cavity point pressure coefficients resulting in peak cavity suction $G = 12$ cm; $H \approx 0$ (left) and mean cavity point pressure coefficients for the peak wind direction of $45^\circ$ on the flat roof (right) .....	64
Figure 3-21: Contour map of instantaneous cavity point pressure coefficients resulting in peak cavity suction $G = 12$ cm; $H = 20$ cm (left) and mean cavity point pressure coefficients for the peak wind direction of $180^\circ$ on the flat roof (right).....	64
Figure 3-22: Distribution of the external-cavity point pressure correlation coefficients for the peak wind direction of $45^\circ$ on the flat roof ( $G = 12$ cm; $H \approx 0$ ) .....	65
Figure 3-23 Contour map of a) instantaneous net point pressures resulting in peak net uplift for the $G = 12$ cm; $H \approx 0$ flat roof configuration, b) mean net point pressure coefficient for the same (peak) wind direction of $45^\circ$ , c) instantaneous external and d) instantaneous cavity point pressures that resulted in peak net uplift .....	66
Figure 3-24: Contour map of a) instantaneous net pressure resulting in peak net point pressure for the $G = 12$ cm; $H = 20$ cm flat roof configuration, b) mean net point pressure coefficient for the same (peak) wind direction of $45^\circ$ , c) instantaneous external and d) instantaneous cavity point pressures that resulted in peak net uplift .....	67
Figure 3-25: The worst case values of the peak (suction) external area-averaged over a single module on (a) the external, upper, surface, (b) in the cavity, and (c) net with respect to $H$ for the sloped roof model (grey) and the flat roof model (black).....	68
Figure 4-1: Sample external (black) and cavity (grey) pressure time histories, area-averaged over a single module for a) a sampling period of 10 seconds and b) $\frac{1}{2}$ second before and after the largest measured external suction.....	71
Figure 4-2: Non-simultaneous peak suction and mean values of the external and cavity pressure coefficients for module 1 (upper) and module 14 (lower) with respect to wind direction for $G = 12$ cm; $H = 20$ cm on the sloped roof .....	72

Figure 4-3: External and cavity RMS values for module 1 (upper) and module 14 (lower) with respect to wind direction for $G = 12 \text{ cm}$ ; $H = 20 \text{ cm}$ and $G = 12 \text{ cm}$ ; $H = 2 \text{ cm}$ on the sloped roof .....	73
Figure 4-4: Sketch of external and cavity pressure distributions for $\varphi < 1$ and $\varphi > 1$ .....	75
Figure 4-5: External and cavity pressures along a line of taps for a single cavity for multiple $H$ (adapted from Oh and Kopp 2015).....	76
Figure 4-6: Mean external and cavity pressures along multiple modules; $G = 1 \text{ mm}$ ; various $H$ from Oh and Kopp (2015).....	78
Figure 4-7: Comparison of mean external and cavity pressures along a single tap line from $G = 1 \text{ mm}$ ; $H = 1.2 \text{ mm}$ (Oh and Kopp, 2015) and $G = 12 \text{ cm}$ ; $H = 2 \text{ cm}$ flat roof configuration ( $270^\circ$ ) from the current study with respect to $x/h$ .....	79
Figure 4-8: Comparison of mean external and cavity pressures along a single tap line from $G = 1 \text{ mm}$ ; $H = 1.2 \text{ mm}$ (Oh and Kopp, 2015) and $G = 12 \text{ cm}$ ; $H = 2 \text{ cm}$ flat roof configuration ( $270^\circ$ ) from the current study normalized over module length.....	81
Figure 4-9: External and cavity pressures along a line of taps for a multiple modules for $G = 15 \text{ mm}$ ; $H = 1.2 \text{ mm}$ (adapted from Oh and Kopp 2015) .....	82
Figure 4-10: Comparison of mean external and cavity pressures along a single tap line from $G = 1 \text{ mm}$ ; $H = 15 \text{ mm}$ (Oh and Kopp, 2015) and $G = 12 \text{ cm}$ ; $H = 20 \text{ cm}$ flat roof configuration ( $270^\circ$ ) from the current study normalized over module length.....	83
Figure 5-1: Pressure equalization coefficient for single modules with respect to $H$ .....	87
Figure 5-2: Pressure equalization coefficient for single modules with respect to $G$ .....	88
Figure 5-3: Pressure equalization coefficients with respect to the $G/H$ ratio for four tributary areas from the sloped roof model.....	90

Figure 5-4: Pressure equalization coefficients with respect to the $G/H$ ratio for four tributary areas from the sloped roof (open markers) and flat roof (solid markers) models .....	91
Figure 5-5: Pressure equalization coefficients with respect to the $G/H$ ratio simulating three module sizes from the sloped roof (left) and flat roof (solid right) models.....	93
Figure 5-6: Worst, peak, cavity (suction) coefficients area-averaged over three areas simulating different module sizes plotted with respect to the $G/H$ ratio from the sloped roof (left) and flat roof (solid right) models.....	94
Figure 5-7: Worst, peak, external (suction) coefficients area-averaged over three areas simulating different module sizes plotted with respect to the $G/H$ ratio from the sloped roof (left) and flat roof (solid right) models.....	94
Figure 5-8: Worst, peak, net (suction) coefficients area-averaged over three areas simulating different module sizes plotted with respect to the $G/H$ ratio from the sloped roof (left) and flat roof (solid right) models.....	95
Figure 5-9: Pressure equalization coefficients with respect to the $G/H$ ratio simulating three module sizes from the sloped roof (left) and flat roof (solid right) models with values from the sealed data plotted with respect to effective (lower) $G/H$ superimposed in red .....	96
Figure 5-10: Peak net suction (left) and pressure equalization coefficients (right) with respect to $G/H$ for two different aspect ratios.....	97
Figure 5-11: Peak net suction (left) and pressure equalization coefficients (right) with respect to $G/H$ for three different aspect ratios.....	98
Figure 6-1: Plan view of the flat roof model.....	100
Figure 6-2: Schematic of array edge effects from flow separation at the leading edge of the array on the current model .....	102

Figure 6-3: Conceptual flow patterns on the external (upper) surface of the array and in the cavity for a range of  $H$  (inspired by from Malavasi and Trabucchi, 2008; Blois and Malavasi, 2007; Martinuzzi et al., 2003; and Auteri et al., 2008) ..... 104

Figure 6-4: External peak suction, mean and RMS pressure coefficients measured along the top row of pressure taps on the middle row of modules for the  $270^\circ$  wind direction for the  $G = 12$  cm configurations on the flat roof..... 107

Figure 6-5: External mean and RMS pressure coefficients measured along the top row of pressure taps on the middle row of modules for the  $270^\circ$  wind direction for the  $G = 12$  cm configurations on the flat roof..... 108

Figure 6-6: Cavity mean and RMS pressure coefficients measured along the top row of pressure taps on the middle row of modules for the  $270^\circ$  wind direction for the  $G = 12$  cm configurations on the flat roof..... 109

Figure 6-7: External mean and RMS pressure coefficients measured along the bottom row of pressure taps on the bottom (field) row of modules for the  $225^\circ$  wind direction for the  $G = 12$  cm configurations on the flat roof ..... 110

Figure 6-8: External mean and RMS pressure coefficients measured along two tap lines on the column of modules adjacent to the field of the roof for the  $225^\circ$  wind direction for the  $G = 12$  cm configurations on the flat roof..... 111

Figure 6-9: External mean and RMS pressure coefficients measured along two tap lines on an interior column of modules for the  $180^\circ$  wind direction for the  $G = 12$  cm configurations on the flat roof..... 112

Figure 6-10: External mean and RMS pressure coefficients measured along two tap lines on an interior row of modules for the  $270^\circ$  wind direction for the shrouded and sealed (4x4/3x4)  $G = 12$  cm configurations on the flat roof..... 113

Figure 6-11: External mean and RMS pressure coefficients measured along the top row of pressure taps on the middle row of modules for the 270° wind direction for the  $G \approx 0$  configurations on the sloped roof ..... 115

Figure 6-12: Cavity mean and RMS pressure coefficients measured along the top row of pressure taps on the middle row of modules for the 270° wind direction for the  $G \approx 0$  configurations on the sloped roof ..... 115

Figure 6-13: Array edge zone as approximated by  $\approx 1(H + t)$  to  $2(H + t)$  (left) and as used for developing design recommendations (right)..... 116

Figure 6-14: The worst case values of the peak (suction) (a) external, (b) cavity, and (c) net pressure coefficients, area-averaged over a single solar module and (d) the pressure equalization coefficient ( $C_{eq}$ ) with respect to  $H$ ; considering only the interior modules. .... 118

Figure 6-15: The worst case values of the peak (suction) (a) external, (b) cavity, and (c) net pressure coefficients, area-averaged over a single solar module and (d) the pressure equalization coefficient ( $C_{eq}$ ) with respect to  $G$ ; considering only the interior modules. .... 119

Figure 6-16: The peak maxima pressure equalization coefficient ( $C_{eq}$ ) for the edge and interior zones for the single module area ( $0.73\text{m}^2$ ) with respect to  $G/H$  for the sloped and flat roof models ..... 120

Figure 6-17: Peak net (suction) pressure coefficients with respect to  $H$  measured in each roof zone on the flat roof model ( $G = 12 \text{ cm}$ )..... 122

Figure 6-18: The peak net (suction) coefficient measured on each module for the  $G = 12 \text{ cm}$ ;  $H = 20 \text{ cm}$  (left) and  $G = 12 \text{ cm}$ ;  $H \approx 0$  (right) configurations on the flat roof model ..... 123

Figure 6-19: Roof edge zones as defined by existing design standards and literature ... 124

Figure 6-20: The pressure equalization coefficient (left) and the mean net pressure coefficient (right) for open and shrouded array for  $G = 12$ ;  $H = 20$  cm and  $G = 12$ ;  $H = 2$  cm on the flat roof model..... 126

Figure 6-21: The mean external (left) and the mean cavity (right) pressure coefficient for open and shrouded array for  $G = 12$ ;  $H = 20$  cm and  $G = 12$ ;  $H = 2$  cm on the flat roof 127

Figure 6-22: Mean external point pressure contours for the a)  $G = 12$  cm;  $H = 20$  cm open array, b)  $G = 12$  cm;  $H = 2$  cm open array, c)  $G = 12$  cm;  $H = 20$  cm shrouded array and d)  $G = 12$  cm;  $H = 2$  cm shrouded array on the flat roof model ..... 128

Figure 6-23: Mean cavity point pressure contours for the a)  $G = 12$  cm;  $H = 20$  cm open array, b)  $G = 12$  cm;  $H = 2$  cm open array, c)  $G = 12$  cm;  $H = 20$  cm shrouded array and d)  $G = 12$  cm;  $H = 2$  cm shrouded array on the flat roof model ..... 129

Figure 6-24: Schematic of potential aerodynamic shroud to mitigate array edge effects ..... 130

Figure 7-1: Schematic of modules used to evaluate the pressure equalization coefficient for the different array and roof zone cases considered for design for the flat roof model ..... 134

Figure 7-2: Schematic of modules used to evaluate the pressure equalization coefficient for the different array and roof zone cases considered for design for the sloped roof model..... 135

Figure 7-3: Pressure equalization coefficients with respect to tributary area and design factor  $\gamma_R$  for a); roof zone 1 and  $G/H < 1$ , b) roof zone 1 and  $G/H \geq 1$ , c) roof zone 2 and  $G/H < 1$ , d) roof zone 2 and  $G/H \geq 1$  ..... 137

Figure 7-4: Pressure equalization coefficients with respect to tributary area and design factors  $\gamma_R$  and  $\gamma_R \cdot \gamma_E$  where  $\gamma_E$  is a single value for a) roof zone 1 and  $G/H < 1$ , b) roof zone 1 and  $G/H \geq 1$ , c) roof zone 2 and  $G/H < 1$ , d) roof zone 2 and  $G/H \geq 1$  ..... 138

Figure 7-5: Pressure equalization coefficients with respect to tributary area and design factors $\gamma_R$ and $\gamma_R \cdot \gamma_E$ where $\gamma_E$ is a separate value for a) roof zone 1 and $G/H < 1$ , b) roof zone 1 and $G/H \geq 1$ , c) roof zone 2 and $G/H < 1$ , d) roof zone 2 and $G/H \geq 1$ .....	139
Figure 7-6: Possible design figure to evaluate $\gamma_R$ and table to determine $\gamma_E$ .....	140
Figure 7-7: Pressure equalization coefficients with respect to tributary area and design factors $\gamma_R$ and $\gamma_R \cdot \gamma_E$ for a) roof zone 1 and $G/H < 1$ , b) roof zone 1 and $G/H \geq 1$ , c) roof zone 2 and $G/H < 1$ , d) roof zone 2 and $G/H \geq 1$ .....	141
Figure 7-8: Design factor, $\gamma$ , for solar installations mounted parallel to roof surfaces of low-rise buildings to be applied to the external pressure coefficient from the components and cladding procedure in existing design standards.....	142
Figure A1 : Model dimensions - sloped roof model .....	156
Figure A2 : Model dimensions - flat roof model .....	157
Figure A3 : Tap labels for pressure taps on the upper surface of the array .....	161
Figure A4 : Tap labels for pressure taps on the lower surface of the array .....	161
Figure A5: Tap labels for pressure taps on the roof surface ( $G=0$ roof piece shown)....	162
Figure A6 : Tap locations on the individual modules.....	162
Figure B1: Instantaneous external pressure coefficients resulting in the peak external suction, area-averaged over a single module for the $G \approx 0$ ; $H \approx 0$ configuration on the sloped roof model .....	164
Figure B2: Instantaneous external pressure distribution, evaluated for the entire array, which results in the peak external suction, area-averaged over a single module for the $G \approx 0$ ; $H \approx 0$ configuration on the sloped roof model.....	165

Figure B3: Instantaneous external pressure distribution, evaluated for the individual modules, which results in the peak external suction, area-averaged over a single module for the $G \approx 0$ ; $H \approx 0$ configuration on the sloped roof model .....	166
Figure B4: Instantaneous external pressure coefficients resulting in the peak external suction, area-averaged over a single module for the $G \approx 0$ ; $H = 20$ cm configuration on the sloped roof model.....	166
Figure B5: Instantaneous external pressure distribution, evaluated for the entire array, which results in the peak external suction, area-averaged over a single module for the $G \approx 0$ ; $H = 20$ cm configuration on the sloped roof model.....	167
Figure B6: Instantaneous external pressure distribution, evaluated for the individual modules, which results in the peak external suction, area-averaged over a single module for the $G \approx 0$ ; $H = 20$ cm configuration on the sloped roof model .....	168
Figure B7: Instantaneous cavity pressure coefficients resulting in the peak cavity suction, area-averaged over a single module for the $G \approx 0$ ; $H = 20$ cm configuration on the sloped roof model.....	168
Figure B8: Instantaneous cavity pressure distribution, evaluated for the entire array, which results in the peak cavity suction, area-averaged over a single module for the $G \approx 0$ ; $H = 20$ cm configuration on the sloped roof model.....	169
Figure B9: Instantaneous cavity pressure distribution, evaluated for the individual modules, which results in the peak cavity suction, area-averaged over a single module for the $G \approx 0$ ; $H = 20$ cm configuration on the sloped roof model.....	170
Figure B10: Instantaneous external pressure coefficients resulting in the peak external suction, area-averaged over a single module for the $G = 12$ cm; $H \approx 0$ configuration on the sloped roof model.....	170

Figure B11: Instantaneous external pressure distribution, evaluated for the entire array, which results in the peak external suction, area-averaged over a single module for the  $G = 12$  cm;  $H \approx 0$  configuration on the sloped roof model ..... 171

Figure B12: Instantaneous external pressure distribution, evaluated for the individual modules, which results in the peak external suction, area-averaged over a single module for the  $G = 12$  cm;  $H \approx 0$  configuration on the sloped roof model ..... 172

## List of Appendices

Appendix A: Wind tunnel testing details.....	156
Appendix B: Different contouring approaches for peak pressure coefficient distributions.....	164

## List of Nomenclature

The nomenclature used throughout the thesis is listed below. The source for design code parameters is indicated in parenthesis where applicable.

$A$	tributary area
$a$	parameter to set the dimensions of roof zones (ASCE 7-10)
$a_i$	weighted area for area-averaged pressure
$a_{pv}$	parameter to set the dimensions of roof zones (SEAOC PV2-2012)
$B$	length of the model
$c$	combination of modules
$C_{eq}$	pressure equalization coefficient
$C_L$	orifice loss coefficient
$Cp_E(t)$	instantaneous external (upper surface) pressure coefficient
$\bar{C}p_E$	mean external (upper surface) pressure coefficient
$Cp_{AE}$	area-averaged external (upper surface) pressure coefficient
$\bar{C}p_{AE}$	area-averaged, mean external pressure coefficient
$\hat{C}p_{AE}$	area-averaged, Lieblein-fitted, peak (suction) external pressure coefficient
$Cp_C(t)$	instantaneous cavity (upper surface) pressure coefficient
$Cp_{AC}$	area-averaged cavity pressure coefficient
$\bar{C}p_{AC}$	area-averaged, mean cavity pressure coefficient
$\hat{C}p_{AC}$	area-averaged, Lieblein-fitted, peak (suction) cavity pressure coefficient
$Cp_N(t)$	instantaneous net (upper surface) pressure coefficient
$Cp_{AN}$	area-averaged net pressure coefficient
$\bar{C}p_{AN}$	area-averaged, mean net pressure coefficient
$\hat{C}p_{AN}$	area-averaged, Lieblein-fitted, peak (suction) net pressure coefficient
$d_x$	module set-back from roof edge (SEAOC PV2-2012)
$E$	array edge factor (SEAOC PV2-2012)
$f$	frequency
$f_H$	cavity friction coefficient
$f_i$	orifice friction coefficient
$G$	gap between the modules

$G/H$	system relative permeability
$(GC_p)$	external pressure coefficient (ASCE 7-10)
$(GC_{pi})$	internal pressure coefficient (ASCE 7-10)
$(GC_{rn})$	combined net pressure coefficient (SEAOC PV2-2012)
$(GC_{rn})_{nom}$	nominal net pressure coefficient (SEAOC PV2-2012)
$H$	cavity depth
$h$	mean roof height for sloped-roof model; eave height for flat roof model
$h_c$	characteristic height (SEAOC PV2-2012)
$h_l$	height between roof surface and lower end of module (SEAOC PV2-2012)
$k_z$	exposure factor (ASCE 7-10)
$k_{zt}$	topography factor (ASCE 7-10)
$k_d$	directionality factor (ASCE 7-10)
$L$	module length
$L_c$	effective cavity length
$n$	point pressures considered for area-averaged pressures
$p$	design wind pressure (ASCE 7-10)
$q_h$	velocity pressure (ASCE 7-10)
Re	Reynolds number
Re <sub>H</sub>	Reynolds number in the cavity
$t$	module thickness
$U$	mean streamwise velocity in the wind tunnel
$U_c$	mean streamwise velocity in the cavity
$U_h$	mean streamwise velocity at mean or eave roof height
$V$	basic wind speed (ASCE 7-10)
$W_L$	width of building on longer building side (SEAOC PV2-2012)
$z_0$	roughness length
$\gamma$	proposed design multiplication factor
$\gamma_C$	chord factor (SEAOC PV2-2012)
$\gamma_E$	array zone factor
$\gamma_P$	parapet height factor (SEAOC PV2-2012)
$\gamma_R$	roof zone factor

$\Delta\bar{C}p_i$	mean pressure drop through the cavity
$\Delta\bar{C}p_o$	mean pressure drop through the orifice
$\theta$	wind direction
$\lambda_L$	length scale
$\lambda_V$	velocity scale
$\nu$	kinematic viscosity of air
$\varphi$	parameter to predict of cavity pressure distribution
$\omega$	module tilt angle (SEAOC PV2-2012)
①	interior roof zone (ASCE 7-10)
②	interior roof zone (ASCE 7-10)

# 1 Introduction

Awareness of our energy consumption as a society is increasing, as is the desire to locally produce energy using so-called “green technologies”. One possible source of green energy is roof-mounted solar, photovoltaic (PV), modules. These modules (sometimes referred to as panels) cover roof surfaces and, thus, are exposed to the elements, including wind. To ensure that the system is adequately designed to withstand the forces expected to act on it during its lifetime, the wind loading on these modules needs to be determined. The majority of building-mounted solar arrays are placed on the roofs of low-rise buildings, so it is the wind field above such structures which control the wind loads. The flow environment and aerodynamics of low-rise buildings are complex due to the interactions of the turbulence in the wind with the turbulence and vortices generated by the large-scale flow separations from the buildings themselves. This leads to large uplift forces on low-rise building roofs, but is also a challenging flow environment for roof-mounted equipment such as solar arrays. Boundary layer wind tunnels can be used to test scale models of roof-mounted solar systems in a multitude of configurations to determine the effect of multiple design variables in an economical and timely fashion and ultimately develop design standards.

## 1.1 Background and Motivation

Technology, construction methods and best practices are constantly evolving in our world. Early adopters require (and encourage) research to determine the effects of key design parameters. However, the required experiments can be expensive and aren't feasible for each installation – although carefully composed research can determine the impact of altering key geometric parameters. Such work can eventually lead to the development of design standards which are accepted by the emerging industry. These design standards, such as building codes, have generalized procedures that are widely accepted and used. Once a procedure or design values are included in a building code, the number of individuals with the knowledge and tools required to engineer such systems grows rapidly, further encouraging the adoption of new technologies. This has been the case with roof-mounted, tilted-panel, array installations.

## 1.2 Previous testing of tilted solar arrays mounted on flat roofs

Over the past decade, roof-mounted solar systems have tended to be tilted arrays of multiple modules installed on the large, low-slope, commercial roofs of low-rise structures. The lack of design provisions in building codes for these initial installations, coupled with their magnitude in size and cost of installation, justified wind tunnel studies to examine the aerodynamics, as well as to quantify the loads. Some of the notable studies include Geurts and van Bentum 2006, 2007; Kopp et al., 2012; Banks, 2013; Kopp 2013; Kopp and Banks; 2013, Cao et al.; 2013; Maffei et al., 2013; and Pratt and Kopp, 2013; although early studies were conducted by Tieleman et al., (1980). These studies identified the role of the building geometry (i.e., building height, plan dimensions, parapet height) and array geometry (panel tilt angle, chord, tributary area, gaps between rows, clearance of panel above roof surface, distance from edge of roof, etc.) in setting the wind loads.

Kopp (2013) noted that the determination of aerodynamic forces, uplift in particular, is crucial for the design of tilted arrays installed on the flat roof of low-rise buildings as they govern the required ballast, or roof penetration, to resist uplift. The forces can be complicated since the wind field is influenced not only by the natural turbulence of wind but also from vortices and separation along building edges (Kopp et al., 2012). It has been established that building size, which controls the size of vortices on the roof, plays an important role in setting the wind loads on low-profile, tilted, roof-mounted arrays (Kopp et al., 2012; Banks, 2013; Pratt and Kopp, 2013). This is due to the conical vortices from cornering wind directions which are strengthened by vortex stretching and continuous separation along the building walls; as such larger wind loads are measured on larger buildings (Kopp et al., 2012, Banks, 2013). The strength of the vortex is significant as they are known to typically cause the largest magnitude suctions on the roof (Kind, 1986) and it is between the vortex's core and reattachment line where the largest peak suctions measured on an array occur (Banks et al., 2000). Banks (2013) cautions against using the existing literature for solar installations where the array rows are not aligned with building edges, as the loads appear to be sensitive to the direction of panel

tilt and swirl direction of the corner vortex. The corner vortices have also been noted to increase the wind loads on the array when there is a parapet (Browne et al., 2013; Banks, 2013).

While the building on which the array is mounted plays a significant role in determining the array wind loads, so too does array geometry. Kopp et al. (2012) found that larger modules were associated with an increase in the wind loads for the higher tilt models, but that module dimensions had minimal impact on the lower tilt systems. The same study reported that the loading mechanisms were different depending on the tilt angle of the modules. They reported that wind pressures on low-tilt arrays ( $5^\circ$ ) were governed by pressure equalization across the modules from the building generated (roof) pressures, while higher tilt arrays ( $30^\circ$ ) were influenced by array-generated flow. The array-generated flow served to augment the loads caused by pressure equalization with the  $2^\circ$  tilt angles having loads approximately 30 – 40% smaller than for  $10^\circ$  tilt (and larger) angles (Kopp, 2013). The same study also found that neither the row spacing nor the minimum height above the roof surface (when kept below 0.41m) had an impact on the net wind loads.

Because the panel loads are different than the (bare) roof loads, recent studies have investigated the applicability of roof zones in current design standards for designing roof mounted arrays. The research has shown that the corner roof zone is not needed as the array aerodynamics are different than the building aerodynamics, with the peak loads on the array not occurring in the corner of the roof, rendering the zone unnecessary (Banks, 2013; Kopp, 2013). Further, Banks (2013) demonstrated that the roof zones established for bare roof design are not (necessarily) appropriate for tilted arrays. This is due to the fact that the largest peak suctions measured on the array occur between the vortex core and the reattachment point (Banks, 2013), whereas the location of peak suctions on flat, bare, roofs is directly beneath the vortex core (Banks et al., 2000). As a result the roof zones for solar design should be enlarged to account for the different location of the peak uplift, set back further from the building edge. This was confirmed by Kopp (2013) who also reported that roof (edge) zones needed to be (generally) larger and on the order of  $0.5\text{-}0.6 H$  for low tilt systems ( $5^\circ$ ) and  $0.8 H$  for systems with higher tilt ( $20^\circ$ ).

With the pressures on the array sensitive to the building induced vortices, it can be deduced that the aerodynamics of roof mounted systems differ from those that are ground mounted. This is due to the fact that they would not be subjected to the building-generated flow field. This was confirmed with simultaneous pressure measurements and particle image velocimetry (PIV) to measure the flow field in an experiment performed by Pratt and Kopp (2012). They noted that it was the vertical velocity component in the vortex, caused by the separated flow off the building edge, which caused the largest uplift on the solar panels.

Wind loads from some of these studies are beginning to appear in design standards such as NEN 7250 (2013) and SEAOC PV2-2012 (2012). However, another fairly common type of roof-mounted array, those with modules parallel to the surface of pitched roofs, usually houses, has received less attention even though such systems are relatively common in some jurisdictions. Design standards specific to solar modules mounted parallel to roof slopes are still underdeveloped with additional wind tunnel studies required to solidify our understanding of the wind loading mechanisms.

### 1.3 Previous testing of solar modules mounted parallel to roofs

The first studies of wind loads on solar arrays mounted parallel to sloped roofs considered the arrays as simple solid panels, i.e., with no gaps between solar modules (Stenabaugh et al., 2010, 2011; Ginger et al., 2011). In these studies the height above the roof surface (i.e., the cavity depth),  $H$ , was a control variable, along with the roof pitch. For example, Ginger et al. (2011) examined the wind loading (and developed design guidelines) on arrays of 7 or 14 modules placed in multiple positions on gable roofs with slopes of  $7.5^\circ$ ,  $15^\circ$ , and  $22.5^\circ$ . The arrays were modeled as solid with no gaps,  $G$ , between individual modules. In this case they found that  $H$  did not have a large impact over their measured range (100mm and 200mm in full-scale). Stenabaugh et al. (2010, 2011) used a similar approach with a single solid panel representing the array and found that the net pressure coefficients were mostly similar to the bare roof external pressure coefficients. However, uplift could be increased when the array was placed at the ridge

(due to positive pressures acting on the underside of the panel near the ridge), consistent with the findings of Aly and Bitsuamlak (2014) who also studied scale models of solar modules mounted parallel to a sloped gable roof surface.

Geurts and Blackmore (2013) conducted full-scale and model-scale tests of a single solar module mounted on a hip roof. Since this study was of a single module there were no modeled gaps, just as for the studies of Stenabaugh et al. (2010, 2011) and Ginger et al. (2011), although the module was of a considerably smaller size. Geurts and Blackmore found that while the effect is small, external peak pressures on the upper surface are higher for larger  $H$ . On the underside of the module, peak positive cavity pressures were found to be larger with larger  $H$ , while peak suction were found to be smaller in magnitude over the range they examined. They found strong correlations between the external and cavity pressures which resulted in relatively small net wind loading due to pressure equalization. Levels of pressure equalization were significantly different from those found in the studies of Stenabaugh et al. (2010, 2011) and Ginger et al. (2011), whose modules were much larger in size. Thus, the generality of the conclusions is not clear for arrays made up of many modules, where gaps between individual modules could alter the local flow-field and influence cavity and net wind pressures, as they do for roof pavers (e.g., Bienkiewicz and Sun, 1992, 1997; Asghari Mooneghi et al., 2014) and other roof-mounted systems (Oh and Kopp, 2014). The omission of modeled gaps could possibly yield substantially different aerodynamics and net wind loads on the panels than what exists in reality.

## 1.4 Loose-laid paving systems

The most relevant work on both the effects of gaps between modules and the cavity depth has been done on loose-laid paver systems installed on flat-roofed, low-rise, buildings (Kind and Wardlaw, 1982; Bienkiewicz and Sun, 1992, 1997; Asghari Mooneghi et al., 2014). Loose-laid pavers are part of double-layer roofing systems, which are sometimes used on flat-roofed, low-rise, commercial structures. Kind and Wardlaw (1982) conducted failure testing to analyze lifting and overturning of roof-mounted pavers, noting that blow-off failures could be prevented with gaps between the pavers (as

opposed to tight fitting joints). Bienkiewicz and Sun (1992, 1997) studied scaled paver installations on the flat roof of a low-rise building in a wind tunnel for a cornering wind direction. Of particular interest to them were the cavity pressures. They found that a cavity beneath the modules, even a small one (i.e.,  $\frac{1}{4}$  paver thickness,  $t$ ), significantly reduced the peak and mean cavity pressures. The cavity pressure distributions with relatively larger cavity depths (i.e.,  $\frac{1}{2} t$ ) were found to be more uniform due to reduced flow resistance. Larger cavity depths (i.e.,  $\geq \frac{1}{4} t$ ) were not found to have a large impact on either the cavity pressure distributions or the peak suction once they are over a particular size. In particular, a cavity that was a  $\frac{1}{4}$  of the paver's thickness yielded a significant reduction in the peak cavity suction with no increased reduction for cavities up to the paver thickness.

Conical vortices are produced from a cornering wind, causing lines on the roof where the flow reattaches (R) and separates (S) for a second time due to the rotation of the vortex (i.e., Bienkiewicz and Sun, 1992 and Holmes, 2007). A schematic of these vortices has been adapted from existing literature and is shown in Figure 1-1. Bienkiewicz and Sun found that the correlation coefficients between the external (upper surface) and cavity pressures were close to unity (with the exception of three pavers near the roof corner) when the pavers were installed without a cavity ( $H \approx 0$ ) and influenced by the reattachment (R) and secondary separation (S) lines. Gradients in the correlation coefficients were noted where the lines crossed pavers. A larger cavity depth was associated with lower correlation coefficients, although they were noted to still be high. Their studies also considered the effect of a parapet, which was determined to have a negligible impact when the cavity was kept small ( $H \approx 0^+$ ). Bienkiewicz and Sun (1997) determined that both the paver size and aspect ratio play a role in the wind resistance of the system, with large, square, pavers being more wind resistant.

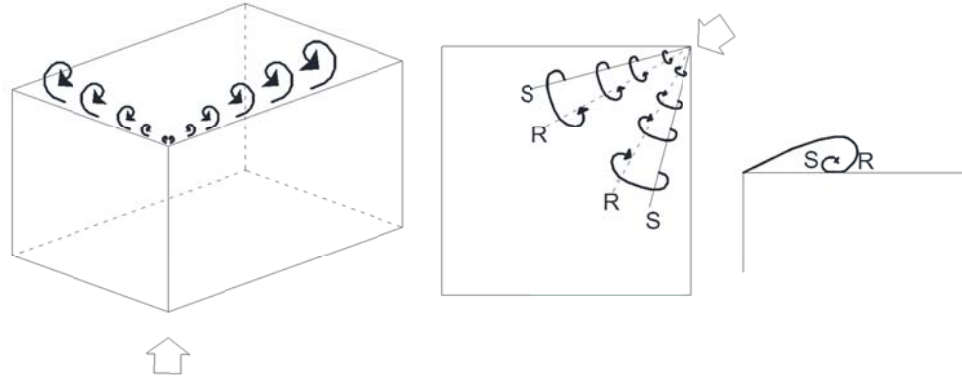


**Figure 1-1: Sketch of the conical vortices from a cornering wind direction with secondary separation and reattachment lines (adapted from Holmes, 2007 and Bienkiewicz and Sun, 1992)**

A related study published by Bienkiewicz and Endo (2009) also focused on the wind tunnel studies of loose-laid paver systems on flat roofs. They used the same wind tunnel model and set-up as the previous paver studies by Bienkiewicz and Sun (1992, 1997), but specifically expanded the scope to include the effect of gaps between pavers. It should be noted that while there was no mention of what the experimental gap,  $G$ , between pavers was in the Bienkiewicz and Sun studies (1992, 1997), it can be inferred that the pavers were installed with some gap, rather than sealed. Bienkiewicz and Endo (2009) note that wind uplift can be reduced with larger  $G$  and that the reduction depends on the permeability ( $G$ ) and the flow resistance in the cavity (controlled by  $H$ ). They further observed that with larger values of the system relative permeability,  $G/H$ , pressure equalization increased, as indicated by the magnitude of the transmitted (cavity) pressure increasing and approaching the limit of the external (upper surface) pressure. For a system with tightly packed modules (small  $G$ ) and some cavity depth, the net uplift was reduced to  $\frac{2}{3}$  of the external pressure. If the cavity depth was further reduced, the net uplift was found to be only  $\frac{1}{2}$  the external pressure. Large-scale studies were performed at the Wall of Wind, which confirmed the dependence on the  $G/H$  ratio, with higher ratios leading to reduced net loads (Asghari Mooneghi et al., 2014). However, it should be noted the studies by Bienkiewicz and Sun (1992, 1997), Bienkiewicz and Endo (2009) and Asghari Mooneghi et al., 2014 only considered a single, cornering, wind direction.

While it is known that a cornering wind is typically associated with the peak suction wind loads on the roof, it is possible that the presented pressure coefficients may not have captured the worst cases needed for design.

The lack of a modeled gap between modules largely hindered pressure equalization and at least partially explains the differences between the findings of Stenabaugh et al. (2010, 2011) and Ginger et al. (2011) with those of Geurts and Blackmore (2013). Stenabaugh et al. and Ginger et al. studied arrays of modules modeled without gaps on gable roofs. They noted that modules located in the interior of the roof can experience net pressures that are higher than the corresponding external pressures on a bare roof. Geurts and Blackmore studied a single module on the interior of a hip roof and found that wind loads were substantially lower than the code-derived external loads on the roof surface. These findings are opposite, and are likely caused by the way the systems were modeled. Without modeling  $G$  accurately, the case of Stenabaugh et al. and Ginger et al., flow into and out of the cavity through openings between modules was largely prevented and the module dimension was artificially enlarged to be the size of the array. Stenabaugh et al. also largely prevented flow from entering the cavity for certain wind directions as the pressure tubes were used to simulate the mounting rail and significantly increased the blockage ratio for flow entering the cavity. This would have altered the cavity pressure distributions, which are known to be impacted by the pressure drop through the orifice ( $G$ ), and the pressure drop through the cavity (a function of cavity length) (i.e., Oh and Kopp, 2015). It is the cavity pressures, transmitted from the external (upper) surface, that reduce the net wind loading on the modules. Geurts and Blackmore noted that the full-scale testing showed that the external and cavity pressures were of the same order of magnitude, indicating a good correlation between them and subsequently low net pressures. This is the process of pressure equalization and is discussed in more detail in the next section and in chapter 4. If the cavity flow is significantly altered through modelling, the transmission of the external pressures (and pressure equalization) would not be as effective, leading to higher net pressures, potentially even higher than bare roof pressures due to the secondary separation off the array. These findings may be overly conservative and warrant further investigation, specifically with a carefully modelled

cavity. It is clear that the gap between modules and cavity depth for roof-mounted solar arrays are significant parameters that need to be considered in the design wind loads for arrays mounted parallel to the roof surface. Together they influence the degree of pressure equalization, which has been noted for its significance in setting the wind loads for both (low) tilted solar arrays and loose-laid pavers on flat roofs of low-rise structures.

## 1.5 Pressure equalization

Roof mounted solar arrays can be considered a double layer system – with the roof as the inner layer and the modules as the outer layer just as roof pavers are. The external (upper) surface and cavity (lower surface of the modules) are exposed to wind flow since there is a void beneath the roof and the underside of the modules. Pressure equalization is a wind loading process that can occur; with the cavity pressure partially approaching that on the upper (external) surface of the array. Perfect pressure equalization is unlikely in practice (since it could only happen for static, uniform, external pressures), however, net pressures on roof-mounted pavers have been found to be less than what would be expected on the bare roof due to this process (Bienkiewicz and Endo, 2009). As such, pressure equalization can play a crucial role in reducing the (net) design wind loads for the outer layer of double layer systems (see Bienkiewicz and Endo, 2009 for roof pavers and Kopp, 2014 for tilted solar installations on flat roofs). The process of pressure equalization is not limited to roof pavers and solar modules, but also impacts cladding systems such as curtain walls, brick veneer or vinyl siding walls, and rainscreen walls (Kumar, 2000).

Rainscreens are used to protect structures from rain infiltration. The systems employ (at least) two layers with a cavity of air in between outer (cladding layer) and an interior layer; the outer one is an air-permeable rainscreen and the inner layer is an air barrier. The outer layers work together to protect the structure with the rainscreen deflecting the majority of the rain and the cavity between the layers providing drainage for any water that does penetrate. Kumar (2000) noted that Pressure Equalized Rainscreens (PER) can be designed to reduce the wind loads on the screen (outer layer) through deliberate venting, openings designed to ensure rapid equalization. The total venting area, in

addition to the dimensions of both the cavity and the vented openings, are key design parameters. Small, deep vents lead to laminar flow, with turbulent flow associated with vents that are large in cross-section, yet shallow in depth (Cook, 1990). Smaller cavities require less airflow to achieve equalization and thus yield a faster response time – important when designing for the short duration peaks across the rainscreen (Kumar, 2000).

While vents are beneficial in ensuring pressure equalization for rainscreens, a similar statement can be made regarding gaps for loose-laid pavers. As previously mentioned, Kind and Wardlaw (1982) found that the inclusion of gaps between individual paver elements could actually prevent the failure when performing blow-off tests. This indicates that resistance to failure of individual pavers was increased when the pavers were not flush with one another but separated by an air gap. In 1991, Okada and Okabe tested failure wind speeds of paver systems with two different cavity depths. They found that a cavity depth (not loose-laid, but mounted with an offset from the roof) resulted in lower failure wind speeds due to relatively poorer pressure equalization. Thus, while gaps are beneficial, relatively large cavity depths are detrimental to pressure equalization, consistent with the discussion on pavers in section 1.4 where pressure equalization is noted to be improved with higher values of  $G/H$ .

While large cavity depths may not be optimal with respect to increasing pressure equalization, they are a required component of dual-layer wall or roof systems which have many uses in the design and construction industries. As such, a number of research studies have highlighted methods to maximize pressure equalization by modifying the cavity.

Kumar (2000) noted that continuous cavities are not always efficient and that compartmentalization improves pressure equalization. He notes that pressure equalization is highly dependent on the spatially-varying, external, pressure variations. Dividing the cavity into compartments can reduce the external pressure gradients and reduce cross-flow between adjacent cavities, improving pressure equalization and reducing the net wind loading on the outer layer. This practice can be particularly useful

around the corner of buildings which can experience large pressure gradients, in fact Morrison and Hershfield Ltd (1990) went so far as to say that compartmentalization is absolutely necessary at the corners of buildings when studying a vinyl siding clad wood-framed wall. Introducing small compartments in these regions can reduce the pressure drop across the outer surface as well as the volume of air required for equalization, reducing the response time of the cavity pressures (Kumar, 2000). Larger compartments can be used in the interior region of a building façade where the external pressure gradients are smaller.

Another way to increase the pressure equalization would be to increase the flow resistance in the cavity. Gerhardt and Janser (1994) noted that increasing the flow resistance within the cavity by adding batten or wire nets has a similar effect to compartmentalization, improving the pressure equalization and reducing the net wind loading on the outer layer.

A number of studies have contributed to theoretical models based on the Helmholtz principle, standard gas law and mass continuity to predict cavity pressures based on external pressures (for a selection see Holmes, 1979; Kumar and Van Schijndel, 1998, 1999; and Latta, 1973).

Oh and Kopp (2014, 2015) conducted wind tunnel studies to characterize cavity pressures in a double-layer system and developed an analytical model, validated with experimental results. Their analytical model was developed noting the many similarities between the double-layer systems of wall systems (rainscreens) and solar arrays. Their parameter,  $\varphi$ , is the ratio of cavity flow pressure drop to the orifice flow pressure drop.  $\varphi$  is dependent on a number of parameters including the  $G/H$  ratio as well as the Reynolds number, such that

$$\varphi = \left[ \frac{G}{H} \right]^2 \left[ \frac{f_H L/H}{2(C_L + f_t t/G)} \right] \quad (1)$$

where  $f_H$  is the friction coefficient through the cavity,  $L$  is the module length,  $f_t$  is the friction loss through the orifice or gap,  $t$  is the module thickness and the  $C_L$  is the orifice loss coefficient. Equation 1 was developed based on a model with a single cavity with a gap before and after the module, limiting the flow to one direction. The friction losses through the orifice are significantly lower than the total loss coefficient, allowing the simplification of Equation 2, yielding,

$$\varphi = \left[ \frac{G}{H} \right]^2 \frac{24}{Re_H} \frac{Lc}{H} \frac{1}{2.5} \quad (2)$$

where  $Lc$  is an effective cavity length,  $Re_H$  is the cavity Reynolds number. A  $\varphi$  value greater than order (1) indicates that cavity flow dominates such that the cavity pressure distribution is liner in nature. Alternatively, when the orifice (gap) flow dominates, the cavity pressure distribution is uniform and yields a  $\varphi$  value less than order (1). The parameter is thought to be robust since the values were found to be order of magnitudes larger or smaller than the transition point between the different flow mechanisms. It is

unclear how the equations to evaluate  $\varphi$  could be used to predict the cavity flow of systems with multiple cavities, multi-directional flows, or even how to precisely define the effective cavity length.

## 1.6 Design Standards

Design wind loads on the external surfaces of low-rise buildings (walls and roof) are well defined in existing standards such as ASCE 7-10 (2010). In that code the design wind pressure,  $p$ , on low-rise building component and cladding (C&C) elements is determined using

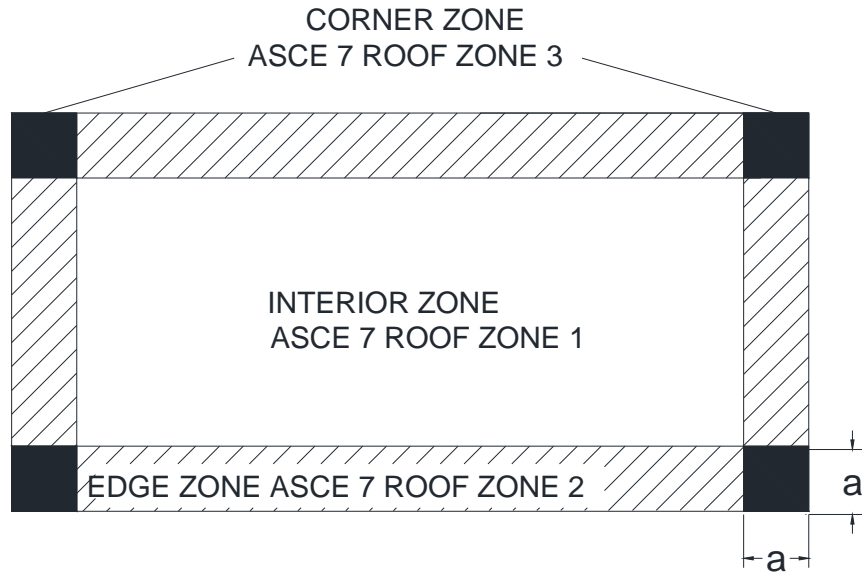
$$p = q_h [(GC_p) - (GC_{pi})] \quad (3)$$

where  $q_h$  is the velocity pressure evaluated at the mean roof height,  $(GC_p)$  is the external pressure coefficient and  $(GC_{pi})$  is the internal pressure coefficient. The velocity pressure is based on the basic wind speed, determined geographically using figures in the code. Higher velocities are given for coastal and mountainous regions. The velocity pressure is also designed to account for directionality, exposure (a measure of how built-up the surroundings are), and velocity speed-up due to topography. For metric units it is evaluated using

$$q_h = 0.613K_zK_{zt}K_dV^2 \quad (4)$$

with  $K_z$  being the exposure factor,  $K_{zt}$  the topography factor, and  $K_d$  the directionality factor. These are all multiplication factors applied to the basic wind speed,  $V^2$ . Each of the factors is determined through tables and figures in the standard and are site/building specific. External pressure coefficients are given in various figures in the standard,

specific to the surface (i.e., wall, roof). For example, the  $(GC_p)$  for roof surfaces are dependent on roof slope, roof zone (corner, edge or interior) and effective wind area. The corner zones have the largest magnitude  $(GC_p)$  and the interior the smallest, with separate  $(GC_p)$  curves plotted with respect to effective wind area. A schematic of the applicable roof zones and  $GC_p$  (suction) values for a gable roof with a slope between  $27^\circ$  and  $45^\circ$  is shown in Figure 1-2 which was adapted from Figure 30.4-2C in ASCE 7-10 (2010). The internal pressure coefficient is determined from a table in the standard and is based on the enclosure (enclosed, partially open or open) of the building. A typical, low-rise, building is considered enclosed which yields a coefficient of  $\pm 0.18$ .



where  $a$  is

- the least of
  - 10% of the least horizontal dimension
  - $0.4h$  where  $h$  is the mean roof height
- but greater than
  - 4% of the least horizontal dimension
  - 0.9 m

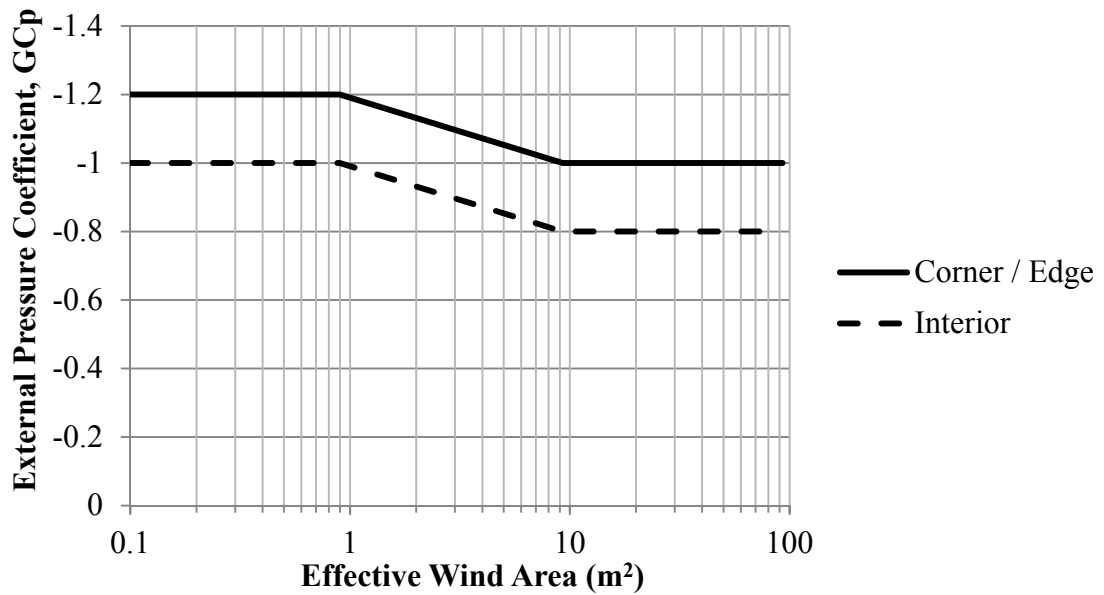


**Figure 1-2: Roof zones and external pressure coefficients for 27 – 45° gable roof slopes adapted from ASCE 7-10 (2010)**

External pressure coefficients in current design standards are largely based on series of wind tunnel studies conducted in the 1970s (see Stathopoulos et al., 2000 for more information). Although Stathopoulos et al. are referring to the National Building Code of Canada (NBCC 10, 2010) in their work, the Canadian and American standards are similar in approach and ASCE 7-10 (2010) references the same studies conducted by Davenport et al. (1977). To compare their results with those in the code, Stathopoulos et al. extracted the most critical experimental peak pressure coefficients from their wind tunnel experiments, which they multiplied by a factor of 0.8 to account for directionality. They note that this approach was the same used for the development of the code itself. The worst peak values from each wind tunnel configuration were used to develop a simplified ( $GC_p$ ) (or equivalent external pressure coefficient) vs. tributary area design curve that “envelopes” the (majority of) experimental results. The design curve needs to strike a balance between covering the experimental values and being both simple and clear for ease of use. As such, it is possible that not all critical, peak, wind tunnel coefficients will be under the design curve, as seen in Stathopoulos et al. (2000). A ( $GC_p$ ) value is obtained from this curve for a specific effective wind area and used in Equation 3 to evaluate the design wind pressure. These provisions are for the external surface of the roof and do not properly account for the unique loading conditions of air-permeable, double layer systems such as roof-mounted solar modules, not explicitly covered in the current edition of both the Canadian and American building codes.

Design procedures pertaining to roof-mounted solar arrays have recently started appearing in building codes in some jurisdictions. Some of them are based on existing Components and Cladding design procedures already present in the standards and use a multiplication factor applied to the external pressure coefficient (see NEN 7250, 2013). Alternatively, SEAOC PV2-2012 (2012) presents design loads in a familiar format based on the C&C approach in ASCE 7-10 (2010), taking advantage of the established procedure, but tailoring it for solar modules. SEAOC PV2-2012 uses a different equation to evaluate the wind design pressure,  $p$  such that

$$p = q_h(GC_{rn}) \quad (5)$$

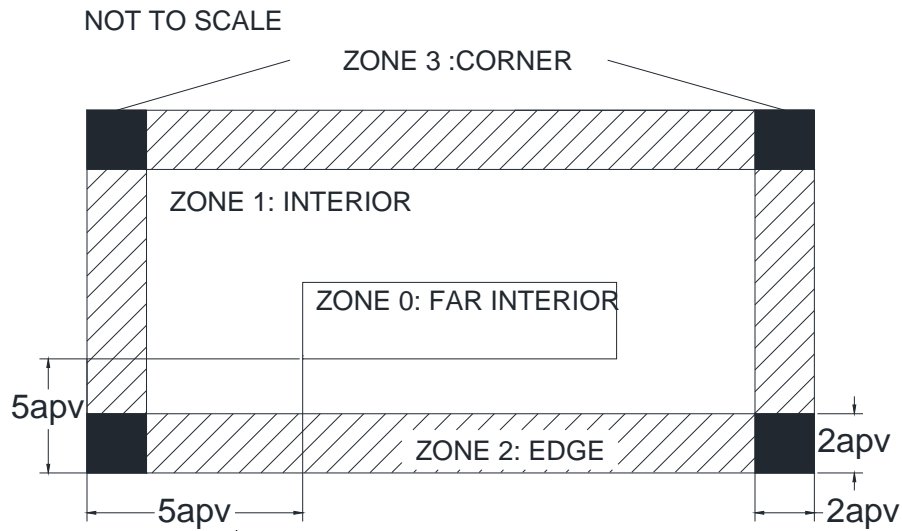
where  $q_h$  is the velocity pressure (consistent with ASCE 7-10) and  $GC_{rn}$  is the combined net pressure for solar modules. It was designed with future incorporation into ASCE 7-10 in mind, using many of the existing procedures and variables, such as the velocity pressure (including exposure, topography, and directionality factors as well as the basic wind speed). Specific to the solar modules is the combined net pressure coefficient for solar panels,  $GC_{rn}$ , where

$$GC_{rn} = \gamma_P E [(GC_{rn})_{nom}(\gamma_C)] \quad (6)$$

and  $\gamma_P$  is the parapet height factor,  $E$  is the array edge factor,  $(GC_{rn})_{nom}$  is the nominal net pressure coefficient and  $\gamma_C$  is the chord factor. The nominal net pressure coefficient is presented in a very similar manner to the external pressure coefficients from ASCE 7-10. The roof is divided into the typical corner, edge and interior zones but also includes a far interior zone. The width of these zones is notably larger, with the justification being discussed earlier in the chapter. Each roof zone has a separate curve  $(GC_{rn})_{nom}$  for a

range of module tilt angles. A sketch based on the roof zone definitions and an example  $(GC_{rn})_{nom}$  curve is shown in Figure 1-3 (based on SEAOC PV2-2012, 2012). The chord and parapet effect factors are straight multiplication factors, evaluated and applied in a manner similar to the topographic factor.

The array edge factor,  $E$ , was developed to account for higher pressures on leading edge, exposed, modules and lower pressures on interior, sheltered modules. Interior, sheltered, modules have a factor of 1 while edge (exposed), modules can have a factor up to 2. Edge modules can have a different factor for different wind directions as the value is based on the setback distance and a characteristic height (dependent on building height, module length and module tilt). The maximum  $E$  value evaluated for any wind direction is used in Equation 6. As such,  $E$  could increase the pressures on selected modules by a factor of 2. A sketch defining sheltered and interior modules and potential array edge factors is shown in Figure 1-4. Once the array edge, chord and parapet factors have been evaluated and the nominal net pressure coefficient has been determined, the combined net pressure coefficient for solar panels can be evaluated using Equation 5 and multiplied by the velocity pressure to calculate the design wind pressure. The approach that SEAOC PV2-2012 took is effective since it takes advantage of adopted, familiar, provisions and develops supplementary equations and parameters to develop guidelines specific to a new system, solar arrays in this case, without starting from scratch.



where  $a_{pv}$  is  $0.5\sqrt{hW_L}$  (not exceeding mean roof height,  $h$ ) and  $W_L$  is the width of the longer building side

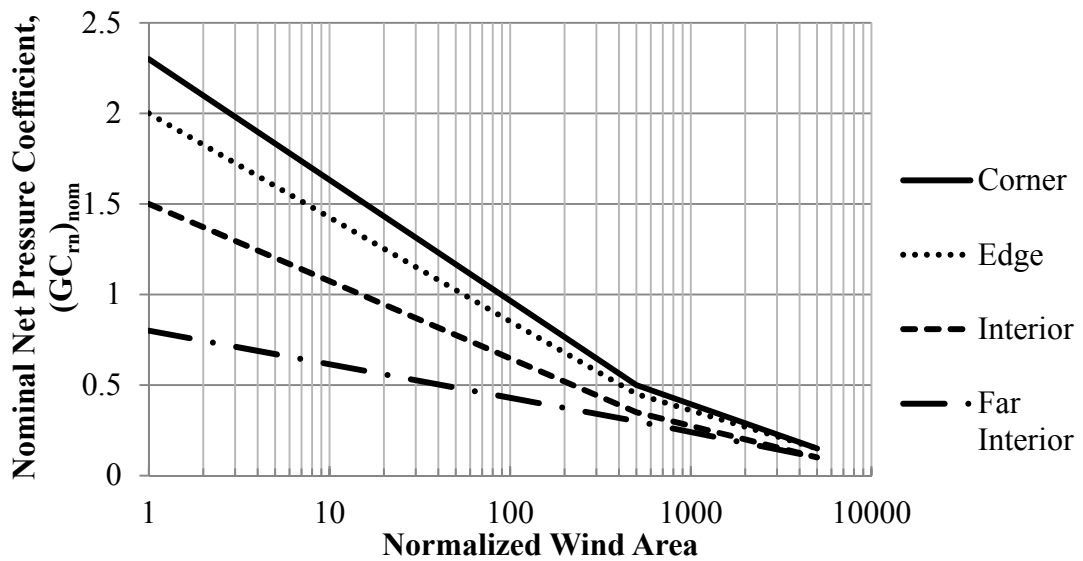


**Figure 1-3: Roof zones and nominal net pressure coefficients adapted from SEAOC PV2-2012 (2012)**

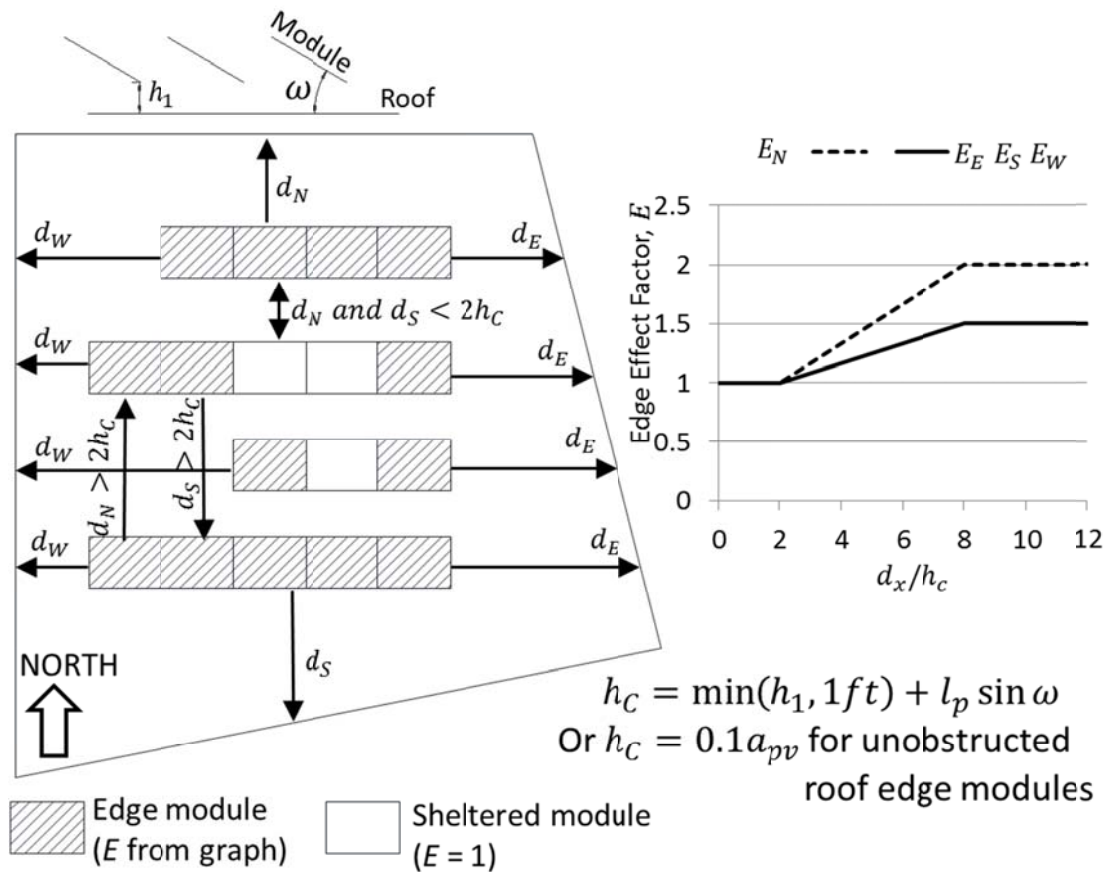


**Figure 1-4: Sketch of edge and sheltered modules with array edge factors adapted from SEAOC PV2-2012 (2012)**

Design recommendations need to be robust enough to account for the change in wind loading acting on the modules, yet generic enough to be applicable for any installation. This becomes a balance between accounting for as many changes as possible (namely reductions to loading that are beneficial in terms of lower magnitude design loads) and simplifying the procedure as much as possible and keeping it consistent with other practices in the standard. If the design procedure is over simplified it could potentially lose some reductions in loading and lead to overly conservative design loads. As discussed above, there are multiple ways to present new design recommendations, whether it be simply modifying external pressure coefficients with a multiplication factor (NEN 7250, 2013) or preserving the procedure outlined in a code but developing a new design wind pressure equation with combined net pressure coefficients and array-specific

parameters (SEAOC PV2-2012, 2012). Either method is effective, as they are both presented in a manner that is consistent with existing provisions, thus facilitating easy adoption. This study focuses on the multiplication approach, assessing its feasibility and developing values. A multiplication factor,  $\gamma$ , would be applied to the existing external pressure coefficients,  $GC_p$ , in the current design standards such that

$$p = q_h[\gamma(GC_p)] \quad (7)$$

where the design net wind pressure,  $p$  is still a function of the velocity pressure,  $q_h$ , as defined by the code. The factor would account for combined effects of both the external (upper) surface and the cavity beneath the modules being exposed to flow (negating the need for an internal pressure coefficient in Equation 3). The external pressure coefficient is evaluated in the same manner as already established and accounts for parameters such as roof slope, roof zones and tributary area. The multiplication factor approach is familiar as it is already used to account for the effects of exposure and topography. Still unknown is how best to present the factor, accounting for array-specific parameters such as  $G$ ,  $H$ , and module size. Truly understanding the wind loading on the solar modules and how it is influenced by key design parameters will aid in developing the most effective design recommendations. As such, the current study strives not only to quantify the wind loads measured, but to add to the current understanding pertaining to wind loads on roof-mounted solar modules, ultimately aiding in the development of effective design recommendations.

## 1.7 Objectives

Roof-mounted solar systems, placed parallel to the roof-surface, for houses and other low-rise structures with sloped or flat roofs are becoming more common, yet there is still a lack of applicable design guidance or standards. This is partly due to a notable lack of literature focusing on the combined effect of gap,  $G$ , and cavity depth,  $H$ , on the wind

loading of an array of solar modules that are mounted parallel to roofs, as opposed to systems with tilted modules or roof pavers. While building dimensions (plan dimensions and mean or eave height) have been noted to have an effect on the wind pressures on tilted arrays, they were not control variables for the current study. Truly defining the effects of just two geometric array parameters ( $G$  and  $H$ ) requires a large number of configurations – many of these would have to be repeated numerous times for varying building dimensions if they too were specifically studied. This is simply beyond the scope of the current study. Instead, two roof slope models were constructed ( $30^\circ$  and flat), each representing a generic, low-rise, building. This study serves to fill the identified gap and determine the effect on wind loading of varying array geometries including;

- Gap between individual modules,  $G$
- Cavity height,  $H$
- Tributary area of array,  $A$
- Roof slope
- Module dimensions

Special attention will be made to determine the effect of and quantify the pressure equalization occurring across the modules as it will alter the net wind loading. With the determination of the effect of array geometry, analysis will shift to focus on developing proposed design recommendations in a format consistent with existing standards. Design wind pressures will need to take into consideration edge effects on both the array and the modules as their position on the roof and within the array alter the wind loads on these modules. When the recommendations are presented as multiplication factors to be applied to established external pressure coefficients in design standards, the effects of building dimensions will inherently be accounted for, having already been incorporated into the external pressure coefficient and code provisions.

## 2 Experimental set-up and analysis procedure

### 2.1 Choice of model scale

Selection of the model length scale is one of the first design decisions for a wind tunnel study with the best choice not always being clear. The model scale must strike a balance between the physical limitations of the wind tunnel and the ability to manufacture and instrument the scale model while respecting numerous scaling parameters.

Typical boundary layer wind tunnels were built and designed to accommodate high-rise buildings at scales of 1/300 to 1/500, with the full depth of the atmospheric boundary layer (ABL) being simulated. The process of determining wind-induced pressures through wind tunnel tests is well established through guidelines in various design standards (i.e., ASCE 7-49, 2012). The accurate determination of full-scale wind loads requires the assumption that the flow around sharp-edged, bluff bodies in turbulent boundary layers is largely independent of the Reynolds number,  $Re$ , effects provided that value is above a threshold of approximately  $2 \times 10^4$  to  $3 \times 10^4$  (Lim et al., 2007).  $Re$  is a ratio of inertial to viscous forces (Schlichting and Gersten, 2000) and can be used to characterize the flow regime. Lim et al. note that the  $Re$  independence was established with limited data, when the experiments and analysis were not an extensive study of  $Re$  effects but rather conducted to highlight the critical importance of appropriately modeling the ABL in the wind tunnel (i.e., thick enough to encompass the model). The  $Re$  insensitivity has been confirmed through a number of studies (i.e., Cherry et al., 1984). The current study is compliant with the practices outlined in ASCE7-49 (2012), which required a large enough  $Re$  to accurately simulate the flow and full-scale pressures. For the current roof model, the  $Re$  number was on the order of  $3 \times 10^5$ . More recently the  $Re$  independence has been questioned (i.e., Lim et al., 2007), however, this is beyond the scope of the current study and not explicitly addressed. The current model may also be subject to  $Re$  effects in the cavity beneath the solar modules and flow through the gaps surrounding individual modules within the array. A discussion of the potential effects is presented later in this chapter.

If a low-rise structure were to be built at the typical boundary layer wind tunnel model scales it is probable that its height would be close to, or even less than, some of the roughness blocks used to simulate the ABL. This would not be appropriate due to the increased measurement errors associated with the lowest elevations within the tunnel. In addition, the relatively small nature of low-rise buildings at the standard wind tunnel length scales leads to challenges in the manufacturability of the models. Architectural details, which can be important for wind loading, are lost when their scaled down dimensions make them too challenging to replicate. Wind tunnel pressure models use pressure transducers to measure the pressure acting at a given point on the model and consequently the loading at that particular point. There are hundreds of these taps on any given model, as each tap can only tell us what is happening at that particular location on the model. In order to accurately determine the overall wind loading acting on the structure, engineering judgement is used to lay out a dense array of taps to measure the point pressures with specific attention made to ensure the worst-case peak pressures are measured. Each measurement location requires surface area on the model to install a pressure tube as well as internal space to connect the tubing to the transducer. Small-scale models severely limit the number of taps which can be installed. This can lead to an underrepresentation of the wind loads, even missing the peak pressures that drive the highest loads. Had 1/300 been chosen as a model scale the current study the model of a low-rise building would have been approximately the size of a deck of cards, with the solar modules less than a half centimeter, much too small to manufacture, instrument and measure accurately in the wind tunnel.

To account for some of the difficulties associated with the testing of low-rise buildings larger models have been used with modification to the modelling of the ABL. This involves only modeling the lower section of the ABL within the wind tunnel. Results from wind tunnel testing at these scales, typically 1/50 to 1/100, have been used to develop design codes and databases (Ho et al., 2005). However, for this study, constructing the model at such a scale would still not provide the resolution required to determine the wind loads accurately and especially the change in loads due to the incorporation of the solar array. For example, a full-scale gap of 1cm is only 0.1mm at a

scale of 1/100, which is not practical. Since gaps of this size are reasonable for the practical application under consideration, larger models are required. At 1/20, the 1 cm gap is 0.5 mm which is more feasible to manufacture and install reliably in the wind tunnel.

The profiles used, discussed in more detail in the next section, were developed for use with 1/50 scale models resulting in a mismatch of scales. While testing with scale mismatches is not ideal, it has been done before and is discussed in Ho et al. (2005). Lin and Surry (1998) noted that the scale mismatch may not be critical when the pressures are averaged over small areas and when they are dominated by local flow separations (such as those at the eaves height). However, Surry (1982) reports that the scale mismatch could be more relevant when the spatial correlation of the loads is important – indicating that the error could be in the 5 - 10 % range for a scale mismatch of a factor of 2.

At 1/20, the larger model scale increases the Reynolds number, which should help the flow simulation, especially in the cavity beneath the modules. While the flow field beneath the modules is not known in full-scale for cases of extreme wind loading, clearly the Reynolds number of the cavity flow,  $Re_H = \frac{U_c H}{\nu}$ , where  $U_c$  is the mean velocity in the cavity,  $H$  is the cavity depth (i.e., the clearance between the roof surface and underside of the solar module) and  $\nu$  is the kinematic viscosity of air, should be greater than the creeping flow range (i.e., much larger than 1). For example, Oh and Kopp (2014) estimated the model-scale  $Re_{H,ms} > 5$ , where the subscript “ms” indicates “model-scale”, which puts the cavity flow in the laminar regime. Since the full-scale  $Re_{H,fs}$  is  $Re_{H,ms}/\lambda_V \lambda_L$ , where the subscript “fs” indicates “full-scale”, larger Reynolds numbers clearly help the simulation. For a length scale,  $\lambda_L = 20$  and velocity scale,  $\lambda_V = 3$ ,  $Re_{H,fs} = 60Re_{H,ms}$  which may keep both flows in the laminar range of  $1 \ll Re_H \ll \sim 2000$ . With smaller model scales, the Reynolds number may not be high enough for inertial effects to come into play. However, if  $Re_{H,fs} > \sim 2000$  and the cavity flow is turbulent in full-scale, this will be practically impossible to achieve with model-scale experiments. Full-scale studies are clearly needed to clarify these issues. In any case, from the perspective of manufacturability of the model and the Reynolds numbers of the

cavity flows, it is clearly desirable to have as large a model as possible. However, from the perspective of simulation of the atmospheric surface layer, large scales are not desirable since integral scales are limited by the size of the wind tunnel. In addition, the blockage ratio should be kept at or below 5 % (Holmes, 2007; ASCE 49-12, 2012).

As a result of these considerations most wind tunnel studies on roof-mounted solar arrays use scales of 1/20 to 1/50 (e.g., Stenabaugh et al., 2010, 2011; Ginger et al., 2011; Kopp et al., 2012; Banks, 2013) as was the Bienkiewicz and Sun (1997) study on roof-pavers. A length scale of  $\lambda_L = 1/20$  was chosen for the current study. Full-scale validation of wind loads for roof-mounted solar arrays is needed and is hoped to be the focus of future studies.

## 2.2 Terrain simulation

The experiments were performed in Boundary Layer Wind Tunnel II at the University of Western Ontario (UWO) which has a working cross section of 3.4 m (11 ft) wide by 2.4 m (8 ft) high at the measurement location, with an upstream fetch of 39 m (128 ft). Figure 2-1 shows the model installed in the wind tunnel, looking upstream. The boundary layer simulation was designed to mimic an open country terrain, having an aerodynamic roughness length,  $z_0$ , of 0.01 m, as defined by Engineering Science Data Unit (ESDU, 1974, 1982, 1983, 1985). This is at the lower end of the accepted range of open country values for  $z_0$ , which is typically 0.01 - 0.05 m in current building codes.

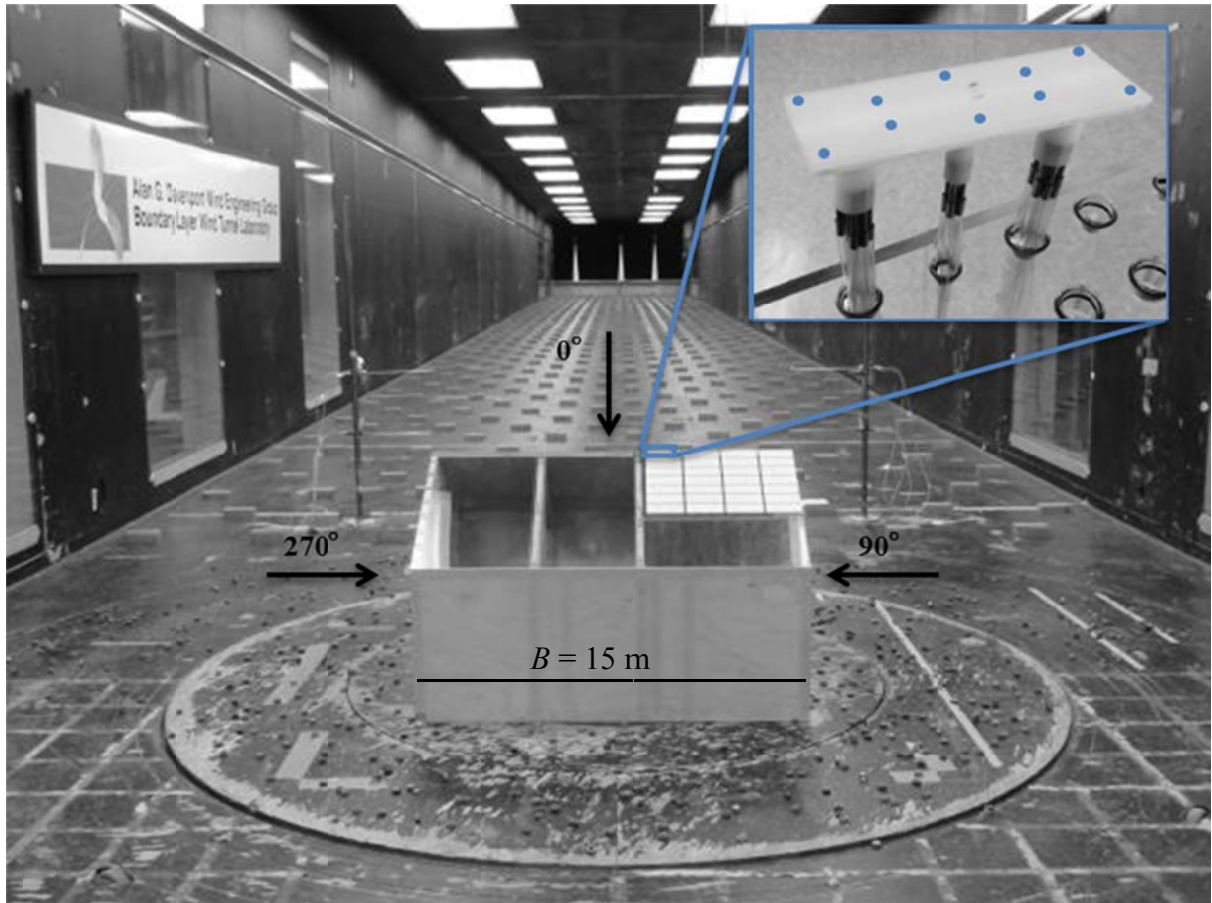


**Figure 2-1: Photo of sloped roof model**

Figure 2-2 depicts the measured and target (ESDU) open country mean longitudinal (streamwise) velocity and turbulence intensity profiles. The mean wind speed profiles have been normalized to the mean roof height (7.8m), using a model scale of 1/20. The figures show that both the experimental mean velocity and turbulence intensity profiles are in reasonable agreement with the target profiles from ESDU up to, and for a short distance above, the roof height of each model.

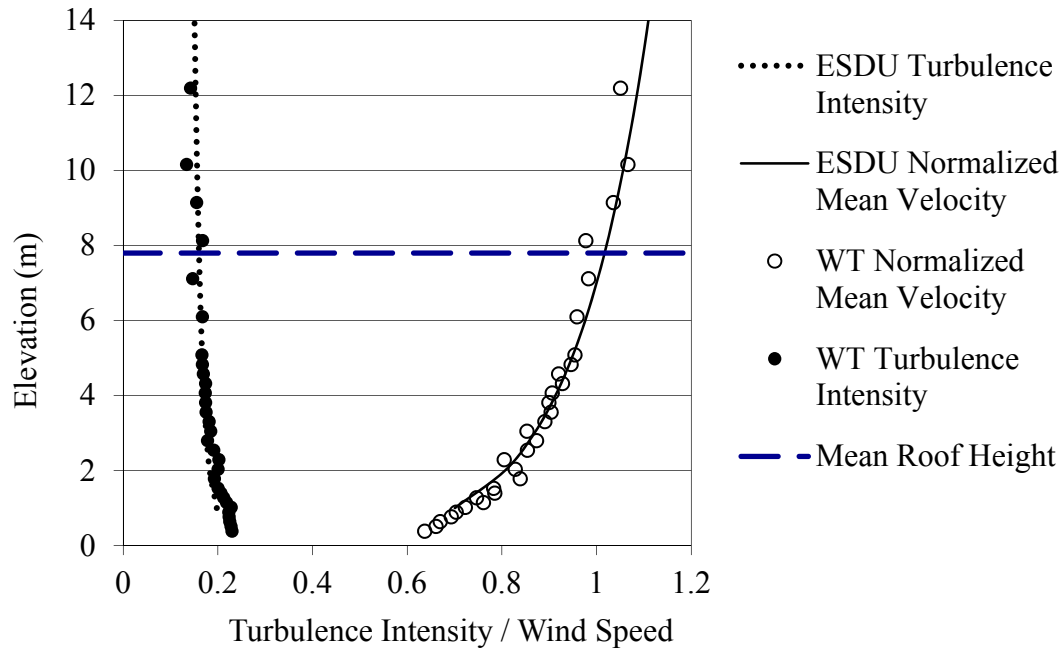


**Figure 2-2: Mean wind speed and streamwise turbulence intensity profiles**

Figure 2-3 depicts the longitudinal wind spectra measured by an X-wire probe in the 1/20 scale wind tunnel simulation, along with the target (ESDU) spectra. The reduced frequency is evaluated using the length of the model,  $B$ , and the mean streamwise velocity at  $h$ ,  $U_h$ . It can be noted that the terrain simulation does not have enough large scale disturbances but that it matches well the energy in the small-scales of turbulence. A good match in the small scales is desired, and while it would be ideal to match the large scales it often is not possible to simulate large length scales in standard boundary layer wind tunnels. If there is a mismatch it is important to assess the drop-off of the measured spectrum as it is proportional to the largest size turbulent structure that is accurately modeled. If the low-frequency cut-off is too far to the right on Figure 2-3, it could indicate that there is not enough large scale turbulence in the simulation which can alter the aerodynamics acting on the model. The cut-off is related to the wave length and the building dimensions. For the current model the cut-off occurs at approximately  $0.2 f/U$ , which signifies that the modeled turbulence is likely adequate for disturbances up to 5 time the length of the building model. This would result in scales of turbulence of approximately 75 m (in full scale) which is believed to be more than sufficient to

accurately capture the pertinent aerodynamics. The discrepancies between the target spectra and those measured in the wind tunnel are within acceptable experimental differences and are typical for large model scales. It represents one of the trade-offs for large models with high geometric resolution. It should be emphasized that model-scaling issues, using large model scales is still a topic of current interest.

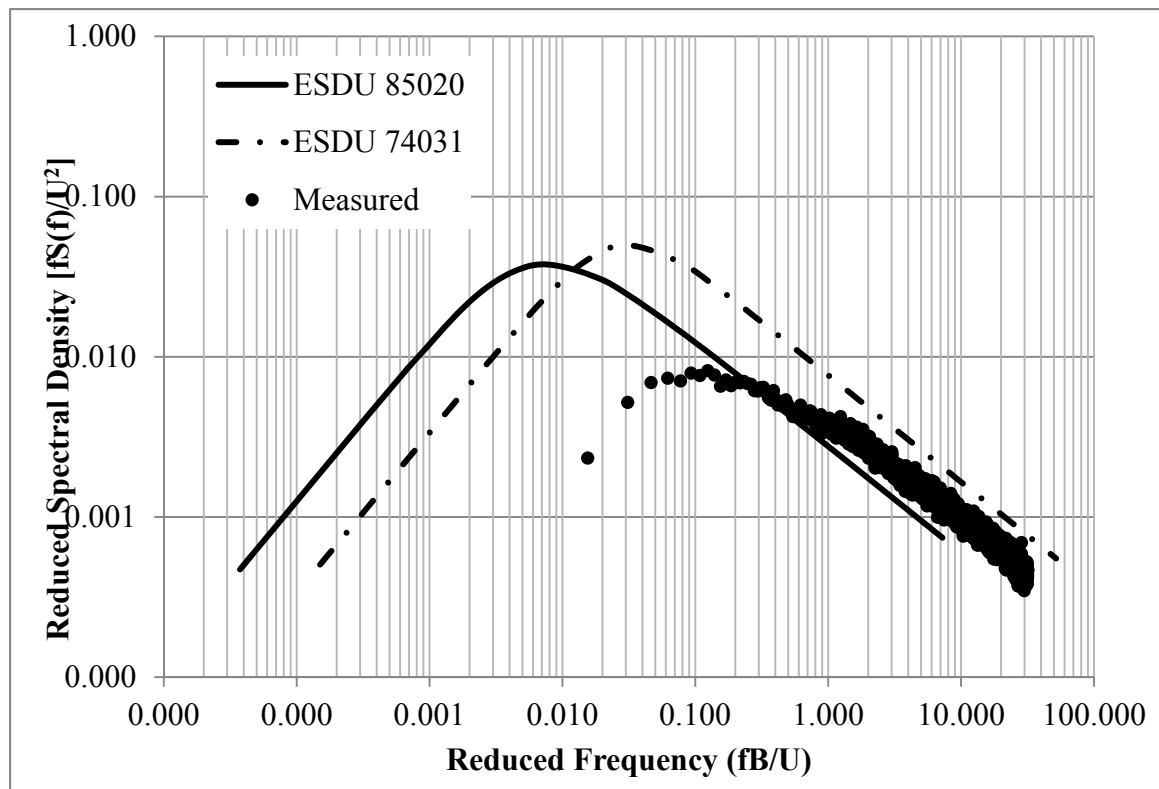


**Figure 2-3: Longitudinal spectrum measurements from the wind tunnel for  $z_0 = 0.01$  m**

### 2.3 Building model and instrumentation

The wind tunnel tests were conducted using 1/20 scale models. The majority of the tests were performed with a model representing a typical two-story house. For a complete list of configurations tested refer to the tables included in Appendix A. The house has a roof slope of  $30^\circ$  (7:12) and plan dimensions of 12.25m by 15m in full-scale. Figure 2-1 shows the model building in the wind tunnel at a wind direction of  $0^\circ$ . In the current study, the Reynolds number ( $Re$ ) based on the mean roof height (and the mean wind

speed at the mean roof height,  $h$ ,  $\bar{U}_h$ ) was approximately  $3 \times 10^5$ . The blockage ratio of the model was 4.2%.

The solar modules were modeled as flat panels with equivalent full-scale dimensions of 50cm x 145.5cm (yielding a module area of 0.73 m<sup>2</sup>). At a length scale of 1/20, the modules had plan dimensions of 2.5cm x 7.28cm. The scaled modules were 0.3cm thick, which was the minimum achievable thickness while still having pressure tubes within the modules. At 1/20 scale, this is close to typical values found in practice. The modules were machined from white Delrin (acetyl) plastic. A 4x7 layout of the modules formed the array, which is shown in Figure 2-1, Figure 2-4 and Figure A6. The upper row of modules was immediately adjacent to the ridge, while the modules on the right in the photographs were immediately adjacent to the gable end.

The array was tested for several gaps ( $G$ ) between individual modules ranging from 0 (in contact but not sealed) to 12cm in full-scale equivalent dimensions. Thus, the area of the roof covered by the array increased with larger values of  $G$ ; dimensions are listed in Table 1. The roof was made with interchangeable parts, one for each gap, to ensure precise placement of the individual modules and to maintain the relative position of the taps located on the roof surface below the array. Figure 2-4 shows drawings of the model with  $G=12$ cm (full-scale), representing the largest array dimensions tested.

In residentially-installed solar systems, there is an air cavity ( $H$ ) between the roof surface and the underside of the solar modules to ensure that there is air ventilation to cool the system, thereby enhancing the electrical efficiency. This spacing was modeled through the use of adjustable posts which supported the individual modules. The posts, three per module, contained the tubes from the pressure taps and were modeled generically, but simulated typical cavity blockage ratios (35-38%) of commercially available mounting systems. These posts were installed through the specific acrylic roof pieces with Buna rubber O-rings to maintain a set spacing height and good seal. Details can be seen in the inset to Figure 2-1 and in Figure 2-4. Machined guides, one for each spacing height, ranging from 1cm to 20cm in full-scale, were used for setting  $H$ . It should be noted that the  $H=0$  configurations are not perfectly flush or sealed but rather represent a nominal

cavity of 0 (i.e., loose-laid). The associated results may not be practical for design but are included herein for the purpose of comparison and discussion. A total of 42 base configurations were tested, representing 6 cavity heights,  $H$ , and 7 gaps,  $G$ . These are listed in Table 1 and in Table A1.

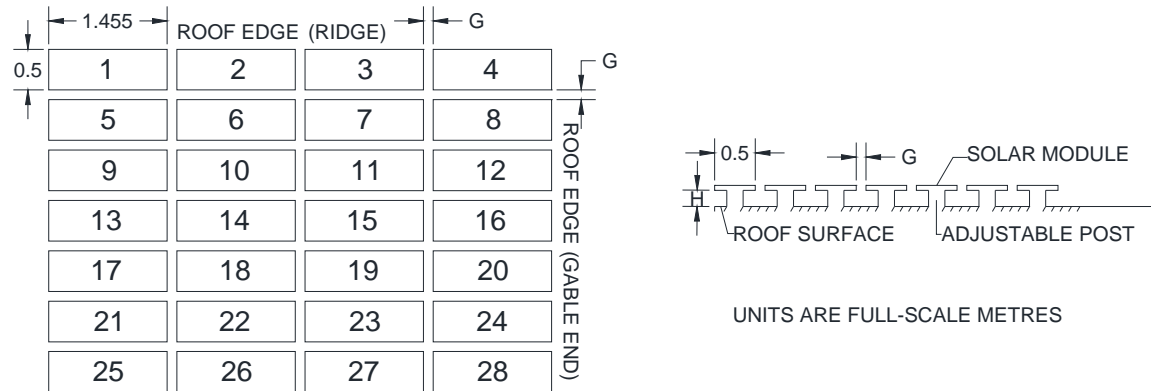


**Figure 2-4: Drawings of the array denoting the gap,  $G$ , and height,  $H$ , variables**

**Table 1: Gap, height and array dimensions**

Gap, $G$ (cm)	0	1	2	3	4	8	12
Overall array dimensions (m)	3.5 x 5.82	3.56 x 5.85	3.62 x 5.88	3.68 x 5.91	3.74 x 5.94	3.98 x 6.06	4.22 x 6.18
Height, $H$ (cm)	0	2	4	8	14	20	-

In order to get useful design information pertaining to the wind-induced loads and load distributions, a high density tap layout is required. Each individual solar module was instrumented with 20 taps; 10 on each of the top and bottom surfaces. The openings for the pressure taps on the upper and lower surface of the modules were connected with air channels within the Delrin modules and ultimately connected to brass tubes within the support posts. Excess air channels, created during the machining process when connecting the tap openings with the brass in the support posts, were plugged with styrene and resin bond. The brass tubes were then connected to the pressure measurement system of the wind tunnel.

The tap layout on the solar modules is depicted in the inset to Figure 2-1, with detailed drawings included in Appendix A. This layout allowed the determination of net pressures at 10 locations on each module, for a total of 280 locations across the array. In addition to the 560 taps on the array, the roof was also instrumented with 54 taps, below the array on the roof surface. The relative positions of these roof taps remained unchanged with larger gaps between modules.

In addition to the sloped roof model, the array was installed on a flat roof model (Figure 2-5a) of a building with full-scale dimensions of 15m x 7.5m and an eave height of 6m to examine the effect of roof slope. Wind tunnel tests on the flat-roof model were limited to the  $G = 12\text{cm}$  configurations and are listed in more detail in Appendix A. The large  $G$  was chosen as the configurations are associated with higher  $G/H$  values which are known to be beneficial for minimizing the wind loading, as found by Bienkiewicz and Endo, 2009 and Asghari Mooneghi et al., 2014. The roof height was set to the same as the eave height on the sloped roof model at 6 m. The array was located in the corner of the building, directly adjacent to the walls (no set-back). This location was chosen as it would yield the highest loads based on known low-rise building aerodynamics.

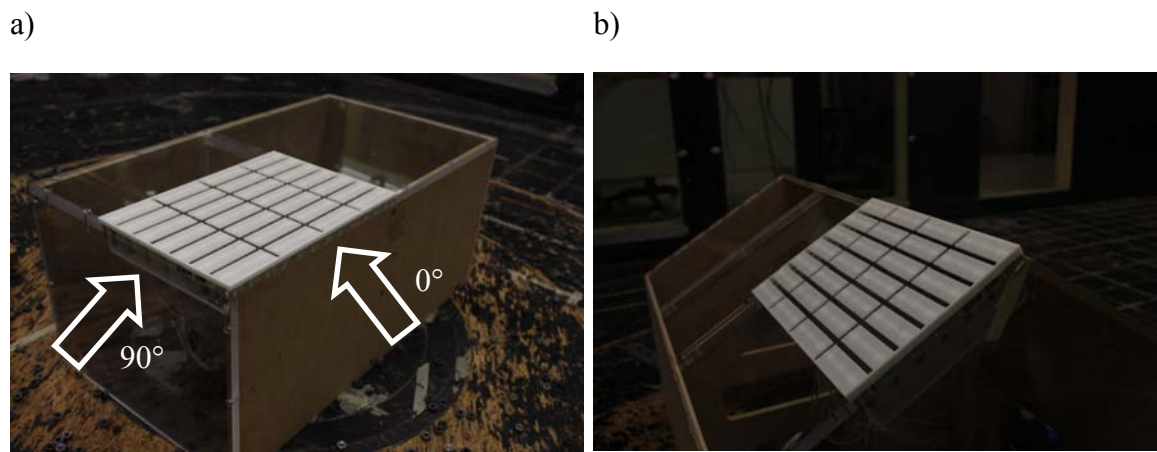


**Figure 2-5 Scale model of a) the flat-roof model and b) the sloped model with the shroud surrounding the array**

For a selected subset of configurations the array was surrounded by a shroud which largely prevented the direct airflow into the cavity from outside the array. The shroud can be seen in Figure 2-5b. A separate shroud was machined from ABS plastic for each  $G$  and  $H$  and was sized such that the bottom of the shroud was sealed with or in contact with the roof surface and the top of the shroud flush with the top of the modules. The shroud was sealed to the roof to the left and bottom of the array (from orientation in Figure 2-1, near the field of the roof) and sealed against the side of the modules on the top and right of the array). While this didn't result in a perfect seal, it blocked the majority of the flow from directly entering the cavity, essentially simulating all modules as "interior" or modules sheltered from direct external flow into the cavity. A summary of the configurations tested is included in Appendix A. When results from this subset of configurations is plotted or discussed they are referred to as "shrouded".

To examine the effect of module dimensions, a number of the shroud configurations were further modified to simulate larger module dimensions. The simulated module dimensions were achieved by taping over the gap between modules which prevented airflow and caused the taped modules to act together as a larger surface area. Modules were taped together in 2x2 (4 modules, 2.91 m<sup>2</sup>) and 4x4/3x4 (16/12 modules, 11.64/8.73 m<sup>2</sup>) combinations, as shown in Figure 2-6 and Figure 2-7. Caution was taken to minimize the impact of tape on the taps on the upper surface of the modules.



**Figure 2-6 Photos of the array taped in the 2x2 set-up (left) and 4x4/3x4 (right)**

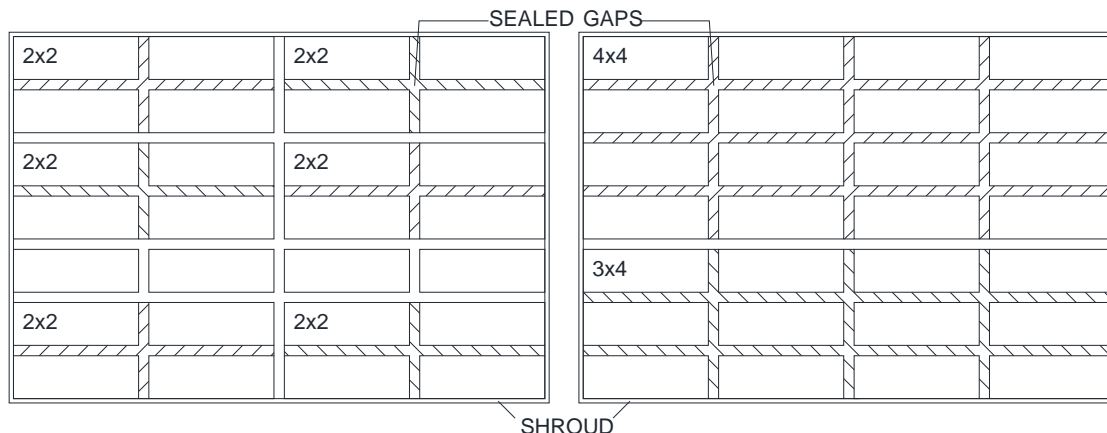


**Figure 2-7: Simulated larger module dimensions**

In total 80 configurations were tested in the wind tunnel including 42 on the sloped roof model, 6 on the flat roof model and 32 shrouded configurations on either the sloped or flat roof model. Detailed lists of the configurations and pertinent design parameters are presented in Appendix A. Note that all dimensions (lengths and areas) will be given in equivalent full-scale values in this thesis (unless noted otherwise).

Pressure measurements were made at a wind tunnel reference speed of approximately 14 m/s, which corresponds to a mean wind speed at the mean roof height of 42 m/s in full-scale, assuming a velocity scale of 1:3. Experiments were performed for 16 wind directions around the compass, in 22.5° increments; please refer to Figure 2-1 for wind direction. Pressures were sampled, essentially simultaneously, for 360 seconds at a rate of 400 samples per second. This leads to an equivalent full-scale sampling period of approximately 40 minutes. The data were digitally low-pass filtered at 200 Hz. The measurements recorded within the sampling cycle have a maximum lag time of about 15/16 of the sampling rate, which is approximately  $15/16 \times 0.0025 \text{ sec} = 2.3 \text{ milli-seconds}$ . This time lag is corrected by linear interpolation of the data within the same sample cycle. Details of the tubing system can be found in Ho et al. (2005).

## 2.4 Area-averages

Wind tunnel test results for low-rise buildings have indicated that the relevant velocity for comparing pressure coefficients is the undisturbed mean velocity at the mean roof height,  $U_h$ , as this is a more meaningful value than the velocity far above the model in the undisturbed flow of the wind tunnel (e.g., Stathopoulos, 1979). Thus, the pressure coefficients presented in this work ( $Cp$ ) have been referenced to the mean velocity at the mean roof height of the model for the sloped-roof model and the eave height for the flat roof model.

Area-averaged pressures are often more relevant for design than point pressures. This is because in practice multiple modules are often interconnected for mounting purposes. Installation racks (each containing multiple modules) are fixed to the roof with the modules mechanically fastened to one another and the rack. This effectively increases the tributary area when calculating design wind pressures as the joined modules act as one larger area. In this study area-averaged pressure coefficients were obtained by integrating the pressures at all taps within an area simultaneously, giving proper weighting to each pressure tap based on its tributary area, relative to the total area being considered. This was done on a time series basis, obtaining the instantaneous area-averaged pressure coefficient for a given area and can be evaluated for the external,  $Cp_{AE}$  (upper surface) and  $Cp_{AC}$  (lower surface) and net pressure  $Cp_{AN}$  coefficients,

$$Cp_{AE}(t) = \frac{\sum_{i=1}^n Cp_E(t) \cdot a_i}{A} \quad (8a)$$

$$Cp_{AC}(t) = \frac{\sum_{i=1}^n Cp_C(t) \cdot a_i}{A} \quad (8b)$$

where  $Cp_E(t)$  and  $Cp_C(t)$  are the time history of the pressure coefficient on the external (upper) surface and in the cavity respectively,  $a$  is the associated tributary area, and  $A$  is

the total of all tributary areas on one surface of the module(s). These coefficients were obtained for various areas from 1 module within each row to all 4 modules in a row, 1 module in a column up to 7 modules in a column, through to the entire 7x4 array (gap areas being neglected). A total of 28 different cases were considered in the module load analysis, with a total of 280 areas. A summary of the areas is presented in Appendix A. Note that gap dimensions are omitted when evaluating the tributary area.

It is the net pressures which are relevant for design since both the top and bottom surfaces of the module are exposed to air flow. The net pressure at a given point, ( $Cp_N$ ), is obtained by subtracting the pressure in the cavity ( $Cp_C$ ) from the corresponding pressure on the external, upper, surface ( $Cp_E$ ), i.e.,

$$Cp_N(t) = (Cp_E(t) - Cp_C(t)) \quad (9)$$

Thus net pressures which are negative are upward acting.

The net, peak, area-averaged and point pressure coefficients presented in this study are not the absolute worst coefficients recorded within the sample time, but are Lieblein-fitted statistical peaks (unless otherwise noted). This involves dividing the recorded time series into ten equal segments and performing the Lieblein BLUE formulation (Lieblein, 1974) with the peak values taken from each of 10 segments. Using the peak values, the mode and dispersion of the Type I extreme value distribution can be employed to estimate a more reliable peak for the entire time series. This is believed to be a more statistically stable quantity than the actual recorded peak values.

## 2.5 Pressure equalization coefficient

Wind loads on individual layers in air permeable, multi-layer cladding systems tend to have reduced wind loads due to pressure equalization (Kumar, 2000). In particular, when the pressures on the inner surface (e.g., the underside of the solar modules) approach those on the outer surface of the layer (e.g., upper surface of the solar modules), the net pressure acting across the layer can be substantially reduced (Bienkiewicz and Sun, 1992, 1997; Kumar, 2000). While current design standards utilize peak external pressures to establish guidelines for components and cladding loads for roof surfaces, these values are likely to be conservative in many circumstances due to the pressure equalization that occurs across the surfaces of the solar modules. Previous studies on roof-mounted solar (and paver) systems have noted that the pressures on the upper and lower surfaces of the modules often partially equalize (see Bienkiewicz and Sun, 1992, 1997; Wood et al., 2001; O'Brien et al., 2004; Bienkiewicz and Endo, 2009; Kopp et al., 2012; Kopp 2013), as discussed in chapter 1.

Geurts (2000) proposed a pressure equalization coefficient,  $C_{eq}$ , a ratio of the pressure difference (net pressure) normalized by the pressure on the outer surface of the roof. In the current study pressure equalization coefficients,  $C_{eq}$ , have been obtained using the ratio of the largest magnitude value of the peak net pressure coefficient ( $\hat{C}p_{AN}$ ) for a particular configuration (denoted by the subscript c) to the largest magnitude value of the peak external pressure coefficient ( $\hat{C}p_{AE}$ ) on the bare roof, which is obtained from the  $G \approx 0$ ;  $H \approx 0$  configuration for sloped roof configurations (and the  $G = 12$  cm;  $H \approx 0$  for the flat roof model configurations, since this is the only data available), i.e.,

$$C_{eq} = \max_{0 \leq \theta \leq 360^\circ}(\max_c \hat{C}p_{AN}) / \max_{0 \leq \theta \leq 360^\circ}(\max_c \hat{C}p_{AE, H \approx 0}) \quad (10)$$

External pressure coefficients from the  $H \approx 0$  configurations are used since they are the closest to bare roof coefficients and, thus, are best to use for normalization to quantify the

change in net wind loading on the solar modules caused by pressure equalization. This approach is consistent with that used to develop the Components and Cladding section of many existing design standards where the worst value is taken from a zone for all wind directions. Using these  $C_{eq}$  values implies that design values for a particular configuration can be taken from external pressure coefficients for the location on the roof, multiplied by  $C_{eq}$  for that configuration. It is believed that developing guidelines for design based on  $C_{eq}$ , a measure of the change in loading, is more robust and will minimize any issues arising from the scale mismatch. Of course, the generality of the results must be assessed (and full-scale studies are recommended because of the as-yet-unresolved issues associated with large-scale models).

### 3 Overview of measured pressure coefficients

Wind loads on structures are an integration of wind pressures acting on the surfaces. Peak loading on the array is caused by the interaction of the building generated flow field and the flow field disturbances from the array elements. Many building elements have single layers, and therefore the net wind loads are the external less the internal pressures. For the current, multi-layer, system there are cavity pressures acting on the underside of the modules, which alter the net loads on the array. For arrays mounted on the sloped roof surface of a low-rise building it is expected that for low-profile solar systems, ( $H$  and  $G$  close to zero), the aerodynamics and loading on the upper surface of the array will be similar to what is observed on the bare roof (Pratt and Kopp, 2013). With larger values of  $G$  and  $H$ , and depending on the placement of the array relative to the roof edges, the loading on the upper surface of the array may no longer be similar to what is observed on bare roofs. Cavity and net pressures have no true source of comparison; however, it is expected that the pressures will follow trends established by studying wind loads on loose-laid roof pavers on flat roofs (i.e., Bienkiewicz and Sun, 1992, 1997; Asghari Mooneghi, 2014).

In this chapter, analysis of the wind pressures focuses on negative pressures (i.e., suction), those acting outward from the surface. This is due to the fact that mounting systems for solar modules need to be designed to ensure that they remain in place during severe wind events, otherwise they can fail and contribute to the debris field and potentially damage other structures. Positive pressures, those acting towards the array or surface, are not explicitly addressed. This is not uncommon when considering wind loading on roof-mounted solar modules (e.g. Banks, 2013), although downward-acting (positive) net pressures can be as large in magnitude as the upward-acting (negative) net pressures (SEAOC PV2-2012, 2012).

This chapter shows how the results from the wind tunnel tests were validated against existing literature. The pressure coefficient distributions for peak loading conditions are compared for varying values of  $G$  and  $H$  for both the sloped and flat roof models. The mean pressure distributions for the same (peak) wind direction are presented in order to

provide insight into the pressure patterns and identify key mechanisms. These contour maps of the pressure coefficients were created by individually contouring each module. This can result in some discontinuities among adjacent modules; however, they reflect the actual measured pressures. This was found to be the best approach to capture the pressure patterns across modules and what occurs along openings. If the contours were evaluated for the array instead of modules, details along the edges of adjacent modules could be lost and certain regions of the module could be contoured at a higher level to maintain continuity with the next module – losing valuable information about pressure gradients across modules. Examples of this can be found in Appendix B. It should be noted that these distributions are not used for design in any way, but rather for visualization. All contour plots presented in this chapter have been done by considering each module individually.

Concluding the chapter is an analysis of Lieblein-fitted, peak-suction pressure coefficients, evaluated for each module, wind direction and configuration. The worst case (minima) values for the external (upper) surface, cavity and net pressures are plotted with respect to  $G$  and  $H$ . These plots show the overall trends that  $G$  and  $H$  have on the worst, peak external, cavity and net pressures. The procedure of extracting the worst case value is common with approaches used to develop building codes and is often referred to as “enveloping”. These values will be considered when developing design guidelines, further discussed in chapters 5 and 6.

### 3.1 Comparison with previous studies

To validate the measurements from the current study pressure coefficients are compared to previously published data. Pressure coefficients along a tap line on the roof surface (perpendicular to the ridge line) for  $30^\circ$  roof slopes have been published in Holmes (1981), Stathopoulos et al. (2000) and Stenabaugh et al. (2010). The results from these studies have been synthesised and are plotted in Figure 3-1. From the current study, pressure coefficients from the  $G \approx 0$ ;  $H \approx 0$  configuration are presented (not the bare roof). The tap line of pressure coefficients are from the middle line of taps on the first column of modules, those adjacent to the field or interior of the roof surface. This line is

approximately 1/3 of the roof length from the gable-end wall. As only the array was instrumented, the line of measurements only extends halfway down the roof surface from the ridgeline. Since the array is mounted on one slope, the windward and leeward measurements are from different wind directions, simulating pressure tap locations on both roof slopes. In Figure 3-1 the windward pressures are from  $180^\circ$  and the leeward pressures are from  $0^\circ$ , noting that the wind directions are defined in Figure 2-1. The comparison studies have varying model and wind simulation parameters. Stathopoulos et al. (2000) used a 1/400 scale model with a mean roof height of  $h = 16.2\text{m}$  and an exposure of  $z_0 = 0.03\text{m}$ ; and presented data were obtained along the centreline of their building. Stenabaugh et al. (2010) and the current study had the same model parameters ( $z_0 = 0.01\text{ m}$ ,  $h = 7.8\text{m}$  and 1/20 scale) but utilized different models and pressure tap layouts. Mean pressures are used as the basis of comparison as they are less sensitive to variations in how the peak pressures are measured and handled in analysis, which can change depending on the laboratory. The mean pressure coefficients from the current study match reasonably well with the previously published data. This indicates that the results from the current study are within experimental differences of other studies, validating that the testing regime and data acquisition system are reliable and that the results are reasonable.

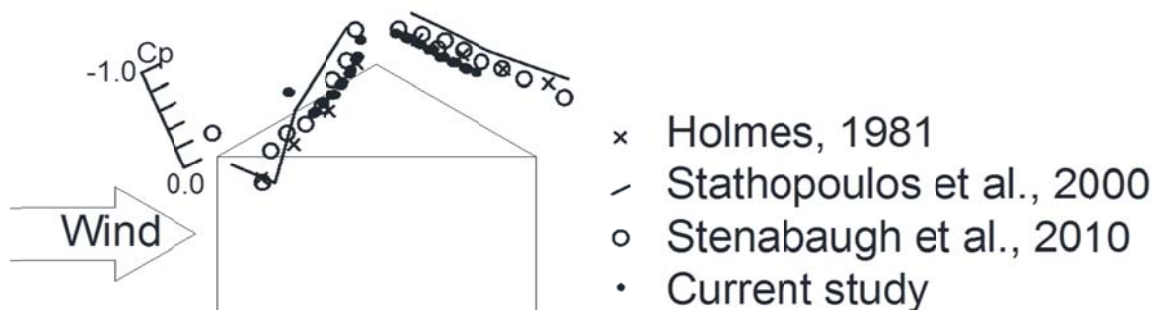


**Figure 3-1: Mean point pressure coefficients from the sloped roof model - comparison with previous studies**

The flat roof model was separately compared with existing literature. The mean pressure coefficients along a center row of modules from the  $G = 12 \text{ cm}$ ;  $H \approx 0$  flat roof configuration are plotted with respect to  $x/h$  in Figure 3-2. The data for comparison was obtained from Oh and Kopp (2015), who validated their low-rise, flat-roofed, model with measurements from the NIST database (Ho et al., 2005) as well as Cheung and Melbourne (1988). The shape of the mean pressure coefficient curve is consistent among the different studies, although there is a spread among the data. The match is reasonable for experimental studies and discrepancies are likely a result of differences in experimental set-up including scales, model dimensions and terrain simulation.

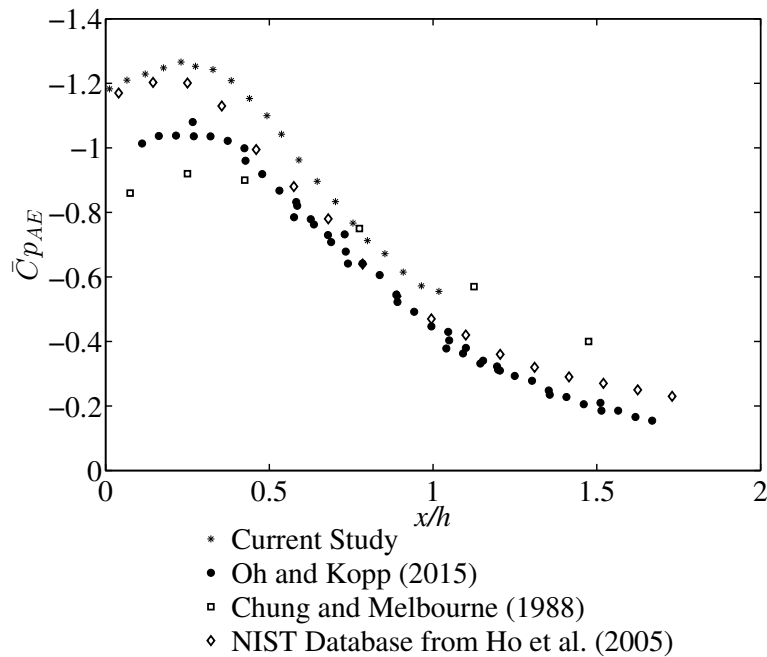


**Figure 3-2: Mean point pressure coefficients from the flat roof model - comparison with previous studies**

Additional comparisons with previously published data are presented throughout the thesis when possible. Comparisons are made to highlight and contrast the similarities and differences in findings of specific loading conditions and subsequent results, not validate the model and thus are located in later sections.

### 3.2 External (upper surface) pressure distributions on the sloped roof model

On any structure the external pressures are those acting on the exterior surface of the structure, specifically the roof and walls. These pressures are variable in space and time and can be highly localized. Peak suction is typically associated with disturbances caused by the building aerodynamics, particularly the separated flows from building edges. Roof pressures on low-rise buildings, which are most relevant to this study, are largely dependent on the building height, roof slope and exposure (and plan dimensions to a lesser extent).

To study the effect of both  $G$  and  $H$  on the peak (and mean) suction coefficients, consider the pressure distributions across the array. The instantaneous point pressure distribution at the occurrence of peak, area-averaged, minimum suction measured on any module for the  $G \approx 0$ ;  $H \approx 0$  configuration, on the  $30^\circ$  sloped roof, is plotted in Figure 3-3 (left). The direction associated with the peak suction, indicated by the arrow in Figure 3-3, was  $112.5^\circ$ , a cornering wind where modules along the bottom of the array (near the field of the roof) are the windward modules. Taps along the leading edge of the array (lower edge of module) experienced the highest suction, with much lower magnitude pressures further into the array, resulting in large pressure gradients. Figure 3-3 (right) is the contour plot for the mean pressure coefficients for the same (peak) wind direction. The pattern is somewhat similar to that at the instant of peak uplift with the modules in the lower corner of the array, adjacent to the gable-end wall, experiencing the largest suction. When generating the contours, each module was considered separately; however, when examining the entire array there is little variation in the contours across adjacent modules. This indicates that with no  $G$  between the modules the upper surface pressures act as if the array is a single surface with minimal discontinuity between individual modules. This is significant when considering the cavity pressures which are influenced by pressure gradients and discussed in more detail below. This configuration is the base case for the current study since it is closest to the bare roof with the modules in an array with no gaps ( $G \approx 0$ ) and no cavity ( $H \approx 0$ ).

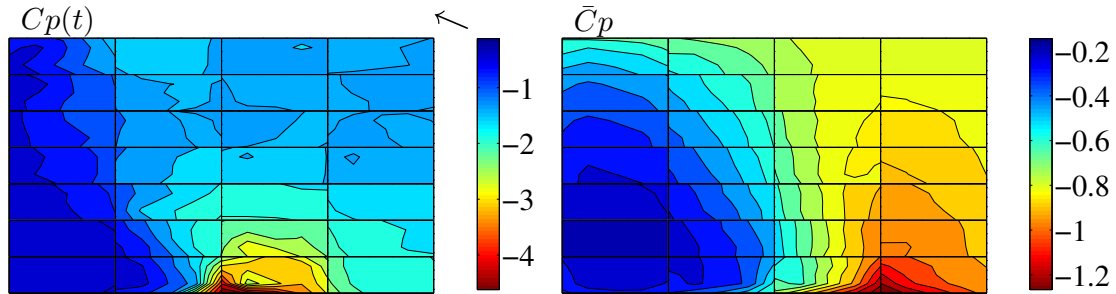


**Figure 3-3: Contour map of instantaneous external point pressures resulting in peak external suction  $G \approx 0$ ;  $H \approx 0$  (left) and mean external point pressures for the peak wind direction of  $112.5^\circ$  (right)**

For a given  $G$ , the peak suction coefficients tend to be larger with larger cavities (as discussed further below). This can be visualized in Figure 3-4 which contains the peak and mean pressure distributions at the instant of peak uplift (suction), area-averaged over a single module for the  $G \approx 0$ ;  $H = 20$  cm configuration. The critical wind direction is a cornering wind at  $292.5^\circ$ , with the array on the leeward roof slope and the prevailing wind impacting the array from across the ridgeline. This results in high suctions on the windward modules which are located in a region of separated flow in the lee of the ridge. The higher magnitude suctions are commonly measured with larger cavities (increased  $H$ ), likely due to (a secondary area of) separation off the windward modules. There are strong pressure gradients on the windward modules (upper left corner of array), with little variation across the remaining modules and smaller magnitude suctions. The highest magnitude external suctions were measured on module 1, upper left in the contour plots. On a bare roof this peak wind direction would also result in a region of separated flow causing large suction values near the ridge line.

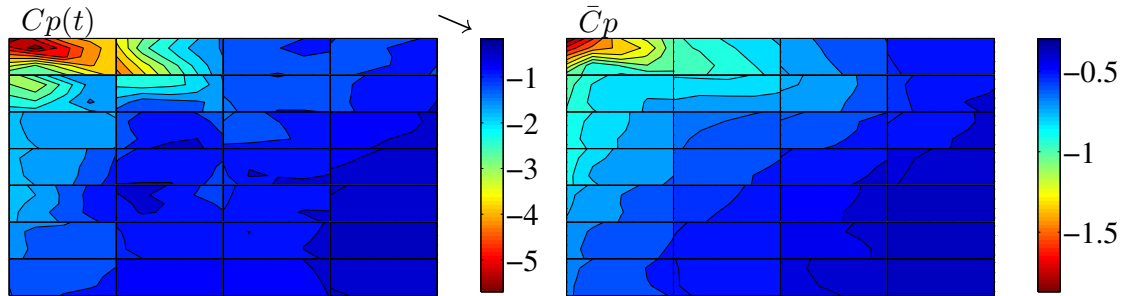


**Figure 3-4: Contour map of instantaneous external point pressures resulting in peak external suction  $G \approx 0$ ;  $H = 20$  cm (left) and mean external point pressures for the peak wind direction of  $292.5^\circ$  (right)**

The majority of commercially available mounting systems for solar systems have a space or air gap between individual modules,  $G$ . These gaps between modules may result in a change of the aerodynamics acting on the upper surface of the modules (Kopp et al., 2012; Pratt and Kopp, 2013; Asghari Mooneghi et al., 2014). With small  $G$  values, the system acts like a single surface with the gaps having little impact on the external pressures; however, with large  $G$  the passage of air through the openings will change the flow field and therefore impact the external pressures. This can be seen with the  $G = 12$  cm model shown in Figure 3-5 (right). The mean external pressure distribution for the peak wind direction of  $315^\circ$  shows higher magnitude suction on the windward edge of module 8 (as defined in Figure 2-4) but at the instance of peak suction (Figure 3-5 left) the larger magnitude peak suction are on the trailing or leeward edge of the module. This is likely caused by flow exiting the cavity in this vicinity at the instance of peak uplift, which varies from the mean distribution for the same wind direction (Figure 3-6). It is difficult to see any significant mean distributions due to the scale of the contours, as the range of values is quite large from positive pressurization along modules adjacent to the ridge-line and suction across most of the array. With  $G = 12$  cm the magnitudes of the peak suction are reduced from when  $G \approx 0$ ; however, there is increased variation in the wind loading from one module to the next. Air enters and exits the cavity through the gaps between individual modules and can influence the external pressures around the perimeter of the modules. This can result in larger pressure gradients across individual modules than the  $G \approx 0$  case where flow between modules was severely restricted. This

reinforces the aerodynamic significance of  $G$  – it lowers the magnitude of the peak suction, while also increasing the pressure gradients where flow is entering or exiting the cavity through  $G$ , potentially leading to more modules experiencing large external suction.

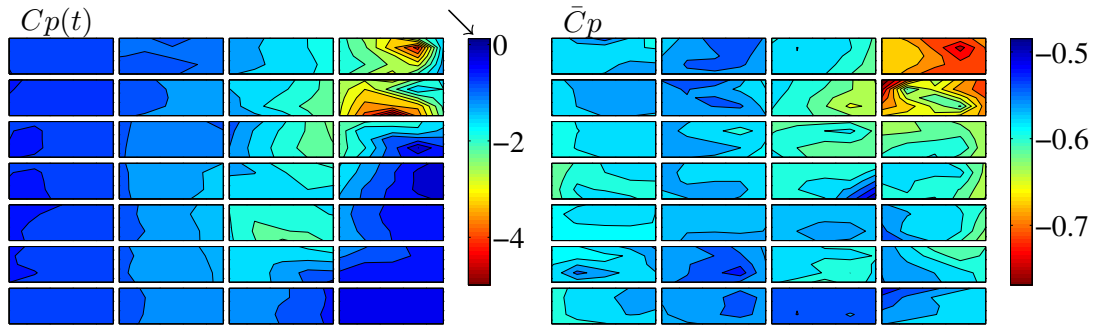


**Figure 3-5: Contour map of instantaneous external point pressures resulting in peak external suction  $G = 12$  cm;  $H \approx 0$  (left) and mean external point pressures for the peak wind direction of  $315^\circ$  (right)**

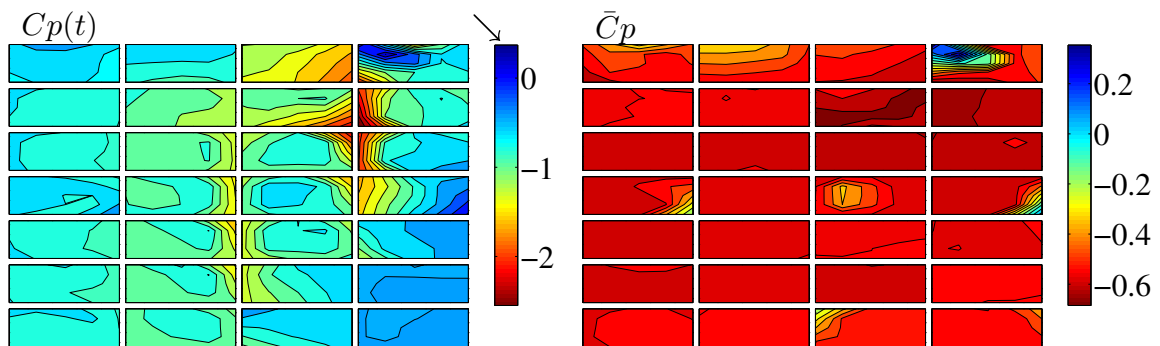


**Figure 3-6: Contour map of instantaneous cavity point pressures at the instant of peak external suction for the  $G = 12$  cm;  $H \approx 0$  configuration (left) and mean cavity point pressures for the peak (external) wind direction of  $315^\circ$  (right)**

From the above contour plots it can be seen that while the majority of the modules experience relatively lower magnitude pressures, selected modules can experience large suction and pressure gradients. The pressure distributions across the array at the instant of peak uplift area-averaged over a single module are typically similar to the mean pressure distributions for the same wind direction. The peak pressures are higher in

magnitude for larger cavity depths but smaller in magnitude when installed with  $G$ . These external pressure distributions are important as they influence the cavity distributions, but can also be modified by flow through  $G$ . Since the cavity pressures are not an exact transmission of the external pressure their peak and mean distributions should also be analyzed.

### 3.3 Cavity (lower surface) pressures on the sloped roof model

Roof-mounted solar modules are mounted on top of the roof cladding, with both their external (upper) surface and cavity (lower surface) exposed to flow. As such, the cavity pressures are relevant to design. The flow in the cavity is complex and is largely influenced by the external pressure and by the array geometric parameters including the depth of the cavity, the size of the gap, and the panel dimensions (e.g., Kumar, 2000; Oh, 2014). Similar to the approach for the externals in the previous section, the peak (suction) and mean cavity point pressure distributions are studied, specifically noting how they are altered by varying the array geometry.

The instantaneous point pressure field at the instance of worst peak suction, area-averaged over a single module, for the  $G \approx 0$ ;  $H \approx 0$  configuration is plotted in Figure 3-7 (left) with the mean pressure map for the same wind direction on the right. This instant does not coincide with the peak measured on the external surface. Despite the contours being mapped separately for each individual module, there is minimal variation at the interface between modules and rather, a continuous pressure gradient across the entire array. In this case the flow enters the cavity (notably shallow in depth as the modules were loose-laid) at the upper right (blue contours) and exits along the upper left and lower centre (orange to red contours). This flow direction is consistent with the overall wind direction, a quartering wind as noted by the arrow in the figure.

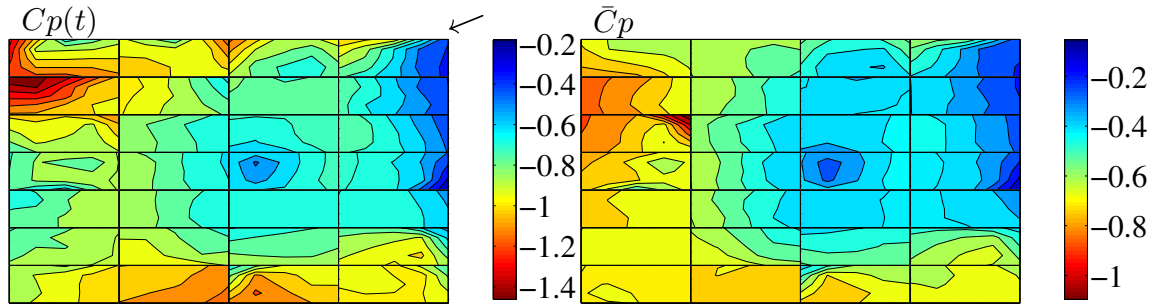


**Figure 3-7: Contour map of instantaneous cavity point pressures resulting in peak cavity suction  $G \approx 0$ ;  $H \approx 0$  (left) and mean cavity point pressures for the peak wind direction of  $67.5^\circ$  (right)**

A relatively large cavity depth ( $H = 20$  cm) beneath the modules significantly alters the cavity pressures. The underside pressure distribution becomes largely uniform across the majority of the array with significant pressure gradients on the windward modules. This is shown when considering the instantaneous peak and mean cavity pressure distribution for the  $G \approx 0$ ;  $H = 20$  cm configuration plotted in Figure 3-8 (left and right respectively). The overall (external) wind is from right to left in the figure. However, the cavity flow is predominately from left to right (higher to lower pressures). Flow enters the cavity along the left edge (near the field of the roof) and exits the cavity along the ridge and at the bottom of the array near field of the roof (greater suction). Additional inflow into the cavity occurs along gable-end column of modules (far right in figure), which are aligned with the overall wind direction. This inflow does not penetrate far into the array, yielding significant pressure gradients, as indicated by the tightly spaced contours. Aside from this region of large pressure gradients, seen in both the instantaneous and mean pressures (Figure 3-8 left), there is reduced variation in the cavity pressures when contrasted against a smaller cavity depth. This indicates that cavity pressures are more uniform with larger  $H$ . This is consistent with the observations of Bienkiewicz and Sun (1992) who attributed the more uniform pressures associated with larger cavities to the lower flow resistance underneath the pavers.

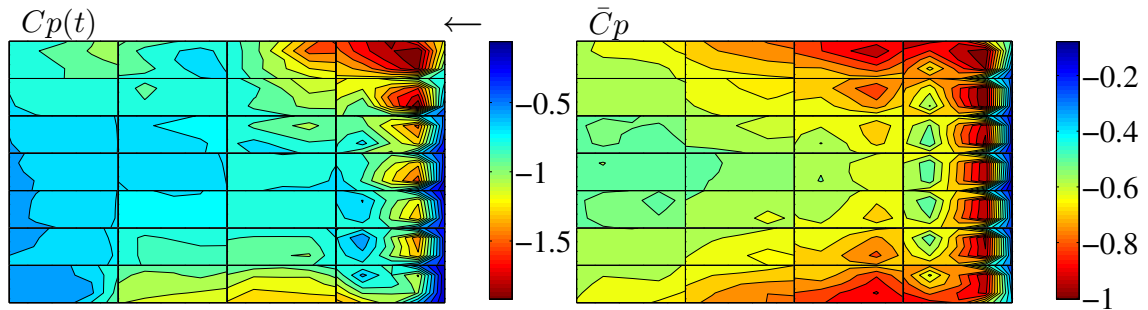


**Figure 3-8: Contour map of instantaneous cavity point pressures resulting in peak cavity suction  $G \approx 0$ ;  $H = 20$  cm (left) and mean cavity point pressures for the peak wind direction of  $90^\circ$  (right)**

While  $H$  is noted to have a strong impact on cavity pressures, the effect of increasing  $G$  is not as significant. The cavity distributions for  $G \approx 0$ ;  $H = 20$  cm (above) are largely similar to those observed for  $G = 12$  cm;  $H = 20$  cm (Figure 3-9 below). When  $G$  was increased the overall cavity flow remained from left to right with an overall (external) flow from right to left ( $90^\circ$ ). The largest impact is noted in the outflow – with  $G$  around each module the peak and mean pressure gradients show that there is outflow through  $G$  between modules. When the modules were flush ( $G \approx 0$ ) the space between modules was limited to model and material imperfections, severely hampering flow. Thus the inflow and outflow was restricted to the perimeter. The increased outflow between modules in the column adjacent to the gable-end wall (right-most column in the figure) is still observed when contrasting the mean distributions for the different  $G$  (Figure 3-9 right for  $G = 12$  cm and Figure 3-8 for  $G \approx 0$ ) but the effect is notably reduced.

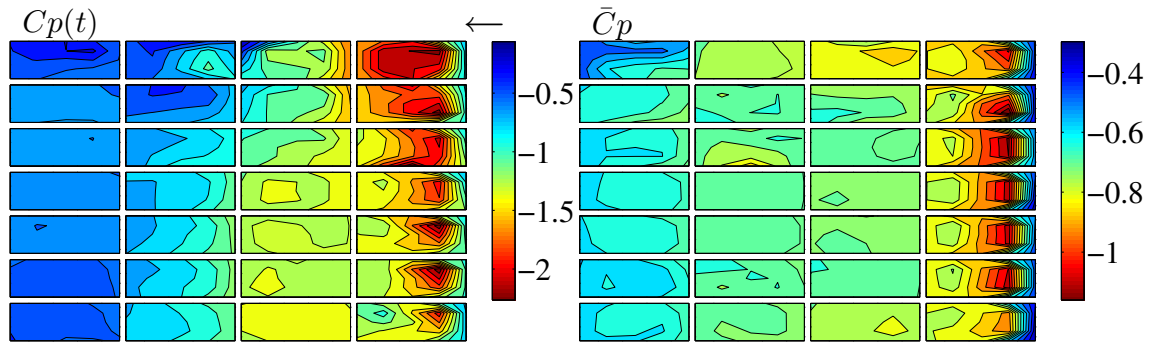


**Figure 3-9: Contour map of instantaneous cavity point pressures resulting in peak cavity suction  $G = 12$  cm;  $H = 20$  cm (left) and mean cavity point pressures for the peak wind direction of  $90^\circ$  (right)**

It should be noted that the peak external distribution and the peak cavity distributions as shown above do not occur at the same instance in time, or even for the same wind direction. They do not represent the combined effects of external and cavity pressures acting on the array at a given instant. The cavity distribution at the instance of peak external uplift for the  $G = 12$  cm;  $H = 20$  cm is shown in Figure 3-10. It is the same configuration as plotted in Figure 3-9 above; however, the instantaneous cavity pressure distributions at the instance of peak external suction and peak cavity suction differ and are not even from the same wind direction. Therefore it is imperative to study the combined (instantaneous) effects of the external and cavity pressures on the array by studying the net pressure distributions as well.

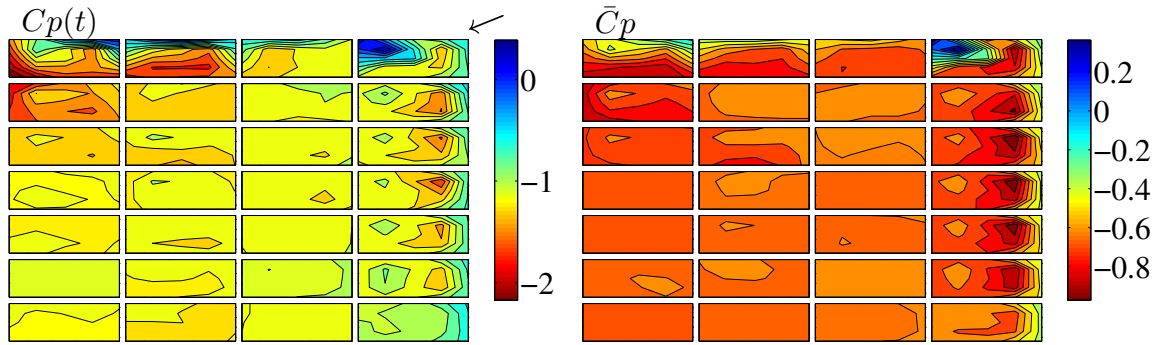


**Figure 3-10: Contour map of instantaneous cavity point pressures at the occurrence of the peak external suction  $G = 12$  cm;  $H = 20$  cm (left) and mean cavity point pressures for the peak external wind direction of  $67.5^\circ$  (right)**

### 3.4 Net pressure distributions on the sloped roof model

Net pressures are considered more relevant for design as both the external (upper) and lower (cavity) surfaces of the modules are exposed to the flow. The difference between the pressures on the external and cavity pressures, the net pressure, better represents the loading acting on the module and thus reflects the loads for which the mounting system should be designed. The magnitudes of the net pressures are evaluated at each instant in the time series. As such, the instance of peak net pressure may not coincide with the peak measured on the external (upper) surface or cavity (lower) surface.

Loading patterns responsible for the peak net suction are of particular interest as it is the net pressures for which the system should be designed. The net pressure distributions show the combined effects of the external and cavity pressures – which vary in space and time. As such, when the instantaneous peak net pressure gradients are plotted, so too are the instantaneous external and cavity distributions that resulted in the peak net pressure. The upper left of the contour figures (a) is the net pressure distribution at the instant of peak net uplift, area-averaged over a single module. For this section the upper right plot (b) represents the mean net uplift for the same, peak net, wind direction. The bottom left (c) and right (d) plots respectively contain the external and cavity surface pressure

distributions at the instant of the peak net uplift (resulting in the pressures in the upper left, instantaneous net pressure plot).

The instantaneous net suction from the  $G \approx 0$ ;  $H \approx 0$  configuration, Figure 3-11a, are largely similar to the external suction at the instant of peak uplift (Figure 3-11c) but are lower in magnitude. This signifies that even when the modules are loose-laid (no modelled cavity but modules were not sealed to the roof surface) the cavity pressures result in the net suction being lower in magnitude than the external suction. The mean pressure distribution for same wind direction is shown in Figure 3-11b. It can be observed that a number of the modules (on the leeward side of the array) have a mean net wind loading of near-zero. The expectation of near-zero mean net wind loading was identified by Geurts and Blackmore (2013) and confirmed in their full-scale study of a single module. Despite some modules achieving the expected, and desirable, near-zero mean net wind loading, it should be noted that this does not happen for every module within the array. Select modules, most notably windward modules and those near the edge of the roof surface, can experience significant mean net suction and pressure gradients. This indicates that larger magnitude net pressures are common for modules directly impacted by the wind flow, while leeward modules can experience some beneficial sheltering effects that serve to reduce net pressures.

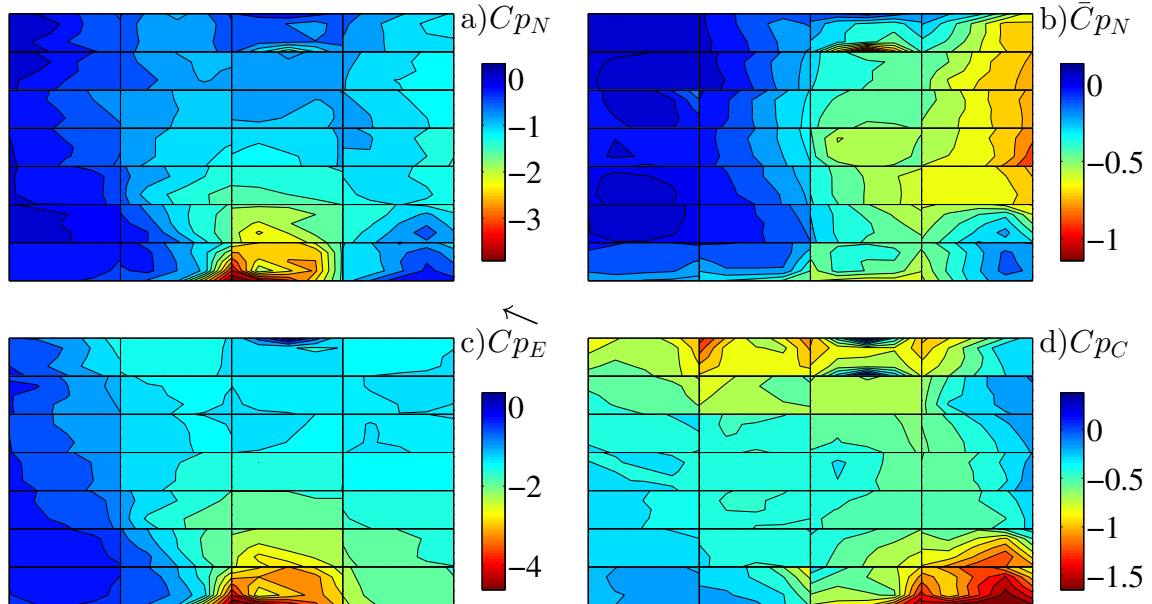


**Figure 3-11: Contour map of a) instantaneous net point pressures resulting in peak net suction  $G \approx 0$ ;  $H \approx 0$ , b) mean net point pressures for the peak wind direction of  $112.5^\circ$ , c) instantaneous external and d) cavity point pressures that resulted in peak net suction**

While the peak net pressures are typically lower in magnitude than those on the upper surface, it is not always the case. With larger cavity depths it is possible that the peak net wind pressures measured at a particular location (or area-averaged over a particular module) may not be reduced from the external pressures on the upper surface. This is caused by positive pressures in the cavity of key modules (Figure 3-12d) when the majority of the array is under external suction. The positive pressure is typically associated with modules along the ridge where large cavities can force the underside of the modules to extend above the roof ridge and be directly impacted by flow from certain wind directions. If positive pressurization of (portions of) the cavity coincides with large external suction it can result in localized net suction which exceed the external suction, as shown in Figure 3-12. This loading condition is not necessarily common, and may only occur a handful of times during the time history. This is evidenced by the fact that the mean net distribution in Figure 3-12b shows significantly lower pressures. However, this possibility must be considered as it drives the peak loading for large cavity depths.

This punitive loading condition can be avoided if the array is mounted at a distance set-back from the roof ridge or gable end such that the lower surface of the array is sheltered from the ridgeline preventing positive pressurization of the cavity. Aly and Bitsuamlak (2014) also recommended avoiding critical roof zones to reduce the net minimum pressures acting on solar modules which were tested in multiple roof zones on a 1:15 scaled wind tunnel model.

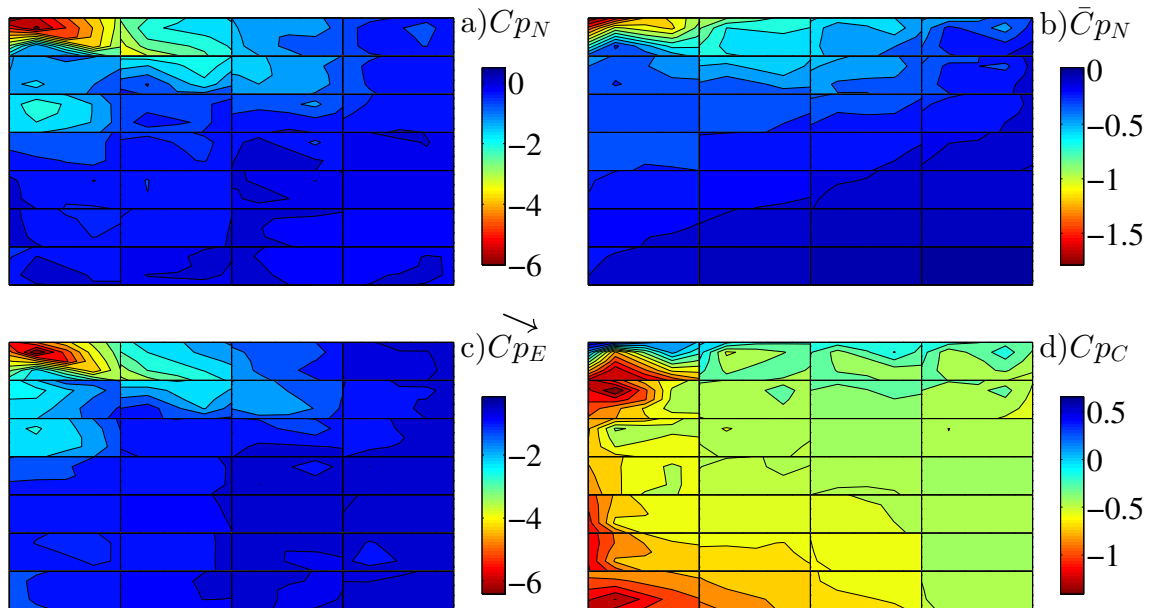


**Figure 3-12: Contour map of a) instantaneous net point pressures resulting in peak net suction  $G \approx 0$ ;  $H = 20$  cm, b) mean net point pressures for the peak wind direction of  $292.5^\circ$ , c) instantaneous external and d) cavity point pressures that resulted in peak net suction**

Consistent with the effect on external suctions,  $G$  reduces the mean suctions, as can be seen by the contour map of the mean net pressures from the peak net uplift wind direction for  $G = 12$  cm;  $H \approx 0$  in Figure 3-13b. The local pressure gradients on individual modules, as discussed earlier, are evident when examining the cavity pressures at the instance of peak net uplift shown in Figure 3-13d. Even on interior, sheltered, modules there are local variations in the pressure gradients at the interface between modules, as the array no longer acts as a single surface but rather local airflow through the gaps influences the pressures on adjacent modules.

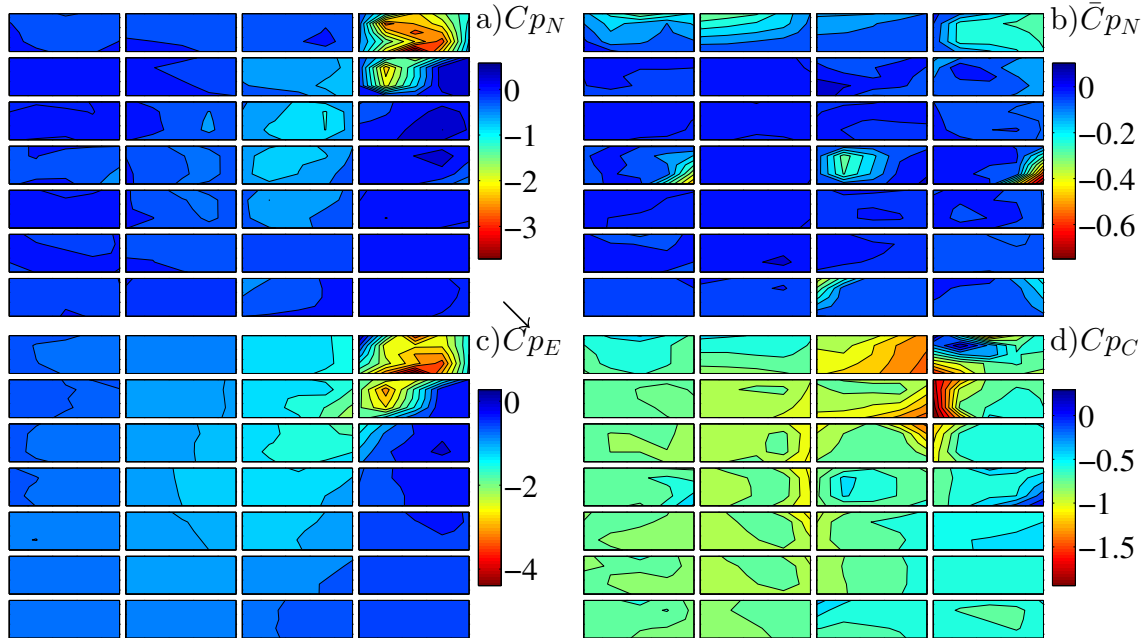


**Figure 3-13: Contour map of a) instantaneous net point pressures resulting in peak net suction  $G = 12$  cm;  $H \approx 0$ , b) mean net point pressures for the peak wind direction of  $315^\circ$ , c) instantaneous external and d) cavity point pressures that resulted in peak net suction**

While Bienkiewicz and Sun (1992) studied roof pavers on a flat roof and not solar modules on a sloped roof, there are a number of comparison points between their study and the current one. They examined the correlation coefficients between the external and cavity pressures of roof pavers for a cornering wind direction, noting that for their test without a spacer (loose-laid) the correlation was largely close to uniform with the exception of three pavers adjacent to the leading-edge corner of the building.

The external-cavity point pressure correlation coefficients for the peak net wind direction for  $G \approx 0$ ;  $H \approx 0$  configuration of the current study are shown in Figure 3-14. The correlation coefficients are lower than those reported by Bienkiewicz and Sun (1992), with the discrepancy likely due to the different aerodynamics of sloped and flat roofed structures governing the pressures. The tap locations that are associated with higher correlation are typically located around the perimeter of the array. This indicates that the time histories around the perimeter of the array are more closely related. The more

correlated the signals are, the higher the degree of pressure equalization, which will be discussed in more detail in subsequent chapters. Pressure taps located further into the array are more likely to have lower correlation coefficients.

0.87	0.48	0.3	0.47	0.7	0.78	0.55	0.31	0.57	0.81	0.81	0.77	0.72	0.79	0.86	0.82	0.62	0.53	0.0072	-0.068
0.51	0.38		0.48		0.51	0.49		0.57		0.68	0.057		0.76		0.76	0.69		0.2	0.15
0.72	0.65	0.63	0.39	0.48	0.5	0.47	0.45	0.47	0.28	0.68	0.64	0.65	0.62	0.66	0.62	0.38	0.1	-0.18	-0.2
0.3	0.46	0.39	0.33	0.37	0.46	0.46	0.51	0.55	0.59	0.62	0.63	0.6	0.64	0.66	0.61	0.27	0.08	-0.0098	0.066
0.69	0.35	0.26	0.37	0.28	0.29	0.49	0.49	0.58	0.51	0.63	0.58	0.54	0.58	0.65	0.51	0.32	0.032	-0.072	-0.2
0.77	0.36	0.48	0.47	0.59	0.54	0.53	0.59	0.64	0.71	0.71	0.61	0.57	0.63	0.69	0.66	0.38	0.26	0.093	0.089
0.76	0.43	0.4	0.32	0.63	0.38	0.62	0.6	0.66	0.71	0.72	0.66	0.59	0.6	0.67	0.64	0.45	0.29	0.14	0.065
0.69	0.37	0.47	0.55	0.7	0.68	0.68	0.69	0.66	0.69	0.68	0.65	0.63	0.63	0.65	0.64	0.51	0.35	0.22	0.12
0.86	0.64	0.55	0.66	0.74	0.75	0.76	0.75	0.69	0.68	0.68	0.66	0.61	0.58	0.59	0.56	0.4	0.31	0.23	0.028
0.87	0.56	0.56	0.61	0.69	0.66	0.69	0.68	0.66	0.67	0.67	0.66	0.64	0.62	0.57	0.51	0.43	0.42	0.35	0.042
0.8	0.51	0.53	0.51	0.67	0.59	0.69	0.69	0.68	0.69	0.48	0.64	0.59	0.54	0.52	0.41	0.21	0.39	0.62	0.019
0.44	0.31	0.4	0.34	0.52	0.68	0.84	0.82	0.69	0.66	0.65	0.64	0.67	0.65	0.6	0.5	0.37	0.79	0.86	0.79
0.52	0.34	0.18	0.46	0.74	0.63	0.6	0.67	0.72	0.86	0.67	0.62	0.61	0.59	0.54	0.49	0.37	0.71	0.72	0.23
0.41	0.43	0.27	0.6	0.4	0.41	0.55	0.4	0.64	0.55	0.52	0.72	0.46	0.48	0.28	0.21	0.27	0.57	0.82	0.59

**Figure 3-14: Distribution of the external-cavity point pressure correlation coefficients for the peak wind direction of 112.5° ( $G \approx 0$ ;  $H \approx 0$ )**

A larger cavity height is associated with lower correlations between the external and cavity pressures, as confirmed when contrasting Figure 3-14 for  $G \approx 0$ ;  $H \approx 0$  and Figure 3-15 for  $G \approx 0$ ;  $H = 20$  cm. This is consistent with the findings for roof pavers (Bienkiewicz and Sun, 1992). It should be noted that these are just general observations as the peak net wind directions for which the correlation coefficients were evaluated for the two cavity heights are different.

-0.12 0.43	0.59 0.6	-0.011 0.45	0.15 0.45	0.0099 0.36	0.067 0.33	0.45 0.27	0.12 0.24	0.45 0.31	0.19 0.29	0.2 0.33	0.42 0.28	0.12 0.28	0.18 0.26	0.17 0.22	0.087 0.3	0.42 0.28	0.19 0.36	0.21 0.37	0.35 0.56
0.39 0.35	0.59 0.57	0.49 0.52	0.41 0.46	0.32 0.4	0.35 0.38	0.3 0.29	0.32 0.29	0.3 0.29	0.31 0.26	0.33 0.26	0.29 0.25	0.32 0.28	0.31 0.34	0.32 0.33	0.34 0.34	0.37 0.34	0.41 0.5	0.46 0.63	0.78 0.62
0.34 0.25	0.44 0.46	0.51 0.48	0.46 0.43	0.4 0.39	0.38 0.4	0.32 0.37	0.3 0.36	0.27 0.32	0.25 0.31	0.26 0.32	0.28 0.29	0.31 0.3	0.33 0.35	0.34 0.36	0.38 0.39	0.41 0.43	0.5 0.54	0.6 0.66	0.76 0.7
0.22 0.15	0.42 0.4	0.48 0.45	0.43 0.43	0.41 0.41	0.42 0.41	0.4 0.4	0.38 0.4	0.35 0.37	0.33 0.38	0.32 0.36	0.33 0.35	0.31 0.39	0.34 0.4	0.36 0.43	0.38 0.46	0.46 0.48	0.51 0.55	0.6 0.67	0.78 0.74
0.24 0.19	0.37 0.36	0.43 0.45	0.44 0.44	0.42 0.44	0.42 0.46	0.41 0.42	0.41 0.45	0.41 0.44	0.4 0.45	0.39 0.46	0.41 0.44	0.39 0.47	0.4 0.48	0.41 0.52	0.44 0.54	0.5 0.54	0.52 0.59	0.6 0.68	0.76 0.77
0.17 0.15	0.42 0.43	0.47 0.55	0.51 0.53	0.5 0.55	0.51 0.58	0.57 0.65	0.51 0.59	0.53 0.55	0.49 0.58	0.48 0.6	0.52 0.57	0.5 0.6	0.54 0.61	0.53 0.66	0.53 0.66	0.57 0.65	0.58 0.69	0.64 0.71	0.78 0.78
0.076 0.47	0.61 0.52	0.61 0.65	0.67 0.66	0.65 0.69	0.65 0.71	0.69 0.69	0.62 0.72	0.66 0.72	0.65 0.75	0.64 0.74	0.67 0.72	0.63 0.76	0.66 0.76	0.66 0.76	0.65 0.76	0.7 0.78	0.67 0.79	0.7 0.75	0.79 0.76

**Figure 3-15: Distribution of the external-cavity point pressure correlation coefficients for the peak wind direction of 292.5° ( $G \approx 0$ ;  $H = 20$  cm)**

Figure 3-16 is the distribution of correlation coefficients from the peak net wind direction of 112.5° for the  $G = 12$  cm;  $H \approx 0$  configuration. Each module has high correlations around the perimeter with lower correlations on the interior of the module. This supports the observation that pressure equalization is improved with the presence of  $G$  around individual modules. High correlation coefficients indicate a higher degree of pressure equalization as noted around the perimeter of the array. The effect is reduced for the interior of the module.

0.91 0.86	0.64 0.44	0.25 0.41	0.51 0.53	0.69 0.87	0.73 0.86	0.79 0.8	0.73 0.81	0.61 0.69	0.48 0.65	0.88 0.98	0.95 0.95	0.95 0.96	0.91 0.97	0.96 0.96	0.89 0.94	0.055 0.81	0.91 0.3	0.43 0.55	0.3 0.83
0.89 0.55	0.72 0.5	0.93 0.75	0.88 0.78	0.98 0.78	0.93 0.96	0.81 0.78	0.75 0.77	0.63 0.78	0.85 0.95	0.75 0.75	0.72 0.74	0.8 0.87	0.58 0.82	0.71 0.96	0.94 0.98	0.72 0.79	0.24 0.85	0.56 0.71	0.92 0.38
0.99 0.97	0.76 0.75	0.5 0.58	0.61 0.65	0.96 0.89	0.99 0.98	0.91 0.86	0.73 0.67	0.53 0.63	0.87 0.94	0.87 0.64	0.66 0.59	0.63 0.72	0.49 0.64	0.95 0.87	0.97 0.98	0.73 0.71	0.57 0.61	0.57 0.61	0.81 0.73
0.98 0.97	0.97 0.97	0.96 0.85	0.51 0.62	0.78 0.69	0.99 0.99	0.82 0.77	0.35 0.47	0.53 0.59	0.93 0.96	0.81 0.76	0.66 0.66	0.63 0.75	0.65 0.75	0.96 0.91	0.99 0.97	0.96 0.97	0.96 0.97	0.74 0.87	0.64 0.82
0.85 0.97	0.65 0.78	0.53 0.91	0.72 0.85	0.95 0.96	0.98 0.97	0.76 0.88	0.38 0.73	0.37 0.65	0.97 0.94	0.92 0.93	0.59 0.71	0.5 0.86	0.68 0.87	0.95 0.93	0.51 0.97	0.82 0.95	0.84 0.97	0.89 0.96	0.83 0.95
0.88 0.97	0.78 0.85	0.55 0.91	0.58 0.8	0.9 0.96	0.99 0.98	0.82 0.97	0.26 0.9	0.45 0.61	0.98 0.92	0.96 0.98	0.81 0.93	0.48 0.93	0.67 0.9	0.78 0.94	0.57 0.97	0.71 0.94	0.66 0.97	0.63 0.91	0.57 0.94
0.97 0.93	0.84 0.11	0.2 0.82	0.36 0.77	0.98 0.94	0.89 0.92	0.78 0.84	0.73 0.86	0.67 0.8	0.96 0.9	0.74 0.95	0.62 0.79	0.66 0.88	0.66 0.9	0.45 0.92	0.92 0.9	0.8 0.91	0.57 0.92	0.82 0.96	0.86 0.94

**Figure 3-16: Distribution of the external-cavity point pressure correlation coefficients for the peak wind direction of 315° ( $G = 12$  cm;  $H \approx 0$ )**

Examining the instantaneous net, external and cavity distributions at the occurrence of the peak net uplift area-averaged for a single module indicates that the net distribution is largely similar to that on the external, upper, surface. The difference is that the net pressures are typically lower in magnitude, having been reduced by the cavity pressures. Although, if the cavity is pressurized with positive pressures, which can occur for certain array placements and wind directions, the net pressures can actually exceed those measured on the external surface. The correlation coefficients between the external and cavity pressures remain relatively high, but are lower in the interior portion of the module.

While pressure distributions can give us a sense of the pressure field on both the array and individual modules, it is the overall pressure acting on an individual module that is relevant for design. The point pressures, as noted in the distributions above, area-averaged over the module according to their tributary area, resulting in a representative pressure for the module. The statistically fit minima can be evaluated and compared to determine how the varying pressure patterns impact the module pressures and is the focus of the next section.

### 3.5 Area-averaged pressure coefficients

Point pressures were area-averaged over individual modules and the Lieblein-fitted minima were extracted. As such, the peak pressure distributions presented earlier in this chapter do not directly correlate to the values presented in this section, which are statistical (suction) minima. The worst case peak value from each configuration is relevant for the eventual development of design recommendations. Systems need to be designed to withstand the largest expected load, here represented by the worst case peak from each configuration. When these peak suction values (external, cavity and net) for each configuration are plotted with respect to either  $G$  or  $H$ , trends are more apparent.

The peak external pressure coefficients,  $\hat{C}p_{AE}$ , are plotted with respect to  $H$  in Figure 3-17a and with respect to  $G$  in Figure 3-18a. Larger  $H$  depths tend to yield larger peak external suction. Geurts and Blackmore (2013) also noted a tendency for peak pressures to increase on the upper surface with larger  $H$ , although they noted the effect to be small. Similar observations were made by Asghari Mooneghi et al. (2014) for roof pavers on a flat roof. Figure 3-18a shows that the highest external suction pressures on the upper surface occur when  $G \approx 0$  (nominally flush) and  $H = 20$  cm. For  $G$  values larger than about 4 cm, there is little difference with the pressures reaching a plateau. The lowest suction coefficients on the upper surface of the module are associated  $G = 2$  cm and  $H = 2$  cm or  $H = 4$  cm.

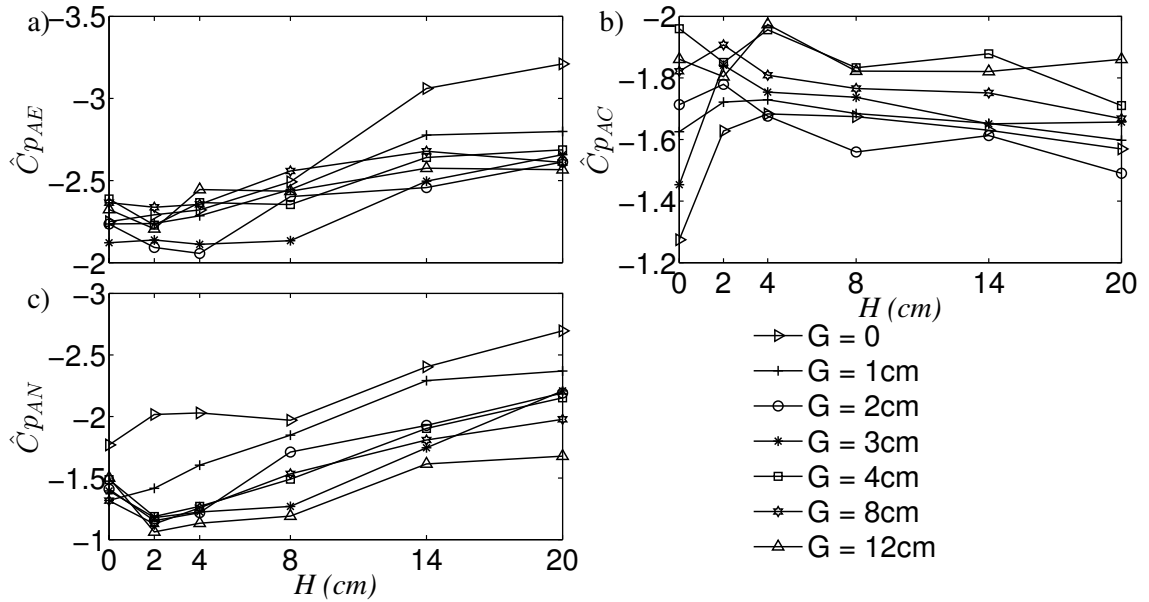


**Figure 3-17:** The worst case values of the peak (suction) external area-averaged over a single module on (a) the external, upper, surface, (b) in the cavity, and (c) net with respect to  $H$

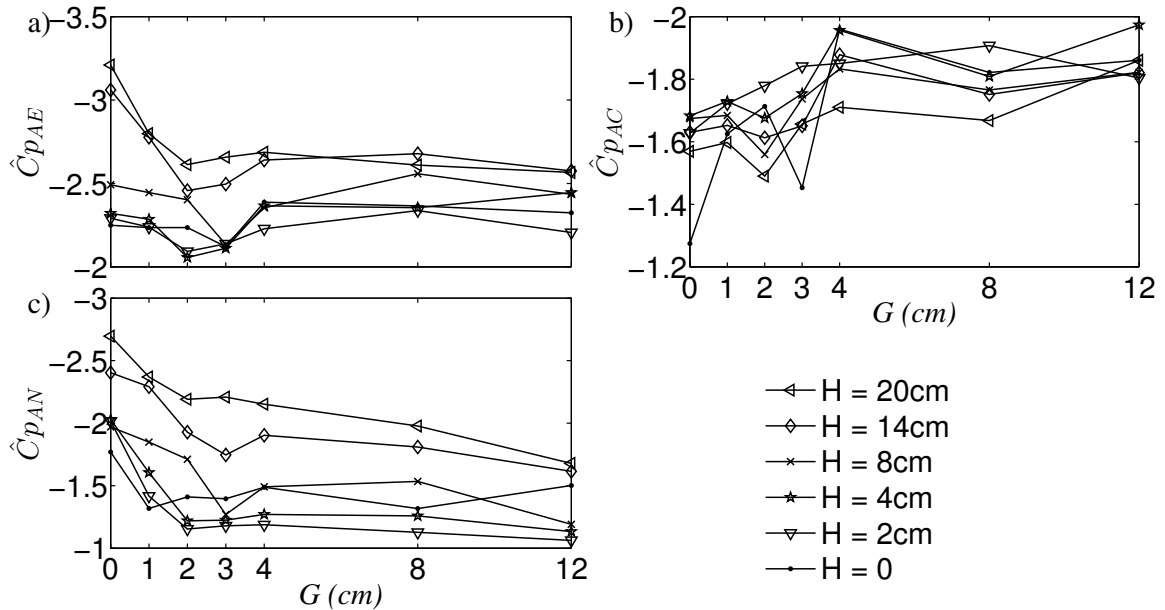


**Figure 3-18:** The worst case values of the peak (suction) external area-averaged over a single module on (a) the external, upper, surface, (b) in the cavity, with respect to  $G$

Figure 3-17b and Figure 3-18b show the worst, peak external suction acting in the cavity below the array, area-averaged over individual modules,  $\hat{C}p_{AC}$ . The most significant finding is that the worst, peak, suction is significantly increased for a non-nominal cavity ( $H > 0$ ), evident when contrasting values for  $H \geq 2$  cm values with  $H \approx 0$  (Figure 3-18b). Larger cavities have little impact on the peak cavity pressures, with the reduction in peak suction having occurred when even a small cavity is introduced to the system. This is consistent with the findings for roof pavers from Bienkiewicz and Sun (1992) who found that even very low cavities reduced the peak and mean suction significantly but that further increasing the cavity height did not have a large impact. Geurts and Blackmore (2013) reported an increase in peak suction on the underside of their single solar module with increasing height. However, the effect was small enough for them to state that the wind pressures on the module can be assumed to be independent of  $H$ . Discrepancies are thought to be partially due to the variations in experimental set-up, including but not limited to, module interaction within the array, blockage underneath the modules and tap density. The difference in findings also indicates the sensitivity of the underside pressures to modeling and experimental set-up, further reinforcing the need for full-scale studies to validate wind tunnel results.

The peak net pressure coefficients, area-averaged over individual modules, are plotted with respect to  $H$  in Figure 3-17c and Figure 3-18c. Immediately it can be seen that the worst peak net pressures have been reduced from the worst peak external pressures (Figure 3-17a). The trends with respect to  $G$  and  $H$  observed with external pressures on the upper surface are consistent with net pressure observations; larger  $H$  is associated with higher overall peak net suction, while larger  $G$  results in lower magnitude peak suction. It is the air flow through  $G$  that improves the wind resistance of the system by reducing the net pressures. Cavity inflow and outflow through  $G$  can even influence the external pressure gradients as discussed earlier. The cavity pressures are largely influenced by the external pressure gradients and the array geometry (which impacts the cavity flow resistance), which is discussed in more detail in chapter 4. Pressure equalization between the externals and the cavity pressures is improved with  $G$ , leading to lower magnitude peak net suction than peak external suction. Larger cavities are

associated with larger magnitude peak net suction since peak externals are larger in magnitude with larger  $H$ . Recall that  $H$  has little impact on peak cavity suction, and thus has little impact on peak net suction. Peak net pressure coefficients are smallest with  $G \geq 2$  cm and  $2$  cm  $\leq H \leq 4$  cm.

These findings were observed from a large dataset of solar modules mounted parallel to the sloped roof of a low-rise building. While the trends of  $G$  and  $H$  were consistent with previous work on both flat roofs (i.e., Bienkiewicz and Sun, 1992) and work on a single module (Geurts and Blackmore, 2013) the array from the current study was installed on a flat roof to confirm the trends established by the sloped roof model are valid for other roof slopes. Only six configurations were tested representing the full range of  $H$  for  $G = 12$  cm as discussed in chapter 2. Establishing that the trends of  $G$  and  $H$  are irrespective of roof slope is a crucial step when proceeding with the development of design provisions. The next section focuses on the pressure patterns observed on the flat roof model as well as the worst case peak external, cavity and net suction with respect to  $H$ , consistent with the approach taken for the sloped roof results.

### 3.6 Pressure coefficients on the flat roof model

Banks (2013) specifically singled out the role that corner vortices play when he discussed the interaction between the roof-mounted array and the building generated wind field. They are known to cause the worst wind loads on the corner of roof surfaces on flat roofs, the justification for roof zones in some building standards. In fact, some of the roof paver studies have exclusively looked at cornering winds to quantify the wind loads (i.e.; Bienkiewicz and Sun, 1992 and Asghari Mooneghi et al., 2014). While the current study tested the array through  $360^\circ$  in  $22.5^\circ$  increments in the wind tunnel, the cornering wind with the array adjacent to both windward walls was found to be critical for peak upper and lower surface pressures as well as net pressures. The loading patterns and sensitivity to cavity height are discussed in more detail below.

The peak wind pressures measured on the upper surface of the array on the flat roof are caused by a cornering wind ( $45^\circ$ , as indicated by the arrow) and featured in Figure 3-19a. The pressure patterns are for the  $G = 12$  cm;  $H \approx 0$  cm configuration, but are indicative of

all cavity heights tested for the flat roof model. The mean pressure field for the peak external wind direction (Figure 3-19b) shows the presence and impact of conical vortices emanating from the windward corner. The effects of these conical vortices were also discussed by Bienkiewicz and Sun (1992) and Banks (2013).

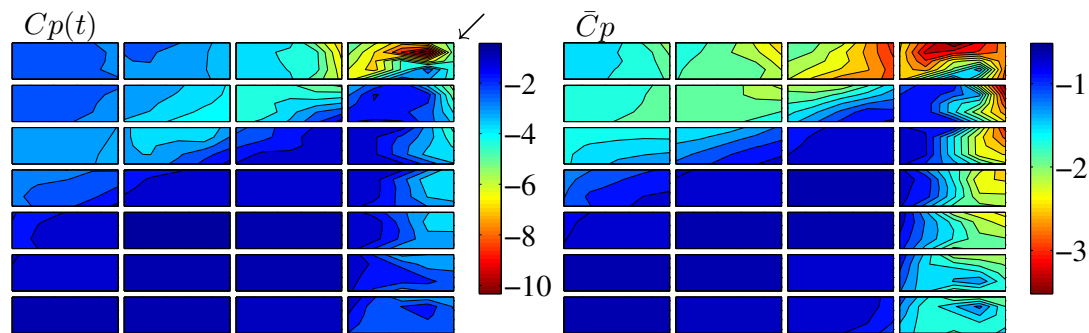


**Figure 3-19: Contour map of instantaneous external point pressure coefficients resulting in peak external uplift  $G = 12$  cm;  $H \approx 0$  (left) and mean external point pressure coefficients for the peak wind direction of  $45^\circ$  on the flat roof (right)**

The cavity pressures are more sensitive to  $H$  than the external pressures, yielding different loading patterns for different  $H$ . The cavity pressures followed the same trends as the upper surface when the cavity is small ( $H \approx 0$ ) with large suctions acting along the lines of the conical vortices (Figure 3-20). In the field of the array the cavity pressures were more uniform and low in magnitude. A larger cavity height ( $H = 20$  cm) resulted in a linear gradient of decreasing cavity pressures from the field of the roof to the larger dimension leading edge wall. This pattern is clearly indicated when considering the mean net pressure distribution (Figure 3-21 right) but is also shown when considering the peak instantaneous distribution (Figure 3-21 left). While there is a notable pressure gradient, the range of mean cavity pressures is significantly reduced, indicating a more uniform distribution.

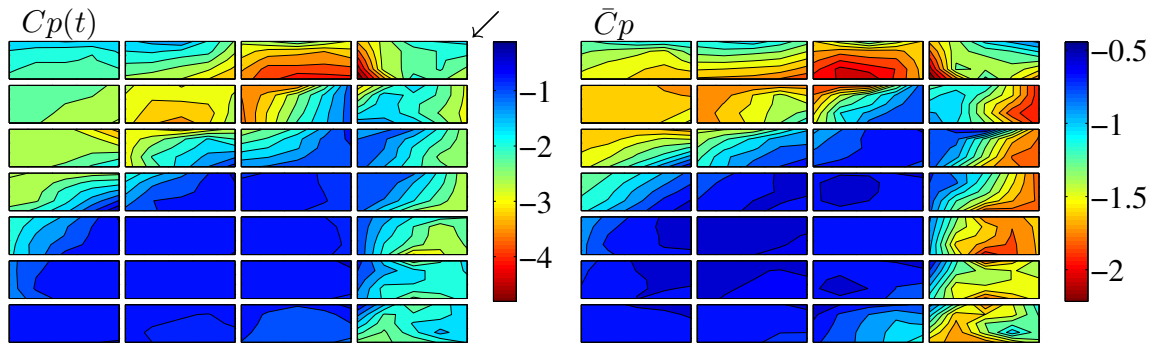


**Figure 3-20: Contour map of instantaneous cavity point pressure coefficients resulting in peak cavity suction  $G = 12$  cm;  $H \approx 0$  (left) and mean cavity point pressure coefficients for the peak wind direction of  $45^\circ$  on the flat roof (right)**

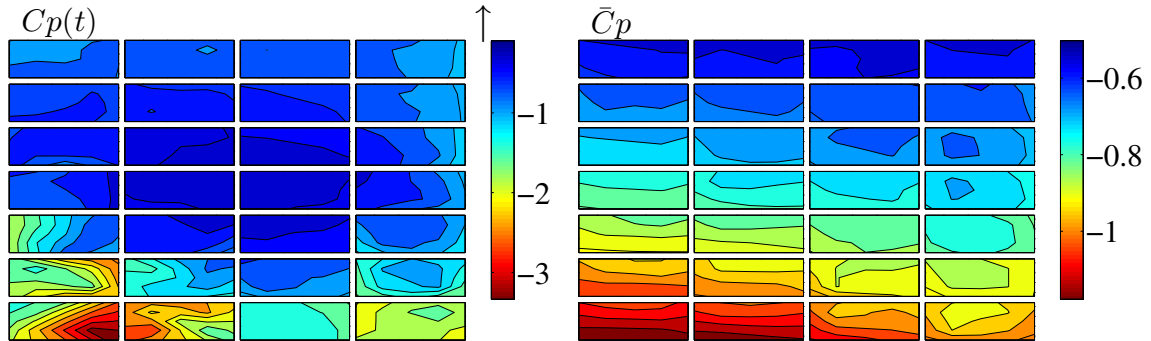


**Figure 3-21: Contour map of instantaneous cavity point pressure coefficients resulting in peak cavity suction  $G = 12$  cm;  $H = 20$  cm (left) and mean cavity point pressure coefficients for the peak wind direction of  $180^\circ$  on the flat roof (right)**

The correlation coefficients were found to be sensitive to the reattachment and secondary separation lines, as shown in Figure 1-1, from the conical vortices (shown in the contours of Figure 3-19 and Figure 3-20) and are plotted in Figure 3-22. This is consistent with the findings of Bienkiewicz and Sun (1992) who examined the distribution of correlation coefficients between upper and lower surface pressures of roof pavers for multiple cavity heights. Their experimental set-up did not explicitly state if their model had gaps between individual pavers (although it is presumed that there was one), which from the sloped roof results of this study are shown to influence the correlations across individual modules. Gaps introduce gradients of correlations across individual modules that govern

the loading pattern for small cavities. Larger cavities yield different correlation coefficient patterns with the gradients across the array being more significant than those on individual modules, although the gradients are strongest along modules on the leeward edges of the array.

0.87 0.9 0.82 0.86 0.75 0.96 0.9 0.93 0.92 0.93	0.84 0.86 0.75 0.78 0.58 0.94 0.85 0.89 0.89 0.87	0.83 0.74 0.7 0.63 0.83 0.88 0.62 0.59 0.74 0.76	0.93 0.84 0.67 0.27 0.56 0.86 0.61 0.69 0.9 0.95
0.96 0.94 0.95 0.93 0.96 0.95 0.92 0.9 0.88 0.72	0.95 0.87 0.93 0.57 0.66 0.93 0.83 0.86 0.82 0.92	0.95 0.81 0.91 0.56 0.52 0.94 0.82 0.85 0.78 0.81	0.87 0.77 0.53 0.75 0.92 0.86 0.84 0.6 0.93 0.95
0.95 0.91 0.95 0.9 0.92 0.93 0.87 0.91 0.89 0.79	0.95 0.94 0.95 0.86 0.95 0.93 0.91 0.91 0.86 0.81	0.97 0.85 0.85 0.58 0.81 0.91 0.63 0.87 0.78 0.85	0.85 0.75 0.18 0.96 0.85 0.9 0.6 0.85 0.96 0.96
0.95 0.92 0.96 0.94 0.93 0.95 0.87 0.93 0.93 0.62	0.96 0.91 0.9 0.85 0.85 0.89 0.89 0.91 0.87 0.88	0.91 0.9 0.8 0.86 0.74 0.91 0.88 0.92 0.89 0.87	0.7 0.87 0.93 0.84 0.84 0.92 0.79 0.91 0.92 0.93
0.95 0.92 0.93 0.92 0.9 0.92 0.92 0.94 0.9 0.87	0.9 0.9 0.8 0.89 0.77 0.94 0.84 0.93 0.91 0.91	0.71 0.81 0.71 0.62 0.6 0.94 0.91 0.89 0.78 0.89	0.59 0.88 0.96 0.94 0.76 0.95 0.81 0.93 0.96 0.92
0.89 0.89 0.89 0.89 0.74 0.89 0.87 0.92 0.89 0.91	0.89 -0.058 0.81 0.84 0.73 0.93 0.94 0.93 0.91 0.9	0.92 0.84 0.7 0.62 0.85 0.94 0.87 0.83 0.76 0.93	0.74 0.92 0.93 0.9 0.71 0.94 0.91 0.95 0.038 0.95
0.88 0.85 0.83 0.85 0.71 0.88 0.81 0.88 0.86 0.92	0.93 0.9 0.82 0.82 0.72 0.92 0.91 0.93 0.87 0.91	0.72 0.49 0.72 0.65 0.88 0.89 0.62 0.84 0.85 0.97	0.87 0.88 0.95 0.85 0.78 0.89 0.86 0.95 0.76 0.9

**Figure 3-22: Distribution of the external-cavity point pressure correlation coefficients for the peak wind direction of 45° on the flat roof ( $G = 12$  cm;  $H \approx 0$ )**

The peak net pressures for small cavities are dominated separated flow from a cornering wind, as shown in Figure 3-23 ( $G = 12$  cm;  $H \approx 0$  flat roof configuration). The net distribution at the moment of peak net uplift is similar to the distribution on the upper surface, but with reduced magnitudes, just as it typically was for the 30° roof slope data. The peak net wind direction, 45°, is associated with conical vortices which are observed on both the external (upper) surface of the modules and in the cavity at the instant of peak net pressure (Figure 3-23c and Figure 3-23d). The pressure distribution due to the conical vortex in the cavity does not significantly reduce the peak uplift on the external surface as the pressures do not coincide spatially. These vortices do not dominate the peak instantaneous (and mean) net pressure distributions for larger cavities (Figure 3-24). As with the sloped roof, leading edge perimeter modules can experience positive pressures from certain wind directions which can cause the cavity to be partially positively pressurized. This is a punitive loading condition that can cause net pressures

to be larger than external pressures and significant pressure gradients across individual modules. This was the case for the  $G = 12$  cm;  $H = 20$  cm with leading edge modules experiencing high net suction and pressure gradients, with relatively lower loading (near-zero net wind loading) elsewhere on the array (where modules were sheltered).

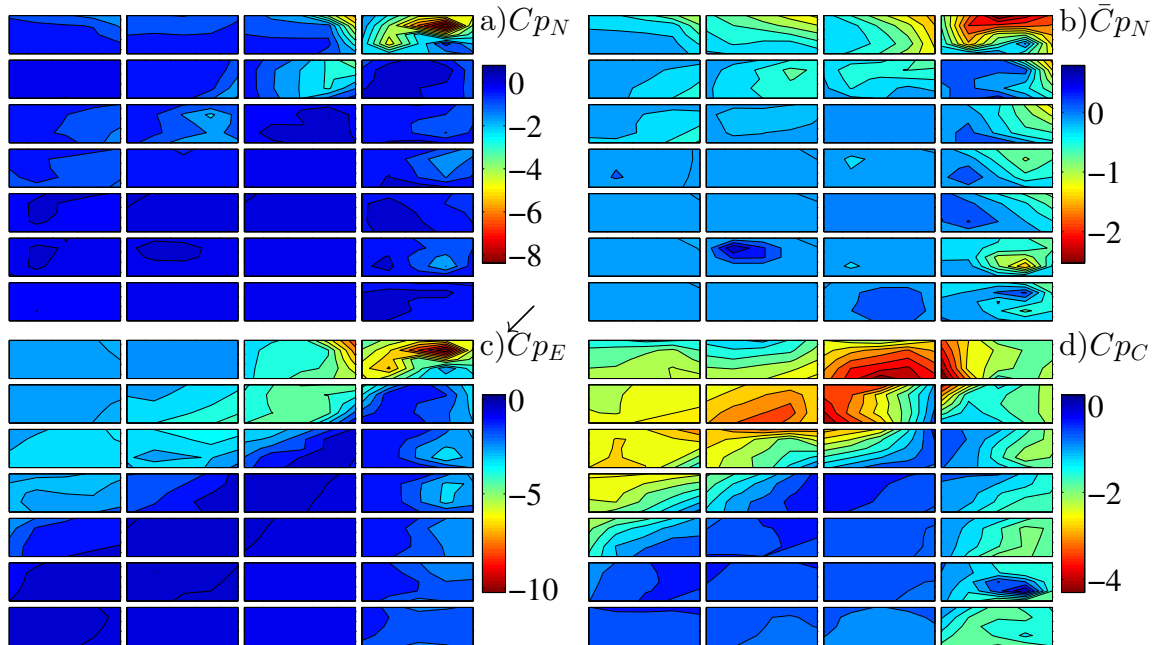


**Figure 3-23 Contour map of a) instantaneous net point pressures resulting in peak net uplift for the  $G = 12$  cm;  $H \approx 0$  flat roof configuration, b) mean net point pressure coefficient for the same (peak) wind direction of  $45^\circ$ , c) instantaneous external and d) instantaneous cavity point pressures that resulted in peak net uplift**

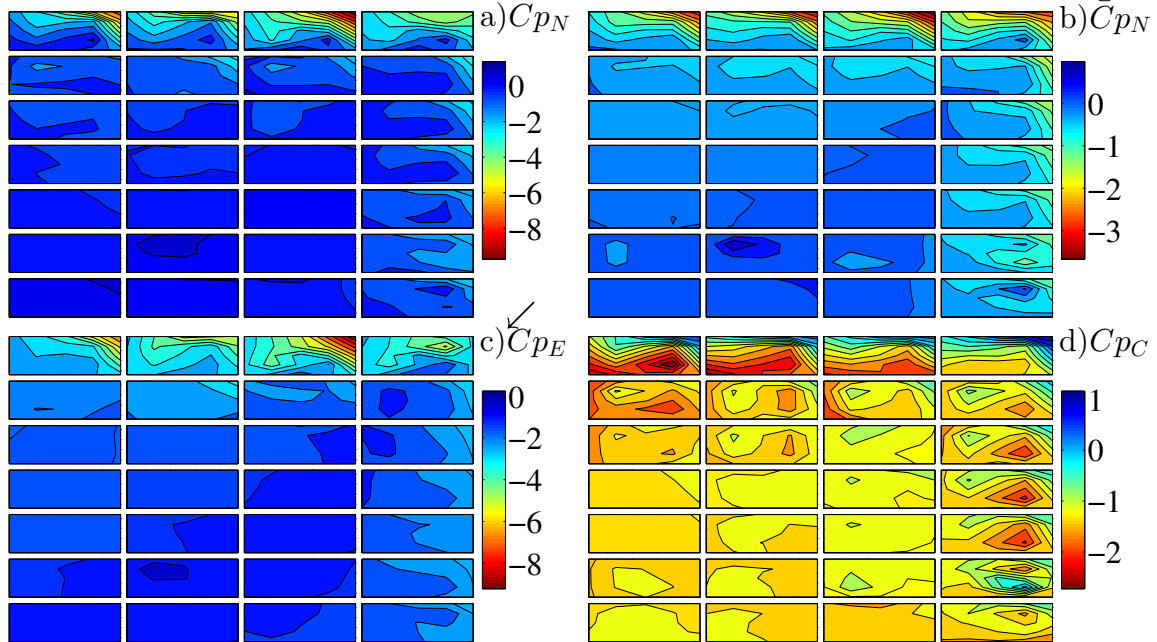


**Figure 3-24: Contour map of a) instantaneous net pressure resulting in peak net point pressure for the  $G = 12$  cm;  $H = 20$  cm flat roof configuration, b) mean net point pressure coefficient for the same (peak) wind direction of  $45^\circ$ , c) instantaneous external and d) instantaneous cavity point pressures that resulted in peak net uplift**

The worst peak external, cavity and net (area-averaged) pressure coefficients from the flat roof are superimposed over the values from the sloped roof (values from Figure 3-17 are plotted in grey) in Figure 3-25. While the worst peak external pressure coefficients increase with large  $H$  for the sloped roof, the opposite is true for the flat roof. Similar to the trend observed for the sloped roof,  $H$  does not have a significant effect on peak external cavity pressure coefficients beyond the incorporation of a (small) cavity to allow pressure equalization. For cavity depths less than  $H = 8$  cm, the worst peak net pressure coefficient decreases with increasing  $H$ . This was also observed for larger  $G$  on the sloped roof, but to a lesser extent. For larger cavity depths ( $H \geq 8$  cm) the worst peak net pressure coefficient increases with  $H$ , consistent with the observations from the sloped roof model. The consistent trend for the worst peak net pressure coefficient is important – while the worst peak external pressures have differing trends for the sloped and flat roofs, the worst peak net pressure trends are consistent between the two roof slopes. This indicates that design recommendations based on the peak net pressures are independent

of roof slope. This makes any recommendations derived from the current data far more applicable, valid for not just the roof slopes experimentally tested.

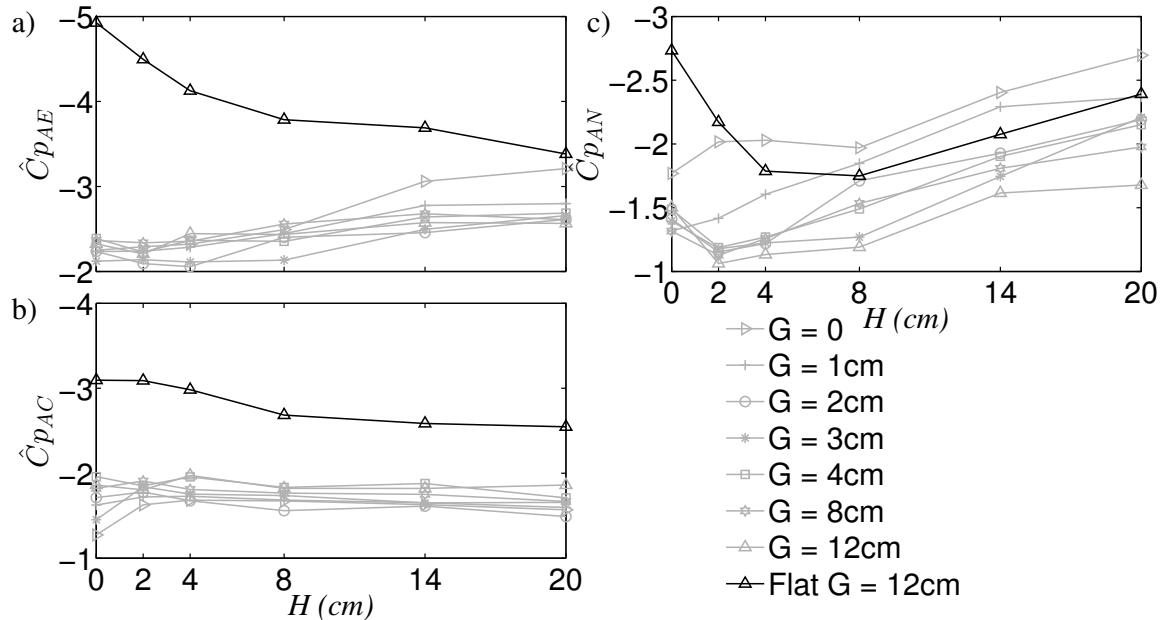


**Figure 3-25: The worst case values of the peak (suction) external area-averaged over a single module on (a) the external, upper, surface, (b) in the cavity, and (c) net with respect to  $H$  for the sloped roof model (grey) and the flat roof model (black)**

### 3.7 Summary

Through the examination of the peak and mean pressure distributions, the basic effects of  $G$  and  $H$  on the pressure field were determined. For low-profile systems (small  $G$  &  $H$ ), the external pressure distributions are largely what would be expected on the bare-roof, although even in this configuration the net pressures experience beneficial effects from the cavity (formed by loose-laid modules) through reduced magnitude pressures. Larger  $H$  can influence the peak external pressure distribution as the flow separates from the elevated surface of the solar modules. The cavity pressure distributions are found to be more uniform for larger  $H$ . The external pressures at the interface between multiple modules can be affected by the flow through the gap, which can cause large pressure gradients and increase the net wind loads. The peak and mean net pressure distributions largely follow those on the exterior surface (typically caused by flow separation off

building or array edges) and are lower in magnitude except for cases where the cavity is experiencing positive pressures. It was also observed that the windward (i.e., array edge) modules can experience large pressure gradients, while interior, sheltered modules can have significantly lower magnitude pressures. Correlation coefficients between the external and cavity pressures are fairly high around the perimeter of the array (and modules to a lesser extent) but lower in the interior.

Overall trends for the effects of  $G$  and  $H$  were noted when plotting the worst case, peak, area-averaged external, cavity and net pressure coefficients. Worst case peak external pressures were found to increase in magnitude with  $H$  for the sloped roof configurations but decrease for the flat roof configurations. The worst case peak external pressures decrease for larger values of  $G$  while the worst case peak cavity pressures increase for large values of  $G$ . The cavity depth,  $H$ , was not found to have a significant effect for the sloped roof configurations on the worst peak cavity pressure after a cavity was introduced; the flat roof shows a slight decreasing trend with increasing values of  $H$ . For both roof slopes, the worst peak net pressure was noted to increase with  $H$ . This is an important finding as the two roof slopes have different external loading patterns and trends with respect to  $H$ ; however, the overall peak net pressures behave in a similar manner. This is expected to be a result of the cavity pressures and pressure equalization between the external and cavity pressures, the focus of the next chapter.

## 4 Pressure Equalization

When solar modules are mounted parallel to the roof of a low-rise building both the upper and lower surfaces are exposed to the flow. This results in external wind pressures being transmitted into, and modified by, the cavity. The difference between these external and cavity pressures is the net pressure, which acts on the module. The external pressures are largely dictated by the building-generated flow-field, with flow separation at the building edges controlling the pressures. The cavity pressures are transmitted from the upper surface pressures through openings into the cavity. They are sensitive to the array geometry, (i.e., the gaps between the modules, cavity depth, panel size, etc.), as well as pressure gradients on the upper surface.

If the external pressure is fully transmitted with no external pressure gradient at the opening then the cavity pressures would be equal to those measured on the upper surface, which would indicate that the system has perfect pressure equalization. This would yield zero net loading across the modules and is not likely in practice where partial pressure equalization is expected. Pressure equalization is desirable for roof-mounted solar systems as it reduces the net wind pressures on the modules, thus reducing their design wind loads (e.g., Kumar, 2000).

### 4.1 Instantaneous Pressure Equalization

Each pressure time history is unique with examples of such pressure time histories shown in Figure 4-1, which shows segments of time histories for module 1 (located in the upper left corner of the array and adjacent to the field of the roof along the ridgeline of the model). The upper plot shows a 10 second sampling period with the externals on the upper surface plotted in black and the cavity pressures in gray. The lower plot contains the pressure trace for 0.5 seconds (model-scale) before and after the peak external value. It can be seen that the cavity measurements largely follow the externals but the values are often lower in magnitude.

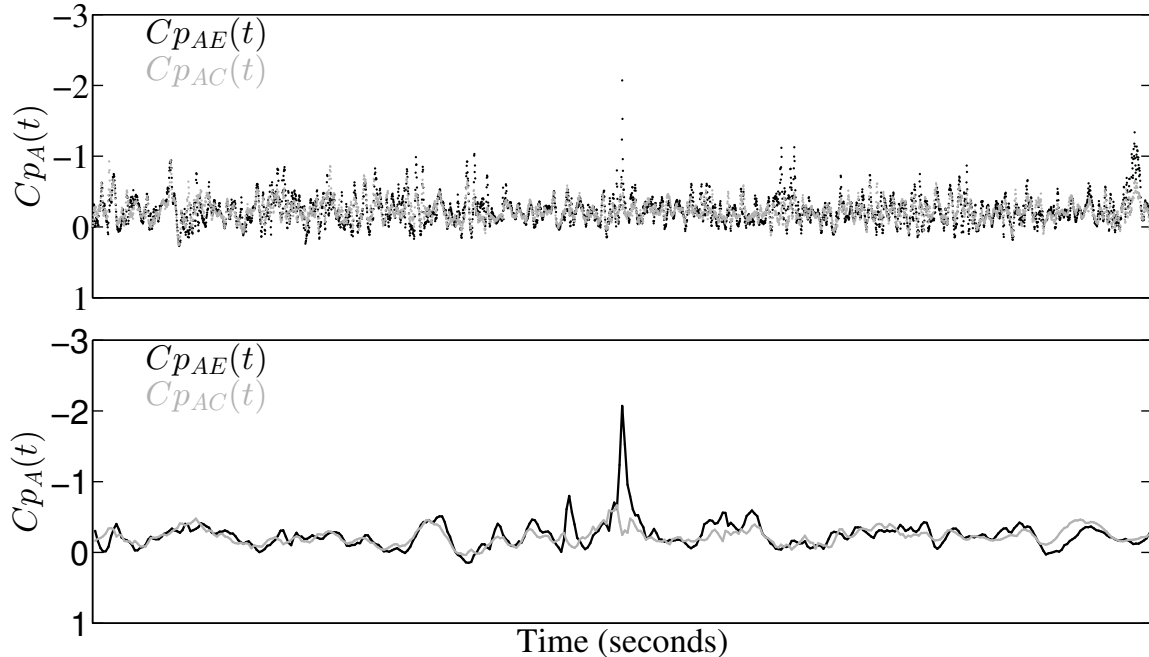


**Figure 4-1: Sample external (black) and cavity (grey) pressure time histories, area-averaged over a single module for a) a sampling period of 10 seconds and b)  $\frac{1}{2}$  second before and after the largest measured external suction**

As can be seen in Figure 4-1, the cavity pressures are typically lower in magnitude than the external pressures, although they largely track them. However, at the moment of the peak external pressure there can be a significant difference between the external and the cavity pressure, especially for different modules and configurations. This can be seen in Figure 4-2 where the non-simultaneous peak minima (suction) and mean values of the external and cavity pressures, area-averaged over a single module, are presented for two specific modules. For module 1, the upper plot, it can be noted that the peak external uplift is much larger than the peak cavity pressure for the wind directions for the largest magnitudes ( $67.5^\circ$  and  $292.5^\circ$ ). When module 14 is considered, the difference between the peak pressures has been significantly reduced. This is due to the fact that module 14 is an interior module and not exposed to the separated flows around the perimeter of the array that produce the largest external pressures. Both modules show that the match between the peak external and cavity pressures is better for off-peak wind directions, which indicates improved pressure equalization. This is because the fluctuating

component of the cavity pressure more effectively tracks the external fluctuations for off peak wind directions, as indicated by the similar external and cavity RMS values plotted in Figure 4-3. Plotted are the RMS values for the external and cavity pressures area-averaged over a single module, specifically module 1 (edge) and module 14 (interior) with respect to wind direction for  $G/H = 0.6$  ( $G = 12$  cm;  $H = 20$  cm) and  $G/H = 0.6$  ( $G = 12$  cm;  $H = 2$  cm). This RMS values indicate that when a module is sheltered the external fluctuating pressure components are lower in magnitude and better transmitted to the cavity as indicated by a small spread between the external and cavity values shown for the interior module (#14). It should also be noted that the transmission of external fluctuations to the cavity is improved for larger  $G/H$  ratios, which was also observed by Oh and Kopp (2015) in wind tunnel studies of a dual-layer roof system.

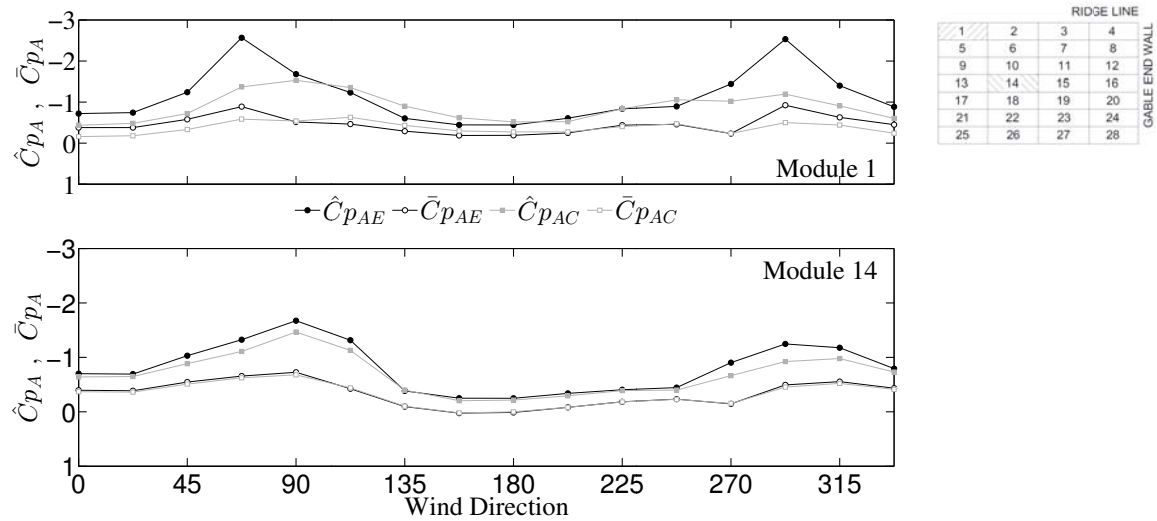


**Figure 4-2: Non-simultaneous peak suction and mean values of the external and cavity pressure coefficients for module 1 (upper) and module 14 (lower) with respect to wind direction for  $G = 12$  cm;  $H = 20$  cm on the sloped roof**

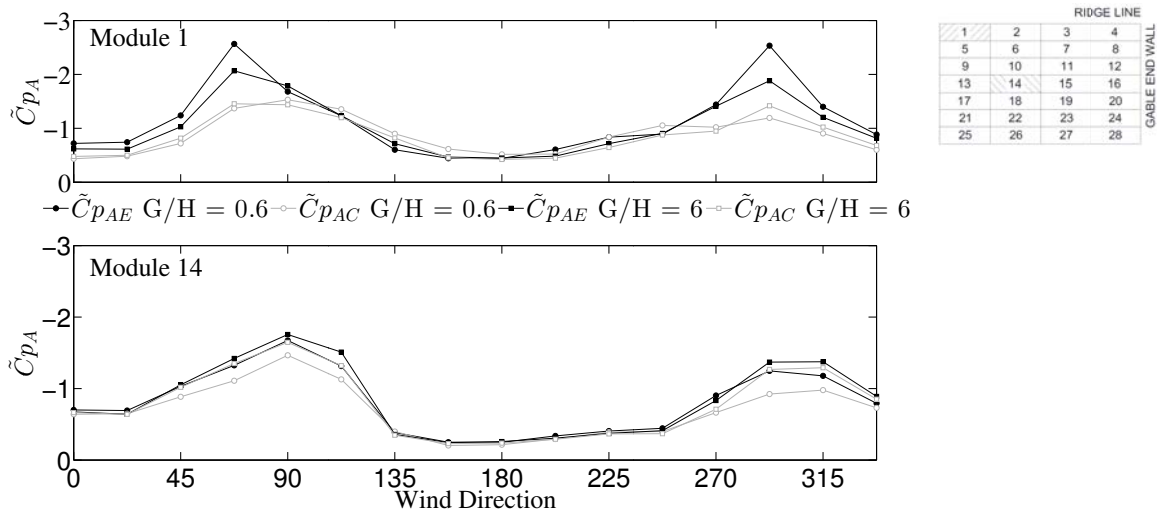


**Figure 4-3: External and cavity RMS values for module 1 (upper) and module 14 (lower) with respect to wind direction for  $G = 12$  cm;  $H = 20$  cm and  $G = 12$  cm;  $H = 2$  cm on the sloped roof**

## 4.2 Parameter describing cavity pressure distributions for a single module

With the external pressure gradients largely defined by the structure, it is the cavity flow behaviour that is of particular interest when studying pressure equalization. Bienkiewicz and Sun (1997) studied the cavity (underneath) pressures on loose-laid roof pavers and discussed how they pertained to wind resistance. They noted that the cavity pressures are dependent on the ratio of  $G/H$ , combining the effect of the air gap around pavers,  $G$  and the cavity depth,  $H$  and the ratio of  $H/t$ , combining the effect of cavity depth and paver thickness,  $t$ . Dependence on the  $G/H$  ratio has been confirmed with large-scale paver studies (Asghari Mooneghi et al., 2014), and expanded to parallel mounted solar modules in chapter 5. Larger  $G/H$  ratios are associated with lower wind loads; however, it has not been used as a design parameter to date. To increase the understanding of cavity pressures, Oh and Kopp (2015) conducted wind tunnel studies to observe the cavity pressure behaviour with respect to varying array geometries. They specifically noted that previous work had limited discussion of the mechanisms responsible for cavity pressure

distributions, with research focusing on the sensitivity to  $G/H$  and external pressure gradients. Of particular interest was noting how the pressures are transmitted through  $G$  and modified by the cavity between openings. A parameter,  $\varphi$ , was introduced as a potentially robust indicator of whether the cavity pressures would be uniform in nature or vary linearly. It is defined as

$$\varphi = \frac{\Delta\bar{C}p_i}{\Delta\bar{C}p_o} \quad (11)$$

the ratio of the flow through the cavity,  $\Delta\bar{C}p_i$ , to the flow through  $G$  (orifice),  $\Delta\bar{C}p_o$ , with the specific equation for a single cavity with two openings presented in chapter 1 (Equation 2). If  $\varphi < \text{order}(1)$  the cavity pressures are uniform with the pressure drop occurring with flow through  $G$ . This is most commonly observed for small  $G/H$  ratios, where larger cavities are associated with lower flow resistance. Alternatively, with  $\varphi > \text{order}(1)$  the cavity pressures vary linearly, similar to Couette flow, i.e., 2D flow between parallel plates. A sketch of this is shown in Figure 4-4. This condition was observed to coincide with higher  $G/H$  ratios and exhibit a higher degree of pressure equalization, a larger portion of the external pressure was transmitted to the cavity yielding lower magnitude net pressures. This was also shown when Oh and Kopp examined the RMS values, indicating that the fluctuating component of the external pressures is more effectively transmitted with a higher  $\varphi$  or  $G/H$  ratio.  $\varphi$  is thought to be more effective at describing the nature of the cavity pressure distribution than  $G/H$  since it incorporates losses specific to the system and the module thickness, which also plays a role. It is also thought to be quite robust as the different flow patterns yield  $\varphi$  values that are order of magnitudes different for single cavities with only 2 openings into it, primarily because of dependence on  $(G/H)^2$ .

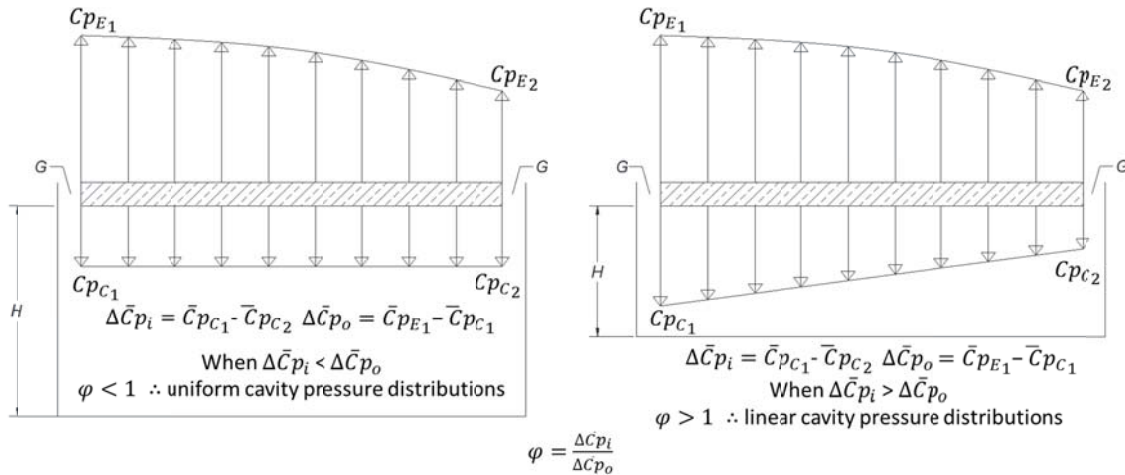


**Figure 4-4: Sketch of external and cavity pressure distributions for  $\varphi < 1$  and  $\varphi > 1$**

Oh and Kopp (2015) developed an equation to determine  $\varphi$  based on their model which had one cavity between two openings ( $G$ ). The windward gap was 2.5 mm and the leeward measured 3.5mm, shown in Figure 4-5, which contains line plots of the mean external and cavity pressures for multiple cavity heights. This configuration limited one gap to have flow into the cavity and one with flow exiting, restricting the pressures to one-dimension, which is not necessarily the case for the current model. The array of modules, each one surrounded by an opening ( $G$ ), allows flow in two-dimensions. As such, the Oh and Kopp equation  $\varphi = \left[ \frac{G}{H} \right]^2 \frac{24}{Re_H} \frac{Lc}{H} \frac{1}{2.5}$  was not used in this study, but rather the conceptual definition of the factor was employed to assess the behaviour of cavity pressure for individual modules. To verify that the definition could indeed be used in lieu of the definition, a comparison of  $\varphi$  values evaluated using both methods, using the single cavity data from their study as shown in Table 2. It can be noted that the  $\varphi$  values respect the boundary of order (1) whether evaluated by the equation or the definition. The definition-based values are not the magnitudes different noted by Oh and Kopp (2015) but still respect the essence of the concept. This indicates that evaluating  $\varphi$  using the definition is applicable and can be used to predict cavity pressure behaviour based on the pressure drop through the cavity and through the orifice. This is beneficial, since the equation was developed for a system with a single cavity, which is not the case for the majority of solar arrays.

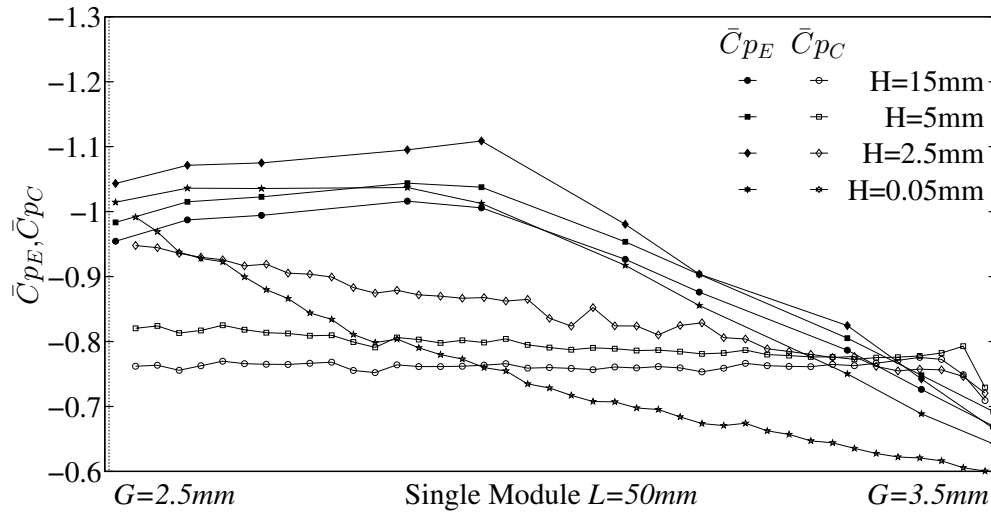


**Figure 4-5: External and cavity pressures along a line of taps for a single cavity for multiple  $H$  (adapted from Oh and Kopp 2015)**

**Table 2:  $G/H$  and  $\Phi$  values calculated using the equation and definition for the single cavity for multiple  $H$  data adapted from Oh and Kopp 2015**

	<b>H = 15 mm</b>	<b>H = 5 mm</b>	<b>H = 2.5 mm</b>	<b>H = 0.5mm</b>
$G/H$ * $G = 2.5$ mm used	0.17	0.5	1	5
$\phi$ by Equation 2	$7.5 \times 10^{-3}$	0.2	2	$5 \times 10^4$
$\phi$ by definition (Equation 11)	0.27	0.56	2.4	12.5

From Figure 4-5 and Table 2 it can be noted that two of their cavity depths resulted in uniform cavity pressure distributions,  $H = 15$  mm and  $H = 5$  mm, as noted by the linear mean cavity pressure coefficients and  $\phi < 1$ . This is expected as larger cavity heights were known to result in more uniform pressure distributions on the underside of roof pavers (i.e. Bienkiewicz and Sun, 1992). These cavity heights are also characterized by  $G/H < 1$ , which is thought to be a boundary for wind loads for the current array, see chapter 5. This is significant as  $\phi < 1$  indicates a more uniform cavity flow and for these

configurations coincides with  $G/H < 1$ , possibly indicating higher magnitude wind loads. This reinforces that  $G/H$  is effective as a rough indicator of the cavity pressure distribution, but  $\phi$  is likely to be more appropriate since it considers more parameters. In its equation form,  $\phi$  also considers the losses specific to the geometry and the thickness of the module. Using the definition directly considers the measured pressure gradients which inherently consider the effects of geometry.

### 4.3 Parameter describing cavity pressure distributions for multiple modules

When considering multiple modules in the array the cavity flow is more complicated, with more openings ( $G$ ) in which air can enter or leave the cavity and influence the pressures. This is seen in Figure 4-6, which plots mean external and cavity pressures along four modules with  $G = 1$  mm for a single cavity with various heights taken from Oh and Kopp (2015). The external mean distributions vary along the length of the system, with roughly linear pressures along modules 1 and 2 (small pressure gradients) and linearly decreasing behaviour along modules 3 and 4. The larger cavities ( $H \geq 2.5$  mm) appear to have fairly uniform mean cavity pressure distributions across the entire system, similar to behaviour observed for the single module case. For modules 3 and 4, the smaller cavity depths tend to have linearly varying mean cavity pressure distributions, again similar to observations for the single module cases. However, the mean cavity pressure distribution on modules 1 (and 2 to a lesser extent) is nearly uniform. This is not to be unexpected as the mean external pressures are also (near) uniform in this region yielding very small gradients. From studying pressure equalization across residential wall systems Kopp and Gavanski (2012) found that for uniform (lab-induced) pressures, the vinyl siding (outer layer) carried almost no load. This indicates that the external pressure gradients play a significant role in pressure equalization. The changing cavity behaviour from uniform to linear across the system indicates that a single  $\phi$  value may not be appropriate and catch the cavity behaviour across the system. The transition point from uniform to linear pressure distributions is not clear, but may correspond to an effective cavity length – alluded to in Oh and Kopp (2015) who used the entire cavity length as opposed to only the cavity beneath the module length to evaluate  $\phi$ .

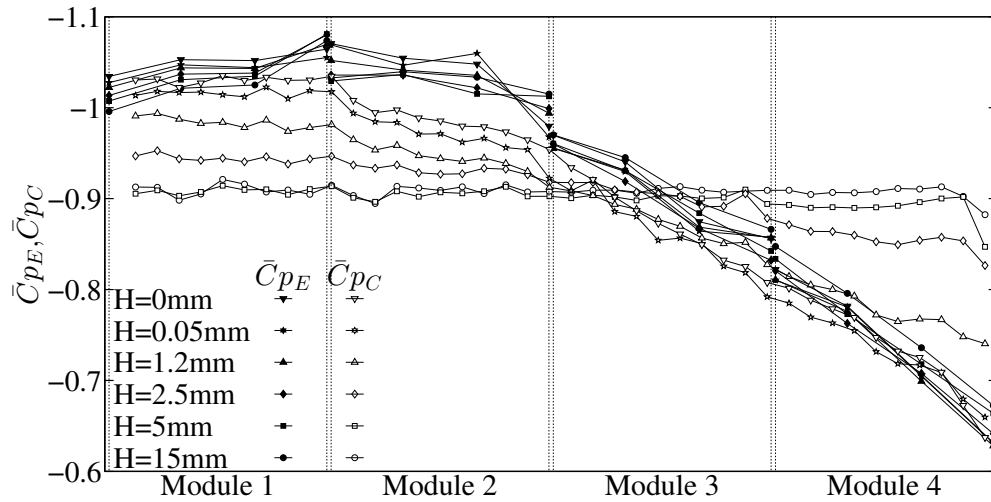


**Figure 4-6: Mean external and cavity pressures along multiple modules;  $G = 1$  mm; various  $H$  from Oh and Kopp (2015)**

To further study the cavity pressure behaviour when there are multiple modules in the along wind direction, data from Oh and Kopp (2015) are contrasted with results from the current study<sup>1</sup>. Mean external and cavity pressures from Oh and Kopp were presented with respect to  $x/h$  with configuration geometry presented in model scale millimeters. Their measurements from  $G = 1$  mm;  $H = 1.2$  mm are contrasted with measurements from the current study, specifically  $G = 12$  cm;  $H = 2$  cm flat roof configuration (1 mm  $H$  in model scale). The wind direction from the current study was  $270^\circ$  where the flow is perpendicular to the short dimension of the building and the array is under separated flow, as close to the Oh and Kopp set-up as possible. These configurations were chosen for comparison because they have the most similar array geometric properties available. The closest cavity depths were chosen as the basis of comparison as Oh and Kopp presented results for a range of  $H$  with a cavity of  $G = 1$  mm (model scale), whereas only

<sup>1</sup> Array geometry (i.e., Gap,  $G$ , and cavity depth,  $H$ ) for the current study are presented throughout this document in equivalent full-scale units as noted in chapter 2. Oh and Kopp (2015) presented results in model scale and did not provide a length scale to evaluate equivalent full-scale values. As such, experimental results from the two studies are not presented in a consistent manner. The dimensionless system relative porosity,  $G/H$  is included for reference when comparing experimental results.

a large  $G$  was tested for the current flat roof model. As such, the results are expected to vary as the  $G/H$  ratios are quite different; 0.8 for Oh and Kopp and 6 for the current study. The data are plotted in Figure 4-7 with the external wind flow from left to right. It can be noted that the shape of the external pressure coefficient distributions are similar, with the current study values being consistently larger in magnitude. (Differences in the magnitudes are likely a result of different model dimensions and wind tunnel terrain simulations.) The module lengths vary between the different models, making it challenging to compare when pressures are presented with respect to a normalized building dimension. Therefore, the data has been replotted with respect to a normalized module length in Figure 4-8 for a small cavity and Figure 4-10 for a large cavity.

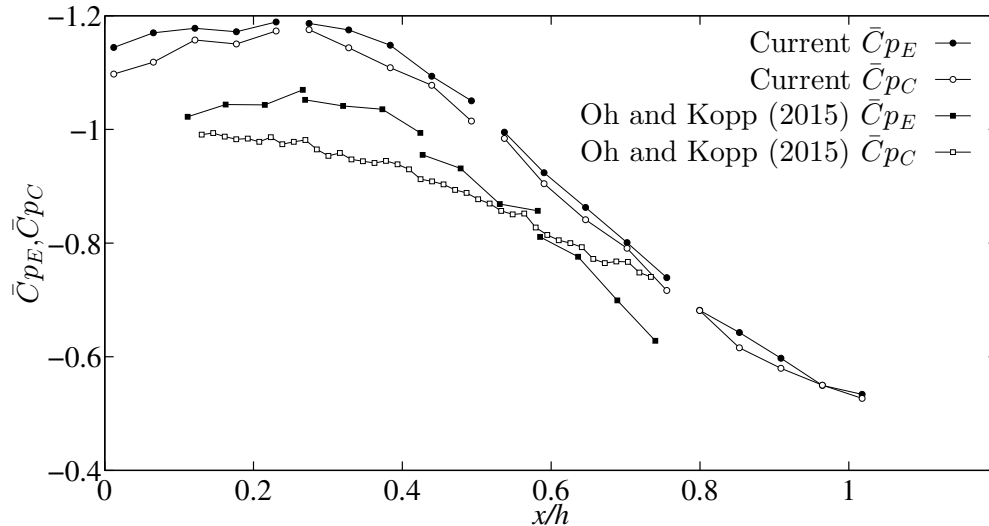


**Figure 4-7: Comparison of mean external and cavity pressures along a single tap line from  $G = 1 \text{ mm}$ ;  $H = 1.2 \text{ mm}$  (Oh and Kopp, 2015) and  $G = 12 \text{ cm}$ ;  $H = 2 \text{ cm}$  flat roof configuration ( $270^\circ$ ) from the current study with respect to  $x/h$**

With the pressures plotted with respect to module, the external flow is again from left to right and the module numbers are labelled. Recall that for the current study the wind is from  $270^\circ$ , thus module 16 is the windward module (module 1 for Oh and Kopp). When data from only one of Oh and Kopp's configurations are plotted it is easier to see that the mean cavity pressures are lower in magnitude than the mean externals for a windward portion of the system, but that this is reversed for a leeward portion of the system. This

was also seen with a single cavity for larger  $G/H$  with Oh and Kopp labelling the zones as “higher suction” and “lower suction”, respectively. The higher uplift in the higher suction zone can be offset by the lower suction zone when the modules are connected. This loading pattern is not observed for the current model where the mean cavity pressures are consistently lower in magnitude than the mean external pressures. Table 3 contains  $\phi$  values that have been evaluated for both studies, considering the overall system as well as individual modules. The single value for the entire system does not take into consideration the changing cavity behaviour as previously discussed.

Evaluating the factor based on modules does seem to largely capture the behaviour of the mean cavity pressure distribution; however, it is not clear that this is the best approach. Of interest is also the pressure gradients on module 1; the external pressure gradient is increasing in magnitude with higher mean suctions on the leeward edge while there is a slight decreasing trend observed for the mean cavity pressures. This is unexpected as the cavity pressures are transmitted from the external pressures. This instead indicates that perhaps the cavity under module 1, module 2 and likely module 3 are working together as a single continuous cavity. If the collective mean cavity pressure distribution over these three modules is examined it is more indicative of what would be expected given the mean external pressure gradient across these three modules. This is more clearly seen in Figure 4-9 which plots the mean external and cavity pressures from Oh and Kopp (2015)  $G = 15 \text{ mm}$ ;  $H = 1.2 \text{ mm}$ . There is virtually no external mean pressure gradient across the first module but there is a decreasing pressure gradient measured in the cavity. It appears as if cavities under multiple modules are acting together as a continuous volume. With this loading pattern present in their results for more than one  $G$  value, it merits further investigation as the boundaries and mechanisms remain unclear.

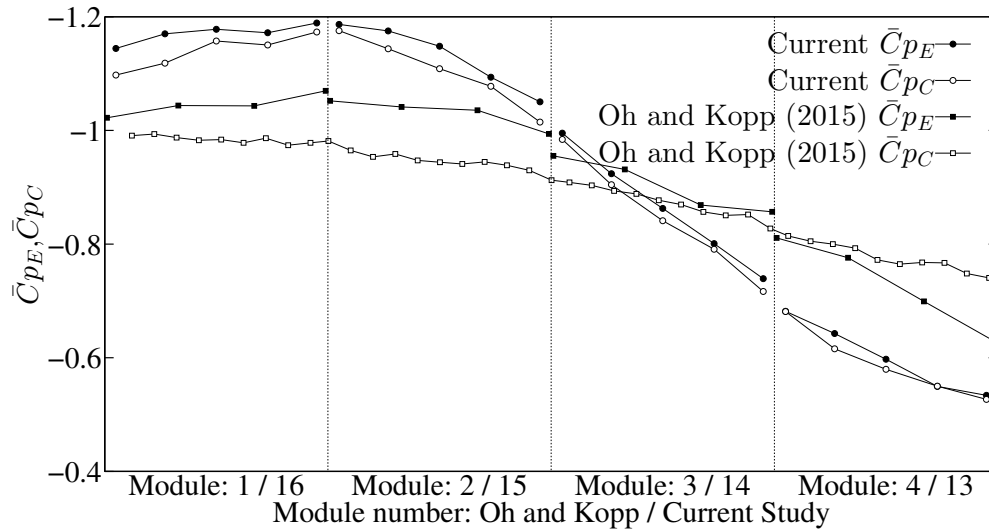


**Figure 4-8: Comparison of mean external and cavity pressures along a single tap line from  $G = 1 \text{ mm}$ ;  $H = 1.2 \text{ mm}$  (Oh and Kopp, 2015) and  $G = 12 \text{ cm}$ ;  $H = 2 \text{ cm}$  flat roof configuration ( $270^\circ$ ) from the current study normalized over module length**

**Table 3: Phi values a small cavity depth from Oh and Kopp 2015  $G = 1 \text{ mm}$ ;  $H = 1.2 \text{ mm}$  and the current study  $G = 12 \text{ cm}$ ;  $H = 2 \text{ cm}$  on the flat roof**

	Entire system	Module 1	Module 2	Module 3	Module 4
Oh and Kopp (2015)	8	0.3	0.98	2	21
Current Study	12	1.6	13	113	386

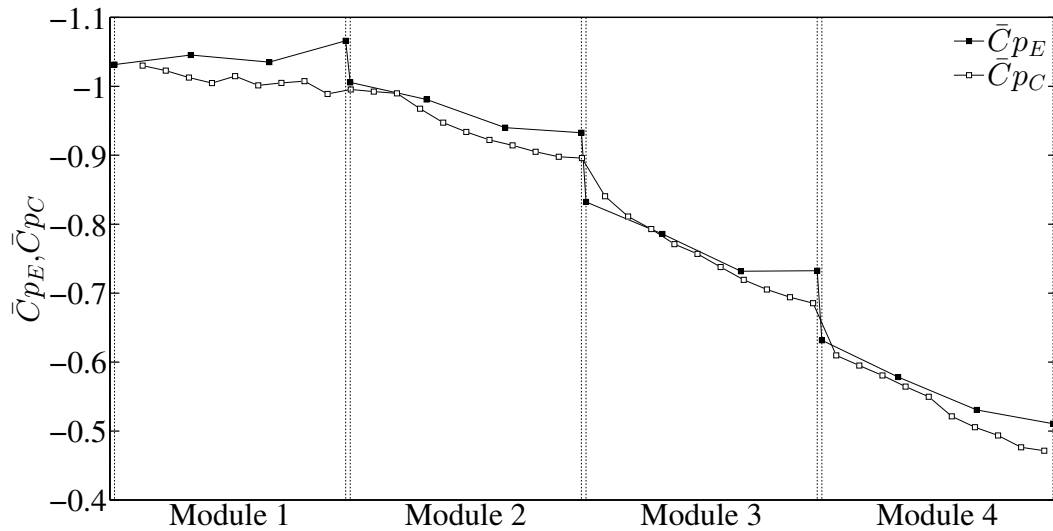


**Figure 4-9: External and cavity pressures along a line of taps for a multiple modules for  $G = 15$  mm;  $H = 1.2$  mm (adapted from Oh and Kopp 2015)**

When a larger cavity is considered, the edge effects from the current model are clearly visible in the large mean pressure gradients on the windward module edge when contrasted against a similar  $H$  from Oh and Kopp (2015). Contrasted in Figure 4-10 are  $G = 1$  mm;  $H = 15$  mm from Oh and Kopp, 2015 and  $G = 12$  cm;  $H = 20$  cm ( $H = 10$  mm model scale, closest for comparison) from the current study. Again, it should be pointed out that the cavity depths were matched as closely as possible but the  $G$  are quite different yielding a  $G/H$  of 0.07 for Oh and Kopp, and 0.6 for the current study. The edge effect seen in the current data is a result of the flow separations from the array edge and is discussed in more detail in Chapter 0. These effects were not measured by Oh and Kopp as their modules were set back from the building edge and flush mounted with the roof surface. As such, air could only enter their cavity through the 5 openings between the modules. The mean cavity pressure was uniform across the system; therefore  $\phi$  was less than 1 for both the system and all individual modules. Their mean externals decrease in magnitude resulting in the neutral pressure line, higher and lower suction zones as discussed above. This condition, with the neutral pressure line, is also observed in the current study, occurring on the leeward module. The cavity pressures for the current model were more linear in nature and not uniform as observed with Oh and Kopp. It

should be noted that  $\varphi$  was unsuccessful in predicting the cavity pressures on the windward module for the current model which had significant pressure gradients and peak pressures that were measured downwind, not adjacent to the edge.

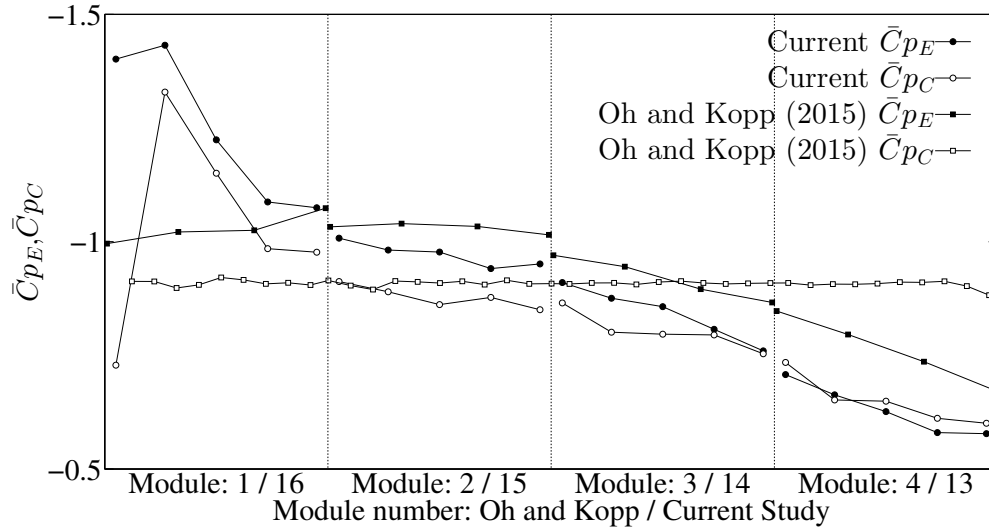


**Figure 4-10: Comparison of mean external and cavity pressures along a single tap line from  $G = 1 \text{ mm}$ ;  $H = 15 \text{ mm}$  (Oh and Kopp, 2015) and  $G = 12 \text{ cm}$ ;  $H = 20 \text{ cm}$  flat roof configuration ( $270^\circ$ ) from the current study normalized over module length**

**Table 4: Phi values for a large cavity system from Oh and Kopp 2015  $G = 1 \text{ mm}$ ;  $H = 15 \text{ mm}$  and the current study  $G = 12 \text{ cm}$ ;  $H = 20 \text{ cm}$  on the flat roof**

	Entire system	Module 1	Module 2	Module 3	Module 4
Oh and Kopp (2015)	0.36	0.02	0.05	0.02	0.43
Current Study	0.19	0.37	0.64	2.7	5

## 4.4 Effective cavity length

It appears that for certain combinations of geometric array properties multiple cavities work together, forming a single continuous effective cavity of variable length. Defining the effective cavity length has practical applications – it is desirable to have an effective cavity length that optimizes pressure equalization with respect to minimizing the wind loading. It is crucial to understand what dictates the boundaries for a given module. From the data presented by Oh and Kopp (2015), it appears that the effective cavity length for their 4 module system is related to the neutral pressure line, NPL. In Figure 4-8 ( $G = 1$  mm;  $H = 1.2$  mm) the NPL appears to be between the third and fourth module which seems to correlate to the cavity length as discussed above. For a larger opening ( $G = 15$  mm;  $H = 1.2$  mm) this correlation between the effective cavity length and NPL is also seen in Figure 4-9. The first effective cavity appears to be roughly two modules in length, ending at the NPL between modules 2 and 3. Downwind cavities are not as clearly defined, with an additional NPL on both module 3 and 4. This could potentially lead to three mode cavities; a small one on the leading edge of module 3, a longer one for the trailing edge of module 3 and perhaps slightly under module 4 and a final cavity under module 4. When  $H$  is increased, as in Figure 4-10 ( $G = 1$  mm;  $H = 15$  mm), a single NPL is observed, however, in this instance the cavity pressures are uniform. This could suggest that there is only one continuous cavity under all of the modules or that there are two cavities, as defined by the NPL, but that both cavities have similar pressures (set by  $H$ ). It should be noted that if a second cavity is considered, the pressure gradient across the orifice should be measured at the end of module 4, on the far side of the cavity. If it were to be measured at the start of the cavity, near the NPL, its value would be small and not indicative of the actual pressure gradients acting on the module. These initial observations indicate that effective cavities can be both longer and shorter than the length of the module. With flow limited to one dimension, observations cannot be made about the effect cavity size in the other direction, a recommended point of future study.

The NPL was observed for some configurations (see Figure 4-10) for the current model, although the pattern was not as clearly and consistently observed as with Oh and Kopp's model (2015). I believe that this could be a result of how the cavity was modelled for the

current study. While it did allow for two-dimensional flow, the model was not explicitly designed to study effective cavity dimensions and thus presents some challenges. Oh and Kopp used modules that were recessed such that the top of the modules was flush with the roof surface and constructed a very clean cavity. Their pressure tubing was passed through the module into the model creating a continuous void with no contamination. The current model had modules raised above the roof surface by three mounting posts per module, used to set the height and pass the pressure tap tubing into the model. These support modules resulted in approximately 35% blockage, not out-of-line for modelling commercial systems. However, the large, central, supports likely had a significant impact on the cavity flow. Future studies will have to carefully design and construct the cavity to better investigate the effective cavity dimensions and how they are altered with array geometry.

## 5 Pressure equalization coefficient

The pressure equalization coefficient,  $C_{eq}$ , serves to quantify the changes in the net wind loads from those on the external surface of the bare roof due to the effects of pressure equalization. It is proposed as the basis for developing design recommendations, specifically a multiplication factor to be applied to the external pressure coefficients in current design standards to account for the wind loading specific to roof-mounted arrays, a double-layered system subject to pressure equalization. This method relies on the assumption that the array does not alter the building aerodynamics, supported by results in chapter 3 that indicate that the external pressures are largely similar to expected bare roof pressures. The external (i.e., upper surface) wind loads used for normalization are the peak suction, for each area-averaged combination, regardless of the wind direction, for the base  $G \approx 0$ ;  $H \approx 0$  configuration. The base configuration is used for normalization as it has the array geometric parameters closest to the bare roof, relevant if the factor is to be applied to external pressure coefficients from a code. The worst, peak, externals from the same configuration as the worst peak net pressure are not used for normalization since they are (possibly minimally) altered. A pressure equalization coefficient greater than 1 indicates that the net pressure is larger in magnitude than the external pressure on the upper surface and is typically associated with positive pressurization of the cavity. Factors less than 1 signify that the net pressures have been reduced. Roof-mounted solar systems can be optimized for wind loading when designing a system with parameters yielding the lowest possible  $C_{eq}$ . This chapter investigates the values of  $C_{eq}$  from the experimental database.

### 5.1 Effects of $G$ and $H$ on $C_{eq}$

The effects of array geometry on the pressure equalization coefficient,  $C_{eq}$ , are determined by noting how the factor varies with changing values of  $G$  and  $H$ . The area-averaged case of a single module is considered below. The pressure equalization coefficients were determined from the worst-case values for each configuration and, thus, are not necessarily from the same modules or wind direction.

In Figure 5-1 it can be noted that the magnitude of  $C_{eq}$  tends to increase with larger values of  $H$ . This signifies that for larger values of  $H$ , the net wind loading is a larger proportion of the external wind loads. This is consistent with the findings of Bienkiewicz and Sun (1992, 1997) who found that  $H$  weakens paver system resistance to wind loading.  $C_{eq}$  is lowest for small cavities since the simple presence of a cavity enables pressure equalization and the larger magnitude externals associated with large  $H$  can be avoided. It appears that the ideal mounting height to maximize the level of pressure equalization is in the  $H = 2$  cm to  $H = 4$  cm range for which the maximum reduction appears to be about 50% (for these module dimensions and configurations tested).

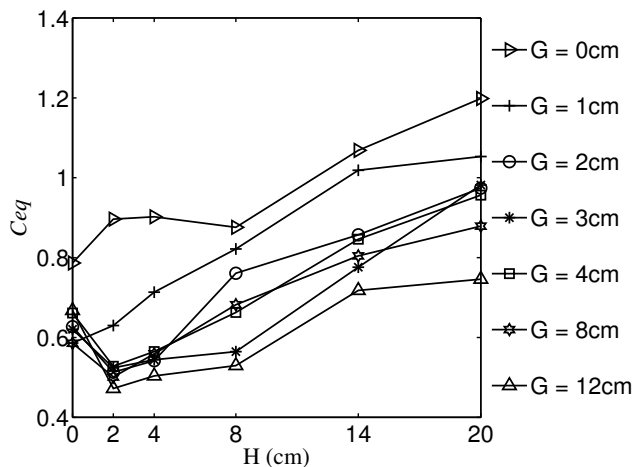


**Figure 5-1: Pressure equalization coefficient for single modules with respect to  $H$**

It can also be noted that the magnitude of  $C_{eq}$  decreases for larger  $G$  at fixed  $H$  (Figure 5-2), with the bulk of the reduction occurring between  $G \approx 0$  and 2 cm. Pressure equalization is improved with larger values of  $G$  (above 0) as the airflow around the modules increases pressure gradients across their external surface, improving the magnitude of the transmitted pressure to the cavity.  $C_{eq}$  declines for larger values of  $G$ , but at a reduced rate, implying that the optimal gap value with respect to minimized loading could be greater than the maximum value examined ( $G = 12$  cm). However, most of the benefit is seen for  $G = 2$  cm (presuming a designer would choose the smallest  $G$  possible to increase the packing density).

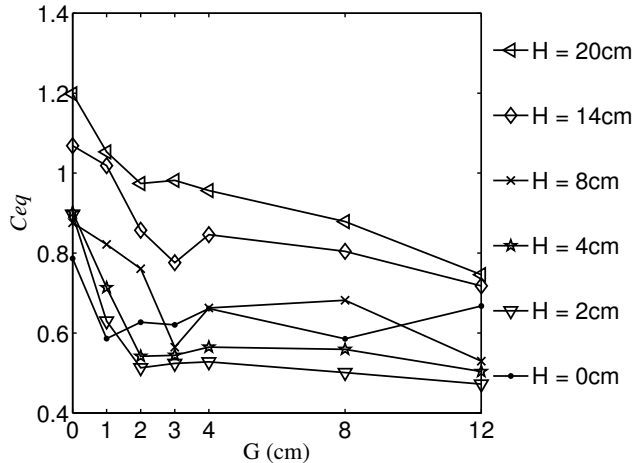


**Figure 5-2: Pressure equalization coefficient for single modules with respect to  $G$**

## 5.2 Effects of area-averaging

The components and cladding sections of many building codes were developed by averaging measured wind tunnel pressures over varying tributary areas. This process yields design recommendations dependant on the component's tributary area. For an array, the smallest tributary area considered is a single module, as areas smaller than a module have little physical meaning for design (for rigid modules). To determine the effect of tributary area multiple modules are combined to determine the effect of increasing dimensions (for instance interconnected modules associated with racking or installation systems).

Bienkiewicz and Sun (1997) used  $G/H$  to quantify the combined effect of both  $G$  and  $H$  on the pressure on the underside of the pavers; herein it is used to study the behaviour of pressure equalization coefficients,  $C_{eq}$ . Four different tributary areas are shown when plotting  $C_{eq}$  with respect to  $G/H$  in Figure 5-3. It can be seen that the  $C_{eq}$  values tend to collapse to a single curve for each tributary area, indicating that  $G/H$  is an appropriate parameter to describe the effect of pressure equalization across the modules, except for small  $G/H$  ratios. For small values of  $G/H$  (i.e.,  $G/H \leq 1$ ) the data follow the same non-linear, decreasing behaviour observed with the pavers for the peak underside pressure (Bienkiewicz and Sun, 1997) but are more variable. Values larger than  $G/H = 1$  yield an asymptotic limit of  $C_{eq}$  values, indicating that for the current module size, installations

with  $G/H > 1$  are optimal with respect to maximizing pressure equalization, as indicated by minimum values of  $C_{eq}$ . This is consistent with the findings of Bienkiewicz and Endo (2009) and Asghari Mooneghi et al. (2014) who noted that a higher  $G/H$  ratio led to improved wind performance of roof pavers (although their range of experimental  $G/H$  was limited to  $0.028 \leq G/H \leq 0.25$ ).

Figure 5-3 shows that the magnitudes of the  $C_{eq}$  values decrease for larger values of the tributary area. This signifies that the peak net array wind loads decrease faster than the bare roof loads do with larger tributary areas. If the net and external pressures decreased at the same rate, the magnitude of  $C_{eq}$  would remain relatively constant with tributary area. This was also noted by Kopp et al. (2012) when they observed that the net roof uplift on a low-rise building with a tilted solar array was lower in magnitude than the equivalent bare-roofed building. The de-correlation of the wind loads on the roof from the additional turbulence created by the array was noted to be the cause of the lower magnitude net uplift on the roof (with an array). With lower  $C_{eq}$  (and thus peak net uplift) with larger tributary areas, there is a significant benefit to mechanically connecting the modules together to reduce net wind loads on the arrays. The benefits of the area-averaging appear to be mostly obtained by 4x4 (11.6m<sup>2</sup>) modules in this configuration, with relatively smaller reductions for larger areas.

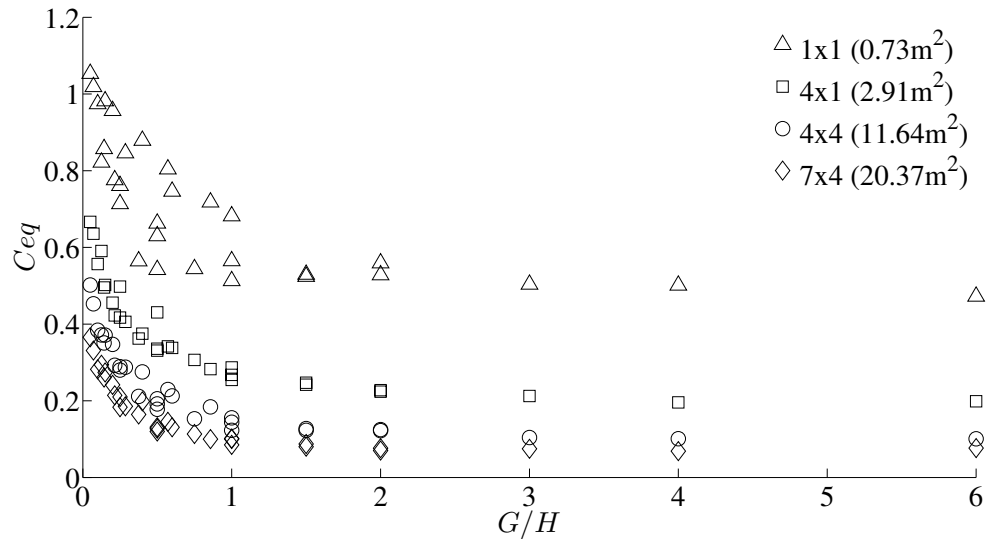


**Figure 5-3: Pressure equalization coefficients with respect to the  $G/H$  ratio for four tributary areas from the sloped roof model**

### 5.3 Effects of roof slope

For the  $C_{eq}$  approach to be effective for design guidelines, the evaluated values need to be similar for a range of roof slopes and building shapes. While it was not feasible to measure all array configurations on a range of roof slopes it was possible to mount the array on the roof of a low-rise structure for a select number of configurations. The full range of  $H$  for the largest gap,  $G = 12$  cm was selected for testing, as discussed in chapter 2.

Figure 5-4 contains the  $C_{eq}$  values for the same area-averaged cases from Figure 5-3 for both the  $30^\circ$  sloped roof (open markers) and flat roof (solid markers) models.

Measurement points from the  $G=12$ cm flat roof configurations follow the curve established by the sloped roof configurations, especially for larger  $G/H$  values. For small  $G/H$  values the flat roof measurements are slightly lower than those from the sloped roof. This indicates that the roof slope does not have a significant impact on the reduction in net wind loading of roof-mounted solar modules and that design recommendations based on the  $C_{eq}$  should be applicable for various roof slopes of low-rise buildings. This is believed to be valid since  $C_{eq}$  appears to be a rather robust indicator of the effect of

pressure equalization – quantifying how the net pressure is varied from the external upper surface of the bare roofed building. The change in net loading due to pressure equalization occurs on the modules regardless of roof slope.

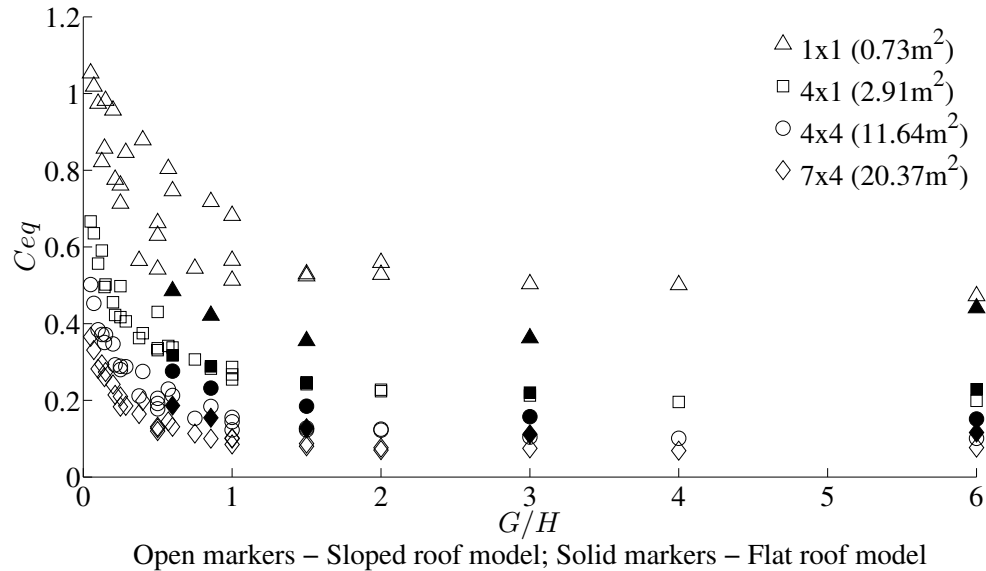


**Figure 5-4: Pressure equalization coefficients with respect to the  $G/H$  ratio for four tributary areas from the sloped roof (open markers) and flat roof (solid markers) models**

## 5.4 Effect of simulated larger modules

It is likely that the size of the module plays a role in setting the wind pressures on the modules because of the correlation effects on the external (upper) surface and changes to the cavity pressures. Bienkiewicz and Sun (1997) found that maximum net uplift decreased with increasing paver size when studying a wind tunnel scaled model with loose-laid roof panels on a flat roof. Recalling that the current set of wind tunnel studies were conducted with a single module dimension, it is not possible to directly study the impact of module size. However, a selected number of configurations were tested with multiple modules taped together to simulate a larger module. Taping the modules prevented airflow between the gaps, preventing pressure equalization and simulating a larger module surface area. Modules were sealed in 2x2, 3x4 and 4x4 combinations, as shown in Figure 2-7. These studies were all conducted with the shroud in place, which is

noted to change both the external and the cavity pressures, as discussed in section 6.6. However, since the base (untaped) and sealed data are both taken from shrouded configurations their only point of difference is the sealed gap to simulate larger modules. Sealing the modules was found to increase  $C_{eq}$  when compared to the values from the same combination of modules, as shown in Figure 5-5. The effect is more pronounced for the flat roof model, with more than a five-fold increase for the largest module simulation (4x4) and a large  $G/H$  ratio. The increase in  $C_{eq}$  is caused by a decrease in the worst, peak, cavity suction for the sealed combination of modules (Figure 5-6) while there was little effect on the worst, peak, external pressure (Figure 5-7). Since the peak external suction remains largely unchanged and the peak cavity suction is lower in magnitude, it can be noted that the worst, peak, net suction coefficients are larger in magnitude when the gap is sealed to simulate larger modules, as indicated by Figure 5-8.

These results are in contrast to the findings from Bienkiewicz and Sun (1997) for loose-laid roof pavers on a flat roof. However, it may be argued that the current comparison is not a true indication of the effect of larger modules since the level of air permeability is reduced. While sealing the modules simulates larger modules, it inhibits pressure equalization by limiting flow through the gaps around modules (effectively limiting effective transmission of external pressures to the cavity). The lower degree of pressure equalization is evidenced by the higher  $C_{eq}$  values. While this comparison does not truly demonstrate the effect of module dimensions at the same level of air permeability, it does strongly indicate the beneficial effect of  $G$  on reducing the net wind pressures and improving pressure equalization. Sealing the gaps effectively decreased the permeability of the array by decreasing the frequency of  $G$ . Attempting to compensate for this with a simple analysis could include plotting the sealed cases with their effective  $G/H$ , ratio which has been reduced based on the number of sealed gaps. For instance, the effective  $G/H$  ratio of the 2x2 sealed combinations is half that of the open case since three gaps are sealed along the column of the array (see Figure 2-7) and similarly the 3x4 and 4x4 combinations have effective  $G/H$  ratios that are a sixth of the open value. This is done in Figure 5-9 where the  $C_{eq}$  values from the sealed cases are plotted with respect to their effective  $G/H$  ratio in red, superimposed over the data from Figure 5-5. The effective

$G/H$  ratios are smaller, shifting the sealed data to the right on the figure. It does not appear that the effective  $G/H$  ratio as calculated provides an appropriate point of comparison with the unsealed data to derive any conclusions regarding the effect of module size. However, the scatter of the graph does indicate that the magnitude of the  $C_{eq}$  vs  $G/H$  curve is dependent on module size, similar to its dependency on tributary area,  $A$ , as seen in Figure 5-3. Additional experiments with arrays with different module dimensions (modelled not simulated) are recommended as a future course of action. Bienkiewicz and Sun also noted that the aspect ratio had an effect on the wind resistance of the system. While the current model and testing regime was not adequately equipped to study module dimensions, it was noted that the  $C_{eq}$  vs  $G/H$  curve appears to be specific to a given module size. The current model did allow for comparison of different aspect ratios was possible and is discussed in the next section.

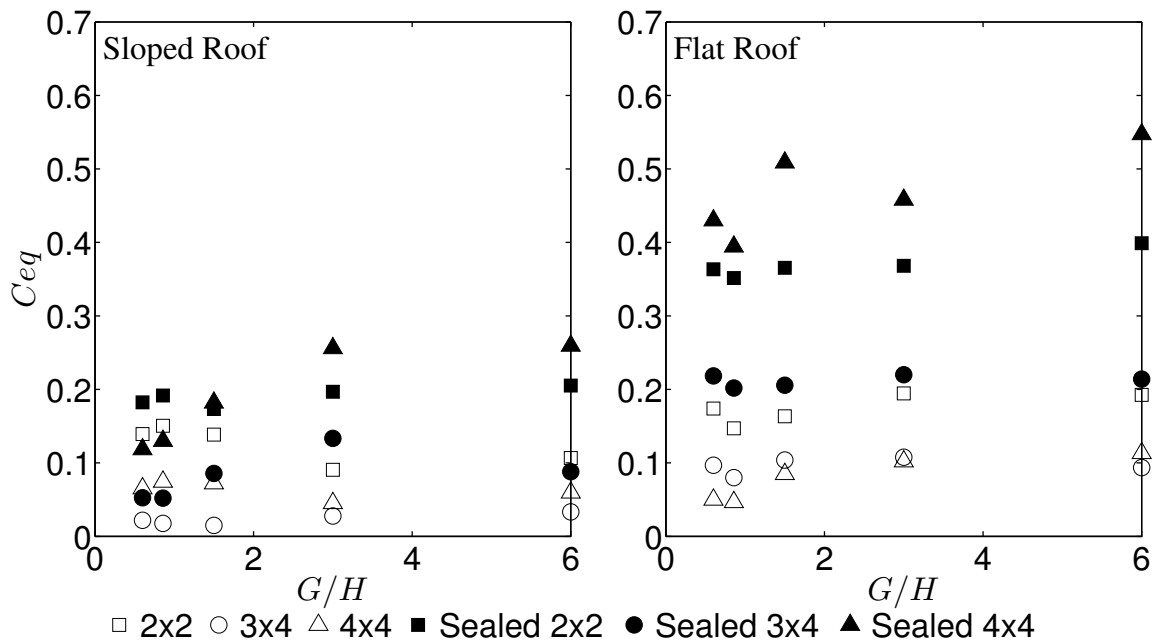


**Figure 5-5: Pressure equalization coefficients with respect to the  $G/H$  ratio simulating three module sizes from the sloped roof (left) and flat roof (solid right) models**

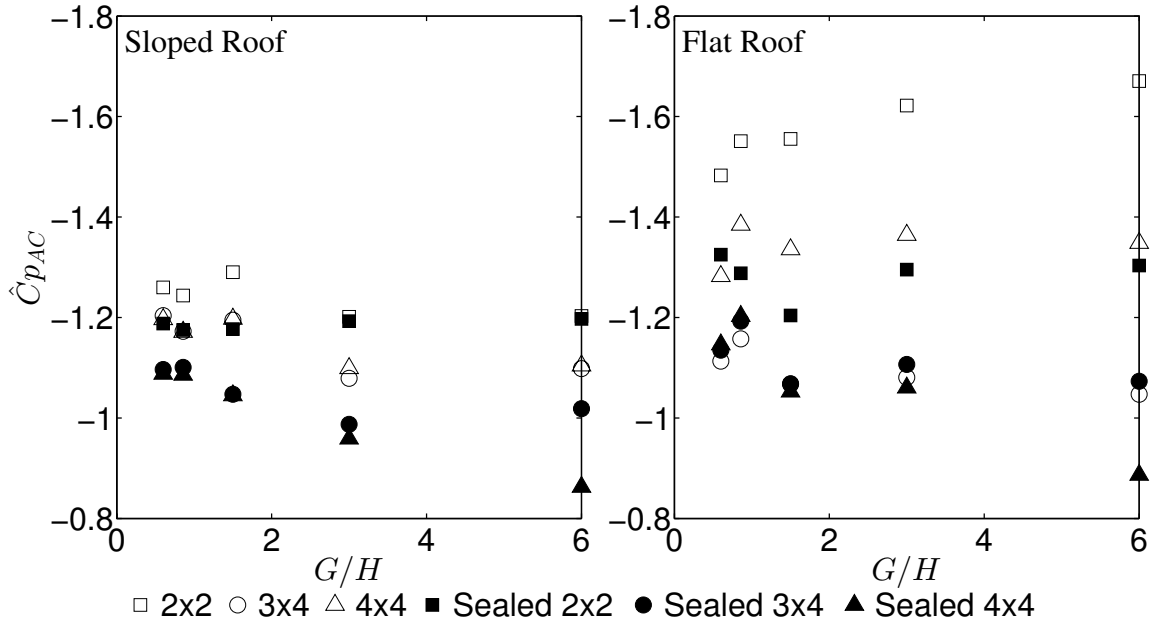


**Figure 5-6: Worst, peak, cavity (suction) coefficients area-averaged over three areas simulating different module sizes plotted with respect to the  $G/H$  ratio from the sloped roof (left) and flat roof (solid right) models**

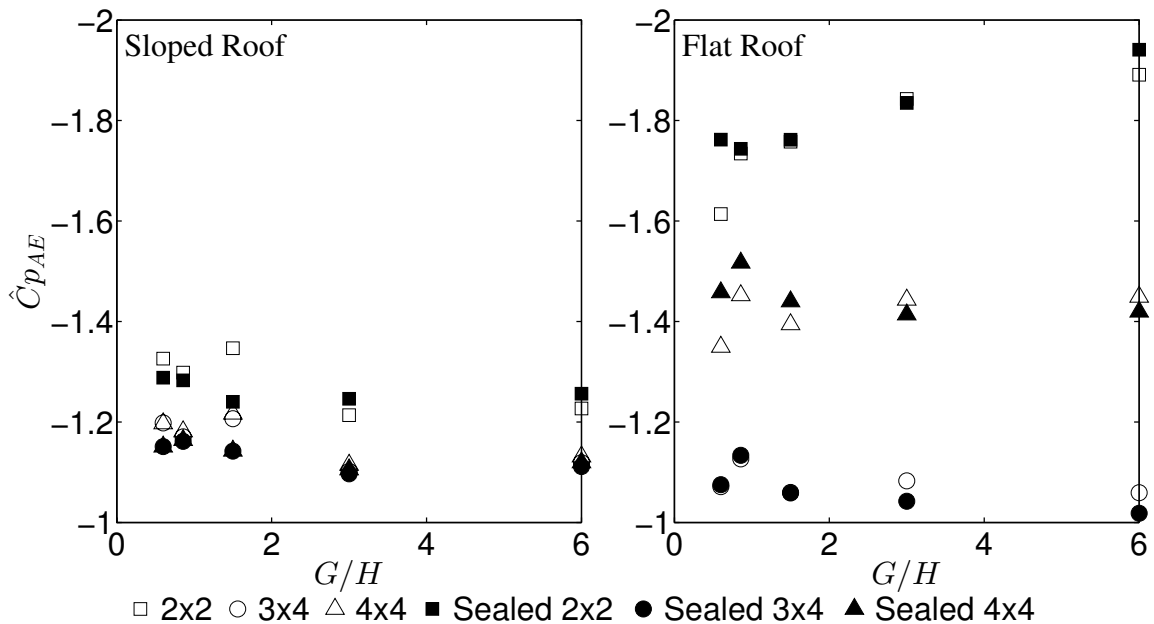


**Figure 5-7: Worst, peak, external (suction) coefficients area-averaged over three areas simulating different module sizes plotted with respect to the  $G/H$  ratio from the sloped roof (left) and flat roof (solid right) models**

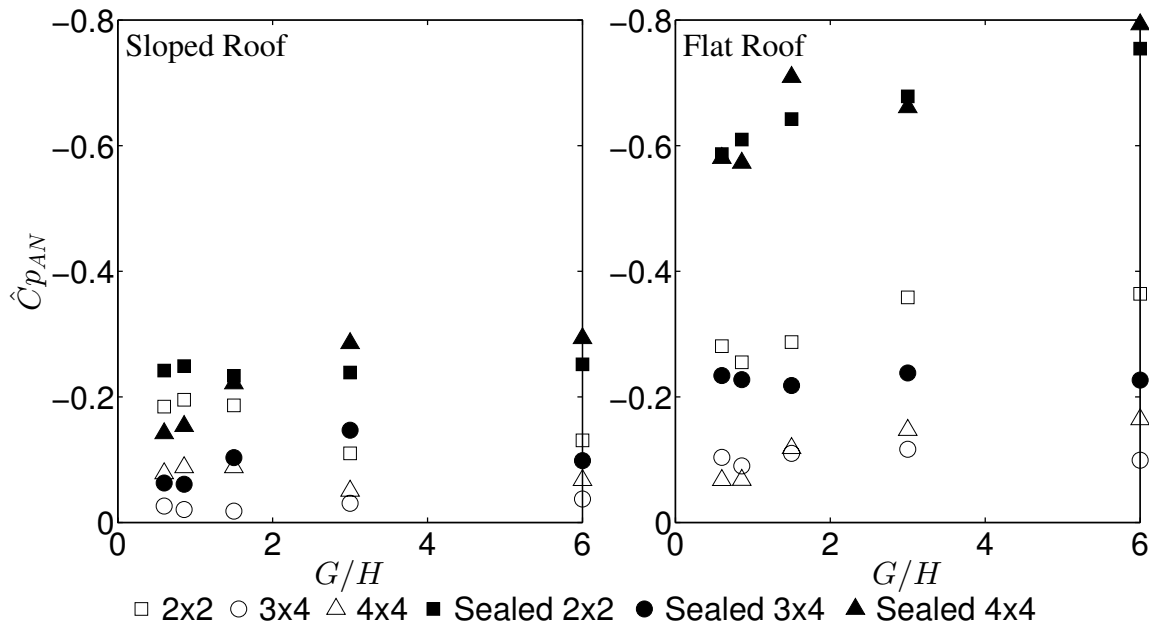


**Figure 5-8: Worst, peak, net (suction) coefficients area-averaged over three areas simulating different module sizes plotted with respect to the  $G/H$  ratio from the sloped roof (left) and flat roof (solid right) models**

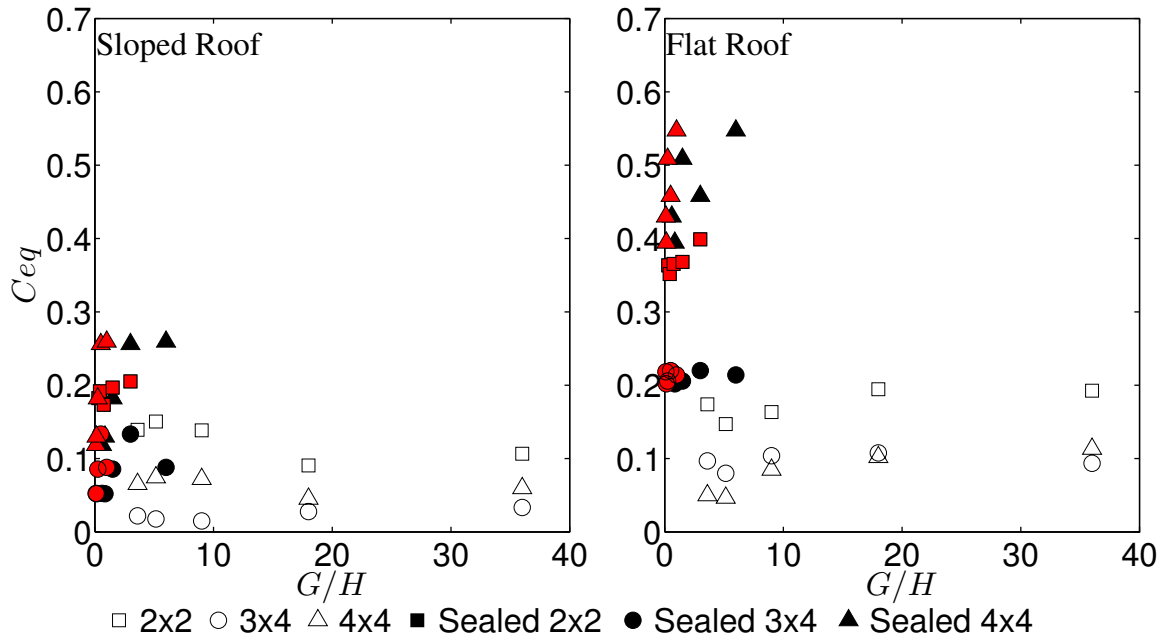


**Figure 5-9: Pressure equalization coefficients with respect to the  $G/H$  ratio simulating three module sizes from the sloped roof (left) and flat roof (solid right) models with values from the sealed data plotted with respect to effective (lower)  $G/H$  superimposed in red**

## 5.5 Effect of module aspect ratio

Along with the size of the module, the aspect ratio can influence the wind loads on the solar modules. Figure 5-10 shows  $\hat{C}p_{AN}$  (left) and  $C_{eq}$  (right) for two tributary areas with different aspect ratios; 1 module deep and 3 across yielding an aspect ratio of 8.7:1 and 3 modules deep and 1 module across yielding an almost square aspect ratio. Data from the sloped (open markers) and flat (solid markers) roof models are plotted. The aspect ratio can be seen to influence the net pressures on the flat roof model where the square area has reduced net pressures for a given  $G/H$  and tributary area. The effect is negligible on the sloped roof, although the net pressures for both aspect ratios are noted to be lower in magnitude than those measured on the flat roof. When considering  $C_{eq}$ , it can be noted that the sloped and flat roof values collapse to two distinct curves; one for the elongated tributary area and a lower magnitude curve of the same shape for square tributary area. This is thought to be a function of external-cavity correlation coefficients

which are highest around the perimeter of the module as seen in Figure 3-22. The degree of pressure equalization is higher for higher correlation coefficients, reducing the net wind pressures. With low aspect ratios the region of higher correlation and pressure equalization represents a larger portion of the module. Larger aspect ratios could experience a gradient in the correlation coefficients, resulting in an interior region of reduced correlation along the relatively longer dimension. This indicates that pressure equalization is improved for near square tributary areas, regardless of roof slope. This is consistent with the findings for roof pavers from Bienkiewicz and Sun (1997) who noted that wind resistance is improved for square pavers when contrasted to longer aspect ratios.

The effects of aspect ratio on the pressure equalization coefficient are most significant for smaller tributary areas. When the tributary area is increased to encompass 6 modules the distinct curves for different aspect ratios are not as well defined, as illustrated in Figure 5-11. This indicates that as the tributary area is increased the aspect ratio has less impact on the pressure equalization.

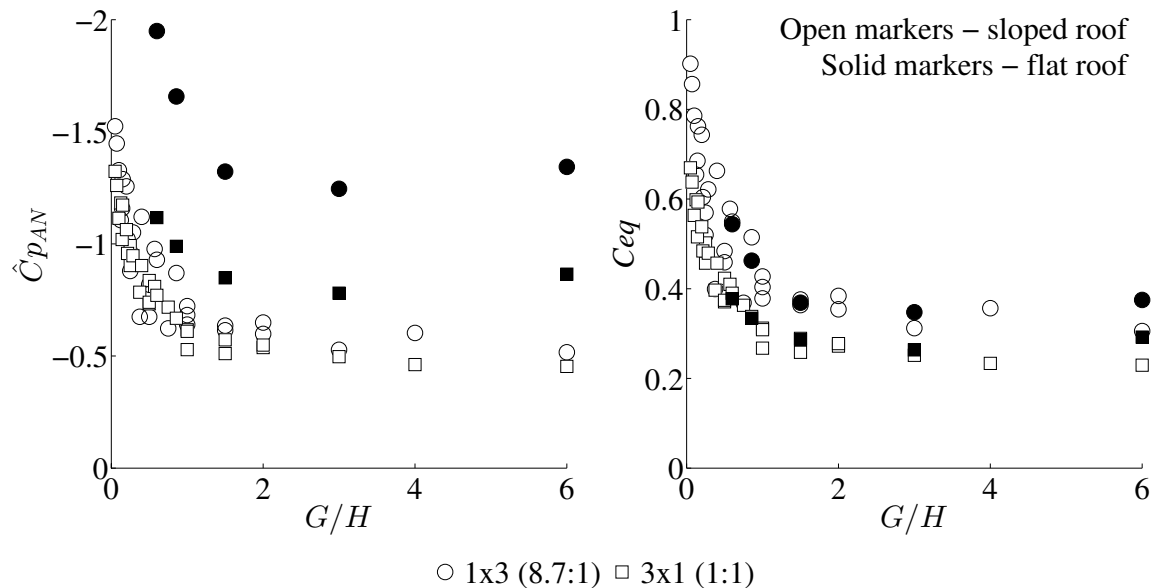


**Figure 5-10: Peak net suction (left) and pressure equalization coefficients (right) with respect to  $G/H$  for two different aspect ratios**

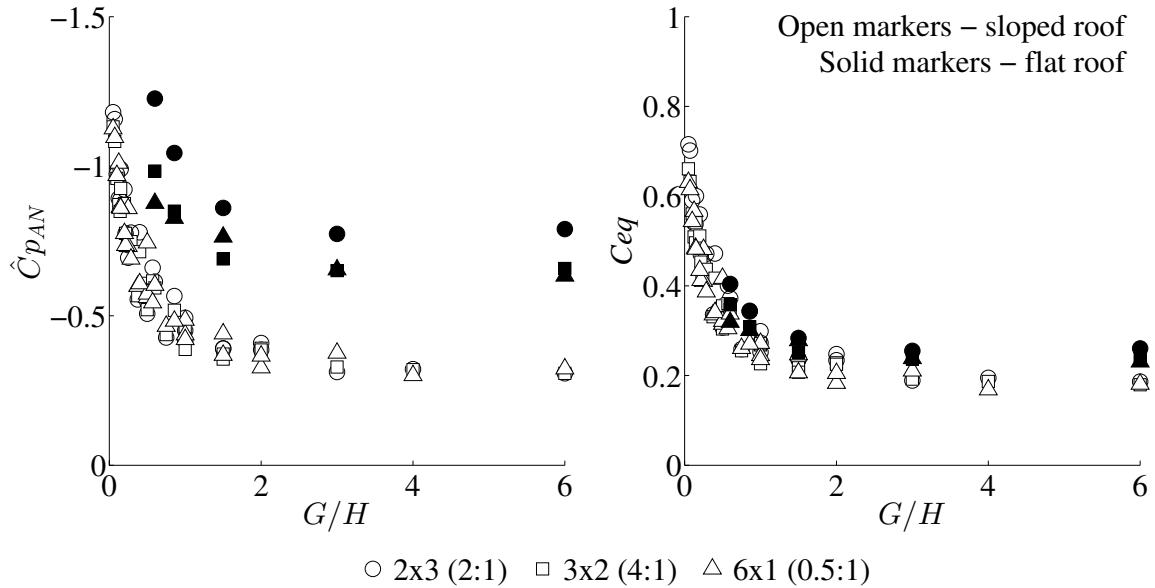


**Figure 5-11: Peak net suction (left) and pressure equalization coefficients (right) with respect to  $G/H$  for three different aspect ratios**

## 5.6 Summary

The pressure equalization pressure coefficient,  $C_{eq}$ , has been observed to be a good parameter on which to base design recommendations. It is found that  $C_{eq}$  can be approximated with a single curve when plotted with respect to  $G/H$  for a given tributary area and module size for both the sloped roof and flat roof models. While there is some spread in the data, it still indicates that using  $C_{eq}$  as a parameter to describe the unit-less change in wind loading is effective and largely independent of roof slope. This simplifies future design recommendations for roof mounted solar modules as roof slope does not need to be specifically addressed, but inherently will be accounted for through the existing external pressure coefficient from the design code.  $C_{eq}$  is noted to account for a number of variations, including aspect ratio, as indicated by the reduced scatter in the  $C_{eq}$  curves from Figure 5-10 and Figure 5-11. While the  $C_{eq}$  showed decreased wind resistance for larger (simulated) module dimensions, it is thought to be a function of modeling and not an accurate finding – thus, should not take away from the effectiveness of using  $C_{eq}$  as the basis of design recommendations. The development of these design

recommendations is covered in chapter 7, while additional roof and array edge effects on the design pressures is addressed in chapter 6.

## 6 Array and roof zones

As was seen in chapter 3, wind-induced pressures across a roof surface are not uniform, with the variations in magnitude addressed in codes and standards by the use of zones wherein each zone is assigned a representative pressure. Corner zones are typically associated with the highest magnitudes, with slightly reduced pressures along edge zones and further reductions in the interior (or field) of the roof. The relative dimensions of these roof zones can be seen in Figure 6-1 with the ASCE 7-10 (2010) roof zones overlaid on the current flat roof model. Array aerodynamics depend on the wind speeds above the roof, which also vary in these regions. As such, the location of the array on the roof surface is a critical parameter in determining the design wind loads.

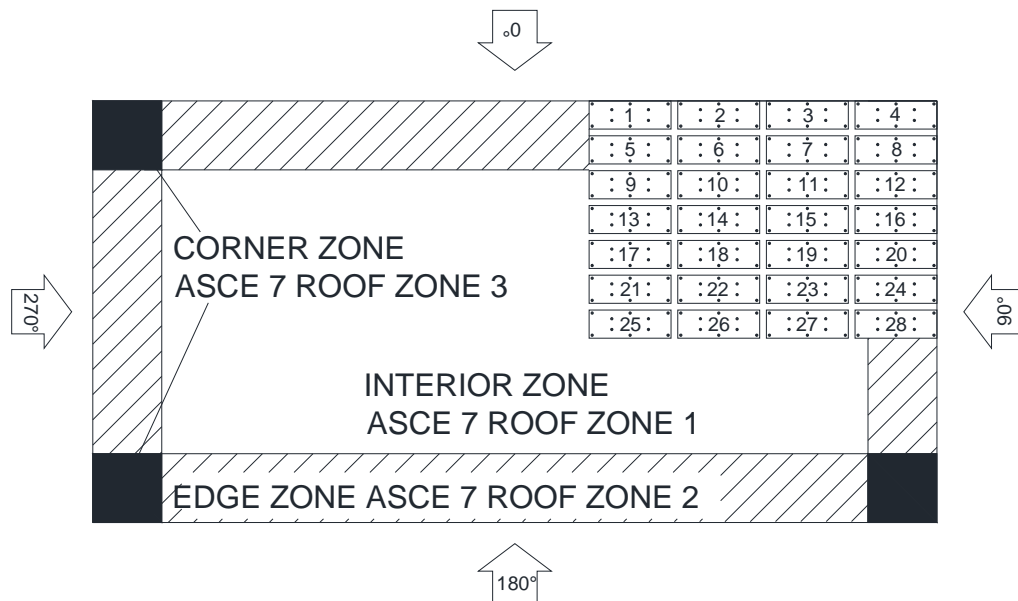


**Figure 6-1: Plan view of the flat roof model**

While the array placement plays a significant role in determining the loads on modules within the array, so too does a module's placement within the array. Modules around the perimeter are directly exposed to the undisturbed flow field, however, those further downstream are subject to a different flow field. The windward modules may shelter those downstream, or experience different edge effects, such as local flow separations, on both the upper and lower surfaces, impacting the wind loads.

Thus, it is imperative to assess and quantify the effects that the position of the array on the roof, and the module positions within the array, have on the net array wind loads. With this information, recommendations for roof zones and array zones can be made and incorporated into design guidelines for roof-mounted solar arrays on low-rise buildings. This chapter addresses these issues.

To account for the increased wind loading on modules subject to array edge effects SEAOC PV2-2012 (2012) uses an edge factor ranging from 1 (no effect) for interior (sheltered) modules and 2 (doubling the pressures) for modules along the northern edge of the array (noted to have the largest uplift for modules that face south in the northern hemisphere). This array edge factor,  $E$ , is calculated for each module and primary wind direction (north, east, south and west). The highest edge factor for any direction is used for design, consistent with many code approaches that take the worst case value. The array edge factor is applied to the nominal net pressure coefficient,  $(GC_{rn})_{nom}$ , which is roof zone specific. In their approach of accounting for array edge effects with a factor and roof edge effects through separate roof zones (each with a different  $(GC_{rn})_{nom}$  curve) there are instances where a module could be subject to both array edge effects and roof edge effects. This could occur for windward modules in both corner and edge roof zones. On the same note, there could be modules downwind of those subject to array edge effects but still in one of the roof edge zones. In either of these cases the flow field is very complex and it would be difficult to fully separate the array edge effects from the roof edge effects. This chapter sets out to determine appropriate dimensions for both the array edge zone and the roof edge zones.

## 6.1 Definition of the “array edge effect distance” or zone

The “array edge effect distance” is the distance into the array for which the local point pressures are directly influenced by the boundary conditions of the incoming flow. Along this distance the pressures exhibit different behaviour than those observed (downstream) within the rest of the array. For the current model, it will be seen that from wind directions with reattached flow the leading edge typically experiences the largest

suctions with a linearly decreasing trend approaching the (relatively) constant pressures observed after this distance. There can also be an edge effect at the trailing edge of the array where airflow into the wake of the array influences the local pressures. The edge distance would be applied around the perimeter of the array, forming an array edge zone. Quantifying this zone, preferably in non-dimensional terms, is crucial for developing design recommendations as the modules that are located within the edge distance are subjected to larger loads.

When considering a solar module mounted parallel to a flat roof, comparisons can be made to a flat-plate mounted at zero incidence, a fundamental case when considering wind-induced pressures. In the current model, the reattached flow from across the roof impacts the array as shown in Figure 6-2 (inspired by Schlichting and Gersten, 2000). Flow separates at the leading edge of the external (upper) surface of the array, creating a separation bubble. The flow reattaches to the array at some distance downstream. The array edge effects are a result of this array-induced separated flow, thus the edge effect distance could be related to the mean reattachment length,  $L_{sep}$ , on the external surface of the array. Modules downstream of the separation bubble would be sheltered from the array edge effect, being subject to flow that had reattached to the array (with lower magnitude, more uniform pressures).

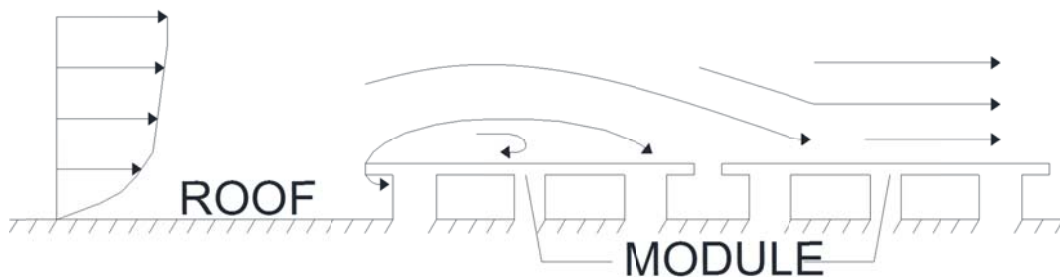


**Figure 6-2: Schematic of array edge effects from flow separation at the leading edge of the array on the current model**

With the cavity open to flow, it is possible that it will be subject to an array edge effect; however the cavity depth is thought to play a large role in dictating any flow separation from the lower surface of the module. For an idealized system with no cavity

obstructions (such as the supports for the current model) it is expected that for large  $H$  the flow separation in the cavity (off the lower surface of the module) will be similar to that on the upper surface (Figure 6-3a). The roof surface does not impede the flow separation in the cavity since the cavity depth is such that it is deeper than the separation bubble thickness. In this situation, the reattachment length is thought to be a function only of  $t$  as the cavity depth does not impede the natural flow separation from the module. For shallower  $H$  of medium height it is possible that the cavity flow can be constrained due to the proximity of the roof surface, as seen in Figure 6-3b. The cavity flow is almost entirely constrained for the smallest  $H$ , where the flow resistance is high. This prevents the formation of a separation bubble on the lower surface of the module (Figure 6-3c). This hypothesis was developed by studying existing literature, specifically flow around a rectangular cylinder near a wall (Malavasi and Trabucchi, 2008; Blois and Malavasi, 2007; Martinuzzi et al., 2003), and the wake interaction between normal flat plates in tandem (Auteri et al., 2008). Blois and Malavasi (2007) used particle image velocimetry to study the flow around a rectangular cylinder spaced at different intervals from a solid wall. They noted that as the distance between the cylinder and the wall was reduced the longitudinal dimension of the separation bubble on the lower surface was reduced. Malavasi and Trabucchi (2008) built on this work, completing numerical simulations of the flow and showing visualizations of the constrained lower surface flow separation as the cylinder was mounted closer to the wall. Martinuzzi et al. (2003) conducted a number of wind tunnel studies of a square cylinder, again at different gaps from a wall. They noted distinct flow regimes based on the gap dimension. Their focus was on vortex shedding, but they note that for large gaps (near the chord dimension of the cylinder) the flow is similar to a no wall case, implying that it has no effect. As the gap was reduced to 30-60% of the chord the viscous effects on the flow in the gap are more significant (cavity flow in the current study). Mean and standard deviations of pressure coefficients on the upper and lower surface of the cylinder (parallel to the wall) were noted to vary with the normalized gap dimension (gap/chord) with the lowest magnitudes typically associated with small gaps (cylinder closest to the wall). Studies on the plates would be more relevant to the current model, where the modules are more aerodynamically similar to a plate than a rectangular cylinder. Auteri et al. (2008) studied flow patterns of two

tandem (parallel) plates mounted at different spacing intervals. The plates were perpendicular to flow but noted similar (flow) interference behaviour for small spaces between the plates and an increased dependence on  $Re$ . From the established literature presented above it is clear that the cavity depth (and module thickness) plays a role in establishing the cavity flow regime under array edge effects. However, it should be noted that due to the design of the module, the separation bubble on the lower surface of the module was severely limited due to the large flow disruption caused by the vertical supports (as seen in Figure 6-2). The unimpeded flow separation in the cavity over a range of  $H$  should be a design consideration for any future research.

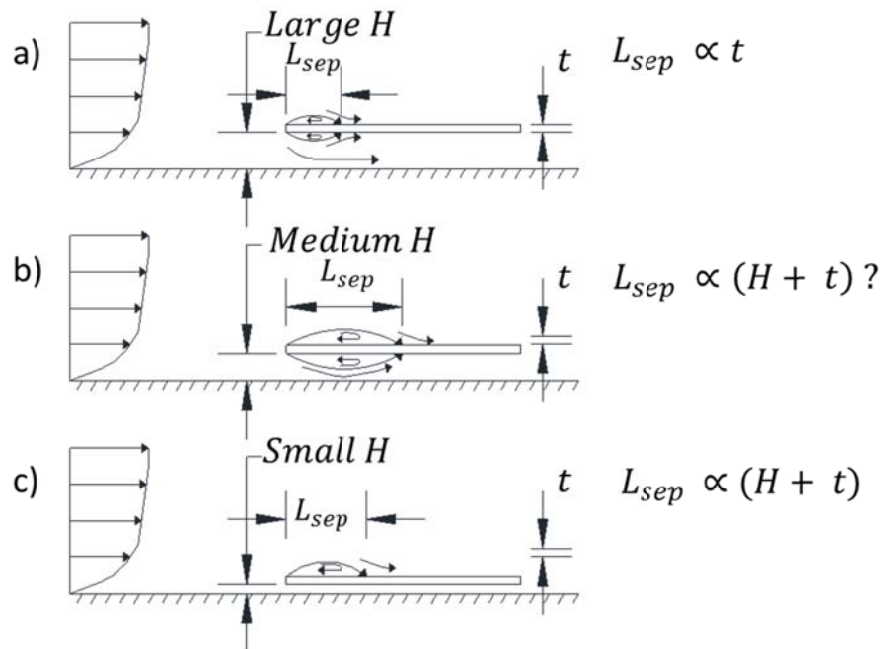


**Figure 6-3: Conceptual flow patterns on the external (upper) surface of the array and in the cavity for a range of  $H$  (inspired by from Malavasi and Trabucchi, 2008; Blois and Malavasi, 2007; Martinuzzi et al., 2003; and Auteri et al., 2008)**

It is expected that the reattachment length, and therefore the array edge distance, will be a function of the cavity depth and/or module thickness. The basis for this is that the reattachment length is often expressed as a function of eave height for low-rise buildings with flat roofs (e.g., Pratt and Kopp 2014). For flow separation off a roof mounted solar array the equivalent parameter could be considered to be the cavity depth,  $H$ , plus the

module thickness,  $t$ . In the next section the array edge effect distance is estimated in terms of cavity depth and module thickness using the point pressures; differentiating the edge effect zone (higher magnitude suction) from the interior section of the array with reattached flow (lower magnitude pressures).

## 6.2 Quantification of the array edge zone using the flat roof model

As previously discussed, for the current model it is difficult to differentiate between the edge effects from the building on the array and from the edge effects caused by the array being elevated from the roof surface. This is especially true for wind directions where the array is along windward walls of the model, experiencing separated flow from the building walls and from the edge of the array. Therefore, to quantify the array edge zone based solely on the impact from the separated flow on the array edge only wind directions for which flow has reattached are considered ( $112.5^\circ - 337.5^\circ$  for the flat roof model as defined by Figure 6-1).

Consider first the case of the array mounted on the flat roof with a wind direction of  $90^\circ$ , parallel to the long dimension of the module (and also the long direction of the building). For this wind direction the flow impacting the array comes from across the roof surface and has reattached to the roof from the initial separation off the building edge. The windward modules are those in the left column when looking at Figure 6-1. This is the simplest case to assess the array edge effects, with fairly uniform, reattached flow impacting the array. Any variation in the pressures across the modules can be attributed to the change in the flow field due to the array, specifically separation off the array edge, as pressure variations on the (bare) roof surface would be minimal for the same wind direction without the array.

Pressure coefficients from lines of pressure taps along the array are presented in this section. The specific line of taps plotted is shown in the schematic inset to the right of each plot. The data are taken from 3 taps along the edge of the module, representing the first, third and fifth point pressure on each module, as well as 2 taps that are slightly setback from the edge, shown as the second and fourth point pressures. While these taps

do not form a continuous line, they are plotted together to improve the spatial resolution when examining the edge effect distance. Additional information on the tap layout is included in Appendix A. Peak suction coefficients are plotted in black with dashed lines, mean pressure coefficients are plotted in black with solid lines and RMS pressure coefficients are plotted in grey. All  $H$  are plotted for the specific value of  $G$  considered. Gaps between the modules are indicated by the vertical dashed lines in the figure and the tap locations on the modules are plotted to scale. The wind direction in these figures is noted by an arrow on both the plot and in the schematic.

External peak suction coefficients as well as mean and RMS pressure coefficients on the upper surface of the array are plotted in Figure 6-4. The windward module (#13) has a strong pressure gradient when examining the peak suction coefficients, with the values decreasing across the module. The peak pressure gradient is reduced on module 14, which is sheltered. Modules 15 and 16, those in leeward positions, have minimal variation in peak pressure coefficients. This indicates that the edge effect is largely limited to only a portion of the windward module when considering the peak suction coefficients. The position of the tap is significant when examining the peak external suction coefficients; taps closer to the edge of the module experience larger magnitude suction coefficients (as discussed in chapter 3). Mean and RMS pressure coefficients are less susceptible to the position of the tap as well as variations associated with varying cavity heights (seen in the reduced spread of the data); they are noted to be much more uniform across the array. However when the three statistical quantities are plotted together it is difficult to see the variations in the mean and RMS values. Since peak suction coefficients are more variable in nature, it is easier to assess the edge effect distance based on mean and RMS values which are more likely to accurately show the transition between pressure influenced by boundary conditions and those unaffected downstream.

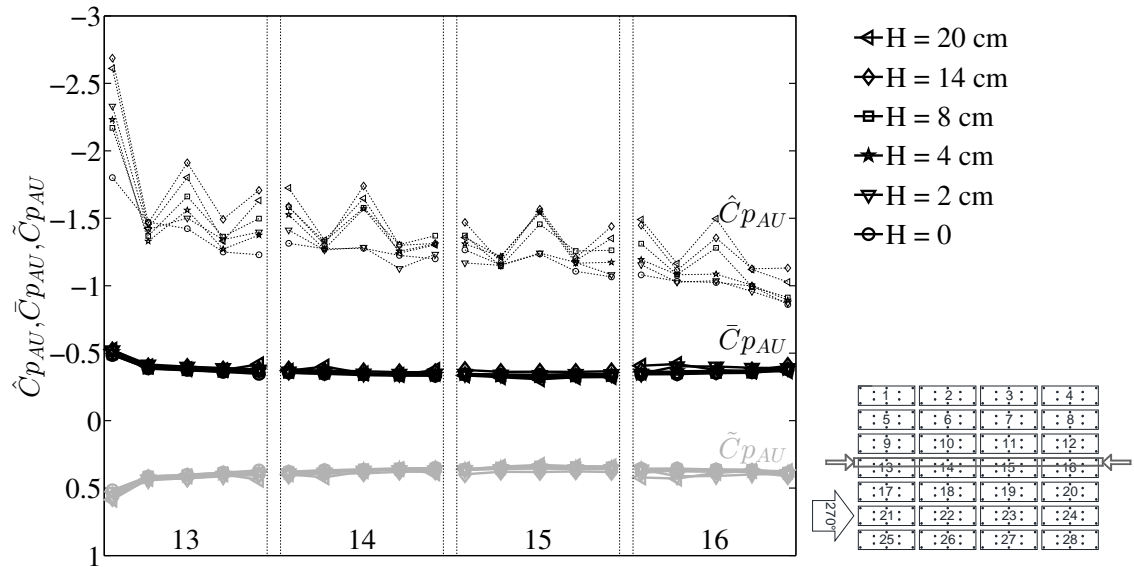


**Figure 6-4: External peak suctions, mean and RMS pressure coefficients measured along the top row of pressure taps on the middle row of modules for the 270° wind direction for the  $G = 12$  cm configurations on the flat roof**

The mean and RMS pressure coefficients, plotted in Figure 6-5, are largely uniform across the array with the exception of the pressure gradient measured between the first two taps on the windward module. There is a plateau of values across the array, which is reached at roughly the second tap. This indicates that the external pressures on the windward  $\frac{1}{4}$  to  $\frac{1}{3}$  of the module are impacted by the separated flow at the array edge; but that the leeward  $\frac{2}{3}$  to  $\frac{3}{4}$  of module 13 and downwind modules are unaffected and experience nearly uniform distributions (notwithstanding the effects of the adjacent gaps between modules on the peak values).

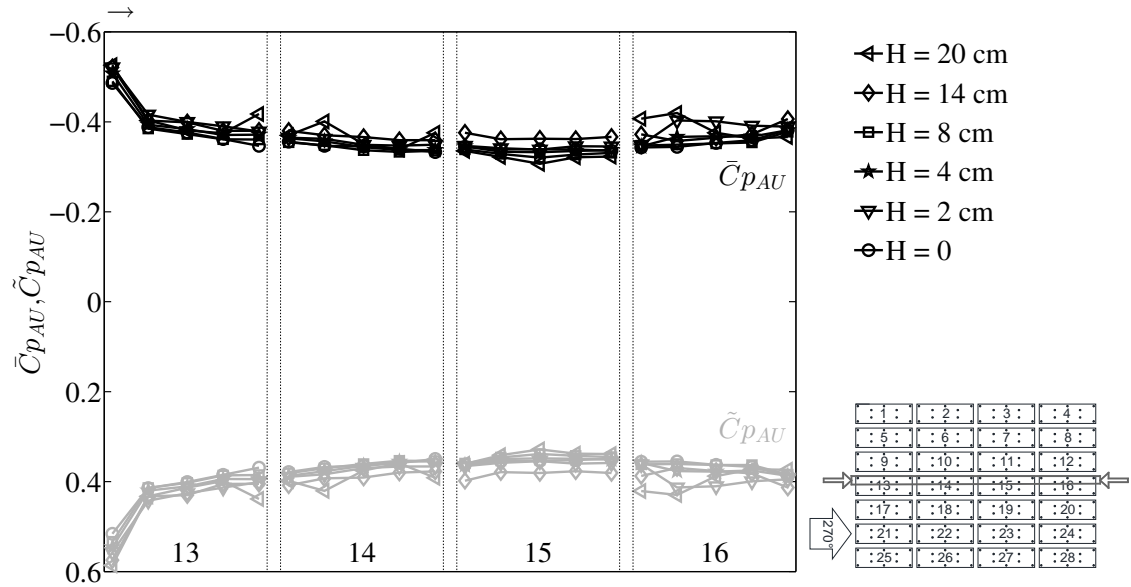


**Figure 6-5: External mean and RMS pressure coefficients measured along the top row of pressure taps on the middle row of modules for the 270° wind direction for the G = 12 cm configurations on the flat roof**

The cavity mean and RMS values for the same line of taps, wind direction and configuration are plotted in Figure 6-6. There does not appear to be an edge effect distance with respect to cavity pressures; the values are uniform across the array. This indicates that, for this wind direction, the cavity pressures are not influenced much by the boundary conditions and that the edge effects are due to the changes on the upper surface of the modules. Recall that the vertical supports that contained the pressure tubing would likely have impeded the cavity flow, disturbing any edge effects that may have been caused by the flow separation at the array edge. While not strongly defined, the spread of values indicates that both the mean and RMS pressure coefficients are increased in magnitude for larger  $H$ . This is most easily seen on module 15, noting the effect is small.

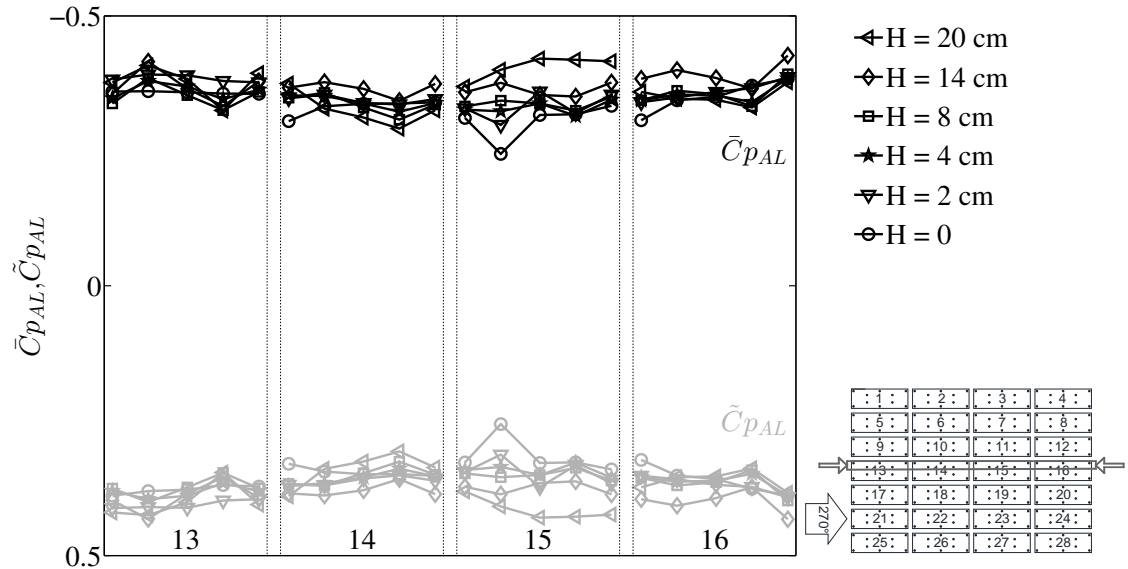


**Figure 6-6: Cavity mean and RMS pressure coefficients measured along the top row of pressure taps on the middle row of modules for the 270° wind direction for the  $G = 12$  cm configurations on the flat roof**

The 270° wind direction is the most simple and results in only one column of windward modules. The impact of the boundary layer on the edge effect distance many vary with wind direction. The quartering wind direction of 225° directly impacts both a column of modules and a row of modules. The external mean and RMS pressure coefficients measured on bottom row of taps or the array are shown in Figure 6-7. From this wind direction these taps are unsheltered, being the closest to the edge of the array. The data show the sensitivity to the position of the tap, as indicated by the higher magnitudes associated with points 1, 3 and 5 which are closer to the edge. This indicates that there is a pressure gradient across the short axis of the module and that for this wind direction the trend between the edge taps (#1, 3 and 5) should be the main focus. There is a strong gradient between taps 1 and 3 on module 25, with lower magnitude, more uniform pressures at leeward tap locations. This supports that even for more aerodynamically complicated wind directions and modules, the pressures reach a fairly uniform plateau after a distance equal to less than half the module length.

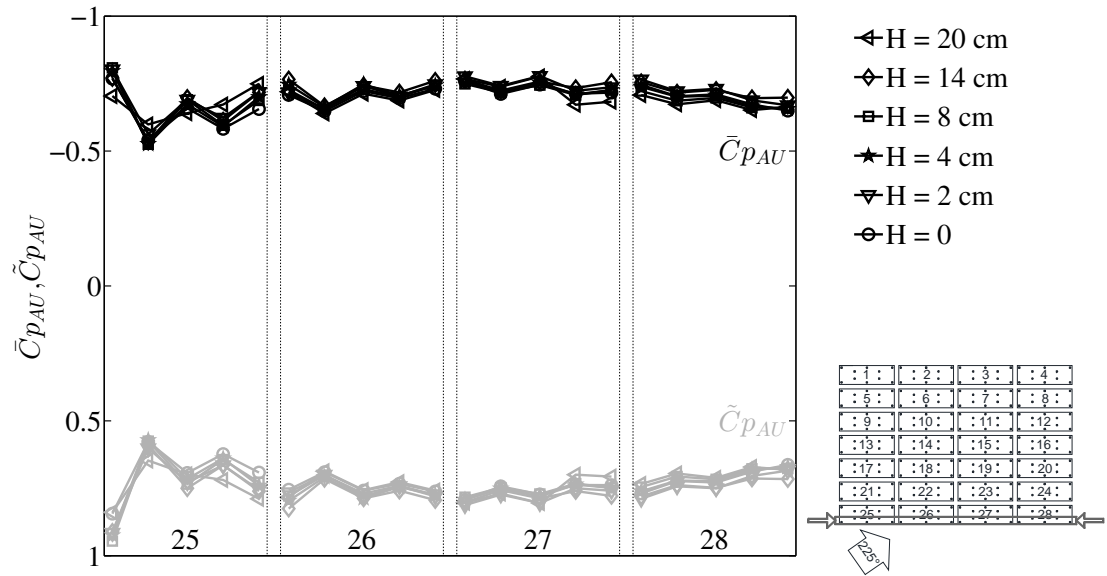
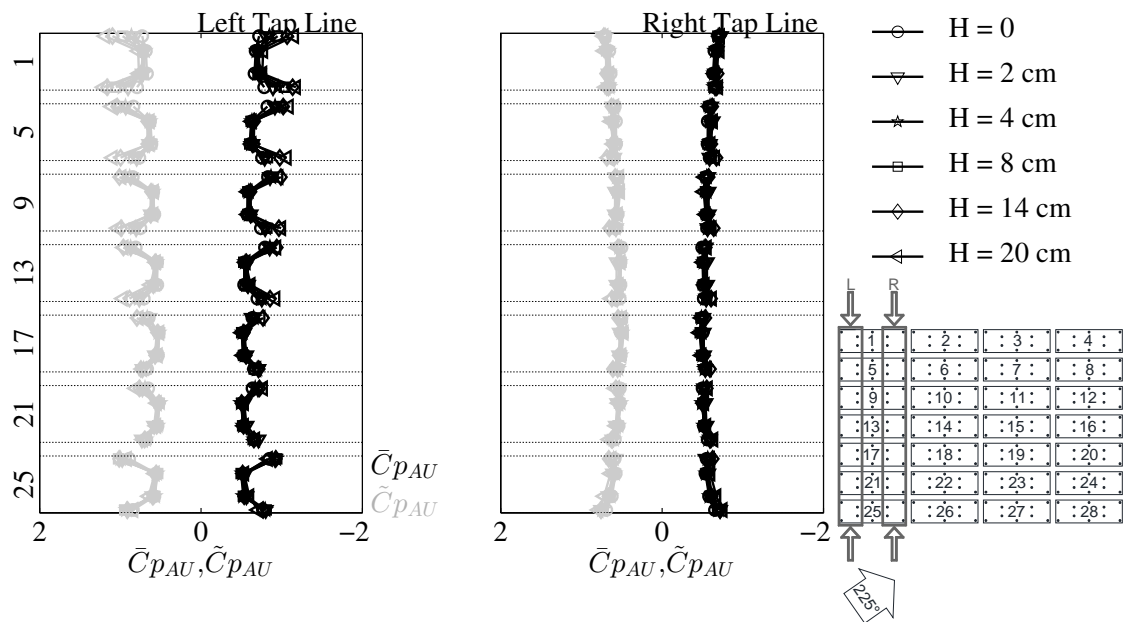


**Figure 6-7: External mean and RMS pressure coefficients measured along the bottom row of pressure taps on the bottom (field) row of modules for the 225° wind direction for the  $G = 12$  cm configurations on the flat roof**

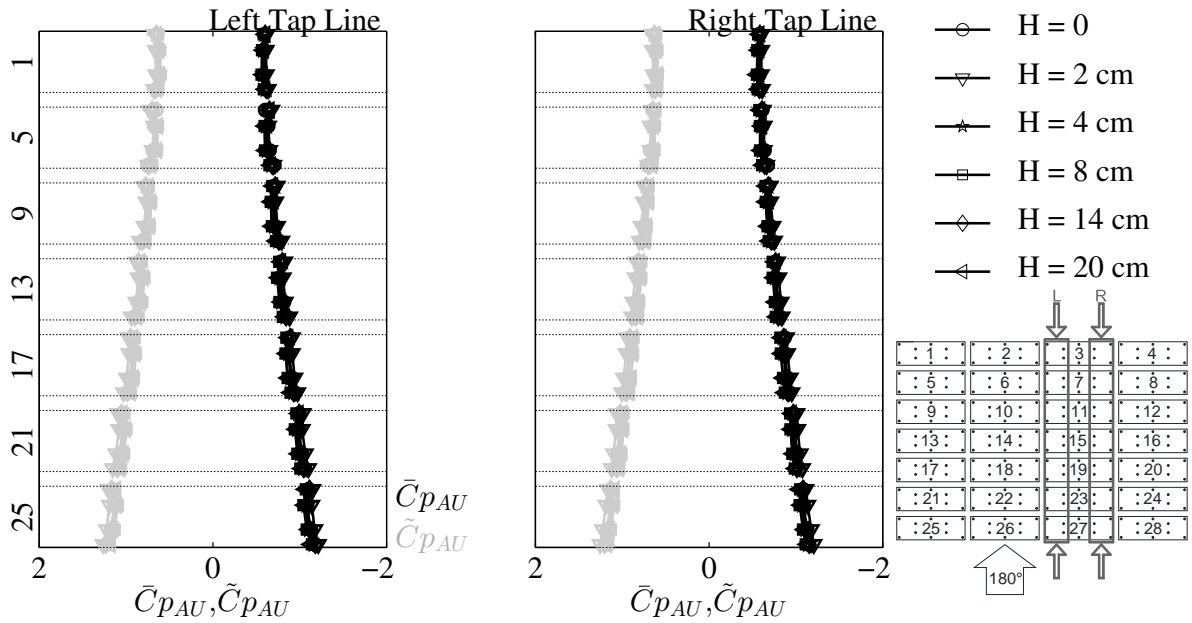
From Figure 6-7 it is clear that there is a pressure gradient measured for both the mean and RMS pressures across the short axis for a cornering wind. Since the module has an aspect ratio of roughly 3:1, the edge effect distance also needs to be confirmed for the short axis of the module.

Figure 6-8 contains two line plots across the short dimension of the module for the column of modules adjacent field of the flat roof model (shown in the inset schematic for each figure). The line on the left is directly exposed to the flow (taps 1, 2, 6 and 7) while the right line is on the leeward half of the first module. The exposed left line of taps shows pressure gradients on both edges of the module such that the interior pressure taps have lower magnitudes. This trend is not observed on the second half of the module or along sheltered columns (Figure 6-9). This confirms what was established above, that pressures set back from the edge by a distance of a half module have more uniform pressures and are not be affected by the boundary conditions. Recall that the edge effect distance will be used to set the dimensions of the edge zone for the array. Considering

this zone to be a half module wide, only the left tap line and bottom row of modules (#25 in this figure) are contained within the zone and subject to a modified flow field. Interior (sections of) modules show uniform pressures, confirming the dimension established above. For a perpendicular wind direction with reattached flow there is no visible pressure gradient on the windward module from the edge effect. While this does not serve to validate the appropriate dimensions for an edge zone, it indicates that the zone, as established by other loading patterns, is not inappropriate but rather conservative.



**Figure 6-8: External mean and RMS pressure coefficients measured along two tap lines on the column of modules adjacent to the field of the roof for the 225° wind direction for the  $G = 12$  cm configurations on the flat roof**



**Figure 6-9: External mean and RMS pressure coefficients measured along two tap lines on an interior column of modules for the 180° wind direction for the  $G = 12$  cm configurations on the flat roof**

Figure 6-10 is a line plot across a row of modules that were sealed together to form an array 4 modules wide and 4 deep. These configurations simulated larger modules by taping modules together, preventing air flow through  $G$  and were done with a shroud surrounding the array. The sealed  $G$  are shown as vertical grey lines and the tap locations are to scale. Even with the simulated larger module the edge effect distance was limited to  $\sim 1/2$  the length of the physical module (not simulated). This signifies that the module length is not a defining parameter of the edge effect distance – the same physical distance was observed for two different module sizes.

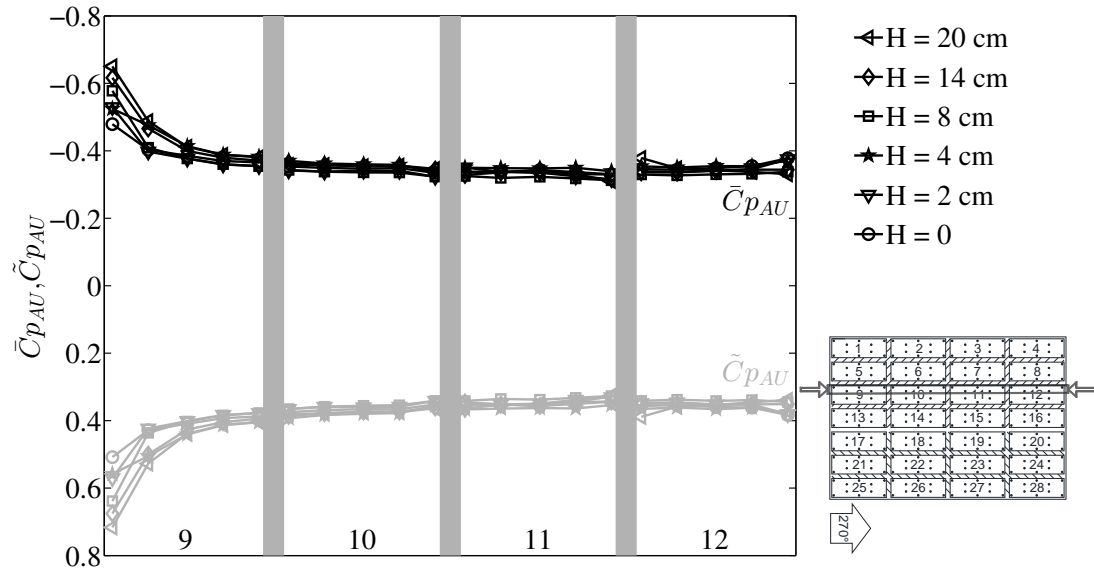


**Figure 6-10: External mean and RMS pressure coefficients measured along two tap lines on an interior row of modules for the 270° wind direction for the shrouded and sealed (4x4/3x4)  $G = 12$  cm configurations on the flat roof**

From re-attached flow, the boundary conditions acting on the array only tend to impact the pressures on a fraction of the windward module. As mentioned earlier, it is expected that the width of the array edge zone is related to the cavity depth plus the module thickness. From the current dataset it appears as if the width of the array edge zone could be approximated as  $\approx 1(H + t)$  to  $2(H + t)$ . Additional testing with  $t$  as a control variable and a cavity with reduced obstructions is recommended to further refine this estimate. However, the approximated array edge zone width can be validated using the sloped roof data, covered below.

### 6.3 Validation of the array edge zone using the sloped roof model

The array edge zone of approximately  $1(H + t)$  to  $2(H + t)$  was validated by testing its validity for  $G \approx 0$  configurations with the array mounted on the sloped roof. Since the modules were used for both roof modules, this can be visually approximated as  $\frac{1}{3}$  of the module length. The aerodynamics of the sloped roof model are more complicated with the array located near the eave, however, as can be seen in Figure 6-11 and Figure 6-12 the approximated edge zone dimension appears to hold. This is confirmed when examining the external mean point pressures in Figure 6-11. Large external pressure gradients between individual pressure taps are limited to the windward edge of module 13. Minor pressure gradients are seen in both the external mean and RMS pressure coefficients for leeward modules, but the edge effects are limited to the established edge zone. Mean and RMS pressure coefficients measured in the cavity do indicate an edge effect that was not observed with the flat roof model (Figure 6-12). The effect is limited to the windward module and the pressure gradients are smaller than the external gradients. Variation is noted in the data from the  $H \approx 0$  configuration; however, this could be a result of modeling imperfections resulting in an uneven cavity. The impacts of any surface imperfections in the material would be exacerbated for this configuration as the modules were in contact, but not sealed with, the roof surface. An array edge zone of  $\approx 1(H + t)$  to  $2(H + t)$  was found to be an appropriate boundary for all edge effects noted in the mean and RMS pressure coefficients on the external, upper, surface as well as in the cavity for both roof slopes and simulated larger modules.

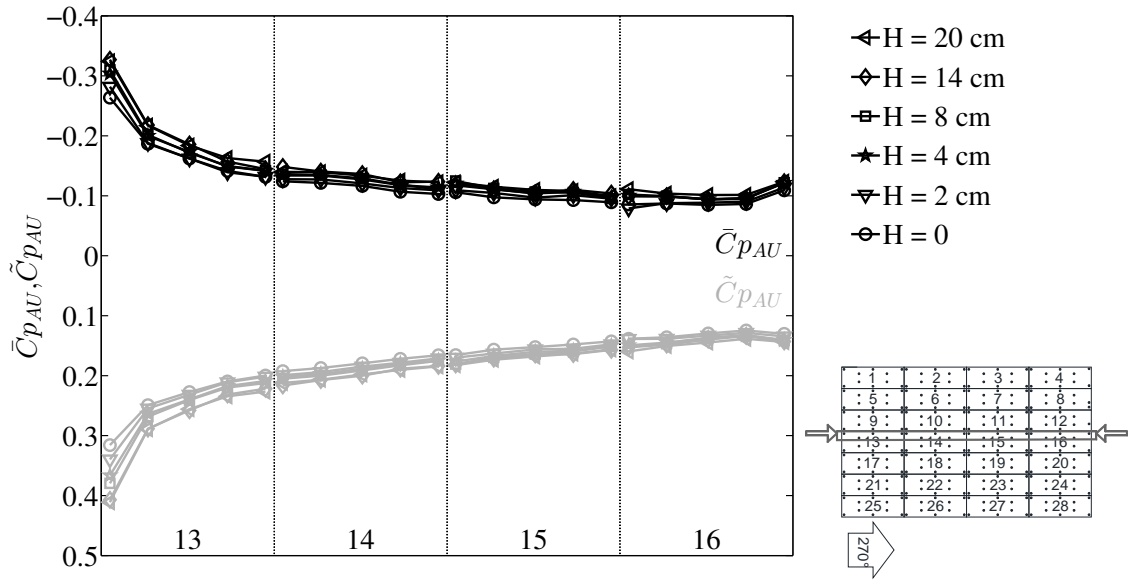


**Figure 6-11: External mean and RMS pressure coefficients measured along the top row of pressure taps on the middle row of modules for the 270° wind direction for the  $G \approx 0$  configurations on the sloped roof**

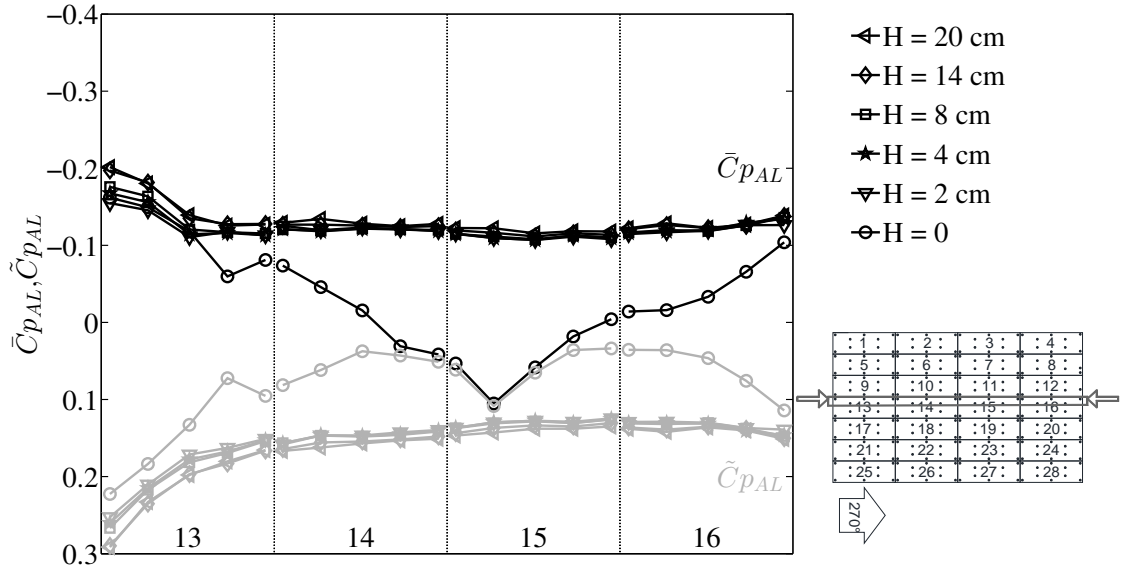


**Figure 6-12: Cavity mean and RMS pressure coefficients measured along the top row of pressure taps on the middle row of modules for the 270° wind direction for the  $G \approx 0$  configurations on the sloped roof**

From the line plots above, the effect of sheltering on interior modules not subject to array-generated flow separation is notable with consistently lower magnitude pressures. These effects are quantified in the next section, separately considering the area-averaged pressures on interior modules not located in the experimentally determined array edge zone.

### 6.4 Wind loading on the interior array zone

With the interior modules sheltered from direct flow their loading patterns differ from those around the perimeter of the array. As such, the effects of  $G$  and  $H$  on interior modules need to be addressed separately. The width of the edge zone was found to be approximately  $\approx 1(H + t)$  to  $2(H + t)$ , less than 1 module in length (Figure 6-13 left). However, since the smallest tributary area relevant for design is a single module the array edge zone was set to be a perimeter of one module around the array for the purpose of determining the pressures on interior modules. This resulted in an interior subset of 10 modules (shown in Figure 6-13 right).

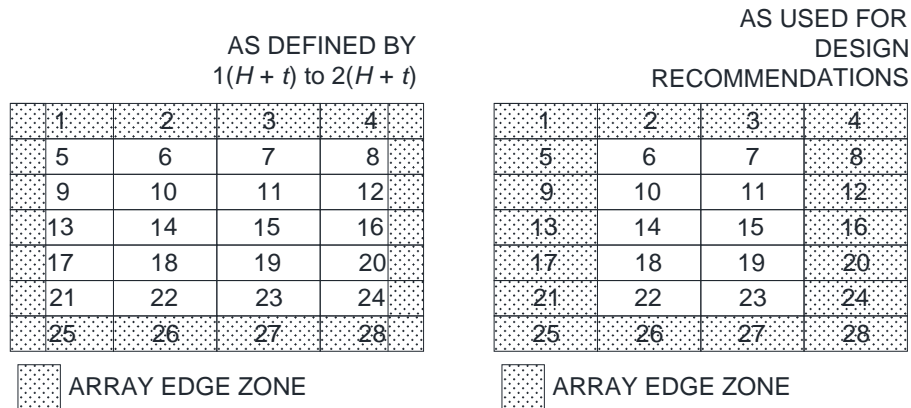


**Figure 6-13: Array edge zone as approximated by  $\approx 1(H + t)$  to  $2(H + t)$  (left) and as used for developing design recommendations (right)**

Pressure coefficients and pressure equalization coefficients from the subset of interior modules are plotted in Figure 6-14 and Figure 6-15. The upper left plots of both figures plot the peak external suctions with respect to  $H$  and  $G$  for the interior subset of single module area-averaging case. There is a marked decrease in the external peak minima

pressure coefficients for the interior modules, indicating the sheltering effect of the perimeter modules (referencing Figure 3-17a and Figure 3-18a). Peak external suction on interior modules are fairly consistent across tested  $H$  values, in contrast to the increasing trend observed when considering the whole array. This indicates that the separation off the array leading edge is sensitive to  $H$  as indicated by the trend of larger magnitude peak suction. However, since the interior modules are not affected by the separation, their peak external suction are largely independent of  $H$ . Figure 6-15a indicates that the interior modules follow the same trends as the overall array with respect to peak minima plotted against  $G$ , yielding a plateau beyond  $G = 4$  cm.

Considering only the interior modules (Figure 6-14b) does not largely alter the magnitude or trend observed for peak cavity suction of the entire array. This indicates that there is negligible sheltering effect for cavity pressures associated with interior modules. This was seen in the line plots where there was no significant edge effects observed for the mean cavity pressures. This signifies that the cavity pressures are not dictated by the boundary flow conditions around the perimeter of the array but reliant on external pressure gradients. Since  $G$  plays a role in setting the external pressure gradients, the trend of larger magnitude cavity pressures with larger  $G$  is also observed when analyzing only the interior modules since they too are impacted by the flow through  $G$  (Figure 6-15b).

Pressure equalization for the interior modules is improved from the values for the whole array, as noted by the lower pressure equalization coefficients,  $C_{eq}$ , in Figure 6-14d. This confirms that the equalization between the external, upper surface and the cavity is more efficient when the modules are sheltered from oncoming flow. When not subjected to localized flow separation and variations around the perimeter of the array the pressures better equalize across the modules. Larger degrees of pressure equalization lead to reduced net wind loading. The beneficial effect of gaps between modules is even more significant when analyzing the interior modules of the array (Figure 6-15d), where smaller  $C_{eq}$  values at higher  $G$  values are evident. This reinforces the notion that gaps between modules are essential for effective pressure equalization across the modules.

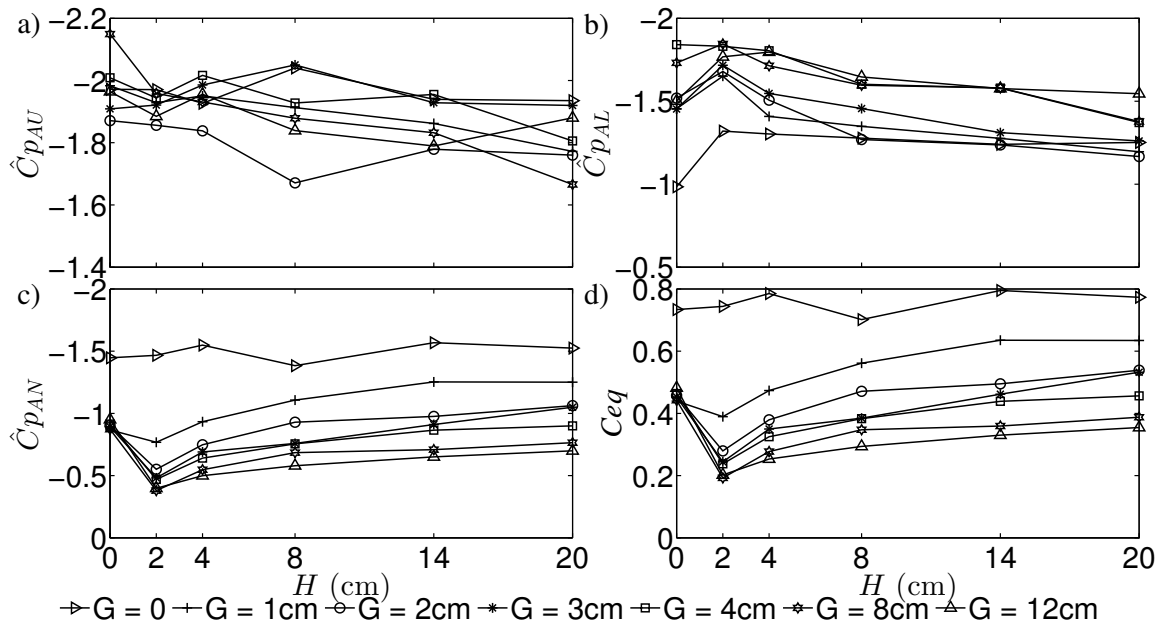


**Figure 6-14:** The worst case values of the peak (suction) (a) external, (b) cavity, and (c) net pressure coefficients, area-averaged over a single solar module and (d) the pressure equalization coefficient ( $C_{eq}$ ) with respect to  $H$ ; considering only the interior modules.

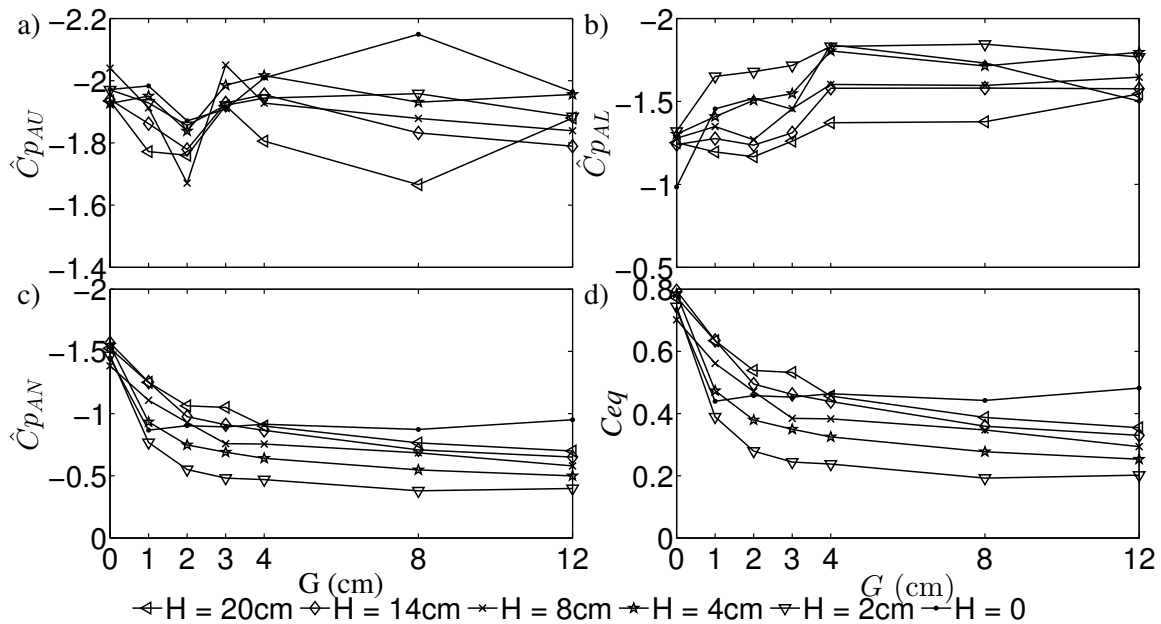


**Figure 6-15: The worst case values of the peak (suction) (a) external, (b) cavity, and (c) net pressure coefficients, area-averaged over a single solar module and (d) the pressure equalization coefficient ( $C_{eq}$ ) with respect to  $G$ ; considering only the interior modules.**

To quantify difference in the degree of pressure equalization for modules under edge effect (perimeter of the array) and those that were sheltered, individual modules were classified as either edge or interior and the pressure equalization coefficient,  $C_{eq}$ , was evaluated for each zone and configuration. The peak net and external area-averaged pressures measured on any individual panel within both the edge and interior zones, for any wind direction were used to evaluate the factors. The normalization using the external area-averaged pressures was done using values measured from the  $G \approx 0$ ;  $H \approx 0$  configuration for the sloped roof and the  $G = 12$  cm;  $H \approx 0$  configuration for the flat roof. It can be noted that for the single module case there are two distinct  $C_{eq}$  curves when the factors are plotted with respect to  $G/H$ ; one for edge module and one for interior modules (Figure 6-16). The factors for the edge modules are higher than those for the interior modules, indicating that the net pressures for edge modules are a higher fraction of the external pressures. This signifies that pressure equalization is more efficient when the

modules are sheltered from oncoming flow as the net pressures are further reduced from the external pressures.

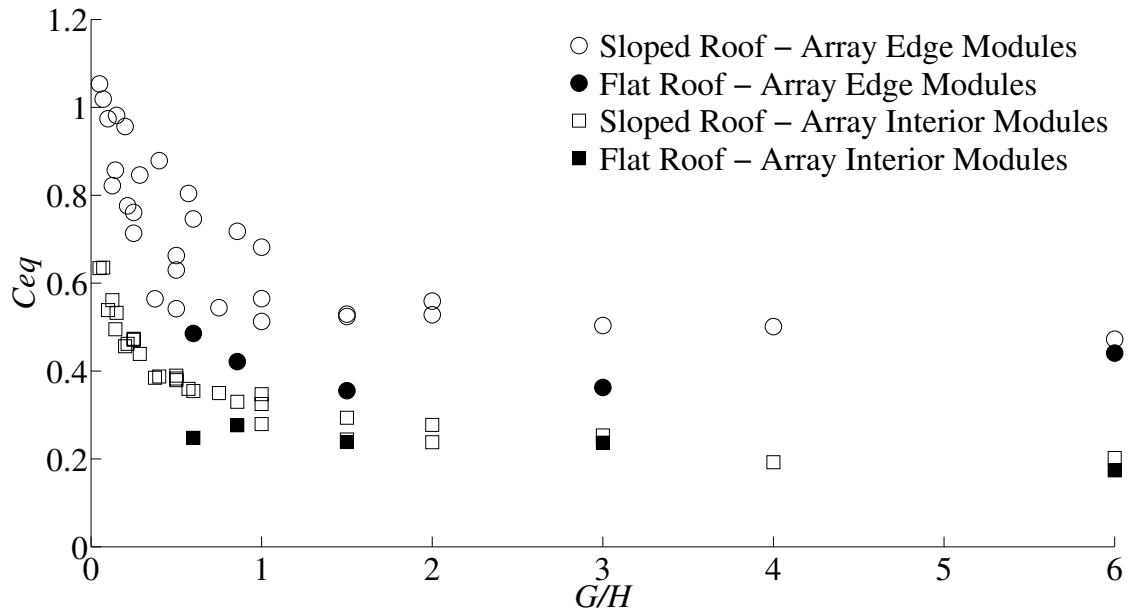


**Figure 6-16: The peak maxima pressure equalization coefficient ( $C_{eq}$ ) for the edge and interior zones for the single module area ( $0.73\text{m}^2$ ) with respect to  $G/H$  for the sloped and flat roof models**

Design wind loads should be developed to distinguish between modules that are subject to array edge effects (around the perimeter of the array) and those that are sheltered. For the current model, array edge zone was quantified from wind directions with reattached flow only, approximating a zone width of  $\approx 1(H + t)$  to  $2(H + t)$ . This was simplified to be a perimeter of a single module around the array as the smallest tributary area used for analysis was a single module. Large pressure equalization coefficients were evaluated in the array edge zone, indicating a lower degree of pressure equalization. Chapter 7 will use the experimentally derived array edge zone dimensions to determine an appropriate factor to account for the higher magnitude pressures from the array-generated flow separation, consistent with  $E$  from SEAOC PV2-2012 (2012). The zone width was assessed from wind directions where the flow had reattached to the roof to ensure that the separation effects were not contaminated by the building-generated flow separation. The

effects from the building-generated flow separation, or roof edge effects, as well as appropriate dimensions for the roof zones are addressed in the next section.

## 6.5 Determination of applicable roof zones

As previously stated, with the array having been tested in a single location on the roof, it is not possible to fully separate the roof zone and array zone effects on wind loads for certain modules and wind directions. For instance modules 1 through 4 on the flat roof are adjacent to the long dimension of the model and are considered windward for a quartering wind at  $45^\circ$  (see Figure 6-1). These modules are located in either the corner roof zone (#4) or edge zone (#1-3) as defined by ASCE 7-10 (2010) but also in the array edge zone as determined in the previous section. Their peak pressures are influenced by both their location on the roof (near the edge) and their position within the array (around the perimeter and unsheltered for the given wind direction). To study the applicability of the established bare-roof design zones, the peak net pressure coefficients,  $C_{pN}$ , were evaluated for each zone.

Each module is categorized based on its position and associated roof zone. When a module crosses multiple zones, the zone in which the majority of the module rests is used for analysis. The peak net pressure, area-averaged over an individual module, measured in each zone as well as the pressure equalization coefficient evaluated for each zone are plotted in Figure 6-17. For small  $H$  the largest suction net pressures were measured on modules in the corner zone. The location of the largest suctions moved to the edge zone for larger cavity heights ( $H \geq 8$  cm). This can be visualized in Figure 6-18 where the largest net suction for each module for the  $G = 12$  cm;  $H = 20$  cm configuration is shown on the left schematic (a). Neglecting the  $H \approx 0$  configuration, which has little significance for design as commercial systems require some cavity for cooling the modules, the largest value occurred not on the corner (zone) module, but adjacent to it. This indicates that the corner zone, as defined for the bare-roof design, is inappropriate for solar modules mounted parallel to roof surfaces as the peak net pressures were measured outside the zone. This is consistent with the findings of both Kopp (2013) and Banks (2013) who observed that for tilted arrays on flat roofs, the zones established in

design standards for bare-roof design are not appropriate – corner zones are not necessary, but existing bare-roof edge zones may be too small. A roof edge zone around the perimeter of the roof surface could adequately account for the larger magnitude net pressures associated with separated flow. The next step is to determine the appropriate width of the proposed edge zone as peak loads may occur further into the roof than accounted for in existing bare-roof standards.

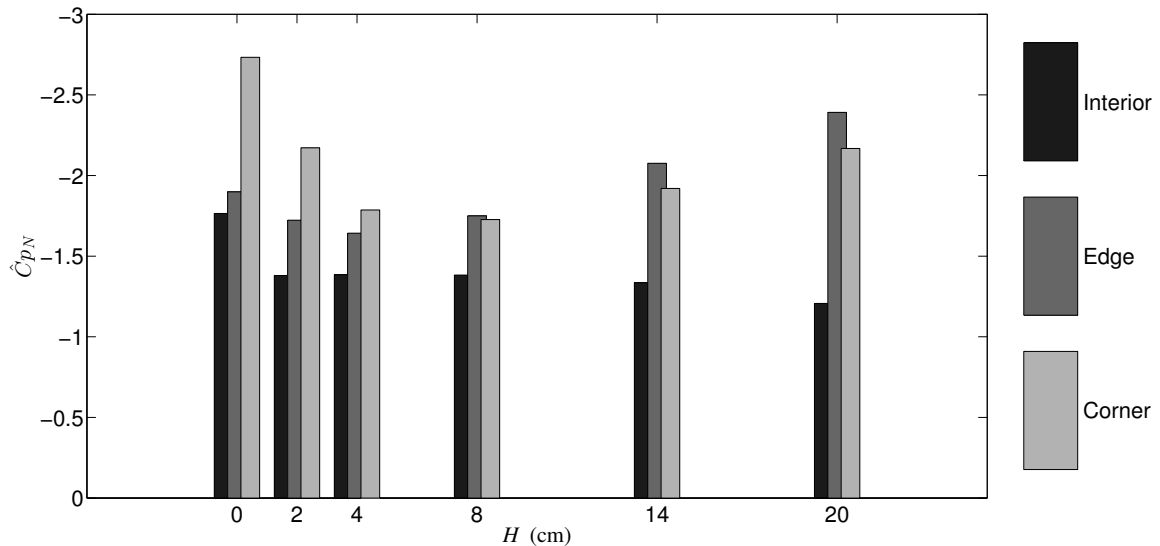


**Figure 6-17: Peak net (suction) pressure coefficients with respect to  $H$  measured in each roof zone on the flat roof model ( $G = 12$  cm)**

The spatial distribution of the peak suction is important to know when setting the width of the roof edge zone. The zone needs to be of sufficient dimensions to contain all modules which are likely to experience larger magnitude loads due to the building generated flow field. The peak net suction on each module, regardless of wind direction are plotted for the flat roof  $G = 12$  cm;  $H = 20$  cm  $G = 12$  cm;  $H \approx 0$  configurations in Figure 6-18. It can be noted that higher magnitude peak net suction are observed on the upper two rows of modules and the right-most column. These modules would experience a flow field that has been disturbed by the separated flow off the building edges. The roof edge zone should be set to account for the increased pressures associated with these edge modules. It should be noted that the bottom row of modules (near the field of the roof) also experience elevated wind loading but to a lesser degree. This is because those

modules experience array edge effects but not building edge effects.

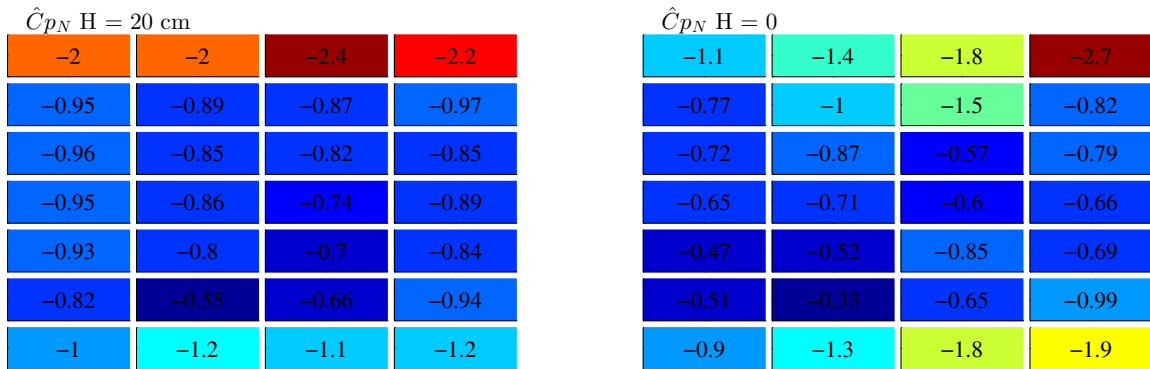


**Figure 6-18: The peak net (suction) coefficient measured on each module for the  $G = 12 \text{ cm}$ ;  $H = 20 \text{ cm}$  (left) and  $G = 12 \text{ cm}$ ;  $H \approx 0$  (right) configurations on the flat roof model**

Since the wind loading on roof-mounted solar modules is largely influenced by building aerodynamics the archetype and dimensions of the building play a significant role in determining the dimensions of the roof zones. Further, there is significant variation in the roof zone dimensions established in design standards and literature. Roof edge zone widths were evaluated for the flat roof model dimensions based on the prescribed procedures or values in ASCE 7-10 (2010), SEAOC PV2-2012 (2012) and Kopp (2013). The width of the zone is in Table 5 and sketched in Figure 6-19.

**Table 5: Roof edge zone widths from design standards and literature for flat roof model**

	Roof zone width (full scale metres)
ASCE 7-10, not less than 0.9 m	0.9
SEAOC PV2-2012, $h$	6
Kopp, $0.6h$ (lower end of range for $5^\circ$ tilt)	3

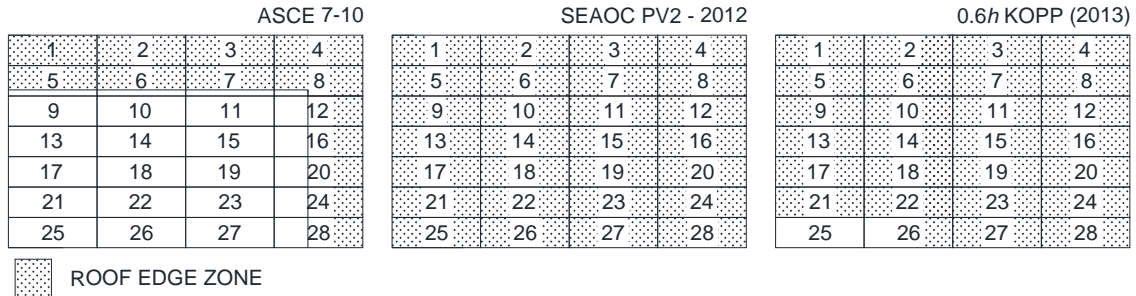


**Figure 6-19: Roof edge zones as defined by existing design standards and literature**

While the roof zone width as determined by ASCE 7-10 (2010) is the smallest zone width based on existing code and literature, it is shown to best match the observed peak net loading patterns. The larger roof edge zones were developed using data from tilted arrays which have a higher profile in the flow field and are typically mounted on buildings with significantly larger plan dimensions. It is likely that edge zone dimensions based on the code developed for bare-roofs is most applicable as parallel-mounted modules are more similar to a flat roof surface than tilted modules which have a higher profile and further disturb the flow field. This indicates that established cladding and coefficients edge zone is sufficient; however, it should be recommended that any modules that cross the boundary between edge and interior should be classified as edge. Since the corner zone is not required, the edge zone should extend around the perimeter of the roof and can be dimensioned based on the guidelines in ASCE 7-10 (2010).

## 6.6 Effects of the shroud

Ideally wind tunnel tests would have been performed with the array mounted in multiple positions on the roof to investigate the array zones at multiple roof locations.

Unfortunately, this was not feasible due to the large number of configurations that would have to be repeated for comparison, considering not only wind tunnel operational time, modifications to the model and computational time for the results. To study the array without the influence of boundary conditions directly impacting the cavity, a shroud was installed around the array to prevent air from directly entering the cavity. This effectively simulated that all modules within the array were interior modules, located far enough into the interior of the array that the flow in the cavity was unaffected by external

flow. The shroud was taped in place and while this did not result in a perfect seal, it was adequate to severely limit the flow directly entering the cavity. Comparisons of the pressure equalization coefficient, the mean net suction, mean external suction and mean cavity suction for the open and shrouded  $G = 12; H = 20$  cm and  $G = 12; H = 2$  cm configurations on the flat roof are plotted below. Module labels are included to get a spatial sense of where the shroud has influenced the results. The plots are square with the open case on the bottom and the shrouded on the left. The  $45^\circ$  line is plotted for reference; if the data follow this line there is no significant impact from the shroud. Values to the left of the line indicate that the shrouded value is larger than the open case, with the opposite true of points to the right of the line.

Overall the shroud improves pressure equalization as indicated by lower magnitude  $C_{eq}$  values. When installed with a large cavity the shroud is also noted to increase the mean externals and significantly increase the mean cavity pressures (Figure 6-21). Since the cavity pressures were increased more than the externals, the shrouded mean net suction are typically lower in magnitude than those measured on the modules of the open array (Figure 6-20 right). This is especially true for the top row of modules (#1-4) for the large cavity. Recall that for the open array the net pressures for these modules are dominated by strong external pressure gradients and positive pressurization of the cavity (seen in the contours of Figure 3-24). The shroud reduced the external pressure gradients and largely eliminated the positive pressurization of the cavity which can be seen in a side-by-side comparison of the mean externals and mean cavity pressures (over all wind directions) for the open (Figure 6-22a and Figure 6-23a) and the shrouded array (Figure 6-22c and Figure 6-23c). This indicates that installing a shroud around the array may be an effective way to avoid punitive loading conditions, increase pressure equalization and in turn reduce the net wind loading on the array.

It should be noted that the shroud can also cause unfavourable loading conditions for certain modules. For the large cavity ( $H = 20$  cm) modules along the bottom row of the array (#25-28), adjacent to the field of the roof, have larger pressure equalization coefficients indicating that the net pressure is a large portion of the external pressure, as noted Figure 6-20. The cause of this is not clear when examining the mean pressures, as

it is caused by an increase in the magnitude of the peak pressures which dominate the design pressures but do not significantly alter the mean when evaluated over a large time series. The peak suctions are caused by flow separated off the now blunt (and relatively tall) edge of the array. The shroud restricts the flow from going under the module, resulting in larger peak uplift on the external, upper, surface.

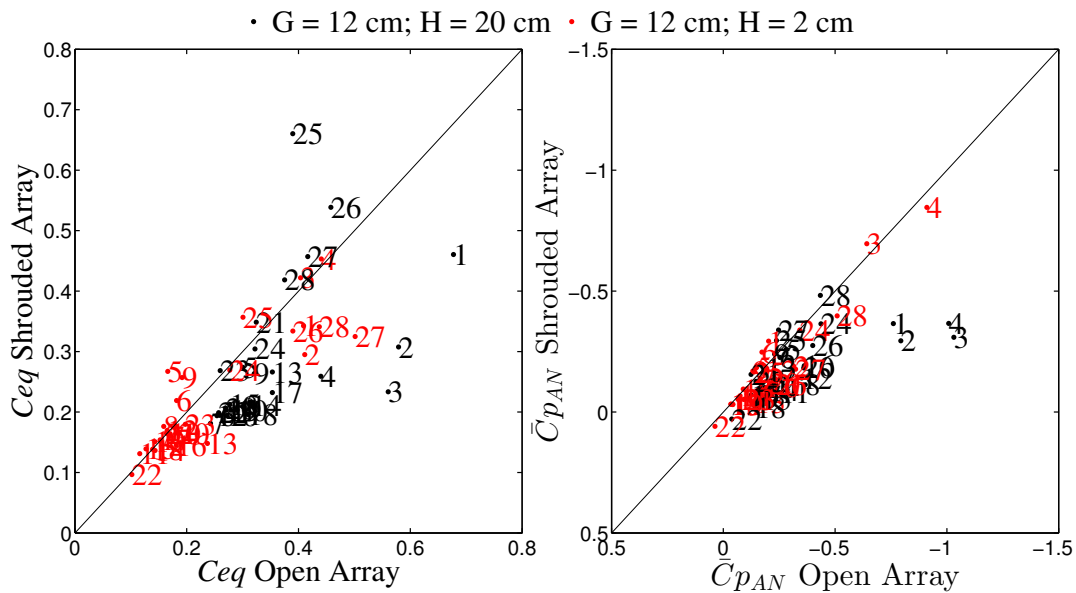


**Figure 6-20: The pressure equalization coefficient (left) and the mean net pressure coefficient (right) for open and shrouded array for  $G = 12$ ;  $H = 20$  cm and  $G = 12$ ;  $H = 2$  cm on the flat roof model**

The effect of the shroud is less significant for the smaller cavity. This is indicated by the mean external and cavity pressures plotted in red in Figure 6-21 which largely follow the 45° line. The minimal effect on cavity pressures is likely due to the fact that the flow resistance was already high for the smaller cavity in the open array. Surrounding the array with a shroud when the flow resistance is already high will have a smaller effect than if the flow resistance was lower, as in the case of a larger  $H$ .

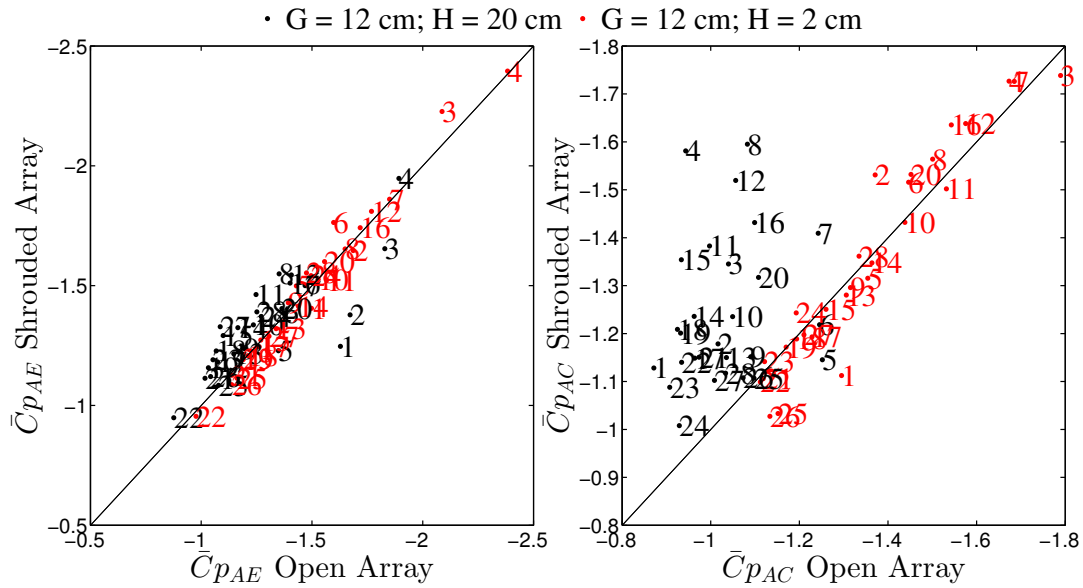


**Figure 6-21: The mean external (left) and the mean cavity (right) pressure coefficient for open and shrouded array for  $G = 12$ ;  $H = 20$  cm and  $G = 12$ ;  $H = 2$  cm on the flat roof**

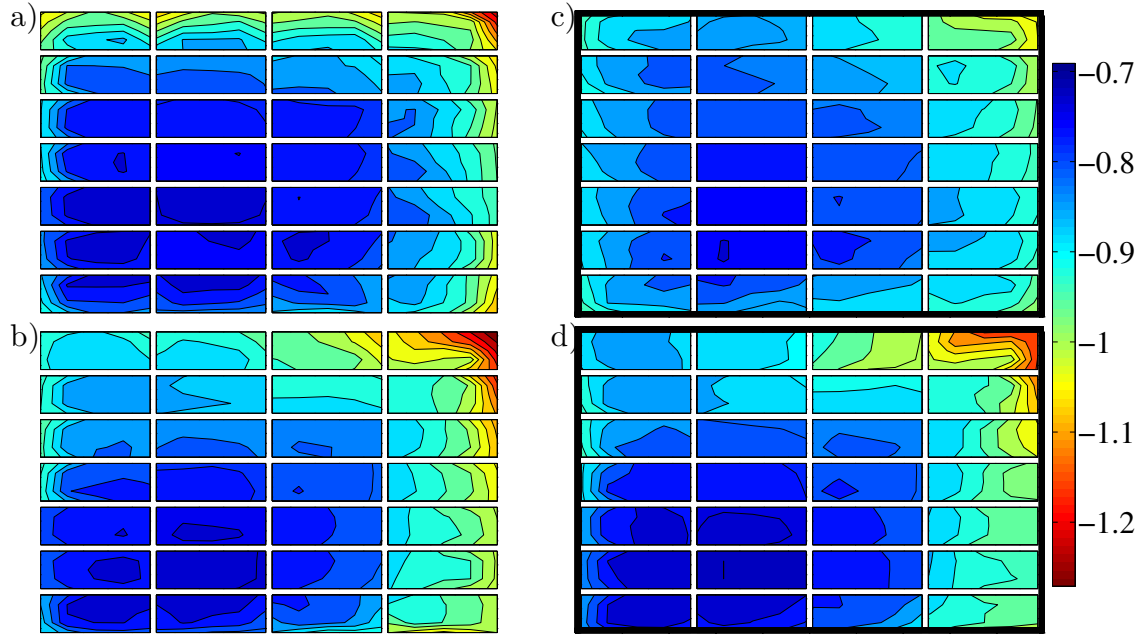


**Figure 6-22: Mean external point pressure contours for the a)  $G = 12$  cm;  $H = 20$  cm open array, b)  $G = 12$  cm;  $H = 2$  cm open array, c)  $G = 12$  cm;  $H = 20$  cm shrouded array and d)  $G = 12$  cm;  $H = 2$  cm shrouded array on the flat roof model**

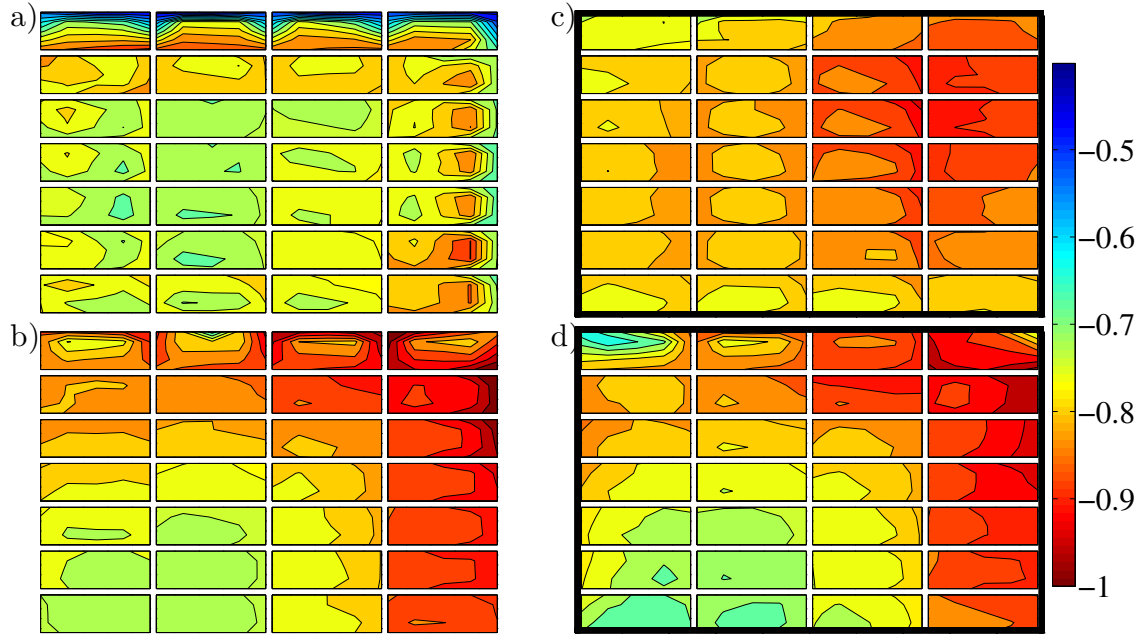


**Figure 6-23: Mean cavity point pressure contours for the a)  $G = 12$  cm;  $H = 20$  cm open array, b)  $G = 12$  cm;  $H = 2$  cm open array, c)  $G = 12$  cm;  $H = 20$  cm shrouded array and d)  $G = 12$  cm;  $H = 2$  cm shrouded array on the flat roof model**

For the current model the shroud was placed around the array to restrict flow into the cavity and simulate modules under no array edge effects. However, the shroud was found to alter the external pressure gradients as shown in the figures above. The definition of array edge effects used herein covers the effect of flow separation off the leading edge module. As such, it is possible that the effect could be largely minimized (if not eliminated) by designing an aerodynamic shroud such that there is no flow separation off the array, sketched in Figure 6-24. If array edge effects could be minimized and the array was placed in the interior of the roof, away from roof edge effects, the peak wind loads could be significantly reduced, especially for modules around the perimeter of the array.

## 6.7 Summary

The current dataset was used to determine appropriate dimensions for both array edge zones and roof edge zones. The array edge zone was found to be approximately  $\approx 1(H + t)$  to  $2(H + t)$  wide around the perimeter of the module. When classifying modules according to their position within the array, any module of which a portion is located in the edge zone is classified as such. For the current model this resulted in a subset of 10 interior modules. A shroud was placed around the array for selected configurations and was found to alter the external pressures as well as prevent flow from directly entering the cavity. It is possible that the array edge effect could be largely eliminated if the array were surrounded by a shroud designed to prevent flow separation around the leading edge of the array. Additional studies are recommended to confirm this hypothesis and assess any possible simplifications for codification. The roof zone dimensions set out by ASCE 7-10 (2010) for (bare) low-rise roofs were found to be sufficient to account for the higher magnitude pressures from building-generated flow separation for arrays mounted parallel to the roof surface with one notable change; corner zones were found to be unnecessary due to the change in aerodynamics caused by the installation of the array. The next chapter focuses on using these zones to develop design recommendations for roof-mounted solar arrays in the form of a multiplication factor to be applied to external pressure coefficients found in current design standards.

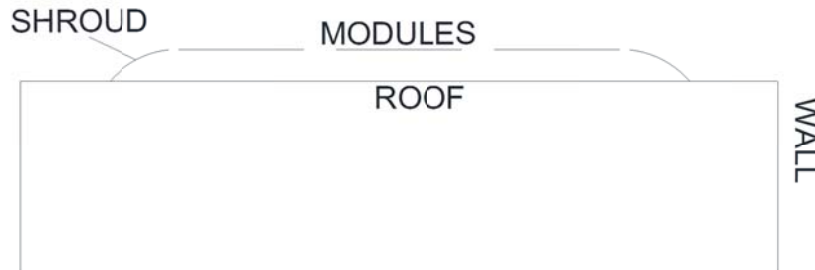


**Figure 6-24: Schematic of potential aerodynamic shroud to mitigate array edge effects**

## 7 Development of design guidelines

The proposed design recommendations for solar modules mounted parallel to low-rise roofs presented herein take advantage of the cladding and components design loads in existing design standards such as ASCE 7-10 (2010). Multiplication factors are presented to account for the change in net wind pressures due to pressure equalization, roof edge effects and array edge effects. This approach was taken to utilize the established knowledge base regarding bare roof loads which is already captured by design standards and to ease the integration into those same standards. This approach was chosen over developing specific standards for each building code, as the proposed factors can be applied to any design standard for installations similar to those tested in the wind tunnel. The approach of developing a multiplication factor to apply to the external components and cladding design pressures is consistent with the that taken in NEN 7250 (2013), a design code for roof and wall-mounted solar installations. The suitability of presenting design recommendations in this fashion is justified by the results presented in chapters 5 and 6.

The multiplication factor to account for the effects of pressure equalization is based on experimental  $C_{eq}$  values. It is presented as a function of tributary area and represents the combined effects of the module's position on the roof and within the array and has been designated  $\gamma$ , where

$$\gamma = \gamma_R \gamma_E \tag{12}$$

where  $\gamma_R$  is the roof zone factor, and  $\gamma_E$  the array zone factor. The roof zone factor is a multiplication factor expressed as a function of tributary area and specific to the (bare) roof zones established by ASCE 7-10 (2010). Their roof zone specifications were noted to be sufficient size to capture the roof edge effects in chapter 6 with the omission of corner zones. To maintain consistency with ASCE 7-10, the interior of the roof is

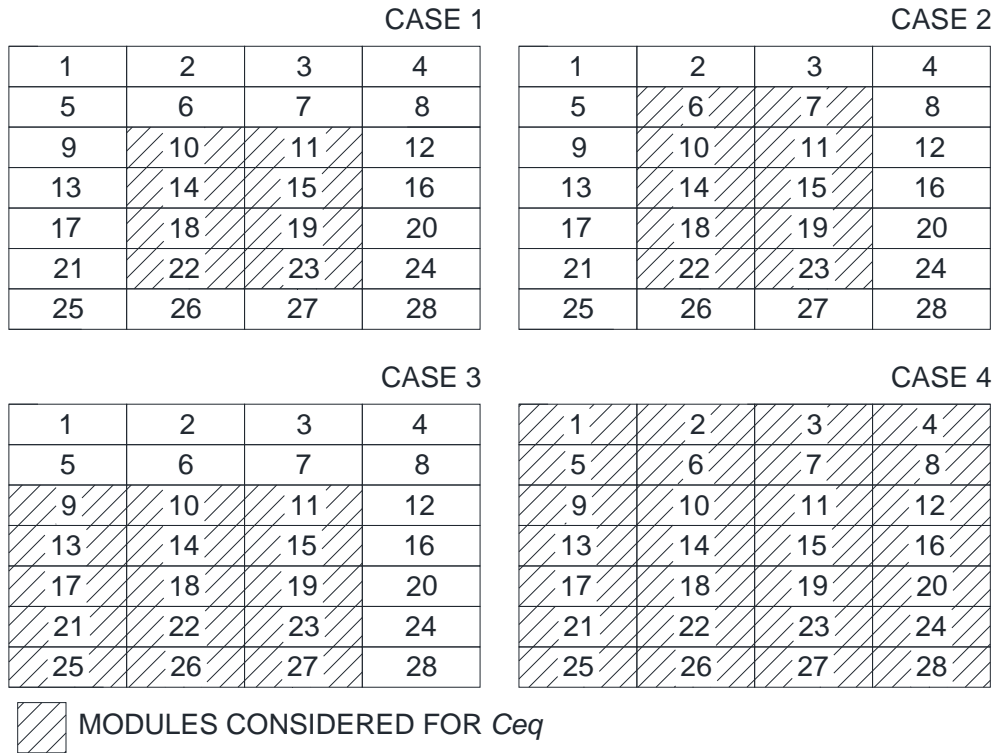
designated as roof zone ① and the edge zone as roof zone ②. The array edge zone was determined to be approximately  $1(H + t)$  to  $2(H + t)$ , simplified to be a perimeter of 1 module around the current array. The array edge factor herein has been presented as a straight multiplication factor from a table to be applied to  $\gamma_R$  or graphed with respect to tributary area as composite  $\gamma_R\gamma_E$  multiplication factor (where  $\gamma$  can be read directly off the graph). The array zone effect by definition has a value of  $\gamma_E = 1$  for modules in the interior of the array. To quantify these factors each module was classified based on its roof zone and array zone. When considering combinations of modules, if a single module was in either edge zone the combination was classified as edge. Since it is not possible to explicitly separate the roof and array edge effects, multiple cases were considered to try to quantify their impact as accurately as possible. A summary of the considered cases is noted in Table 6.

**Table 6: Analysis cases representing combinations of array and roof zones considered for the development of the roof zone factor,  $\gamma_R$ , and the array zone factor,  $\gamma_E$**

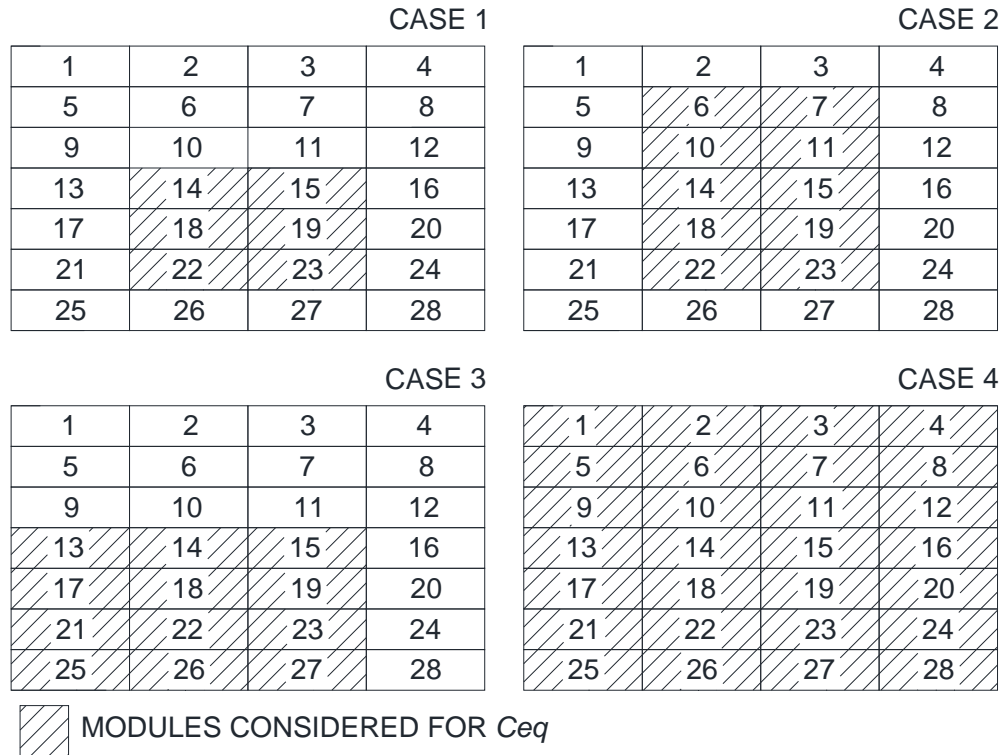
	Array Zone	Roof Zone	Factor of interest
Case 1	Interior	Interior	$\gamma_R$ for roof zone ①
Case 2	Interior	Edge	$\gamma_R$ for roof zone ②
Case 3	Edge	Interior	$\gamma_E$ for roof zone ①
Case 4	Edge	Edge	$\gamma_E$ for roof zone ②

Case 1 was used to determine the appropriate multiplication factor for modules in the interior of the roof and in the interior of the array. Case 2 also considers modules in the interior of the array, but adds the modules located in roof zone ② (still neglecting modules around the perimeter of the array). Establishing separate  $C_{eq}$  vs  $A$  curves for different roof zones is consistent with the approach taken by SEAOC PV2-2012 (2012) and accounts for the roof zone effects on the interior modules of the array. Case 3 builds on case 1 but also encompasses modules around the perimeter (edge zone) of the array

(but not in the roof edge zone). This allows for the determination of changes in  $C_{eq}$  as a result of the array edge effects from wind directions associated with reattached flow on the roof. Case 4 considers all modules within the array and thus leads to the determination of an appropriate factor based on  $C_{eq}$  for both array and roof edge effects. Array interior modules were still considered in Case 3 and 4, even though the factor of interest was  $\gamma_E$ ; larger tributary areas were often a combination of array edge and array interior modules with the combination classified as array edge if any module within the combination was in the array edge zone. A schematic of the modules used in each case is shown in Figure 7-1 for the flat roof model and Figure 7-2 for the sloped roof model. The applicable modules in the cases differ for the flat and sloped roof models as the roof edge zone as defined by ASCE 7-10 (2010) is based on the eave height for the flat roof model and the mean roof height for the sloped roof model. This results in a zone width of 0.9 m for the flat roof model, covering two rows along the building edge and 1.23 m for the sloped roof model, covering three rows of modules.



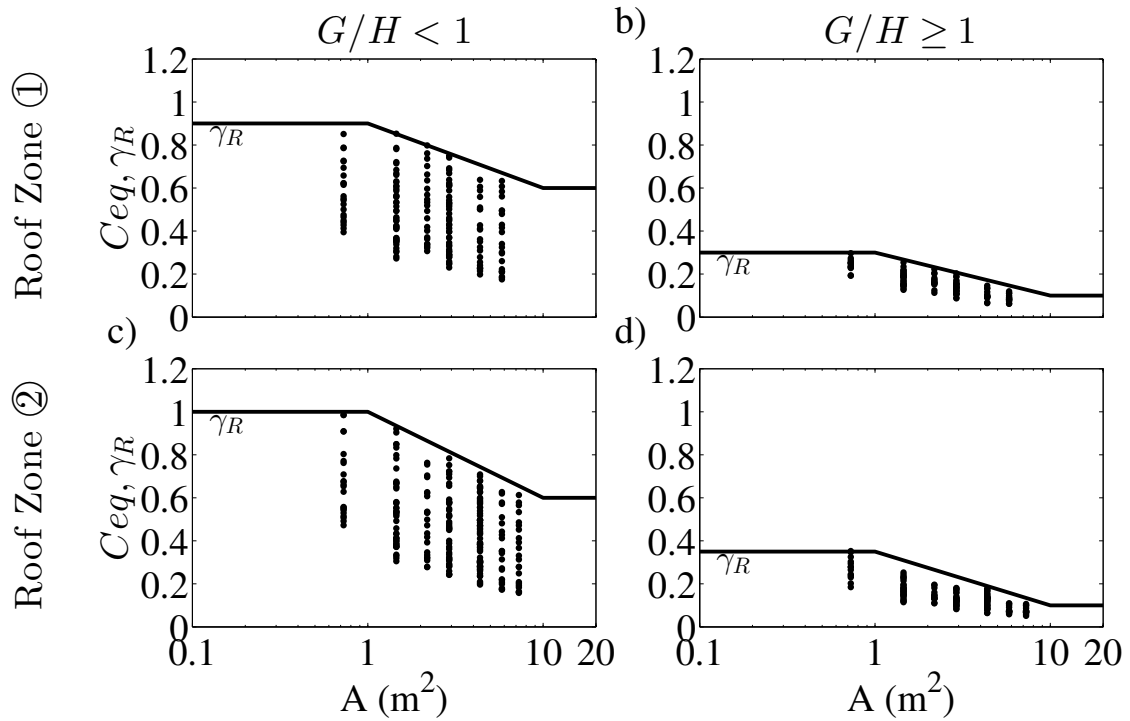
**Figure 7-1: Schematic of modules used to evaluate the pressure equalization coefficient for the different array and roof zone cases considered for design for the flat roof model**



**Figure 7-2: Schematic of modules used to evaluate the pressure equalization coefficient for the different array and roof zone cases considered for design for the sloped roof model**

To account for the higher degree of pressure equalization of systems with  $G/H \geq 1$ , those configurations were handled separately, yielding a total of four  $\gamma_R$  vs tributary area graphs; for roof zones ① and ②, and for  $G/H < 1$  and  $G/H \geq 1$ . Individual  $C_{eq}$  values were evaluated for each configuration and tributary area and are plotted for case 1 in Figure 7-3a for  $G/H < 1$  and Figure 7-3b for  $G/H \geq 1$ . The  $C_{eq}$  values case 2 are plotted in Figure 7-3c and Figure 7-3d. These values have a significant spread, representing the extents of parameters tested.  $\gamma_R$  recommendations are plotted as the solid lines in Figure 7-3 and were determined by enveloping the  $C_{eq}$  values. Enveloping the worst case value for a specific tributary area to develop design recommendations has been used in the past (i.e., Stathopoulos et al., 2000) and was in chapter 1. These lines (and those in subsequent figures) were set to encompass the majority of experimental results. The current dataset, while extensive in terms of the number of configurations tested, is still

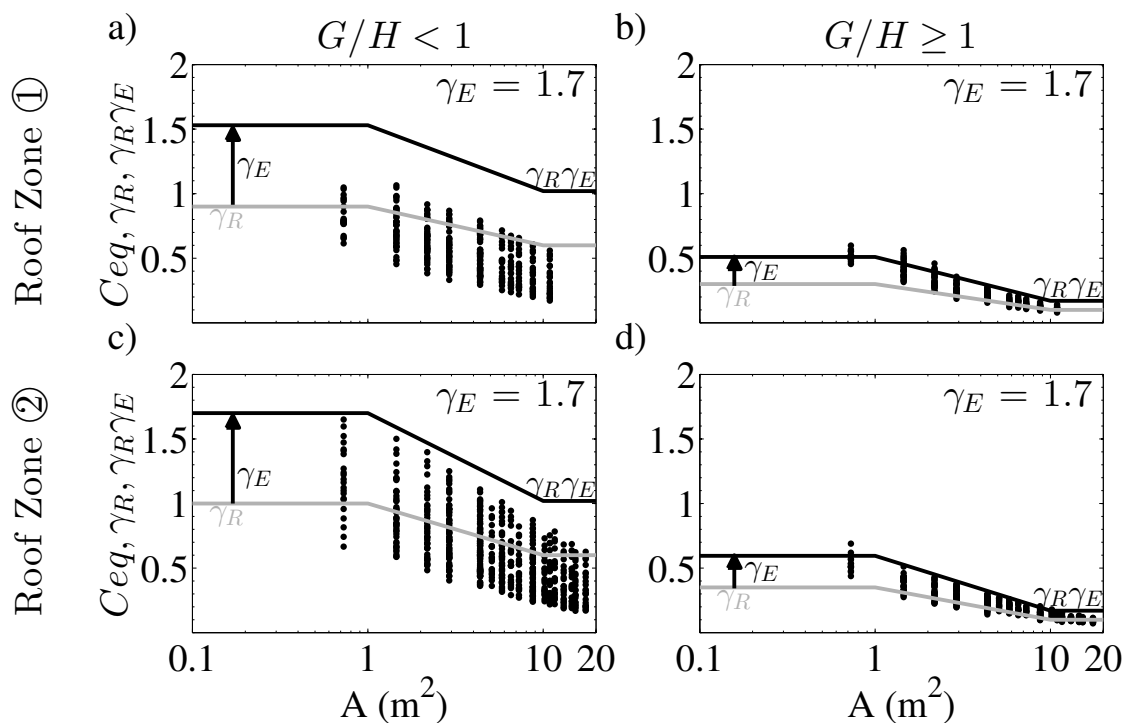
small for the purpose of developing design recommendations. As such, any recommendations should encompass the experimental data to ensure that proposed recommendations are conservative in nature. However, they must also strike a balance and not be overly punitive if based only on the highest experimental values. The shape of the curve, linear up to approximately 1 m<sup>2</sup>, linearly decreasing up to 10 m<sup>2</sup> and then linear is set to be consistent with those in ASCE 7-10 (2010) (except where noted). As such, when the  $\gamma_R$  (and  $\gamma_R\gamma_E$ ) curves are based solely on the highest experimental values they can be overly conservative, notably for larger tributary areas, when restricted to have the flat-linear-flat shape. Thus the proposed design recommendations have been established to “best” envelope the majority of the experimental results, which could perhaps result in a small number of outliers above the established curve. This can be seen in Figure 7-5 at small tributary areas and also in the work of Stathopoulos et al. (2000). While there can be some discussion regarding further refinement of the proposed  $\gamma_R$  and  $\gamma_R\gamma_E$  values herein, they are presented as recommendations, based on the current research, for the purpose of discussion.



**Figure 7-3: Pressure equalization coefficients with respect to tributary area and design factor  $\gamma_R$  for a) roof zone 1 and  $G/H < 1$ , b) roof zone 1 and  $G/H \geq 1$ , c) roof zone 2 and  $G/H < 1$ , d) roof zone 2 and  $G/H \geq 1$**

Figure 7-4 has the  $\gamma_R$  recommendations plotted in grey with  $C_{eq}$  values from cases 3 and 4. Since the only difference is the addition of the modules under array edge effects, the change in  $C_{eq}$  can be attributed to the effects of the array-generated flow separation. The increase in  $C_{eq}$  values is used to determine an appropriate multiplication factor to account for array edge effects,  $\gamma_E$ . The  $C_{eq}$  from modules in both the array edge zone and roof zone ① (interior) are plotted in Figure 7-4a and Figure 7-7b for  $G/H < 1$  and  $G/H \geq 1$  respectively. Values from the entire array (including array and roof edge zones) are plotted in Figure 7-4c for  $G/H < 1$  and Figure 7-7d for  $G/H \geq 1$ . It should be noted that the combined array and roof edge zone effects can result in pressure equalization coefficients that are greater than 1, signifying that the net pressures were larger in magnitude than the externals. This loading condition was previously discussed and is only seen in small tributary areas and can be avoided if the modules are set back from the roof perimeter, out of the edge zone. To account for the array edge effects a single

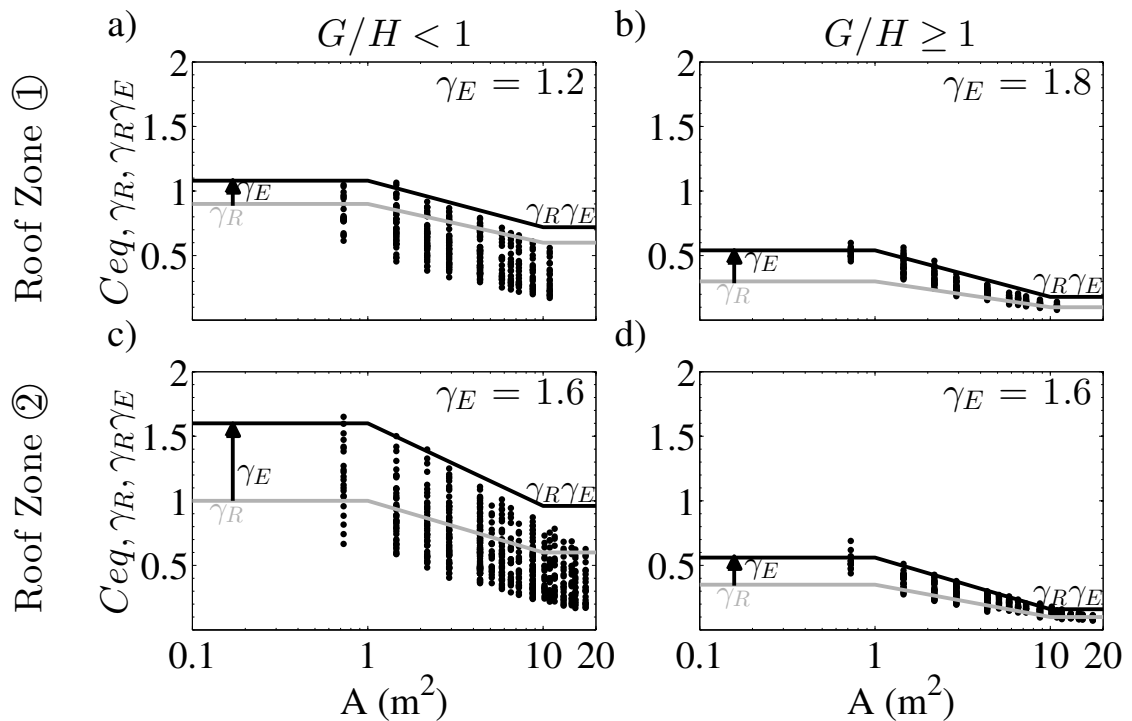
multiplier,  $\gamma_E = 1.7$ , was applied to the  $\gamma_R$  recommendations (in grey), yielding the solid black line for the combined effects of  $\gamma_R \cdot \gamma_E$ . This is the simplest approach, as a single value is given as  $\gamma_E$ ; however, it can be observed that this results in overly conservative design values for modules in the array edge zone and roof zone ① with  $G/H$  (Figure 7-4a) and potentially underestimate values for the same array edge zone and roof zone ① with high  $G/H$  (Figure 7-4b). While a single  $\gamma_E$  value may be the simplest approach, it may not be the most appropriate. A potential source of refinement is to employ a separate  $\gamma_E$  for each case (or subplot) in Figure 7-4.



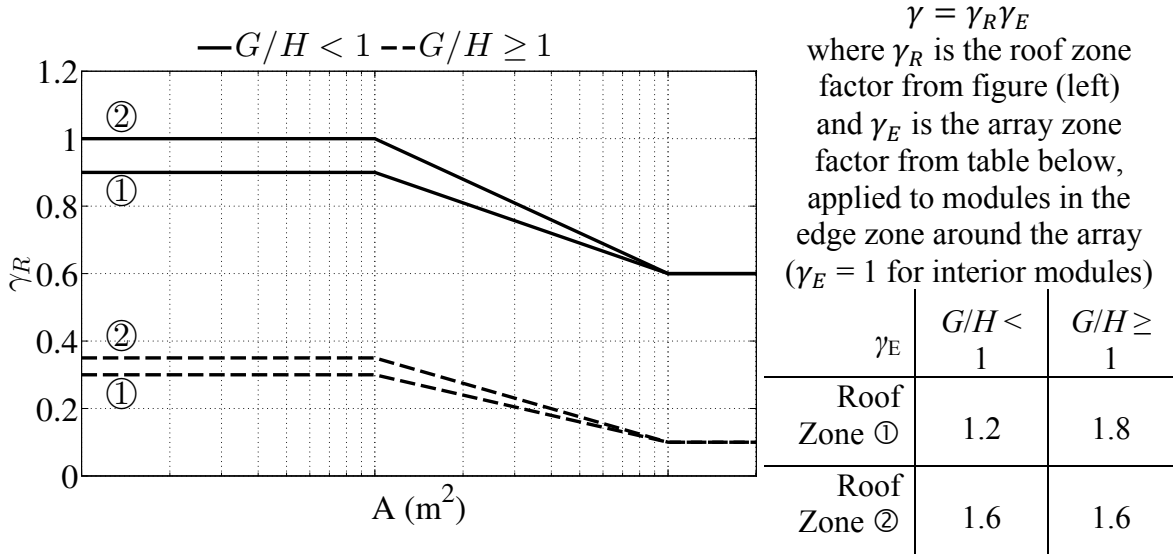
**Figure 7-4: Pressure equalization coefficients with respect to tributary area and design factors  $\gamma_R$  and  $\gamma_R \cdot \gamma_E$  where  $\gamma_E$  is a single value for a) roof zone 1 and  $G/H < 1$ , b) roof zone 1 and  $G/H \geq 1$ , c) roof zone 2 and  $G/H < 1$ , d) roof zone 2 and  $G/H \geq 1$**

Figure 7-5 contains the same  $C_{eq}$  values from Figure 7-4, however, the  $\gamma_E$  has been refined to be specific to the case (subplot) with the values shown in the upper right of each plot. When refined in this situation  $\gamma_E$  ranges in value from 1.2 to 1.8 and better envelope the experimental data. These design recommendations could be presented in a design standard with a  $\gamma_R$  vs  $A$  plot and a table for  $\gamma_E$ , as shown in Figure 7-6. While this

approach better envelopes the experimental data, there are still possible areas for further refinement, especially for large tributary areas as seen in Figure 7-5a and Figure 7-5c. This is because the array edge effect is not linear with tributary area, with the effect being largely reduced for large areas. To account for this, specific  $\gamma_R \cdot \gamma_E$  design lines are plotted as dashed lines in Figure 7-7.



**Figure 7-5: Pressure equalization coefficients with respect to tributary area and design factors  $\gamma_R$  and  $\gamma_R \cdot \gamma_E$  where  $\gamma_E$  is a separate value for a) roof zone 1 and  $G/H < 1$ , b) roof zone 1 and  $G/H \geq 1$ , c) roof zone 2 and  $G/H < 1$ , d) roof zone 2 and  $G/H \geq 1$**



**Figure 7-6: Possible design figure to evaluate  $\gamma_R$  and table to determine  $\gamma_E$**

The same experimental  $Ceq$  values from Figure 7-4 and Figure 7-5 are plotted in Figure 7-7. The roof zone factor,  $\gamma_R$ , is plotted in grey for reference. Instead of using a multiplication factor to account for the array edge effects which is applied to  $\gamma_R$  as applicable to yield a  $\gamma_R \cdot \gamma_E$  curve, the experimental data is enveloped directly, regardless of the shape of the  $\gamma_R$  curve. This takes advantage of the lower  $Ceq$  values at large  $A$ , regardless of array zone. Both the  $\gamma_R$  and  $\gamma_R \cdot \gamma_E$  curves would have to be plotted for design standards as  $\gamma_E$  is no longer expressed as a straight multiplication factor. A potential figure for inclusion in a design standard is Figure 7-8.

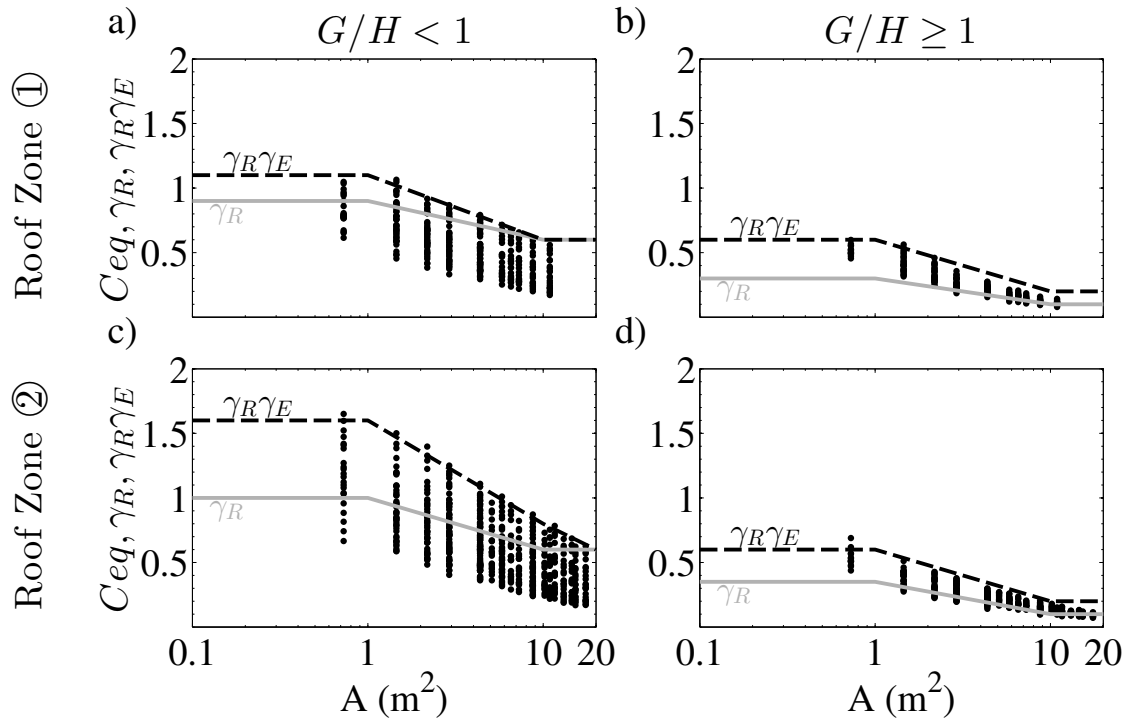


**Figure 7-7: Pressure equalization coefficients with respect to tributary area and design factors  $\gamma_R$  and  $\gamma_R \cdot \gamma_E$  for a) roof zone 1 and  $G/H < 1$ , b) roof zone 1 and  $G/H \geq 1$ , c) roof zone 2 and  $G/H < 1$ , d) roof zone 2 and  $G/H \geq 1$**

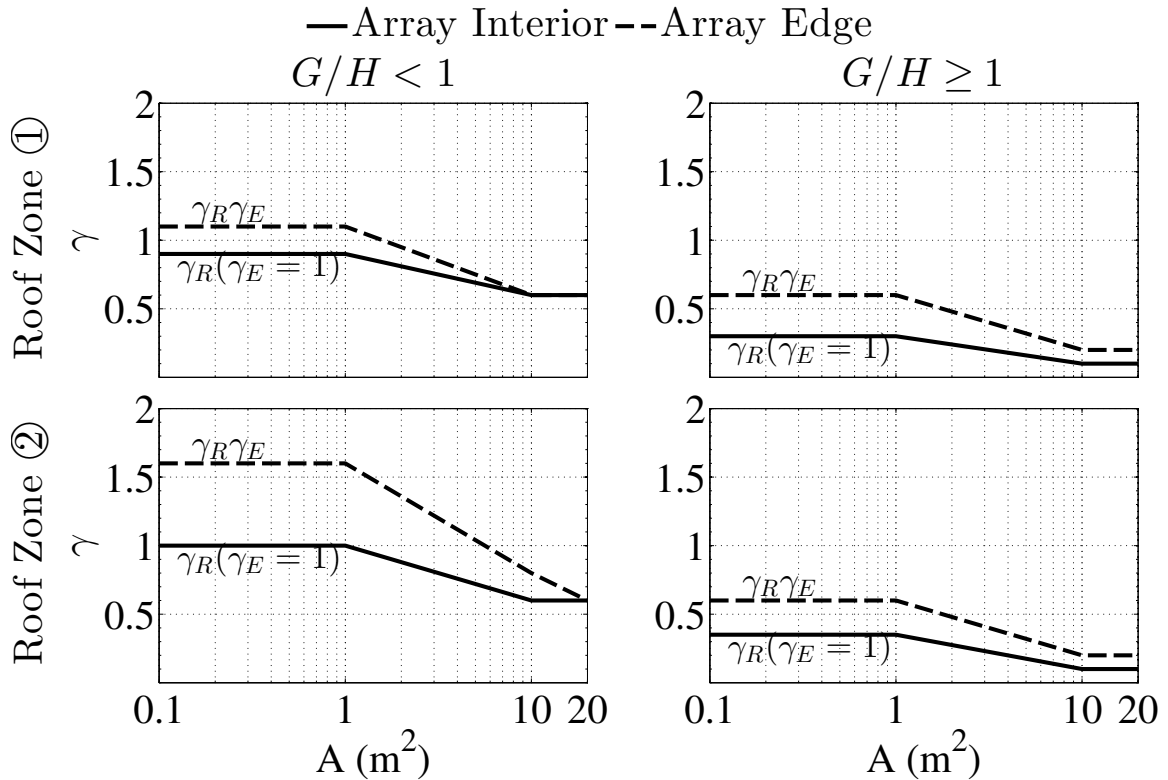


**Figure 7-8: Design factor,  $\gamma$ , for solar installations mounted parallel to roof surfaces of low-rise buildings to be applied to the external pressure coefficient from the components and cladding procedure in existing design standards**

For the current dataset Figure 7-8 represents the most refined design recommendations possible. Future studies are recommended to better separate the roof and array edge effects by testing the module in multiple locations (various setbacks from the roof edge). SEAOC PV2-2012 (2012) notes that there is a range of setback for which there is only roof edge effects acting on the perimeter of the array. This is due to a situation where the building-generated flow separation is impacting the array, but the flow has not reorganized sufficiently to produce significant loading along the perimeter (leading edge) of the array from array-induced separation. Developing an array edge factor similar to their  $E$ , which is dependent on the setback from the building edge, is likely a more effective and appropriate approach, however, it is beyond the scope of the current investigation. Additional studies are recommended to further separate the roof edge effects from the array edge effects. In the meantime, the design factor,  $\gamma$ , presented in

Figure 7-8 could be considered for inclusion in future design codes to be applied to their external pressure coefficient from the Components and Cladding procedure. The modified external pressure coefficient can then be multiplied by the velocity pressure,  $q_z$ , to determine the design wind pressure,  $p$ , as indicated in Equation 7. The design factor,  $\gamma$ , will typically reduce the external pressures from the design standard to better reflect the actual loading on the solar modules which are exposed to flow on both the external (upper) surface and within the cavity and therefore affected by pressure equalization. The design factor is a combination of the roof zone factor,  $\gamma_R$ , and the array zone factor,  $\gamma_E$  where  $\gamma_E = 1$  for modules in the interior array zone. Separate design recommendations are presented in Figure 7-8 with respect to tributary array for different roof zones (zone ① interior and zone ② edge) and different levels of system relative permeability ( $G/H < 1$  and  $G/H \geq 1$ ). The solid line is to be used for modules in the interior array zones where  $\gamma_E = 1$ . The dashed line is a composite  $\gamma_R \cdot \gamma_E$  factor to be used for modules in the edge zone of the array. For modules in the interior of the array and in roof zone ①,  $\gamma$  can be as low as 0.2 for systems with  $G/H \geq 1$  and a large tributary area ( $> 10 \text{ m}^2$ ). This represents an 80% reduction in the external roof loads. The design factor,  $\gamma$ , can be directly applied to the external pressure coefficient derived from the applicable code standard for installations mounted parallel to the roof surface with  $G$  of 12 cm or less and  $H$  up to 20 cm.

## 8 Conclusions

The flow field in which the solar modules are embedded is complex and largely dominated by the building-induced separation. A series of wind tunnel tests were undertaken to quantify the wind pressures acting on an array of 28 modules. The array was mounted parallel to the roof surface of two building models, one with a 30° roof slope and the other with a flat roof. The lateral spacing between array modules,  $G$ , and the cavity depth,  $H$ , were control variables and were found to be significant parameters when considering wind pressures on the array which affect the external, and cavity pressures as well as the net panel loads. The external mean pressure distributions are largely similar to what would be expected for a bare roof and the net pressure distributions tended to follow the external pressure distributions with reduced magnitudes. Cavity pressure distributions were found to be sensitive to cavity depth with larger  $H$  resulting in more uniform mean pressure distributions. Point measurements were area-averaged over individual models to determine the effect of  $G$  and  $H$  on statistical (Lieblein, 1974) peak, area-averaged pressures. A small, non-zero,  $H$  reduced the peak cavity suction. Further increasing  $H$  had little effect on the magnitude of the peak cavity suction but increased the peak external suction, and thus increased the peak net suction. Large  $G$  reduced the magnitude of the peak external suction and increased the magnitude of the peak cavity suction; lowering the peak net pressures and improving (i.e., increasing) pressure equalization. This was due to increased flow in and out of the cavity through the openings ( $G$ ) around the modules which introduced local pressure gradients at interfaces between adjacent modules. The external pressure gradients, which can be influenced by flow entering or exiting the cavity through  $G$ , played a role in setting the cavity pressures and thus the degree of pressure equalization.

Pressure equalization (typically) reduces the net load from that on the external surface. With the external pressures primarily dictated by the building-generated flow field and local separation off the array, the transmitted cavity pressure distribution was crucial to pressure equalization. The geometric array parameter,  $G/H$ , was found to be effective at describing the combined effect of  $G$  and  $H$  with higher ratios associated with increased pressure equalization. Oh and Kopp (2015) derived  $\phi$  to describe cavity behaviour for a

single cavity. They specifically studied the mechanisms responsible for setting the cavity pressure distributions. Parameter values less than order (1), common with small  $G/H$  ratios, indicate uniform cavity pressures driven by the pressure drop through  $G$  and low flow resistance in the cavity. This led to lower degrees of pressure equalization.  $\phi$  values greater than 1 indicated linearly varying cavity pressures, dominated by the pressure drop along the length of the cavity and higher flow resistance in the cavity. This was typically associated with larger  $G/H$  ratios and higher degrees of pressure equalization due to the fact that the cavity pressure distribution more closely mirrored the external pressure distribution. In this study, the parameter use was expanded to the multiple cavity configurations from Oh and Kopp as well as the current model. However, the parameter definition was used instead of the equation, which was developed for a single cavity only. It was found that the boundary of order (1) holds for arrays with multiple modules, indicating that it is likely a robust indicator of cavity pressure behaviour. The  $\phi$  equation is dependent on the effective cavity length, which is noted to be an important parameter and not as clearly defined in the data as expected. Results from both the current study and Oh and Kopp indicate that cavities beneath multiple modules may act together as one continuous cavity, with the effective cavity length thought to be some function of the neutral pressure line (where the external and cavity pressures are equal, resulting in a net pressure of zero acting on the module). Additional experiments are recommended to explicitly study the effective cavity length and its impact on pressure equalization.

The pressure equalization coefficient,  $C_{eq}$ , first used by Geurts (2000), describes the change in (peak) net pressure normalized by the (peak) external pressure. Smaller  $C_{eq}$  values are desirable for design as it means that the cavity pressure is largely similar to the external pressure, yielding a low net pressure and high degree of pressure equalization. It should be noted that  $C_{eq}$  can exceed 1 for certain conditions, indicating that the net pressure is larger in magnitude than the external pressure on the upper surface. This is associated with cases where the module is directly adjacent to the building edge and the cavity is subject to positive pressures, with large suction on the external surface. This punitive loading condition can be avoided if the modules are set back from the roof edge. The pressure equalization factor can be used to quantify the degree of pressure

equalization and serve as the basis for developing design recommendations.  $C_{eq}$  is thought to be an effective parameter for design recommendations as it is robust and accounts for numerous variations, as indicated by the reduced scatter of the data when it collapsed to a single curve when plotted with respect to  $G/H$  for a given tributary area. Roof slope was not observed to significantly alter the values, indicating that the factor captures the changes in the net loading due to pressure equalization regardless of loading patterns, which were noted to vary between roof models and wind directions, further justifying its use as the basis for developing design standards.  $C_{eq}$  was found to be lower for larger tributary areas and for near square aspect ratios (for a fixed tributary area), although the effect was most significant for small areas. It approached a lower asymptote for values of  $G/H \geq 1$ , indicating that the increased effectiveness of pressure equalization had been reached. As such, systems with  $G/H < 1$  and  $G/H \geq 1$  are treated separately for design recommendations.

Having established  $C_{eq}$  as an effective basis for design recommendations, the focus turned to assessing the array and roof edge effects. The array edge zone was assessed to be approximately  $\approx 1(H + t)$  to  $2(H + t)$  wide around the perimeter of the array by examining the mean and RMS pressure coefficients along lines of taps from wind directions with flow reattached to the roof surface. A shroud around array designed to restrict flow from entering the cavity around the perimeter of the array was found to reduce the magnitude of the cavity pressures, but also influence the external pressures. It is postulated that an aerodynamic shroud designed to prevent flow separation off the leading edge of the array could minimize, or eliminate, array edge effects. The (bare) roof zones dimensions established by ASCE 7-10 (2010) were found to be sufficient in size to capture the taps with higher magnitude pressures as a result of building-generated flow separation. Only edge and interior roof zones were used for design recommendations as the largest magnitude net pressures were found to occur in the edge zone, rendering the corner zones unnecessary.

Design wind loads are presented as a multiplication factor,  $\gamma$ , to be applied to the external pressure coefficient from the Components and Cladding (C&C) provision of current design standards. This methodology is more versatile; having not been developed for a

specific code, it can be applied to any bare roof design load. The factor is designed to account for the changes in the net wind loads acting on the array due to pressure equalization. Since it is based on  $C_{eq}$ , which is a measure of how much the net pressure is changed from the external pressure, when it is applied to the code specified external pressure it takes advantage of the extensive knowledge base of low-rise wind loads. The justification behind this approach is the versatility  $C_{eq}$  and the observation that the external (upper) surface pressures were noted to be largely unchanged from those expected for a bare roof. The design factor,  $\gamma$ , was developed by enveloping the experimental  $C_{eq}$  values and is a combination of the roof zone factor,  $\gamma_R$ , and the array zone factor,  $\gamma_E$ . To determine appropriate values of the factors, modules (and combinations of modules) were classified based on their roof and array zone. The roof zone factor is presented as a function of roof zone (interior or edge) and tributary area and was developed by enveloping  $C_{eq}$  values from the interior of the array in either the interior and edge roof zones. The array zone factor was first presented as a single value of 1.7 to be applied to the roof zone factor, accounting for the higher  $C_{eq}$  from modules in the edge array zone. This was found to be ineffective as it was overly conservative for interior array modules in the interior of the roof for small  $G/H$  but resulted in values that were not conservative for large  $G/H$ . The array edge factor was refined to be a separate value for each  $\gamma_R$  curve, which provided a better fit for the data but failed to account for the reduced array edge effects for large tributary areas where the  $C_{eq}$  values in the array edge zone approached those in the interior array zone. The final design recommendations provided two  $\gamma$  vs. tributary area curves for each roof zone and range of  $G/H$ ; one for use on modules within the interior of the array where  $\gamma_E = 1$  (the solid line in Figure 7-8) and another for when modules are located in the array edge zone (dashed line). It is recommended that these design recommendations be considered for inclusion in future design standards to fill a current void, providing design wind loads for air-permeable, double-layer roofing systems such as parallel mounted solar arrays. The design factor accounts for the effects of pressure equalization, the position of the module on the roof and within the array. It is designed to be used in conjunction with the C&C provisions; applied to the external pressure coefficient, which would then be multiplied by the velocity pressure to obtain the design wind pressure for the module. Future wind tunnel

testing is recommended to better separate the roof and edge effects, something not possible for the current model as the array was only placed in the one (edge) position on the roof surface. While this results in conservative values, refinement is possible with additional testing.

## References

- Aly, A., & Bitsuamlak, G. (2014). Wind-induced pressures on solar panels mounted on residential homes. *Journal of Architectural Engineering*, 20(1): 4013003.
- American Society of Civil Engineers. (2010). *ASCE Standard ASCE/SEI 7-10 Minimum design loads for buildings and other structures*. Reston, VA: American Society of Civil Engineers.
- American Society of Civil Engineers. (2012). *ASCE Standard ASCE/SEI 49-12 Wind Tunnel Testing for Buildings and Other Structures*. Reston, VA: American Society of Civil Engineers.
- Asghari Mooneghi, M., Irwin, P., & Gan Chowdhury, A. (2014). Large-scale testing on wind uplift of roof pavers. *Journal of Wind Engineering and Industrial Aerodynamics*, 128: 22-36.
- Auteri, F., Belan, M., Gibertini, G., & Grassi, D. (2008). Normal flat plates in tandem: An experimental investigation. *Journal of Wind Engineering and Industrial Aerodynamics*, 96: 872-879.
- Banks, D. (2013). The role of corner vortices in dictating peak wind loads on tilted flat solar panels mounted on large, flat roofs. *Journal of Wind Engineering and Industrial Aerodynamics*, 123: 192-201.
- Banks, D., Merony, R., Sarkar, P., Zhao, Z., & Wu, F. (2000). Flow visualization of conical vortices on flat roofs with simultaneous surface pressure measurement. *Journal of Wind Engineering and Industrial Aerodynamics*, 84: 65-85.
- Bienkiewicz, B., & Endo, M. (2009). Wind considerations for loose-laid and photovoltaic roofing systems. *2009 Structures Congress - Don't Mess with Structural Engineers: Expanding Our Role* (pp. 2578-2587). Reston, VA: American Society of Civil Engineers.

- Bienkiewicz, B., & Sun, Y. (1992). Wind-tunnel study of wind loading on loose-laid roofing systems. *Journal of Wind Engineering and Industrial Aerodynamics*, 41-44: 1817-1828.
- Binekiewicz, B., & Sun, Y. (1997). Wind loading and resistance of loose-laid roof paver systems. *Journal of Wind Engineering and Industrial Aerodynamics*, 72(1-3): 401-410.
- Blois, G., & Malavasi, S. (2007). Flow structure around a rectangular cylinder near a solid surface. *XVIII AIMETA Conference*. Brescia, Italy.
- Browne, M., Gibbons, M., Gamble, S., & Galsworthy, J. (2013). Wind loading on tilted roof-top solar arrays: The parapet effect. *Journal of Wind Engineering and Industrial Aerodynamics*, 123: 202-213.
- Cao, J., Yoshida, A., Saha, P., & Tamura, Y. (2013). Wind loading characteristics of solar arrays mounted on flat roofs. *Journal of Wind Engineering and Industrial Aerodynamics*, 123: 214-225.
- Cherry, N., Hillier, R., & Latour, M. (1984). Unsteady measurements in a separating and reattaching flow. *Journal of Fluid Mechanics*, 144: 13-46.
- Cheung, J., & Melbourne, W. (1988). Wind loading on a porous roof. *Journal of Wind Engineering and Industrial Aerodynamics*, 29: 19-28.
- Cook, N. (1990). *The Designer's Guide to Wind Loading of Building Structures: Static structures*. London, UK: Building Research Establishment.
- Davenport, A., Surry, D., & Stathopoulos, T. (1977). *Wind loads on low rise buildings: final report of phases I and II*. London, Canada: University of Western Ontario.
- Engineering Data Science Unit (ESDU). (1983). *Strong winds in the atmosphere boundary layer Part 2: Discrete gust speeds (ESDU 83045)*. London, UK: Engineering Data Science Unit (ESDU).

- Engineering Data Science Unit (ESDU). (1985). *Characteristics of atmospheric turbulence near the ground. Part II: single point data for strong winds (neutral atmosphere) (ESDU 85020)*. London, UK: Engineering Data Science Unit (ESDU).
- Engineering Science Data Unit (ESDU). (1974). *Characteristics of atmospheric turbulence near the ground (ESDU 74031)*. London, UK: Engineering Science Data Unit (ESDU).
- Engineering Science Data Unit (ESDU). (1982). *Strong winds in the atmosphere boundary layer Part 1: Mean-hourly wind speeds (ESDU 82026)*. London, UK: Engineering Science Data Unit (ESDU).
- Gerhardt, H., & Janser, F. (1994). Wind loads on wind permeable facades. *Journal of Wind Engineering and Industrial Aerodynamics*, 53(1-2): 37-48.
- Geurts, C. (2000). Wind loads on permeable roof covering products. *Fourth Colloquium on Bluff Body Aerodynamics and Applications*. Bochum, Germany: Ruhr Universitat.
- Geurts, C., & Blackmore, P. (2013). Wind loads on stand-off photovoltaic systems on pitched roofs. *Journal of Wind Engineering and Industrial Aerodynamics*, 123: 239-249.
- Geurts, C., & Van Bentum, C. (2007). Wind loads on solar energy roofs. *Heron*, 52(3) 201-222.
- Geurts, C., & VanBentum, C. (2006). *Wind Loads on Active Roofs: Part 1. Introduction and Classification of Systems 2006-D-R0203*. Delft, Netherlands: Netherlands Organization for Applied Scientific Research (TNO).
- Ginger, J., Payne, M., Stark, G., Sumant, B., & Leitch, C. (2011). *Investigation on Wind Loads Applied to Solar Panels Mounted on Roofs*. Townsville, Australia: Cyclone Testing Station.

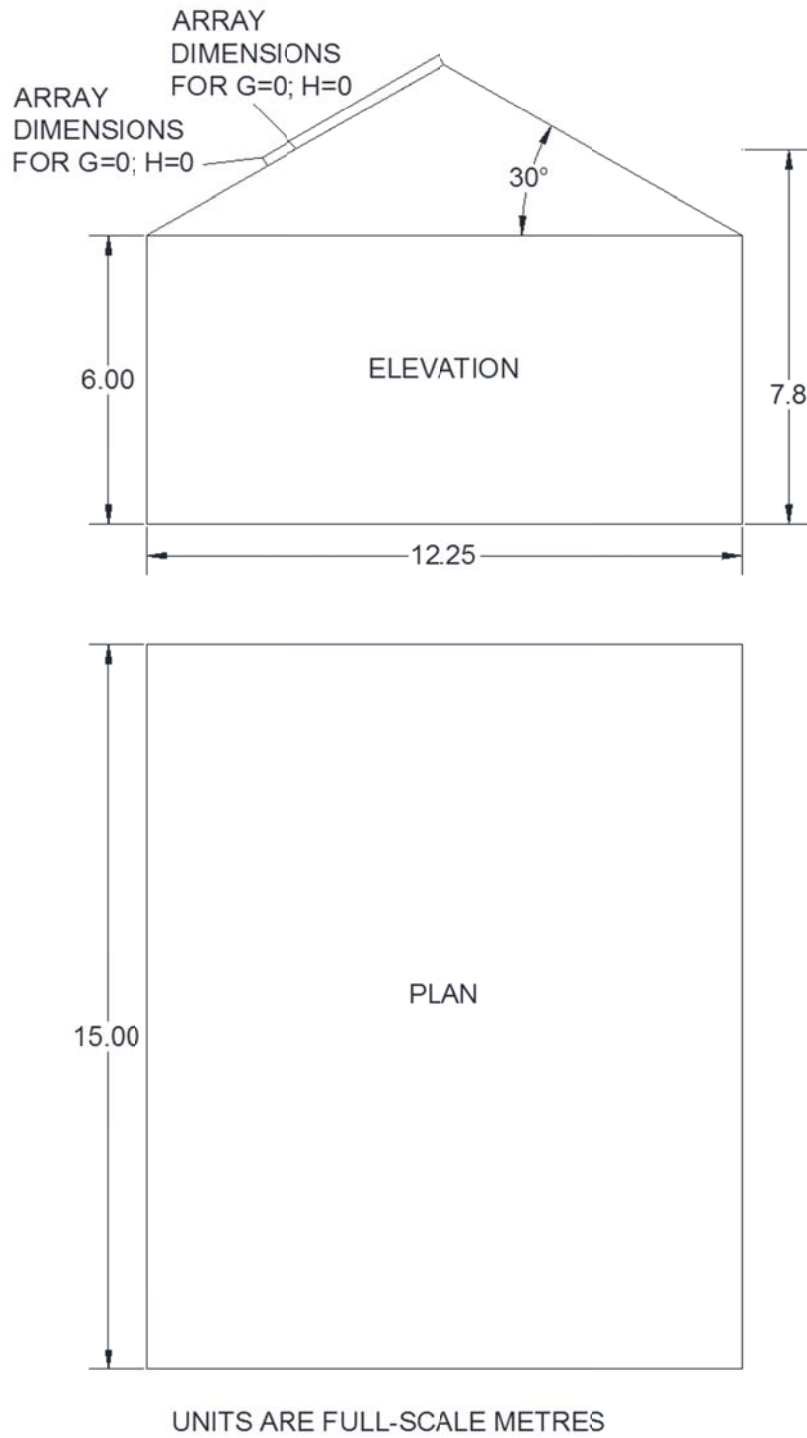
- Ho, T., Surry, D., Morrish, D., & Kopp, G. (2005). The UWO contribution to the NIST aerodynamic database for wind loads on low buildings: Part 1 Archiving format and basic aerodynamic data. *Journal of Wind Engineering and Industrial Aerodynamics*, 93(1): 1-30.
- Holmes, J. (1979). Mean and fluctuating internal pressure induced by wind. *5th International Conference on Wind Engineering*, (pp. 435-450). Fort Collins, Colorado.
- Holmes, J. (1981). *Wind Pressures on Houses with High Pitched Roofs*. Townsville, Australia: Department of Civil and Systems Engineering, James Cook University of North Queensland.
- Holmes, J. (2007). *Wind Loading of Structures*. New York, New York: Taylor & Francis.
- Kind, R. (1986). Worst suctions near edges of flat rooftops on low-rise buildings. *Journal of Wind Engineering and Industrial Aerodynamics*, 25(1): 31-47.
- Kind, R., & Wardlaw, R. (1982). Failure mechanism of loose-laid roof-insulation systems. *Journal of Wind Engineering and Industrial Aerodynamics*, 9: 325-341.
- Kopp, G. (2013). Wind loads on low profile, tilted, solar arrays placed on large, flat, low-rise building roofs. *Journal of Structural Engineering*, 140(2): 04013057.
- Kopp, G., & Banks, D. (2013). Use of the wind tunnel test method for obtaining design wind loads on roof-mounted solar arrays. *Journal of Structural Engineering*, 139(2): 284-287.
- Kopp, G., Farquhar, S., & Morrison, M. (2012). Aerodynamic mechanisms for wind loads on tilted, roof-mounted, solar arrays. *Journal of Wind Engineering and Industrial Aerodynamics*, 111: 40-52.
- Kumar, K. (2000). Pressure equalization of rainscreen walls: a critical review. *Building and Environment*, 35: 161-179.

- Kumar, K., & A.W.M, V. S. (1999). Prediction of pressure equalization performance of rainscreen walls. *Wind and Structures*, 2(4): 325- 345.
- Kumar, K., & Van Schijndel, A. (1998). Cavity pressure dynamics of rainscreen walls. *4th UK Conference on Wind Engineering*. Bristol, UK.
- Latta, J. (1973). *Walls, windows and roofs for the Canadian climate - a summary of the current basis for selection and design*. Ottawa, Canada: National Research Council of Canada.
- Lieblein, J. (1974). *Efficient Methods of Extreme-value Methodology*. Washington, D.C.: National Bureau of Standards.
- Lim, H., Castro, I., & Hoxey, R. (2007). Bluff bodies in deep turbulent boundary layers: Reynolds-number issues. *Journal of Fluid Mechanics*, 571: 97-118.
- Lin, J., & Surry, D. (1998). The variation of peak loads with tributary area near corners on flat low building roofs. *Journal of Wind Engineering and Industrial Aerodynamics*, 77-78: 185-196.
- Maffei, J., Telleen, K., Ward, R., Kopp, G., & Schellenberg, A. (2013). Wind design practice and recommendations for solar arrays on low-slope roofs. *Journal of Structural Engineering*, 140(2): 04013040.
- Malavasi, S., & Trabucchi, N. (2008). Numerical Investigation of the flow around a rectangular cylinder near a solid wall. *BBAA VI International Colloquium on: Bluff Bodies Aerodynamics & Applications*. Milano, Italy.
- Martinuzzi, R., Bailey, S., & Kopp, G. (2003). Influence of wall proximity on vortex shedding from a square cylinder. *Experiments in Fluids*, 34: 585-596.
- Morrison Hershfield Limited. (1990). *A study of the rainscreen concept applied to cladding systems on wood-framed walls*. Ottawa, Canada: Morrison Hershfield Limited.

- National Research Council of Canada. (2010). *NBC 2010 National Building Code of Canada and commentaries (NRCC 53301)*. Ottawa, Canada: National Research Council of Canada.
- Nederlands Normalisatie – Instituut. (2013). *NEN 7250 Solar Energy Systems Integration in Roofs and Facades – Building Aspects*. Ontwerp, Netherlands: Nederlands Normalisatie – Instituut.
- O'Brien, C., Neff, D., Bienkiewicz, B., & Dinwoodie, T. (2004). Optimization of wind resistance of photo voltaic roofing systems. *Structures 2001* (pp. 2578-2587). Reston, VA: American Society of Civil Engineers.
- Oh, J., & Kopp, G. (2014). Modelling of spatially and temporally-varying cavity pressures in air permeable, double-layer roof systems. *Building and Environment*, 82: 135-150.
- Oh, J., & Kopp, G. (2015). An experimental study of pressure distributions within an air-permeable, double-layer roof system in regions of separated flow. *Journal of Wind Engineering and Industrial Aerodynamics*, 138: 1-12.
- Okada, H., & Okabe, M. (1991). Wind tunnel tests to determine the wind forces on roof blocks for existing buildings. *Journal of Wind Engineering and Industrial Aerodynamics*, 38: 393-403.
- Pratt, R., & Kopp, G. (2013). Velocity measurements around low-profile, tilted, solar arrays mounted on large flat-roofs, for wall normal wind directions. *Journal of Wind Engineering and Industrial Aerodynamics*, 123(2): 226-238.
- Pratt, R., & Kopp, G. (2014). Velocity field measurements above the roof of a low-rise building during peak suction. *Journal of Wind Engineering and Industrial Aerodynamics*, 133: 234-241.
- Schlichting, H., & Gersten, K. (2000). *Boundary Layer Theory*. New York, NY: Springer Science & Business Media.

- SEAO Solar Photovoltaic Systems Committee. (2012). *SEAO PV2-2012 Wind Design for Low-profile Solar Photovoltaic Arrays on Flat Roofs*. Sacramento, California.: Structural Engineers Association of California.
- Standards Australia. (2012). *AS/NZS 1170.2:2011 Structural design actions*. Sydney, Australia: Standards Australia.
- Stathopoulos, T. (1979). *Turbulent Wind Action on Low Rise Structures*. London, Canada: The University of Western Ontario.
- Stathopoulos, T., Wang, K., & Wu, H. (2000). Proposed new Canadian wind provisions for the design of gable roofs. *Canadian Journal of Civil Engineering*, 27(5): 1059-1072.
- Stenabaugh, S., Iida, Y., Kopp, G., & Karava, P. (2015). Wind loads on photovoltaic arrays mounted parallel to sloped roofs on low-rise buildings. *Journal of Wind Engineering and Industrial Aerodynamics*, 139 16-26.
- Stenabaugh, S., Karava, P., & Kopp, G. (2010). *Design Wind Loads for Photovoltaic Systems on Sloped Roofs of Residential Buildings*. London, Canada: Boundary Layer Wind Tunnel Laboratory.
- Stenabaugh, S., Karava, P., & Kopp, G. (2011). Design wind loads for photovoltaic systems on sloped roofs of residential buildings. *13 ICWE*. Amsterdam, Netherlands.
- Surry, D. (1982). *Consequences of distortions in the flow including mismatching scales and intensities of turbulence*. ISBN: 0521252784; 978-052125278-2.
- Tieleman, H., Akins, R., & Sparks, P. (1980). *An investigation of wind loads on solar collectors*. Blacksburg, VA: Virginia Polytechnic Institute and State University.
- Wood, G., Denoon, R., & Kwok, K. (2001). Wind loads on industrial solar panel arrays and supporting roof structure. *Wind and Structures*, 4(6): 481-494.

## Appendix A: Wind tunnel testing details

**Figure A1 : Model dimensions - sloped roof model**

UNITS ARE FULL-SCALE METRES

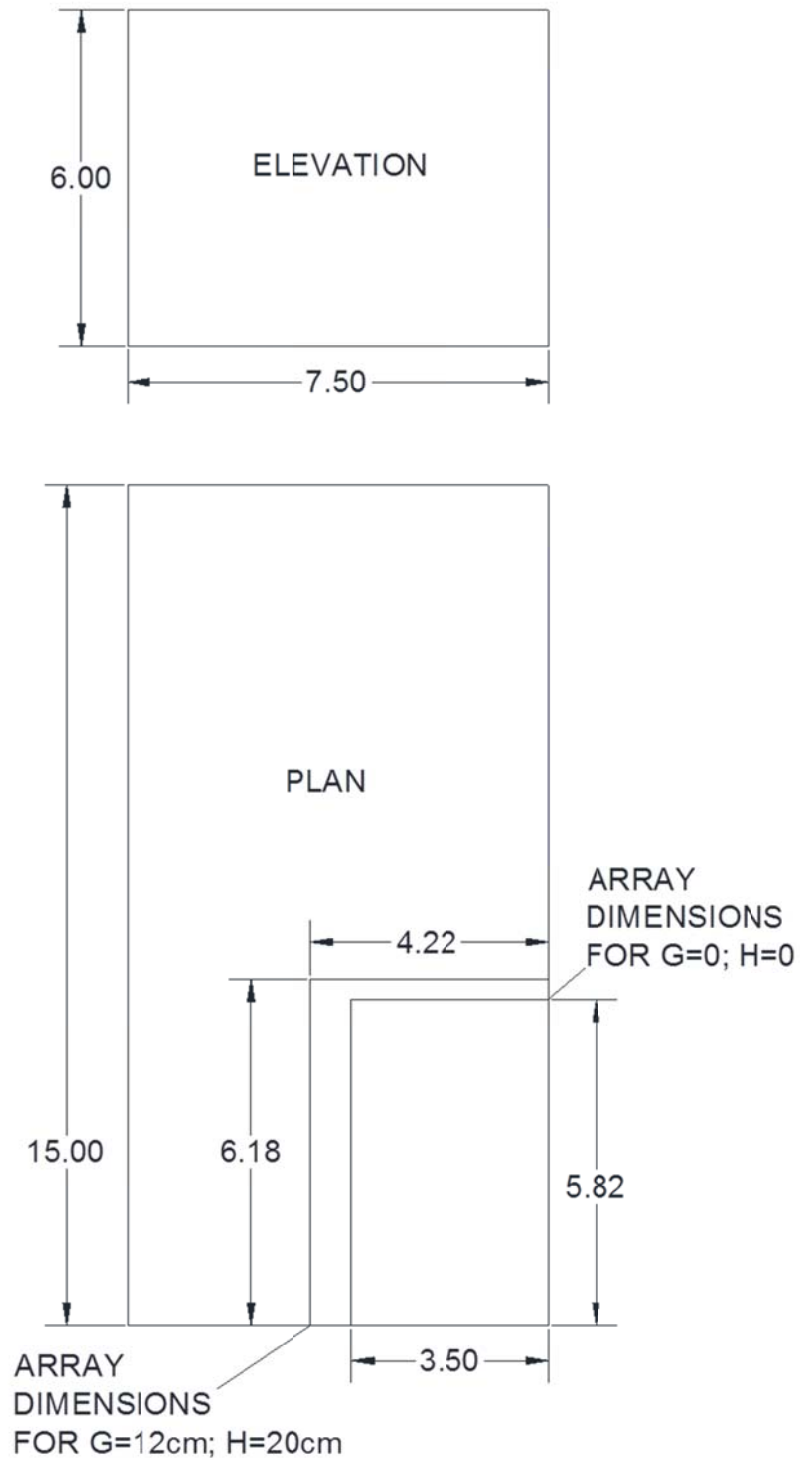


**Figure A2 : Model dimensions - flat roof model**

**Table A1: Sloped-roof configurations (base configurations, original 42)**

Configuration label	Gap, G, (cm)	Height, H, (cm)	G/H if applicable
11	0	20	-
12	0	14	-
13	0	8	-
14	0	5	-
15	0	2	-
16	0	0	-
21	1	20	0.05
22	1	14	0.07
23	1	8	0.13
24	1	5	0.20
25	1	2	0.50
26	1	0	-
31	2	20	0.10
32	2	14	0.14
33	2	8	0.25
34	2	5	0.40
35	2	2	1.00
36	2	0	-
41	3	20	0.15
42	3	14	0.21
43	3	8	0.38
44	3	5	0.60
45	3	2	1.50
46	3	0	-
51	4	20	0.20
52	4	14	0.29
53	4	8	0.50
54	4	5	0.80
55	4	2	2.00
56	4	0	-
61	8	20	0.40
62	8	14	0.57
63	8	8	1.00
64	8	5	1.60
65	8	2	4.00
66	8	0	-
71	12	20	0.60
72	12	14	0.86
73	12	8	1.50
74	12	5	2.40
75	12	2	6.00
76	12	0	-

**Table A2 : Flat-roof configurations**

Configuration label	Gap, G, (cm)	Height, H, (cm)	G/H if applicable
91	12	20	0.60
92	12	14	0.86
93	12	8	1.50
94	12	5	2.40
95	12	2	6.00
96	12	0	-

**Table A3 : Shroud sloped-roof configurations**

Configuration label	Gap, G, (cm)	Height, H, (cm)	G/H if applicable	Simulated panel size (modules)
11A	0	20	0.60	1x1
12A	0	14	0.86	1x1
13A	0	8	1.50	1x1
14A	0	5	2.40	1x1
15A	0	2	6.00	1x1
16A	0	0	-	1x1
11B	0	20	0.60	2x2
13B	0	8	1.50	2x2
15B	0	2	6.00	2x2
16B	0	0	-	2x2
11C	0	20	0.60	4x4 / 3x4
13C	0	8	1.50	4x4 / 3x4
15C	0	2	6.00	4x4 / 3x4
16C	0	0	-	4x4 / 3x4
71A	12	20	0.60	1x1
72A	12	14	0.86	1x1
73A	12	8	1.50	1x1
74A	12	5	2.40	1x1
75A	12	2	6.00	1x1
76A	12	0	-	1x1
71B	12	20	0.60	2x2
72B	12	14	0.86	2x2
73B	12	8	1.50	2x2
74B	12	5	2.40	2x2
75B	12	2	6.00	2x2
76B	12	0	-	2x2
71C	12	20	0.60	4x4 / 3x4
72C	12	14	0.86	4x4 / 3x4
73C	12	8	1.50	4x4 / 3x4
74C	12	5	2.40	4x4 / 3x4
75C	12	2	6.00	4x4 / 3x4
76C	12	0	-	4x4 / 3x4

**Table A4: Shroud flat-roof configurations**

Configuration label	Gap, G, (cm)	Height, H, (cm)	G/H if applicable	Simulated panel size (modules)
91A	12	20	0.60	1x1
92A	12	14	0.86	1x1
93A	12	8	1.50	1x1
94A	12	5	2.40	1x1
95A	12	2	6.00	1x1
96A	12	0	-	1x1
91B	12	20	0.60	2x2
92B	12	14	0.86	2x2
93B	12	8	1.50	2x2
94B	12	5	2.40	2x2
95B	12	2	6.00	2x2
96B	12	0	-	2x2
91C	12	20	0.60	4x4 / 3x4
92C	12	14	0.86	4x4 / 3x4
93C	12	8	1.50	4x4 / 3x4
94C	12	5	2.40	4x4 / 3x4
95C	12	2	6.00	4x4 / 3x4
96C	12	0	-	4x4 / 3x4

101 <sup>o+</sup>	102 <sup>o+</sup>	103 <sup>o+</sup>	104 <sup>o+</sup>	105 <sup>o+</sup>	205 <sup>o+</sup>	206 <sup>o+</sup>	207 <sup>o+</sup>	208 <sup>o+</sup>	209 <sup>o+</sup>	309 <sup>o+</sup>	310 <sup>o+</sup>	311 <sup>o+</sup>	312 <sup>o+</sup>	313 <sup>o+</sup>	413 <sup>o+</sup>	414 <sup>o+</sup>	415 <sup>o+</sup>	416 <sup>o+</sup>	501 <sup>o+</sup>
106 <sup>o+</sup>	107 <sup>o+</sup>	108 <sup>o+</sup>	109 <sup>o+</sup>	110 <sup>o+</sup>	210 <sup>o+</sup>	211 <sup>o+</sup>	212 <sup>o+</sup>	213 <sup>o+</sup>	214 <sup>o+</sup>	314 <sup>o+</sup>	315 <sup>o+</sup>	316 <sup>o+</sup>	401 <sup>o+</sup>	402 <sup>o+</sup>	502 <sup>o+</sup>	503 <sup>o+</sup>	504 <sup>o+</sup>	505 <sup>o+</sup>	506 <sup>o+</sup>
601 <sup>o+</sup>	602 <sup>o+</sup>	603 <sup>o+</sup>	604 <sup>o+</sup>	605 <sup>o+</sup>	705 <sup>o+</sup>	706 <sup>o+</sup>	707 <sup>o+</sup>	708 <sup>o+</sup>	709 <sup>o+</sup>	809 <sup>o+</sup>	810 <sup>o+</sup>	811 <sup>o+</sup>	812 <sup>o+</sup>	813 <sup>o+</sup>	913 <sup>o+</sup>	914 <sup>o+</sup>	915 <sup>o+</sup>	916 <sup>o+</sup>	1001 <sup>o+</sup>
606 <sup>o+</sup>	607 <sup>o+</sup>	608 <sup>o+</sup>	609 <sup>o+</sup>	610 <sup>o+</sup>	710 <sup>o+</sup>	711 <sup>o+</sup>	712 <sup>o+</sup>	713 <sup>o+</sup>	714 <sup>o+</sup>	814 <sup>o+</sup>	815 <sup>o+</sup>	816 <sup>o+</sup>	901 <sup>o+</sup>	902 <sup>o+</sup>	1002 <sup>o+</sup>	1003 <sup>o+</sup>	1004 <sup>o+</sup>	1005 <sup>o+</sup>	1006 <sup>o+</sup>
1101 <sup>o+</sup>	1102 <sup>o+</sup>	1103 <sup>o+</sup>	1104 <sup>o+</sup>	1105 <sup>o+</sup>	1205 <sup>o+</sup>	1206 <sup>o+</sup>	1207 <sup>o+</sup>	1208 <sup>o+</sup>	1209 <sup>o+</sup>	1309 <sup>o+</sup>	1310 <sup>o+</sup>	1311 <sup>o+</sup>	1312 <sup>o+</sup>	1313 <sup>o+</sup>	1413 <sup>o+</sup>	1414 <sup>o+</sup>	1415 <sup>o+</sup>	1416 <sup>o+</sup>	1501 <sup>o+</sup>
1106 <sup>o+</sup>	1107 <sup>o+</sup>	1108 <sup>o+</sup>	1109 <sup>o+</sup>	1110 <sup>o+</sup>	1210 <sup>o+</sup>	1211 <sup>o+</sup>	1212 <sup>o+</sup>	1213 <sup>o+</sup>	1214 <sup>o+</sup>	1314 <sup>o+</sup>	1315 <sup>o+</sup>	1316 <sup>o+</sup>	1401 <sup>o+</sup>	1402 <sup>o+</sup>	1502 <sup>o+</sup>	1503 <sup>o+</sup>	1504 <sup>o+</sup>	1505 <sup>o+</sup>	1506 <sup>o+</sup>
1601 <sup>o+</sup>	1602 <sup>o+</sup>	1603 <sup>o+</sup>	1604 <sup>o+</sup>	1605 <sup>o+</sup>	1705 <sup>o+</sup>	1706 <sup>o+</sup>	1707 <sup>o+</sup>	1708 <sup>o+</sup>	1709 <sup>o+</sup>	1809 <sup>o+</sup>	1810 <sup>o+</sup>	1811 <sup>o+</sup>	1812 <sup>o+</sup>	1813 <sup>o+</sup>	1913 <sup>o+</sup>	1914 <sup>o+</sup>	1915 <sup>o+</sup>	1916 <sup>o+</sup>	2001 <sup>o+</sup>
1606 <sup>o+</sup>	1607 <sup>o+</sup>	1608 <sup>o+</sup>	1609 <sup>o+</sup>	1610 <sup>o+</sup>	1710 <sup>o+</sup>	1711 <sup>o+</sup>	1712 <sup>o+</sup>	1713 <sup>o+</sup>	1714 <sup>o+</sup>	1814 <sup>o+</sup>	1815 <sup>o+</sup>	1316 <sup>o+</sup>	1901 <sup>o+</sup>	1902 <sup>o+</sup>	2002 <sup>o+</sup>	2003 <sup>o+</sup>	2004 <sup>o+</sup>	2005 <sup>o+</sup>	2006 <sup>o+</sup>
2101 <sup>o+</sup>	2102 <sup>o+</sup>	2103 <sup>o+</sup>	2104 <sup>o+</sup>	2105 <sup>o+</sup>	2205 <sup>o+</sup>	2206 <sup>o+</sup>	2207 <sup>o+</sup>	2208 <sup>o+</sup>	2209 <sup>o+</sup>	2309 <sup>o+</sup>	2310 <sup>o+</sup>	2311 <sup>o+</sup>	2312 <sup>o+</sup>	2313 <sup>o+</sup>	2413 <sup>o+</sup>	2414 <sup>o+</sup>	2415 <sup>o+</sup>	2416 <sup>o+</sup>	2501 <sup>o+</sup>
2106 <sup>o+</sup>	2107 <sup>o+</sup>	2108 <sup>o+</sup>	2109 <sup>o+</sup>	2110 <sup>o+</sup>	2210 <sup>o+</sup>	2211 <sup>o+</sup>	2212 <sup>o+</sup>	2213 <sup>o+</sup>	2214 <sup>o+</sup>	2314 <sup>o+</sup>	2315 <sup>o+</sup>	2316 <sup>o+</sup>	2401 <sup>o+</sup>	2402 <sup>o+</sup>	2502 <sup>o+</sup>	2503 <sup>o+</sup>	2504 <sup>o+</sup>	2505 <sup>o+</sup>	2506 <sup>o+</sup>
2601 <sup>o+</sup>	2602 <sup>o+</sup>	2603 <sup>o+</sup>	2604 <sup>o+</sup>	2605 <sup>o+</sup>	2705 <sup>o+</sup>	2706 <sup>o+</sup>	2707 <sup>o+</sup>	2708 <sup>o+</sup>	2709 <sup>o+</sup>	2809 <sup>o+</sup>	2810 <sup>o+</sup>	2811 <sup>o+</sup>	2812 <sup>o+</sup>	2813 <sup>o+</sup>	2913 <sup>o+</sup>	2914 <sup>o+</sup>	2915 <sup>o+</sup>	2916 <sup>o+</sup>	3001 <sup>o+</sup>
2606 <sup>o+</sup>	2607 <sup>o+</sup>	2608 <sup>o+</sup>	2609 <sup>o+</sup>	2610 <sup>o+</sup>	2710 <sup>o+</sup>	2711 <sup>o+</sup>	2712 <sup>o+</sup>	2713 <sup>o+</sup>	2714 <sup>o+</sup>	2814 <sup>o+</sup>	2815 <sup>o+</sup>	2816 <sup>o+</sup>	2901 <sup>o+</sup>	2902 <sup>o+</sup>	3002 <sup>o+</sup>	3003 <sup>o+</sup>	3004 <sup>o+</sup>	3005 <sup>o+</sup>	3006 <sup>o+</sup>
3101 <sup>o+</sup>	3102 <sup>o+</sup>	3103 <sup>o+</sup>	3104 <sup>o+</sup>	3105 <sup>o+</sup>	3205 <sup>o+</sup>	3206 <sup>o+</sup>	3207 <sup>o+</sup>	3208 <sup>o+</sup>	3209 <sup>o+</sup>	3309 <sup>o+</sup>	3310 <sup>o+</sup>	3311 <sup>o+</sup>	3312 <sup>o+</sup>	3313 <sup>o+</sup>	3413 <sup>o+</sup>	3414 <sup>o+</sup>	3415 <sup>o+</sup>	3416 <sup>o+</sup>	3501 <sup>o+</sup>
3106 <sup>o+</sup>	3107 <sup>o+</sup>	3108 <sup>o+</sup>	3109 <sup>o+</sup>	3110 <sup>o+</sup>	3210 <sup>o+</sup>	3211 <sup>o+</sup>	3212 <sup>o+</sup>	3213 <sup>o+</sup>	3214 <sup>o+</sup>	3314 <sup>o+</sup>	3315 <sup>o+</sup>	3316 <sup>o+</sup>	3401 <sup>o+</sup>	3402 <sup>o+</sup>	3502 <sup>o+</sup>	3503 <sup>o+</sup>	3504 <sup>o+</sup>	3505 <sup>o+</sup>	3506 <sup>o+</sup>

Figure A3 : Tap labels for pressure taps on the upper surface of the array

111 <sup>o+</sup>	112 <sup>o+</sup>	113 <sup>o+</sup>	114 <sup>o+</sup>	115 <sup>o+</sup>	215 <sup>o+</sup>	216 <sup>o+</sup>	301 <sup>o+</sup>	302 <sup>o+</sup>	303 <sup>o+</sup>	403 <sup>o+</sup>	404 <sup>o+</sup>	405 <sup>o+</sup>	406 <sup>o+</sup>	407 <sup>o+</sup>	507 <sup>o+</sup>	508 <sup>o+</sup>	509 <sup>o+</sup>	510 <sup>o+</sup>	511 <sup>o+</sup>
116 <sup>o+</sup>	201 <sup>o+</sup>	202 <sup>o+</sup>	203 <sup>o+</sup>	204 <sup>o+</sup>	304 <sup>o+</sup>	305 <sup>o+</sup>	306 <sup>o+</sup>	307 <sup>o+</sup>	308 <sup>o+</sup>	408 <sup>o+</sup>	409 <sup>o+</sup>	410 <sup>o+</sup>	411 <sup>o+</sup>	412 <sup>o+</sup>	512 <sup>o+</sup>	513 <sup>o+</sup>	514 <sup>o+</sup>	515 <sup>o+</sup>	516 <sup>o+</sup>
611 <sup>o+</sup>	612 <sup>o+</sup>	613 <sup>o+</sup>	614 <sup>o+</sup>	615 <sup>o+</sup>	715 <sup>o+</sup>	716 <sup>o+</sup>	801 <sup>o+</sup>	802 <sup>o+</sup>	803 <sup>o+</sup>	903 <sup>o+</sup>	904 <sup>o+</sup>	905 <sup>o+</sup>	906 <sup>o+</sup>	907 <sup>o+</sup>	1007 <sup>o+</sup>	1008 <sup>o+</sup>	1009 <sup>o+</sup>	1010 <sup>o+</sup>	1011 <sup>o+</sup>
616 <sup>o+</sup>	701 <sup>o+</sup>	702 <sup>o+</sup>	703 <sup>o+</sup>	704 <sup>o+</sup>	804 <sup>o+</sup>	805 <sup>o+</sup>	806 <sup>o+</sup>	807 <sup>o+</sup>	808 <sup>o+</sup>	908 <sup>o+</sup>	909 <sup>o+</sup>	910 <sup>o+</sup>	911 <sup>o+</sup>	912 <sup>o+</sup>	1012 <sup>o+</sup>	1013 <sup>o+</sup>	1014 <sup>o+</sup>	1015 <sup>o+</sup>	1016 <sup>o+</sup>
1111 <sup>o+</sup>	1112 <sup>o+</sup>	1113 <sup>o+</sup>	1114 <sup>o+</sup>	1115 <sup>o+</sup>	1215 <sup>o+</sup>	1216 <sup>o+</sup>	1301 <sup>o+</sup>	1302 <sup>o+</sup>	1303 <sup>o+</sup>	1403 <sup>o+</sup>	1404 <sup>o+</sup>	1405 <sup>o+</sup>	1406 <sup>o+</sup>	1407 <sup>o+</sup>	1507 <sup>o+</sup>	1508 <sup>o+</sup>	1509 <sup>o+</sup>	1510 <sup>o+</sup>	1511 <sup>o+</sup>
1116 <sup>o+</sup>	1201 <sup>o+</sup>	1202 <sup>o+</sup>	1203 <sup>o+</sup>	1204 <sup>o+</sup>	1304 <sup>o+</sup>	1305 <sup>o+</sup>	1306 <sup>o+</sup>	1307 <sup>o+</sup>	1308 <sup>o+</sup>	1408 <sup>o+</sup>	1409 <sup>o+</sup>	1410 <sup>o+</sup>	1411 <sup>o+</sup>	1412 <sup>o+</sup>	1512 <sup>o+</sup>	1513 <sup>o+</sup>	1514 <sup>o+</sup>	1515 <sup>o+</sup>	1516 <sup>o+</sup>
1611 <sup>o+</sup>	1612 <sup>o+</sup>	1613 <sup>o+</sup>	1614 <sup>o+</sup>	1615 <sup>o+</sup>	1715 <sup>o+</sup>	1716 <sup>o+</sup>	1801 <sup>o+</sup>	1802 <sup>o+</sup>	1803 <sup>o+</sup>	1903 <sup>o+</sup>	1904 <sup>o+</sup>	1905 <sup>o+</sup>	1906 <sup>o+</sup>	1907 <sup>o+</sup>	2007 <sup>o+</sup>	2008 <sup>o+</sup>	2009 <sup>o+</sup>	2010 <sup>o+</sup>	2011 <sup>o+</sup>
1616 <sup>o+</sup>	1701 <sup>o+</sup>	1702 <sup>o+</sup>	1703 <sup>o+</sup>	1704 <sup>o+</sup>	1804 <sup>o+</sup>	1805 <sup>o+</sup>	1806 <sup>o+</sup>	1807 <sup>o+</sup>	1808 <sup>o+</sup>	1908 <sup>o+</sup>	1909 <sup>o+</sup>	1910 <sup>o+</sup>	1911 <sup>o+</sup>	1912 <sup>o+</sup>	2012 <sup>o+</sup>	2013 <sup>o+</sup>	2014 <sup>o+</sup>	2015 <sup>o+</sup>	2016 <sup>o+</sup>
2111 <sup>o+</sup>	2112 <sup>o+</sup>	2113 <sup>o+</sup>	2114 <sup>o+</sup>	2115 <sup>o+</sup>	2215 <sup>o+</sup>	2216 <sup>o+</sup>	2301 <sup>o+</sup>	2302 <sup>o+</sup>	2303 <sup>o+</sup>	2403 <sup>o+</sup>	2404 <sup>o+</sup>	2405 <sup>o+</sup>	2406 <sup>o+</sup>	2407 <sup>o+</sup>	2507 <sup>o+</sup>	2508 <sup>o+</sup>	2509 <sup>o+</sup>	2510 <sup>o+</sup>	2511 <sup>o+</sup>
2116 <sup>o+</sup>	2201 <sup>o+</sup>	2202 <sup>o+</sup>	2203 <sup>o+</sup>	2204 <sup>o+</sup>	2304 <sup>o+</sup>	2305 <sup>o+</sup>	2306 <sup>o+</sup>	2307 <sup>o+</sup>	2308 <sup>o+</sup>	2408 <sup>o+</sup>	2409 <sup>o+</sup>	2410 <sup>o+</sup>	2411 <sup>o+</sup>	2412 <sup>o+</sup>	2512 <sup>o+</sup>	2513 <sup>o+</sup>	2514 <sup>o+</sup>	2515 <sup>o+</sup>	2516 <sup>o+</sup>
2611 <sup>o+</sup>	2612 <sup>o+</sup>	2613 <sup>o+</sup>	2614 <sup>o+</sup>	2615 <sup>o+</sup>	2715 <sup>o+</sup>	2716 <sup>o+</sup>	2801 <sup>o+</sup>	2802 <sup>o+</sup>	2803 <sup>o+</sup>	2903 <sup>o+</sup>	2904 <sup>o+</sup>	2905 <sup>o+</sup>	2906 <sup>o+</sup>	2907 <sup>o+</sup>	3007 <sup>o+</sup>	3008 <sup>o+</sup>	3009 <sup>o+</sup>	3010 <sup>o+</sup>	3011 <sup>o+</sup>
2616 <sup>o+</sup>	2701 <sup>o+</sup>	2702 <sup>o+</sup>	2703 <sup>o+</sup>	2704 <sup>o+</sup>	2804 <sup>o+</sup>	2805 <sup>o+</sup>	2806 <sup>o+</sup>	2807 <sup>o+</sup>	2808 <sup>o+</sup>	2908 <sup>o+</sup>	2909 <sup>o+</sup>	2910 <sup>o+</sup>	2911 <sup>o+</sup>	2912 <sup>o+</sup>	3012 <sup>o+</sup>	3013 <sup>o+</sup>	3014 <sup>o+</sup>	3015 <sup>o+</sup>	3016 <sup>o+</sup>
3111 <sup>o+</sup>	3112 <sup>o+</sup>	3113 <sup>o+</sup>	3114 <sup>o+</sup>	3115 <sup>o+</sup>	3215 <sup>o+</sup>	3216 <sup>o+</sup>	3301 <sup>o+</sup>	3302 <sup>o+</sup>	3303 <sup>o+</sup>	3403 <sup>o+</sup>	3404 <sup>o+</sup>	3405 <sup>o+</sup>	3406 <sup>o+</sup>	3407 <sup>o+</sup>	3507 <sup>o+</sup>	3508 <sup>o+</sup>	3509 <sup>o+</sup>	3510 <sup>o+</sup>	3511 <sup>o+</sup>
3116 <sup>o+</sup>	3201 <sup>o+</sup>	3202 <sup>o+</sup>	3203 <sup>o+</sup>	3204 <sup>o+</sup>	3304 <sup>o+</sup>	3305 <sup>o+</sup>	3306 <sup>o+</sup>	3307 <sup>o+</sup>	3308 <sup>o+</sup>	3408 <sup>o+</sup>	3409 <sup>o+</sup>	3410 <sup>o+</sup>	3411 <sup>o+</sup>	3412 <sup>o+</sup>	3512 <sup>o+</sup>	3513 <sup>o+</sup>	3514 <sup>o+</sup>	3515 <sup>o+</sup>	3516 <sup>o+</sup>

Figure A4 : Tap labels for pressure taps on the lower surface of the array

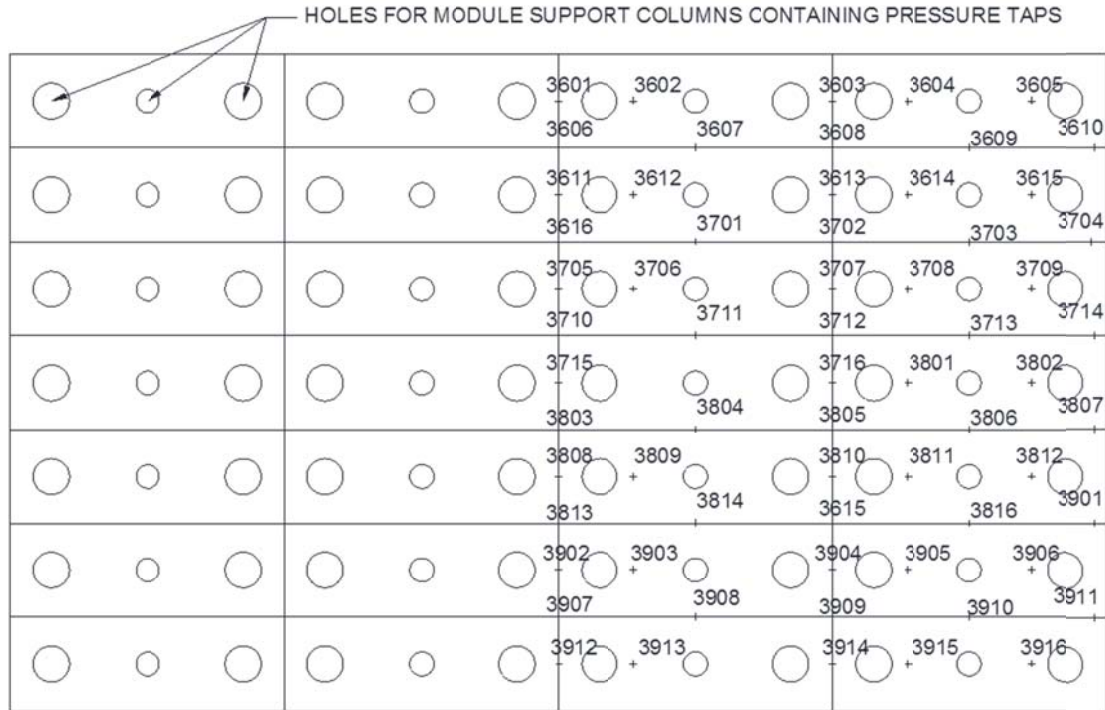


**Figure A5: Tap labels for pressure taps on the roof surface ( $G=0$  roof piece shown)**

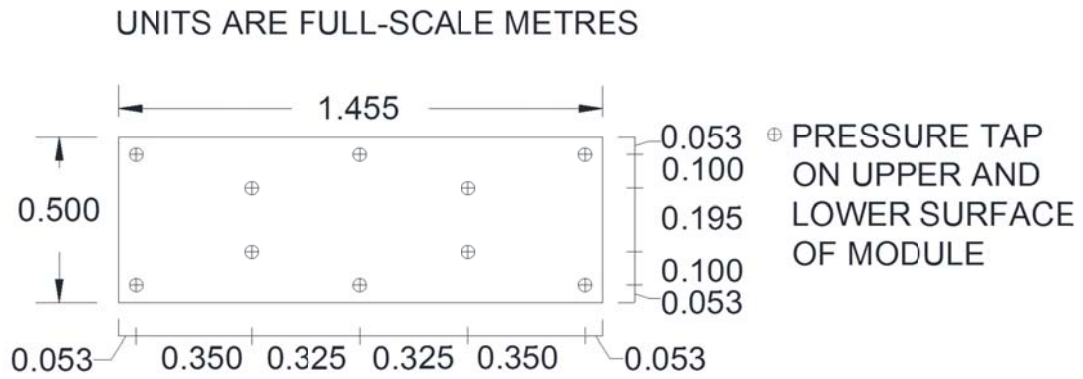


**Figure A6 : Tap locations on the individual modules**

**Table A5 : Tributary area combinations**

Area Case	Number of Panels included in average	Number of Positions, $c$	Tributary Area, $A$ (m <sup>2</sup> )
1x1	1	28	0.73
1x2	2	21	1.46
1x3	3	14	2.18
1x4	4	7	2.91
2x1	2	24	1.46
2x2	4	18	2.91
2x3	6	12	4.37
2x4	8	6	5.82
3x1	3	20	2.18
3x2	6	15	4.37
3x3	9	10	6.55
3x4	12	5	8.73
4x1	4	16	2.91
4x2	8	12	5.82
4x3	12	8	8.73
4x4	16	4	11.64
5x1	5	12	3.64
5x2	10	9	7.28
5x3	15	6	10.91
5x4	20	3	14.55
6x1	6	8	4.37
6x2	12	6	8.73
6x3	18	4	13.10
6x4	24	2	17.46
7x1	7	4	5.09
7x2	14	3	10.19
7x3	21	2	15.28
7x4	28	1	20.37

## Appendix B: Different contouring approaches for peak pressure coefficient distributions

-0.63 -0.32 -0.52	-0.74 -1 -1.1	-1.5 -1.5 -1.1	-1.5 -1.5 -1.4	-1.3 -1.4 -1.2	-1.3 -1.2 -1.2	-1.3 -1.3 -1.1	-1.3 -1.3 -1.3	-1.4 -1.4 -1.4	-1.4 -1.4 -1.3	-1.3 -1.3 -1.3
-0.31 -0.27 -0.52	-0.68 -0.92 -0.89	-1 -1 -0.96	-1.2 -1.3 -1.1	-1.5 -1.3 -1.4	-1.3 -1.4 -1.4	-1.4 -1.4 -1.4	-1.4 -1.4 -1.4	-1.4 -1.3 -1.3	-1.2 -1.2 -1.2	-1.2 -1.2 -1.3
-0.33 -0.53 -0.46	-0.73 -0.88 0.72	-0.97 -1 -0.93	-1 -1 -1	-1.3 -1.4 -1.4	-1.2 -1.1 -1.1	-1.2 -1.4 -1.5	-1.4 -1.4 -1.3	-1.4 -1.3 -1.3	-1.3 -1.3 -1.3	-1.4 -1.4 -1.4
-0.29 -0.37 -0.42	-0.59 -0.65 0.63	-0.88 -1 -0.94	-0.97 -1.2 -1.2	-1.2 -1.4 -1.4	-1.3 -1.3 -1.5	-1.4 -1.5 -1.5	-1.3 -1.3 -1.3	-1.3 -1.3 -1.3	-1.4 -1.4 -1.4	-1.4 -1.4 -1.4
-0.12 -0.32 -0.25	-0.49 -0.49 -0.5	-0.84 -0.88 -0.69	-0.88 -1.1 -1.4	-1.4 -1.5 -1.8	-1.6 -1.7 -1.9	-1.6 -1.6 -1.8	-1.6 -1.6 -1.9	-1.6 -1.5 -1.5	-1.5 -1.5 -1.5	-1.5 -1.5 -1.5
-0.2 -0.22 -0.13	-0.29 -0.26 0.25	-0.49 -0.49 -0.29	-0.62 -0.89 -0.56	-1.4 -1.7 -1.7	-1.9 -2.1 -2.7	-2 -2.2 -2.3	-2.1 -2.1 -2.2	-1.9 -1.8 -1.8	-1.6 -1.6 -1.6	-1.4 -1.6 -1.6
-0.26 -0.18 -0.2	-0.18 -0.21 0.17	-0.25 -0.32 -0.47	-0.32 -0.39 -0.31	-0.96 -1.4 -1.1	-2 -2 -4.2	-2.2 -3 -3.1	-2.2 -2.2 -2.8	-2 -1.8 -1.9	-1.7 -1.7 -1.7	-1.6 -1.7 -1.8

**Figure B1: Instantaneous external pressure coefficients resulting in the peak external suction, area-averaged over a single module for the  $G \approx 0$ ;  $H \approx 0$  configuration on the sloped roof model**

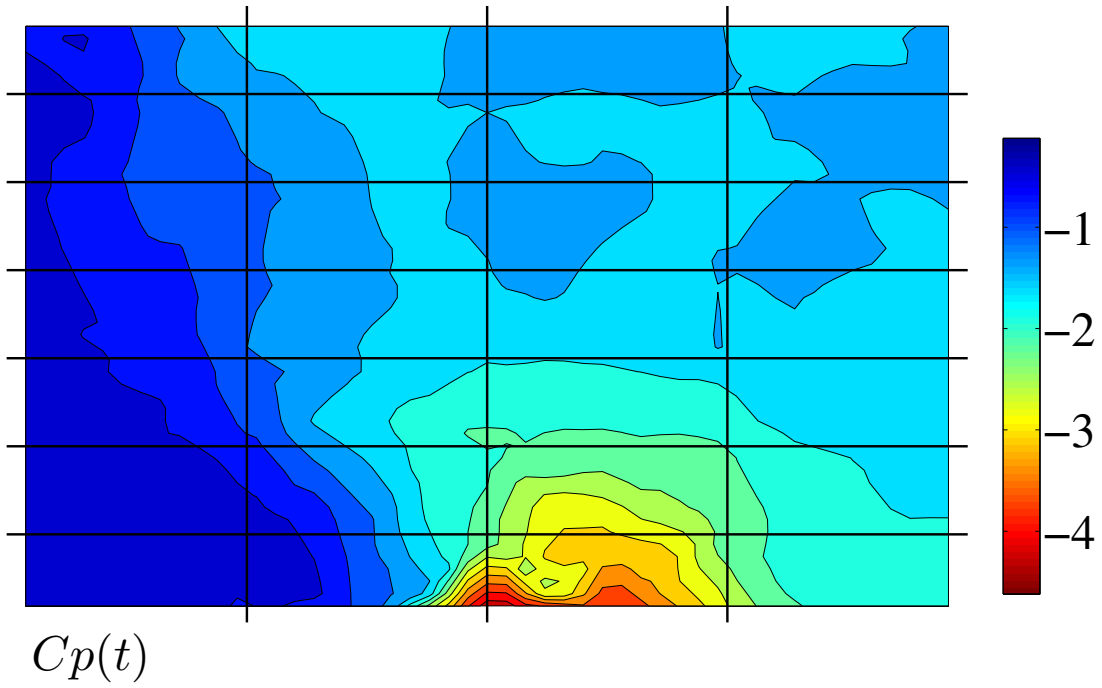


**Figure B2: Instantaneous external pressure distribution, evaluated for the entire array, which results in the peak external suction, area-averaged over a single module for the  $G \approx 0$ ;  $H \approx 0$  configuration on the sloped roof model**

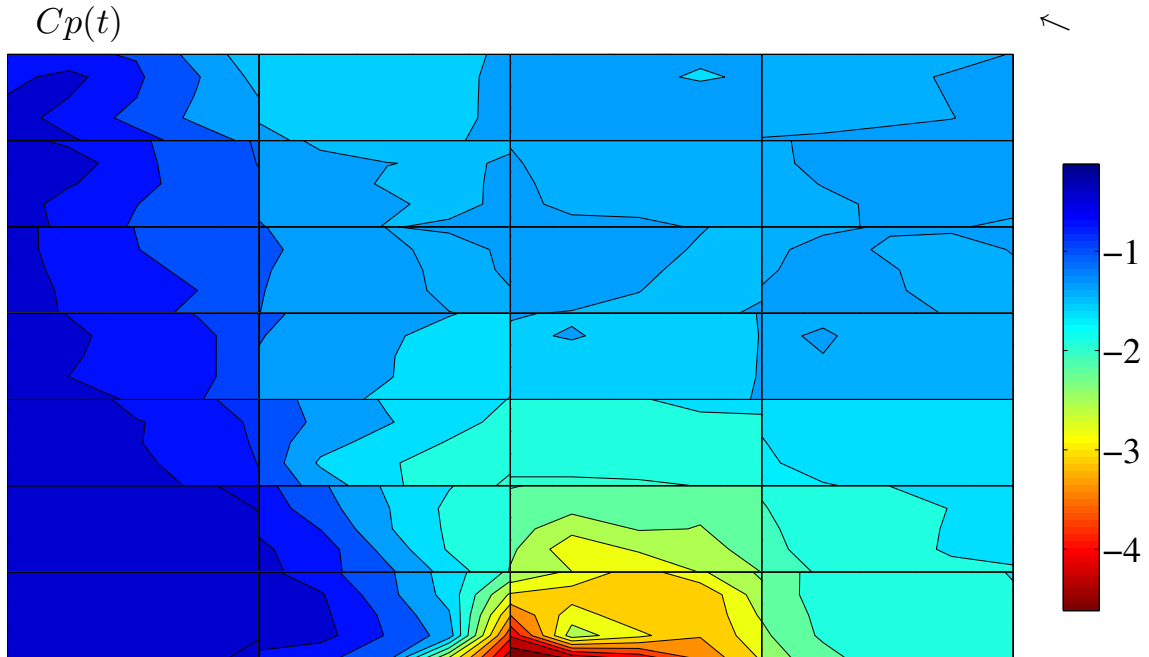


**Figure B3: Instantaneous external pressure distribution, evaluated for the individual modules, which results in the peak external suction, area-averaged over a single module for the  $G \approx 0$ ;  $H \approx 0$  configuration on the sloped roof model**

-5.7	-5.5	-3.9	-4	-3.6	-3.4	-2.5	-2.2	-1.5	-1.2	-1.1	-1.2	-1	-0.67	-0.76	-0.87	-1.2	-1.2	-0.68	-0.77
-2.3	-2.7	-2.7	-3.9	-3.7	-4.4	-3.3	-2.8	-1.9	-1.3	-1.1	-1	-0.84	-1.2	-1.1	-1.1	-1.1	-0.64	-0.77	-0.95
-3	-3.1	-1.5	-1.5	-1.5	-2.4	-2.2	-2.3	-2	-1.2	-1.1	-0.95	-0.86	-1.2	-1.1	-1.3	-0.85	-0.71	-0.69	-0.68
-1.8	-2.3	-1.8	-1.2	-1.6	-1.2	-1	-1	-1.2	-1.4	-1.4	-1.1	-0.87	-0.96	-0.91	-0.92	-0.87	-0.88	-0.76	-0.46
-1.7	-1.5	-1.3	-1.4	-1.7	-1.1	-0.69	-0.67	-0.71	-1.2	-1.4	-0.99	-0.73	-0.82	-0.82	-0.79	-0.77	-0.82	-0.7	-0.36
-1.8	-1.6	-1.5	-1.4	-1.3	-1	-0.87	-0.23	-0.53	-0.71	-0.83	-1	-0.67	-0.87	-0.8	-0.73	-0.68	-0.46	-0.44	-0.22
-1.7	-1.5	-1.5	-1.2	-0.93	-1.1	-0.54	-0.53	-0.76	-0.77	-0.77	-0.58	-0.56	-0.76	-0.82	-0.78	-0.54	-0.52	-0.26	-0.21
-1.9	-1.5	-1.4	-1.2	-0.71	-0.51	-0.61	-0.48	-0.69	-1.2	-1.1	-0.51	-0.46	-0.58	-0.41	-0.33	-0.41	-0.43	-0.25	-0.16
-1.9	-1.6	-1.2	-0.79	-0.57	-0.48	-0.47	-0.54	-0.93	-1.2	-0.98	-0.8	-0.63	-0.73	-0.69	-0.59	-0.39	-0.4	-0.24	-0.24
-1.7	-1.4	-1.2	-0.82	-0.75	-0.71	-0.51	-0.56	-0.6	-0.77	-0.86	-0.81	-0.87	-0.5	-0.47	-0.39	-0.24	-0.22	-0.37	-0.33
-1.6	-1.1	-1.3	-1.2	-0.95	-0.89	-0.84	-0.71	-0.69	-0.78	-0.86	-0.91	-0.72	-0.57	-0.51	-0.42	-0.33	-0.24	-0.3	-0.35
-1.3	-1.2	-1.1	-1.2	-1.1	-1	-0.79	-0.8	-0.72	-0.72	-0.71	-0.87	-0.78	-0.52	-0.47	-0.44	-0.36	-0.35	-0.4	-0.38
-1.2	-1.1	-1.1	-0.92	-0.92	-0.78	-0.84	-0.85	-0.67	-0.84	-0.83	-0.78	-0.6	-0.56	-0.45	-0.45	-0.38	-0.31	-0.29	-0.37
-1.3	-1.2	-0.87	-0.91	-0.84	-0.66	-0.77	-0.71	-0.76	-0.7	-0.61	-0.78	-0.77	-0.61	-0.52	-0.55	-0.45	-0.49	-0.41	-0.45

**Figure B4: Instantaneous external pressure coefficients resulting in the peak external suction, area-averaged over a single module for the  $G \approx 0$ ;  $H = 20$  cm configuration on the sloped roof model**

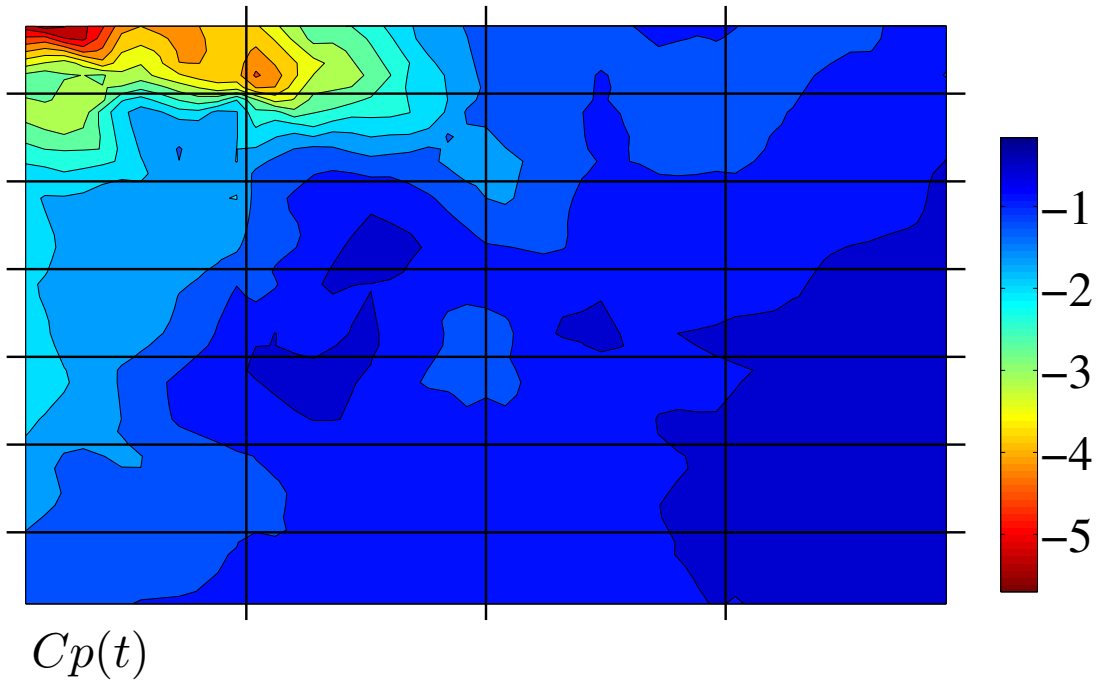


**Figure B5: Instantaneous external pressure distribution, evaluated for the entire array, which results in the peak external suction, area-averaged over a single module for the  $G \approx 0$ ;  $H = 20$  cm configuration on the sloped roof model**

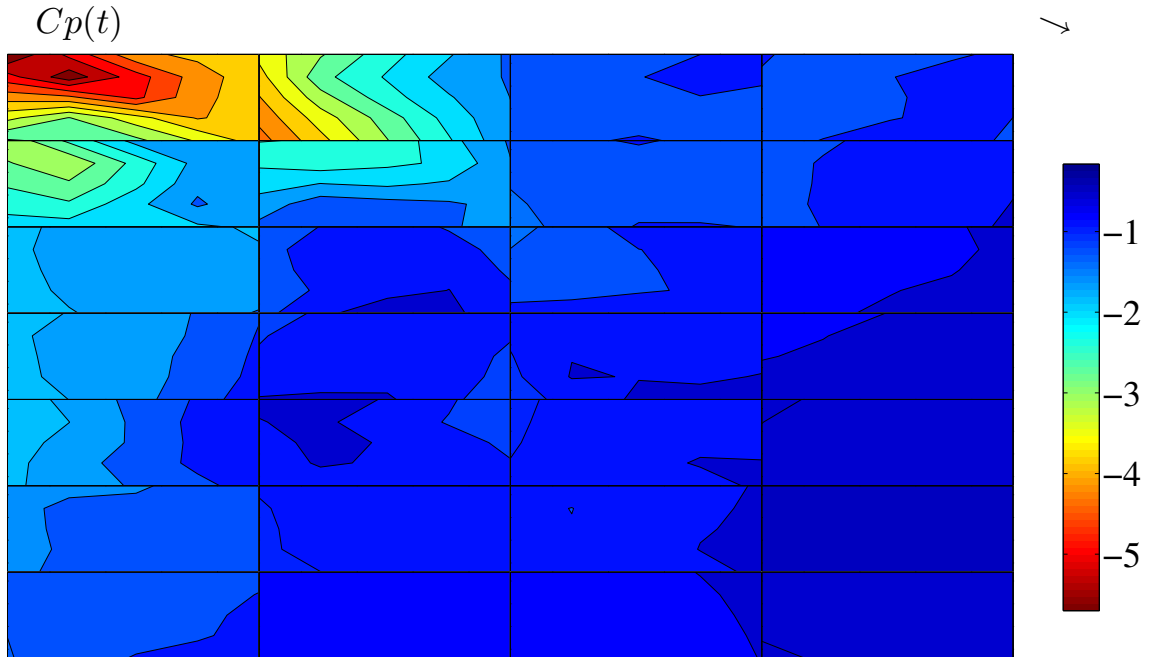


**Figure B6: Instantaneous external pressure distribution, evaluated for the individual modules, which results in the peak external suction, area-averaged over a single module for the  $G \approx 0$ ;  $H = 20$  cm configuration on the sloped roof model**

-0.78	-0.8	-0.79	-0.94	-1	-0.95	-0.76	-0.81	-0.63	-0.75	-0.72	-0.87	-1.1	-1.5	-1.6	-1.5	-1.6	-1.8	-1.9	-1.2
-0.77	-0.72	-0.8	-0.88	-0.86	-0.79	-0.85	-0.71	-0.61	-0.67	-0.7	-0.88	-0.95	-1.2	-1.1	-1.2	-1.3	-1.1	-1.8	-0.68
-0.7	-0.75	-0.77	-0.76	-0.79	-0.78	-0.82	-0.79	-0.73	-0.75	-0.73	-0.77	-1	-1.1	-1.1	-1.2	-1.1	-1	-1.5	-0.72
-0.66	-0.73	-0.7	-0.69	-0.73	-0.73	-0.79	-0.71	-0.7	-0.7	-0.69	-0.83	-0.78	-0.96	-0.88	-0.94	-0.82	-0.85	-1.9	-0.35
-0.58	-0.65	-0.64	-0.64	-0.68	-0.64	-0.67	-0.65	-0.74	-0.72	-0.69	-0.83	-0.78	-0.97	-0.88	-0.9	-0.87	-0.98	-1.5	-0.41
-0.54	-0.63	-0.63	-0.61	-0.68	-0.67	-0.66	-0.6	-0.66	-0.73	-0.71	-0.64	-0.64	-0.79	-0.76	-0.79	-0.64	-1.1	-1.2	-0.15
-0.53	-0.6	-0.61	-0.62	-0.67	-0.65	-0.64	-0.62	-0.64	-0.69	-0.74	-0.79	-0.66	-0.74	-0.71	-0.72	-0.75	-0.91	-1.3	-0.28
-0.52	-0.56	-0.6	-0.61	-0.68	-0.69	-0.66	-0.64	-0.63	-0.68	-0.75	-0.69	-0.64	-0.77	-0.62	-0.59	-0.82	-0.83	-1.5	-0.089
-0.5	-0.57	-0.6	-0.62	-0.68	-0.73	-0.72	-0.65	-0.68	-0.7	-0.71	-0.69	-0.69	-0.8	-0.69	-0.65	-0.55	-0.88	-1.1	-0.12
-0.43	-0.59	-0.57	-0.58	-0.7	-0.69	-0.74	-0.72	-0.71	-0.73	-0.73	-0.71	-0.7	-0.77	-0.78	-0.75	-0.6	-0.81	-1.3	-0.24
-0.46	-0.55	-0.59	-0.63	-0.71	-0.74	-0.82	-0.74	-0.76	-0.77	-0.77	-0.81	-0.74	-0.82	-0.67	-0.67	-0.43	-0.79	-1.4	-0.2
-0.59	-0.57	-0.57	-0.57	-0.71	-0.76	-0.82	-0.87	-0.86	-0.84	-0.88	-0.9	-0.92	-0.94	-0.72	-0.75	-0.6	-0.68	-1.3	-0.24
-0.49	-0.52	-0.53	-0.57	-0.77	-0.82	-0.98	-0.89	-0.9	-0.88	-0.84	-1	-0.89	-1	-0.75	-0.75	-0.52	-0.82	-1.1	-0.06
-0.45	-0.5	-0.49	-0.53	-0.89	-1	-1	-1.1	-1.1	-1.2	-1.2	-1.2	-1.2	-1.2	-1.3	-1.4	-0.91	-0.97	-0.93	-0.062

**Figure B7: Instantaneous cavity pressure coefficients resulting in the peak cavity suction, area-averaged over a single module for the  $G \approx 0$ ;  $H = 20$  cm configuration on the sloped roof model**

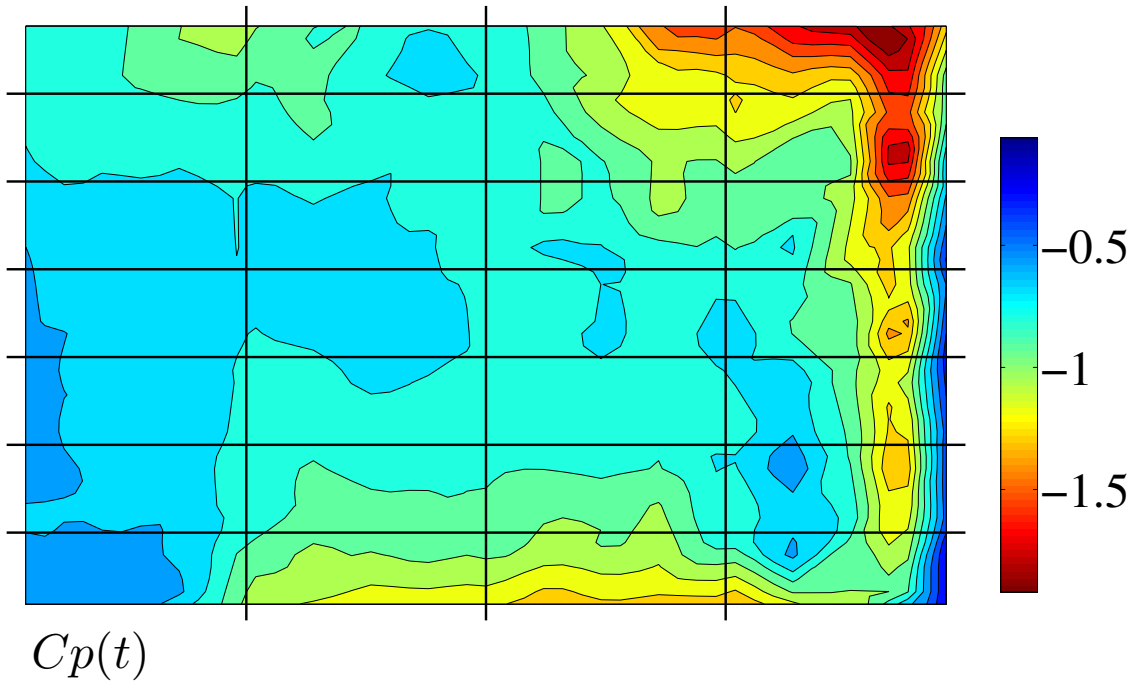


**Figure B8: Instantaneous cavity pressure distribution, evaluated for the entire array, which results in the peak cavity suction, area-averaged over a single module for the  $G \approx 0$ ;  $H = 20$  cm configuration on the sloped roof model**

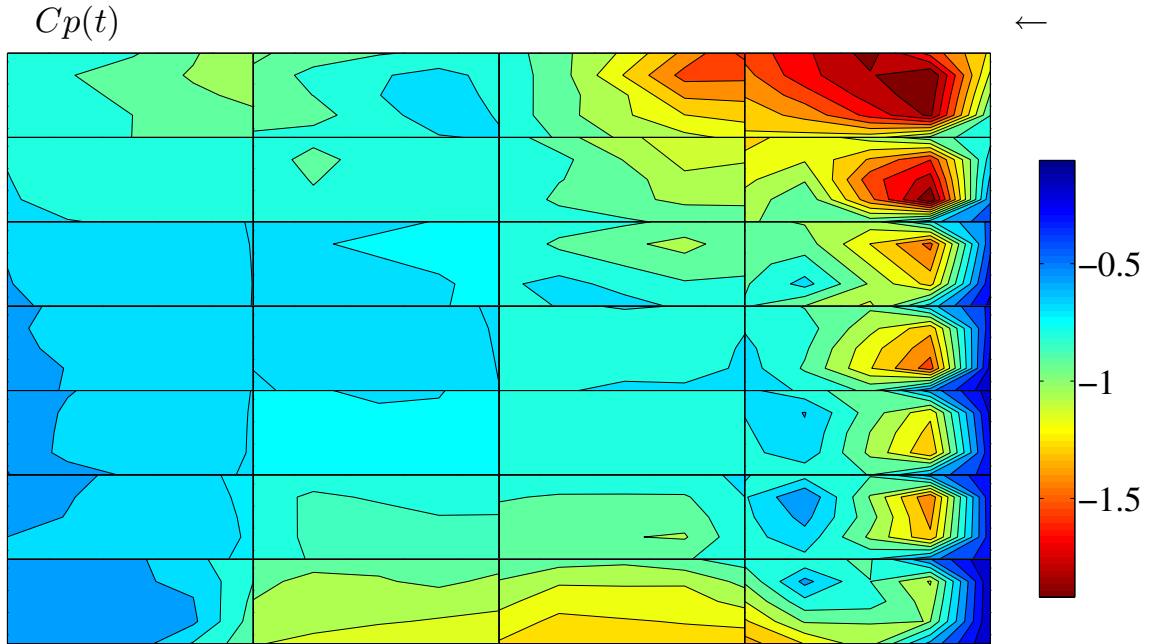


**Figure B9:** Instantaneous cavity pressure distribution, evaluated for the individual modules, which results in the peak cavity suction, area-averaged over a single module for the  $G \approx 0$ ;  $H = 20$  cm configuration on the sloped roof model

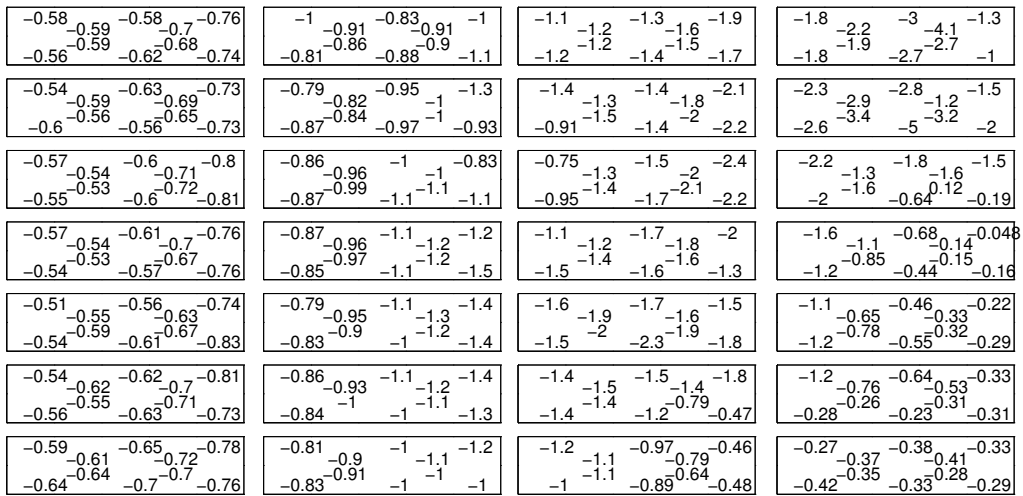


**Figure B10:** Instantaneous external pressure coefficients resulting in the peak external suction, area-averaged over a single module for the  $G = 12$  cm;  $H \approx 0$  configuration on the sloped roof model

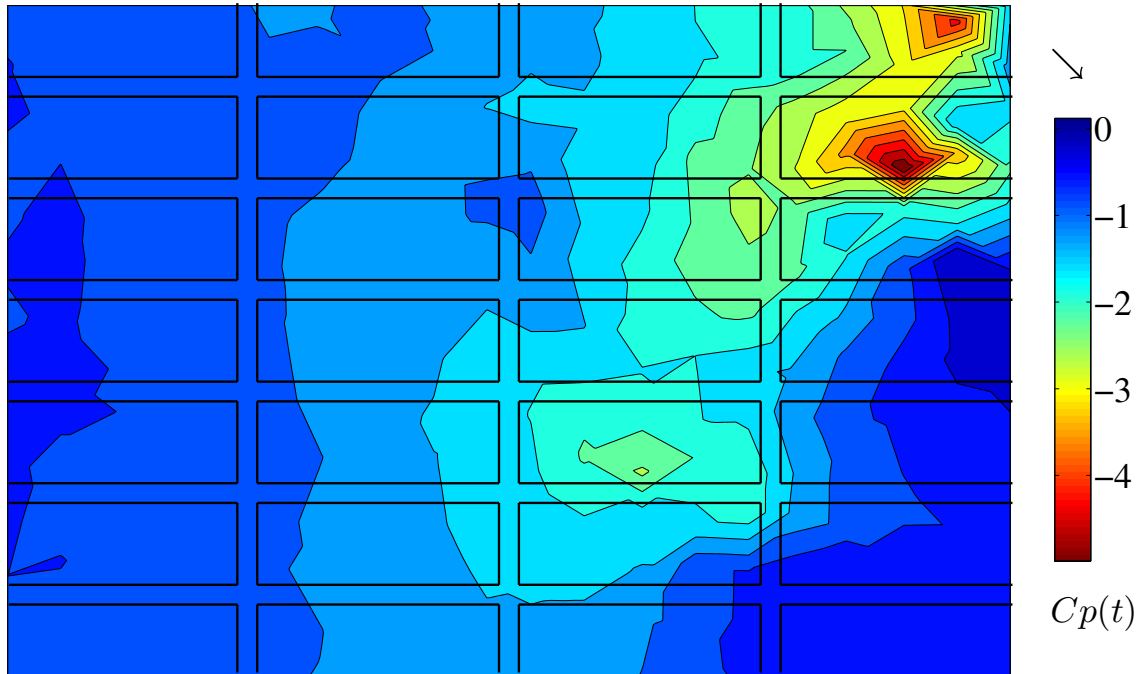


**Figure B11: Instantaneous external pressure distribution, evaluated for the entire array, which results in the peak external suction, area-averaged over a single module for the  $G = 12$  cm;  $H \approx 0$  configuration on the sloped roof model**

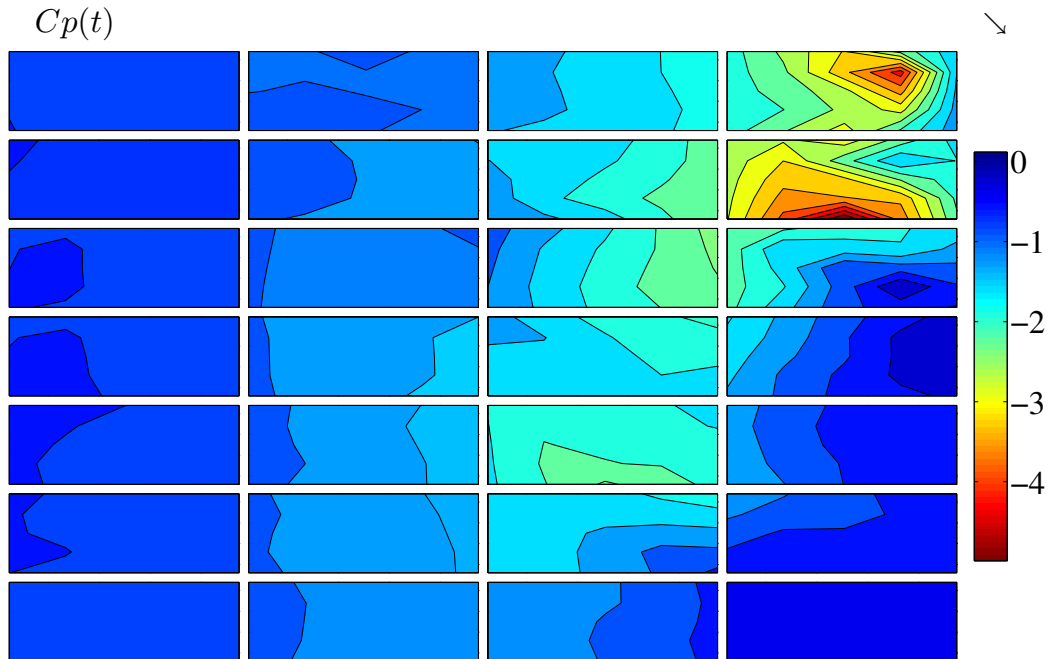


**Figure B12: Instantaneous external pressure distribution, evaluated for the individual modules, which results in the peak external suction, area-averaged over a single module for the  $G = 12$  cm;  $H \approx 0$  configuration on the sloped roof model**

## Curriculum Vitae

- Name:** Sarah Elizabeth Stenabaugh
- Post-secondary Education and Degrees:** University of Western Ontario  
London, Ontario, Canada  
2004 - 2009 B.Eng.
- Honours and Awards:** Top graduate oral presentation  
Department of Civil & Environmental Engineering Seminar Series  
2011
- Top undergraduate paper and oral presentation  
Canadian Society of Civil Engineering Annual Conference
- Related Work Experience:** Teaching Assistant  
The University of Western Ontario  
2010 – 2014
- Engineering Intern – Junior Technical Coordinator  
Rowan Williams Davies & Irwin Inc. (RWDI)  
2007 – 2008
- Publications:**
1. **Stenabaugh, S.,** Iida, Y., Kopp, G., & Karava, P. (2015). Wind loads on photovoltaic arrays mounted parallel to sloped roofs on low-rise buildings. *Journal of Wind Engineering and Industrial Aerodynamics*, 139 16-26.
  2. **Stenabaugh, S.,** Karava, P., & Kopp, G. (2011). Design wind loads for photovoltaic systems on sloped roofs of residential buildings. *13 ICWE*. Amsterdam, Netherlands.
  3. **Stenabaugh, S.,** Karava, P., & Kopp, G. (2010). *Design Wind Loads for Photovoltaic Systems on Sloped Roofs of Residential Buildings*. London, Canada: Boundary Layer Wind Tunnel Laboratory.